Ultrasound micromolding technique and real-time X-ray diffraction using synchrotron radiation. Applications to porous scaffolds for biomedical devices and study of thermal-induced transitions.

Cristian Olmo

Ultrasound micromolding technique and real-time X-ray diffraction using synchrotron radiation. Applications to porous scaffolds for biomedical devices and study of thermal-induced transitions.

Cristian Olmo Osuna

Directors: Dr. Jordi Puiggalí Dr. Mª Lourdes Franco

Department of Chemical Engineering
Polytechnic University of Catalonia

Barcelona, 2021

A mi padre,

Gracias.

Acknowledgments

I would like to express my deepest gratitude to my supervisors Prof. Dr.Jordi Puiggalí and Dr. Mª Lourdes Franco for giving me the opportunity to work in this project and be part of their team. I express my thanks to them for sharing their time and expertise and the valuable guidance within all this research.

I would like to extend my gratitude to Dr. Luis Javier del Valle for all the support provided, their time and the company during long nights spent in the synchrotron. I would also like to acknowledge the assistance and help provided by Dr. M. Teresa Casas.

I would also like to extend my gratitude to all the colleagues of PSEP and IMEM research group, especially to Ina and Angelica for their endless support and company. Many thanks for the collaboration of Juan Carlos Martinez, for his assistance during the work done in ALBA synchrotron and all the help provided.

I also like to express my thanks to my colleagues in Parets, with whom I share another lab. Many thanks for all the support provided and the time spent in and out of the office. I would like to express my gratitude to Arantxa Ametllo to provide me with the opportunity to combine this project with the job.

I would like to express my heartfelt thanks to my whole family and friends. Many thanks for all the shared time, the company in the tough time and all the happiness you provide me. Thanks for your support during all these years, just thanks for being there.

Abstract

Current market trend is moving to miniaturized specimens, especially in the biomedical field seeking high effective and less invasive treatment. For example, nanoneedles for controlled drug release or high resolution scaffold to mimic tissues fissures and textures. Ultrasound (US) micromolding is a new technique developed to the aim of producing microsized pieces based on the use of ultrasound waves as a heating source. This heating method is highly precise and can lead to extremely short cycling times compared to other conventional techniques. Moreover, the dosage of the equipment is also accurately designed to supply just the required amount of material. Thus, this method overwhelms other techniques to produce microsized pieces in terms of energy and material efficiencies.

This US micromolding technique has been proved to be suitable to the production of microsized pieces based on commodities, such as polyethylene, polymethylene oxide and polypropylene and biodegradable polyesters such as polylactide and polybutylene succinate. This PhD work explores further possibilities of ultrasound micromolding to the production of polymers with added value. The work is divided in two main blocks: the production of micropieces based on biodegradable polymers focused on biomedical applications and the application of this technique as a new method to obtain nanocomposites with a homogenous dispersion of the reinforcing material.

Polylactide (PLA) was selected as polymer matrix in the first block to produce drug loaded pieces and scaffolds with antibacterial activity or increased osteoconductivity by the incorporation of hydroxyapatite (HAp). Chlorhexidine (CHX) and triclosan (TCS), selected as representative bactericide agents, were successfully loaded with a homogenous distribution into the polymer matrix. Although high concentrations of CHX leads to PLA degradation and the subsequent deterioration of mechanical properties, this is minimal compared with that attained by using conventional melting processes. Drugs were slowly released from micropieces and presented clear bactericide and bacteriostatic effect against both Gram-positive and Gram-negative bacteria. Microporous scaffolds have been produced from the subsequent leaching of incorporated salts. By using NaCl cavitation problems could be avoided but pores interconnections were insufficient and a small amount of water soluble polymer (i.e. polyethylene glycol) was required in order to improve the leaching process. Final scaffolds showed enhanced cell proliferation compared to non-porous PLA. PLA/HAp scaffolds with a porosity degree close to 35% could be achieved with relatively good mechanical properties. Incorporation of HAp increased the thermal stability, hydrophilicity and cell proliferation with respect to neat PLA specimens.

Ultrasound waves are usually combined with the conventional method to produce nanocomposite (i.e. solution intercalation and melt mixing) to avoid nanoparticles aggregation and improve their distribution within the polymer matrix. Hence the second block of this PhD work studies the use of ultrasound micromolding technology in nanocomposites production. To this end, Poly(ε-caprolactone) and polyamide 12 were selected as polymer matrices whereas multi-walled carbon nanotubes (MWCNT) and Nanofil 757 (a non-organo modified clay) were chosen as reinforcing agent.

Both neat polymers and their nanocomposites were successfully micromolded with minimal polymer degradation under optimal molding condition (amplitude, force and time). US micromolding technique was revealed to be efficient in getting fully exfoliated nanocomposites according to X-ray diffraction data and TEM images, even when Nanofil 757 was selected. Moreover, the influence of both, MWCNT and Nanofil 757, on crystallization behavior and morphology were systematically studied by time resolved synchrotron experiments. Carbon nanotubes were effective nucleating agents and had a great influence on crystallinity. The incorporation of the clay by US micromolding had a clear influence on the final crystalline structure. An exhaustive study has been performed with the system Nylon 12/N757 finding that contrary to other processing technologies α' form was remains at room temperature, probably as consequence of crystallization in presence of nanoclay sheets and under a high shear stress. Crystalline polymorphic transitions of nylon 12 (i.e., the named α, α', γ and γ' forms) were also evaluated through analyses of real time synchrotron.

A final chapter of this thesis is devoted to the study of structural transitions of nylons 12 9, 8 9, 4 9, 4 5 and copolymers derived from 1,4-diaminobutane and different ratios of glutaric and azelaic acids (nylon 4, 5+9) in order to achieve deeper knowledge on the series of even-odd polyamides. These polyamides show different crystalline structure and structural transitions compared to the conventional polyamides, which root cause is still unclear.

Resumen

El uso de piezas de tamaño reducido se ha extendido en los últimos años como sinónimo de evolución tecnológica, especialmente en biomedicina, donde se están realizando grandes avances con el fin de mejorar la eficiencia de los tratamientos terapéuticos y aumentar el uso de procedimientos menos invasivos. Un ejemplo es el uso de agujas de escala nanométrica para una dosificación de fármaco más precisa o de complejos *scaffolds* capaces de reproducir con precisión las geometrías de una fisura en un tejido o hueso dañado. El micromoldeo por ultrasonidos es una novedosa técnica de moldeo nacida de la necesidad de obtener un método eficiente para la obtención de micropiezas. La técnica se caracteriza por el uso de ultrasonidos como fuente de calor donde el material se calienta desde dentro debido a la fricción. Gracias a la eficacia de este sistema de calefacción el micromoldeo por ultrasonidos presenta tiempos de ciclo extremadamente cortos y un alto rendimiento energético. Además, el equipo está dotado con un preciso sistema de dosificación que minimiza el desecho de material.

En anteriores trabajos se ha demostrado la viabilidad de esta técnica para moldear micro piezas basadas en poliolefinas comerciales y poliésteres biodegradables, ofreciendo grandes ventajas sobre el resto de técnicas de micro-moldeo. Partiendo de estos antecedentes el presente trabajo explora la posibilidad de producir micropiezas basadas en polímeros con un alto valor añadido. Concretamente el trabajo aquí expuesto se divide en dos partes, un primer bloque enfocado en explorar posibles aplicaciones biomédicas de micropiezas basadas en polímeros biodegradables y un segundo bloque en el que se estudia la posibilidad del uso de dicha técnica para la preparación de nanocompuestos.

La polilactida (PLA) fue seleccionada como polímero biodegradable en el primer bloque para la producción de micropiezas cargadas con fármacos y *scaffolds* con actividad antibacteriana o reforzada con hidroxiapatita (HAp) para incrementar su osteoconductividad. Actualmente el PLA se está utilizando en una gran variedad de aplicaciones biomédicas ya que es biocompatible y está aprobado para ensayos clínicos por la Administración de Medicamentos y Alimentos (*Food and Drug Administration*, FDA). Como agentes bactericidas se escogieron la clorhexidina (CHX) y el triclosan (TCS), ambos fármacos se cargaron con éxito en la matriz de PLA presentando una distribución uniforme. A pesar de que el uso de altas concentraciones de CHX era limitante ya que causaba una degradación del polímero ésta era insignificante comparada con la degradación sufrida al moldear PLA/CHX mediante otros sistemas de calentamiento convencionales. Ambos fármacos presentaron una lenta liberación desde la micropieza y una clara actividad antibacteriana. Los *scaffolds* porosos se prepararon por un proceso indirecto al remover la sal soluble en agua tras ser moldeada junto al polímero. Aunque era factible obtener piezas de PLA cargadas con NaCl sin problemas de cavitación o degradación del polímero la conexión entre los poros era insuficiente y una gran cantidad de sal quedaba retenida en la pieza final. Con tal de incrementar dicha interconexión y conseguir un *scaffolds* poroso libre de NaCl fue necesario agregar una pequeña cantidad de polímero soluble en agua, polietilenglicol (PEG). Los *scaffolds* finales cargados con TCS presentan una mejora en la proliferación

celular respecto a la pieza no porosa, un efecto bactericida y bacteriostático y una liberación más rápida. Durante el micromoldeo de las piezas PLA/HAp fue crítico el uso HAp libre de impurezas para evitar cavitaciones y amarilleamiento en las muestras. La incorporación de HAp mejoró la estabilidad térmica, la hidrofobicidad y la proliferación y colonización celular.

Los procesos convencionales para la producción de nanocompuestos (preparación por disolución y mezclado en fundido) suelen usar ondas de ultrasonidos para mejorar el proceso y evitar la aglomeración de las nanopartículas, aumentando así las interacciones refuerzo-polímero. Con esta premisa en mente el segundo bloque de esta tesis estudia el uso del micromoldeo por ultrasonidos para la producción de nanocompuestos. Específicamente se estudia la producción de dos tipos de nanocompuestos: una matriz de policaprolactona (PCL) con nanotubos de carbono (MWCNT) y una matriz de poliamida 12 (Nylon 12) con arcilla. Con las adecuadas condiciones de moldeo ambos nanocompuestos, así como sus polímeros no cargados, pudieron moldearse con una degradación insignificante. Tal como muestran los datos de difracción de rayos X y las imágenes de Microscopia Electrónica de Transmisión, el micromoldeo por ultrasonidos es un proceso adecuado para la obtención de nanocompuestos exfoliados en un solo paso, incluso cuando la arcilla utilizada no ha sido modificada orgánicamente (N757). La influencia de ambos agentes externos (MWCNT y N757) en el proceso de cristalización y la morfología cristalina se han estudiado mediante experimentos de sincrotrón en tiempo real. Los nanotubos de carbono actuaron como agentes nucleantes y tuvieron una clara influencia en la morfología cristalina, cuyo efecto se estudió a través de los datos de difracción de bajo ángulo (SAXS). La estructura final del nylon 12 cambió con la incorporación de la arcilla. Al contrario que con los otros procesos para obtener nanocompuestos la forma α', estable solo a alta temperatura, se mantuvo presente a temperatura ambiente en la muestras de nylon 12 micromoldeado en presencia de arcilla. Las transiciones polimórficas del nylon 12(formas α, α', γ y γ') también fueron estudiadas mediante los datos recopilados en los experimentos con radiación sincrotrón.

En un último bloque se han estudiado también las estructuras y transiciones estructurales de los nylons 12 9, 8 9, 4 9, 4 5, así como varias copoliamides derivadas de la 1,4-butanodiamina y distintas proporciones de ácidos glutárico y azelaico (nylon 4,5+9) mediante datos calorimétricos, espectrocópicos y de difracción de rayos X recogidos en barridos de calentamiento y enfriamiento. Estas poliamidas tipo *par-impar* muestran estructuras peculiares y unas transiciones estructurales diferentes a las de otras poliamidas convencionales y cuyo origen aún no está claro.

Table of Contents

1. Introduction

Polymers are macromolecules characterized by high molecular weight; these are formed by joining a large number of small molecules called monomers. Due its high molecular weight, polymers show good mechanical and thermal properties such as elasticity, flexibility, scratch resistance, high melting point and chemical resistance in comparison with other organic compounds. Polymers can be classified by different criteria such as source (natural and synthetic), synthesis process (condensation and addition), structural shape (linear, branched and network), thermal processing behaviour (thermoplastics and thermosets).

Although, there are some polymers in the nature, for example cellulose, silk or protein, nowadays there are many synthetic polymers. They are commonly known as plastics and due to their versatility and possibility to perform in several conditions these synthetic polymers are substituting conventional material (paper, steel, glass) in a wide range of applications. Depending on the final application, polymers are known as *commodity* or *speciality*. Polymers on the first group belong to daily use plastic such as bottles or chairs; these are massively produced and cheap. In the other hand *speciality* polymers, also known as high performing polymer, aim specific properties and are focused in certain market sectors, for example coating with barrier or flame retardant properties, polymer fibres used in engineering, biomaterials or micro electronical devices.

In the recent decades the use of polymers to produce microsized pieces has largely extended specifically in electronical, biomedical and biotechnology fields. Polymers are lighter, cheaper to manufacture and can be tuned to fit specific performances in comparison with metals or ceramics which are commonly used in this kind of application. For example polymers are used in electronical devices with small complex geometries, to replace metal in structural components where strength, rigidity and aesthetics are important. They are also widely employed as biomaterials for many applications such as sutures, materials for tissue regeneration, scaffolds and systems for controlled release of drugs in biomedicine and biotechnology in the search of biocompatibility and biodegradability.

1.1. Ultrasound micromolding: microsized pieces

The use of ultrasound field as heating source is an already well-known technique used when highly precise heating is required, for example in plastic welding. In this procedure a specific spots need to be accurately heated in order to melt just the welding points.[1, 2] Ultrasound heating is generated as a result of the inner friction between polymer chains. In contrast with the conventional heating process with ultrasound the material is heated in to outside. This process is clean, fast and energy efficient. Moreover, ultrasound vibration increases the motion of molecular chains and reduces the relaxation time of chain segments, leading to a viscosity drop and increasing the flow index.[3] Based on this concepts and the urgent need of equipment to mass production of micro scaled pieces that rises in the

last decades, especially for electronical or biomedical application (Some examples are shown in **Fig. 1-1**), several equipment have been developed to fill this gap.[4]

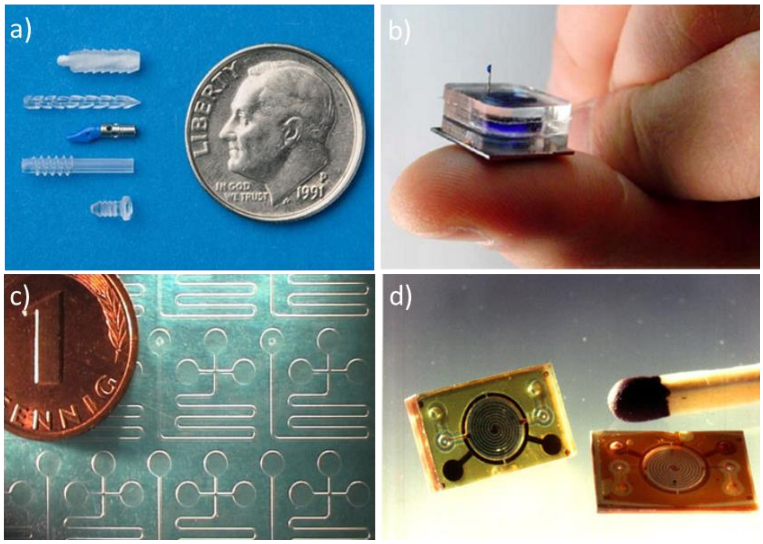

Fig. 1-1. *Examples of microsized pieces; implants screws (**a**), nanoneedles device (**b**), microchip (**c**) pump for microfluidic (**d**).*

Despite micro-injection molding is one of the most suitable systems for mass production it still have to afford two important challenges: material degradation and waste.[5] Microinjection equipment is a simple adaptation of conventional injection equipment where a microsized mold is connected by an adapted pipe. Hence microinjection is overdesigned; the amount of molten material in the extruder-based plasticization system is substantially bigger than the volume to be molded leading to long heating periods of the raw material which can produce thermal degradation. Moreover, the dosing system is not accurately designed and a big amount of raw material is wasted on the feeding system (sprues, gates, funnels). This has an important cost factor, especially for polymers required in high-performance applications.[6, 7] Ultrasound micromolding attained the best permanence over the current system to mass production of micro-sized specimens. It is highly energy efficient with shorter cycling time and an accurate dosing system with reduced wasted material. Although this process is economically efficient, quite high investment is still needed for installation and optimization of the molding condition and equipment. The molding parameters of this technique, wave amplitude and pumping pressure, are abstract compared to the conventional variables, time and temperature. Several studies are still on going in order to further understanding of the ultrasound transport mechanism within polymer material and its effect on the final properties. It has been concluded that an accurate setting up of the molding condition is needed for each polymer and polymer systems to avoid polymer degradation. [8]

The micromolding assays in this thesis are done by a first-generation prototype Ultrasound Molding Machine (Sonorus®, Ultrasion S.L., Barcelona, Spain) shown in **Fig. 1-2**. This is composed by a digital ultrasound generator (1000 W–30 kHz), a controller (3010 DG digital system, Mecasonic,

Barcelona, Spain), a focused piezoelectric transducer (Mecasonic, Barcelona, Spain), which converts electrical energy into kinetic energy and creates oscillatory movement, and an acoustic unit constituted by a booster and a sonotrode that operates in longitudinal vibration. The first element amplifies or reduces the wave amplitude (0–137.5 μm) while the second transfers vibration energy to the material and provides the pressure/force required to transfer it into the mold. The equipment is also provided with an electric servomotor control (Berneker and Rainer, Barcelona, Spain) fitted with software from Ultrasion S.L. (Barcelona, Spain), a little plasticizing camera and a mold capable to prepare 8 test specimens of dimensions 1.5 cm × 0.1 cm × 0.1 cm, and upgraded with an automatic ejection system.

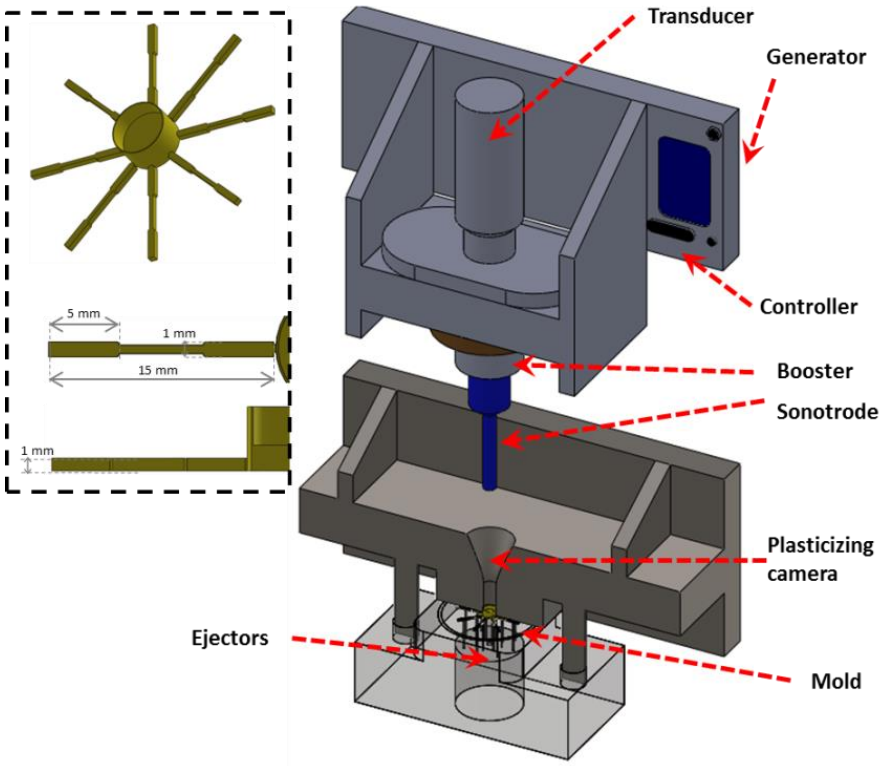

Fig. 1-2. *Scheme showing the main parts of the ultrasound micromolding equipment.*

As shown in **Fig. 1-3**, the complete molding process consists in three stages. In the first stage the mold is closed and the sonotrode is in the feeding position. (Stage I in **Fig. 1-3**). Then, the powdered polymer or mixture is loaded to the plasticizing camera by hand or automatically. The second stage is the main one; the powdered sample will be molded. It is also split in three sub processes: the sonotrode compacts the powdered mixture acting like a piston (II-a), then the sonotrode begins to vibrate as a consequence of the ultrasound vibration according to the given amplitude regulated by the booster. The polymer begins to flow and fills the mold cavities (II-b). After the time set up in the equipment the sonotrode vibration stops and the mold is cooled down while the sample is still compacted by the sonotrode. (II-c). In a final stage, with the mold open and the sonotrode in the feeding position, the sample is released from the mold by an ejection system.

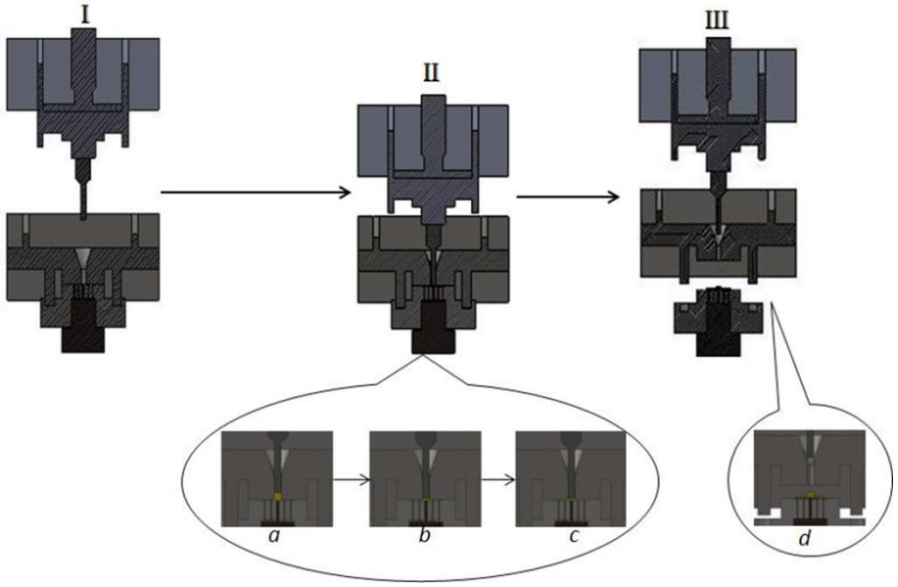

Fig. 1-3. *Scheme showing an example of a processed specimen and a schematic representation of the molding process (I: Feeding, II: Molding and III: Ejection stages).*

The work exposed in this thesis explores the viability of ultrasound micromolding to produce microsized pieces for biomedical application based on biodegradable polyester (polylactide); controlled drug release systems, production of biodegradable porous scaffolds and polymer matrix loaded with inorganic compound such as hydroxyapatite to improve biocompatibility. Manufacturing of nanocomposites in one step is also explored, specifically a polyester such as polycaprolactone reinforced with carbon nanotubes and clay nanocomposites with polyamide (nylon 12) matrix.

1.2. Biodegradable polymers

Biodegradable polymers are a special class of polymer that can be decomposed to natural products such as water, CO_2, N_2, biomass and inorganic salts. The polymer chain is broken down by the action of microorganism such as bacteria or fungi.

Although its main application is still to replace the use of non-recyclable polymer; especially for the one-use plastics such as shopping bags or disposable cups,[9, 10] in the recent decades this class of polymers also have earned a place in more sophisticated application specially for medical application. Its capacity to be decomposed by the host to nontoxic products brings many new opportunities. For example they are largely being used in tissue engineering as a temporary supports, since they are self-absorbing the surgical posttreatments are not needed.[11]

Polycaprolactone (PCL)

Polycaprolactone is a synthetic biodegradable polyester prepared by ring opening of ε-caprolactone (**Fig. 1-4**). PCL has very good chemical resistance and elastic properties, is hydrophobic and high crystalline, with low glass transition temperature and melting point (-60 ºC and 60 ºC, respectively). PCL has been approved by the food drug administration (FDA) for clinical assays and is

highly used as biomaterial, in particular for the preparation of long-term implantable devices and for drug delivery systems.[12, 13] The main limitations of PCL are a consequence of its relatively poor mechanical and thermal properties, thus nanocomposite based on PCL have brought a great interest in academic and industrial field. These also perform in a wide range of application with enhanced properties such as thermal stability, barrier performance or rapid biodegradability.[14, 15]

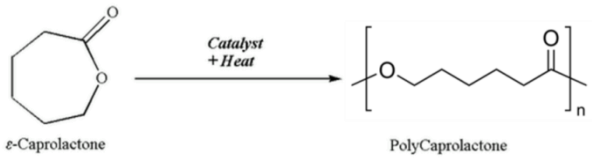

Fig. 1-4. *Representation of ε-caprolactone and polycaprolactone structures.*

Polylactide (PLA)

Polylactide is a biodegradable polyester that can be obtained from a renewal source such as sugar cane and starch. PLA is prepared by polycondensation of lactic acid or by ring opening of cyclic lactide dimer (**Fig. 1-5**), both raw material are byproduct of lactic fermentation. PLA has low crystallinity with a glass transition temperature and melting point around 60 ºC and 170ºC, respectively. PLA has good mechanical properties and processability, it is biocompatible, has low immunogenicity and is FDA-approved for clinical assays.[16] Therefore, its use in the biomedical field is widely extended. PLA is employed in medical implants such as screws, pins or meshes[17, 18], bio-absorbable sutures[19, 20], tissue engineering applications[21] and drug-delivery systems[22].

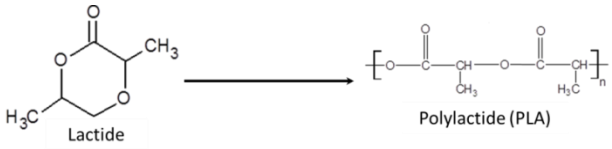

Fig. 1-5. *Representation of lactide dimer and polylactide structures.*

1.3. Biomedical applications

Nowadays there is an increasing market demand in the use of microsized specimens for medical and biotechnological application. The large amount of miniaturized medical devices such as microneedles and systems for microfluidic, in order to have more accurate and minimal invasive surgeries, is a clear example of that.[23, 24] Nano-sized biomaterials are also an example of these applications; these can be used in tissue engineering as temporal support to allow tissue or bone regeneration or even as a tissue replacement shaping challenging geometries.[25] Additionally, these biomaterials can also be used as a drug delivery system which prevent possible infections and facilitate the tissue acceptation.[26]

1.3.1. Drug delivery systems

The conventional systems for drug dosing such as pills or injections are limited in some applications due to their low targeting of the drug activity and the imprecise control of the drug concentration. Drugs have short life time in the bloodstream, these are consumed before reaching their objective, and thus overdesigned doses are needed in order to guarantee the drug activity. Moreover, the drugs also diffuse within the healthy tissues and organs spreading its drug activity, which leads to poor drug-targeting and additionally drug amount waste. Large amount of works have carried out in order to design proper drug delivery systems and improve the drug activity efficiency.[27]

Polymer-drug systems have attained very good results. The concept of this system is to use the polymer as a vehicle or support to protect the drug until it reaches the objective. These systems are also being used in biomaterial field to control the release, to preserve the drug activity longer time and avoid overdoses. The drug release can follow exponential and constant profiles or even more complex ones with delay or pulsatile releases, some examples are shown in **Fig. 1-6a**. Achieving these release profile is quite complex hence the polymer-drug system must be properly designed. Among all the parameters that affect like polymer drug affinity, type of polymer, drug pathway and target condition the release mechanism is one of the most important. Schematic representations of the typical mechanisms are shown in **Fig. 1-6b**.[28]

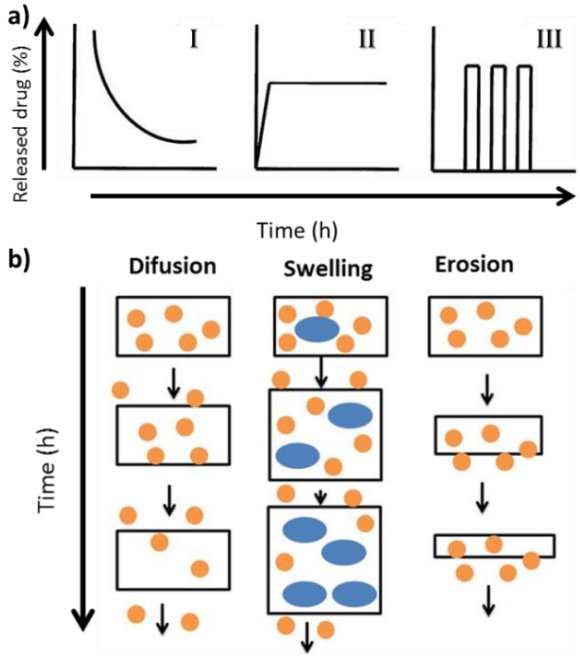

Fig. 1-6. ***a****) Examples of released profiles: exponential decreased (I), constant (II) and pulsatile (III).* ***b****) Schematic representation of typical drug released mechanism (orange circles represents the drug and the blue ones water).*

Recently it has been studied the possibility of use smart polymer for drug delivery. These polymers respond to external signal, for example pH or temperature variation. The release mechanisms of these polymers are based on a shape or morphology modification in response to external signal

variation. Hence the drug is released just in the moment is required. For example antibacterial drug released in response to pH variation, insulin dosage depending on the glucose bloodstream concentration (*Fig. 1-7*) or systems that response to external magnetic field to provide a pulsatile profile.[29]

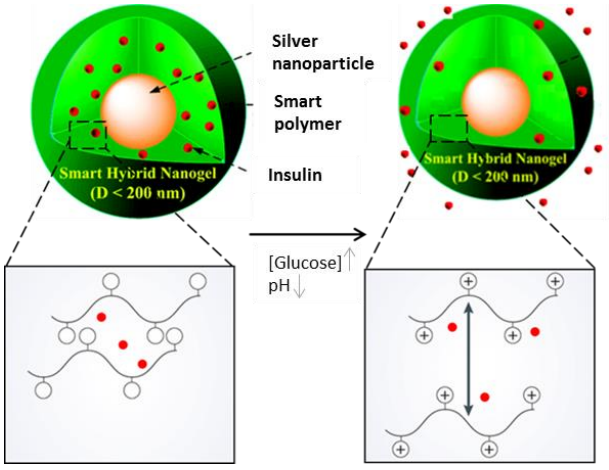

Fig. 1-7. *Drug delivery system based on smart polymer able to release insulin in response of glucose concentration.*

Conventional melt processing methods, such as injection or extrusion systems, are limited for mass production of drug delivery systems. Their long cycle time, high temperatures and mechanical stresses leads, in most cases, to drug degradation and biologically inactive agents. Due to its characteristic short cycle times and high effectiveness heating, ultrasound micromolding seems a proper procedure to produce drug-delivery pieces with their final shape in a single step.[30] [31]

1.3.2. Tissue engineering: Scaffold

In the recent decades, the tissue engineering has emerged with the goal of developing new materials to enhance tissues and bones self-regeneration. These act as a template to the tissue growth and can improve their final performance with additional functions.[32, 33] Efforts are mainly focused to guide cell growth,[34] to increase the biodegradability of temporal supports, to decrease cytoxicity,[35]to produce nanocomposites reinforced with particles or fibers in order to improve adhesion and cell proliferation,[36] to incorporate growth factors and other bioactive agents in order to stimulate cell growth[37, 38], to give an antimicrobial response or other effects such as radical scavenging,[39] and finally to develop materials with electroconductive properties that make feasible an electrical stimulation or a controlled drug release.[40]

Tissue engineering has developed the so-called scaffolds (**Fig. 1-8**), which are biomaterials that mimic the extracellular matrix of a tissue. Scaffolds are three-dimensional supports usually with high porous density which can enhance the tissue regeneration by increasing the cell adhesion and proliferation.[41] Furthermore, porous scaffolds may also enhance cell transit and diffusion of nutrients and growth factors.[42]

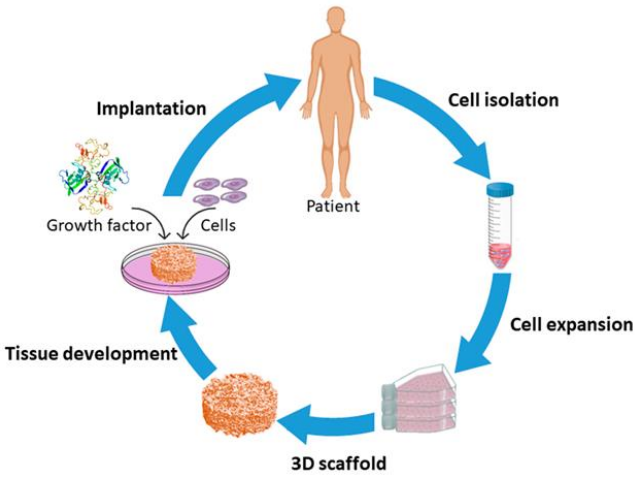

Fig. 1-8. *Schematic representation of scaffold application.*

In the beginning those scaffolds were produced by animal tissue but now the use of polymer material to fabricate them is more common. Polymers can provide such a huge range of properties, are easier to obtain and bring more versatile applications. Biodegradable polymers are usually employed when scaffolds must have a temporary function and act as templates for tissue repair and regeneration. Polymers used in the scaffold have to be appropriately selected thus degradation rate and maintenance of structural properties should be in agreement with the time required for tissue regeneration.[43, 44]

There are several methods to obtain a porous polymeric scaffold; some of them can directly generate the pores while in other cases a secondary treatment is needed. Deposition and assembly of micro/nanofibers is a common one-step process. These meshes can be produced by the bonding of different fibers, where some of them (with lower melting point) act as a reticulation point, or by electrospinning. The binding process is simpler but the porosity grade is not under such accurate control as could be achieved through electrospinning.[45, 46] Most of direct processes developed for scaffold production are limited to a laboratory scale and are not widely applied in the industrial field. In the other hand, indirect procedures are more common in big mass production and also they allow a fabrication with the desired final shape.[47] Conventional industrial procedures, such as extrusion or injection can be applied when are combined with the salt leaching technique. In this case, the polymer is mixed with a water-soluble salt and then molded. Porosity is created after removing the salt by water immersion. Porous size and density can be accurately controlled through the selection of both particle size and the incorporated amount of salt.[48, 49] Some examples of scaffold made from these methods are shown in **Fig. 1-9**.

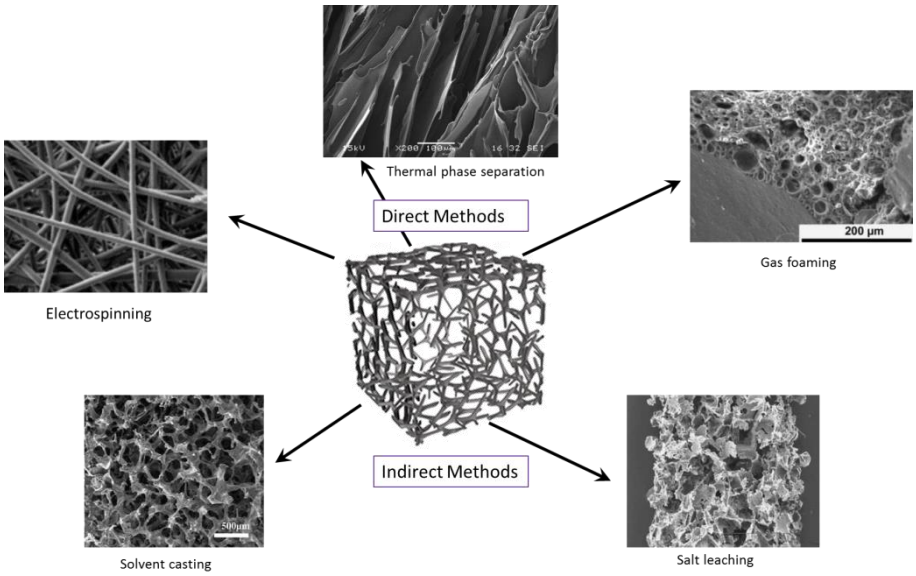

Fig. 1-9. *Conventional methods to produce polymer scaffolds.*[47, 48, 50-52]

There is a need in the market to reach a proper method to produce high-resolution scaffolds able to produce shape profiles with nanosized ending to mimic fissures and textures of naturally occurring tissues. Despite 3D printing can reach this scale with high accurate ending, it is still high cost production to be used for mass production.[53, 54]

Moreover, scaffolds can also be considered as drug releasing systems because due to their porosity these have high specific surface and, therefore can release larger amount of drug. The polymer matrix is loaded with the appropriate active agent, for example triclosan, which is commonly used as a biocide, providing a temporary support with bactericide effect.[55]

1.3.3. Hydroxyapatite composites

As above mentioned the aim of tissue engineering is the regeneration of the damaged tissue using a biocompatible, biodegradable and cell colonizable material. Although tissue graphing has been very useful for long time it is still a challenging process; autograph (tissue from own patient) gathering is expensive, painful and anatomically limited; and allograph (external tissue) is too sensitive to patient rejection. Therefore, efforts focus to develop biocompatible synthetic polymeric systems to produce porous matrices (scaffolds). One of the most promising approaches is having polymer matrix loaded with hydroxyapatite (HAp) particles.[56]

Hydroxyapatite is a calcium phosphate mineral with the formula $Ca_{10}(PO_4)_6(OH)_2$, its crystalline structure is shown in **Fig. 1-10**. It is the main inorganic constituent of bones, represents around 70% of human bone weight. HAp is found in nature and can alternatively be synthesized by precipitation or hydrolysis following well-standardized procedures.[57, 58] The use of HAp alone as a ceramic implant is limited because it is extremely brittle with low mechanical strength and fatigue

failure.[59, 60] Thus, HAp is usually employed in a wide variety of biomedical applications in the form of composites, providing high bioactivity and biocompatibility to the polymer matrix.

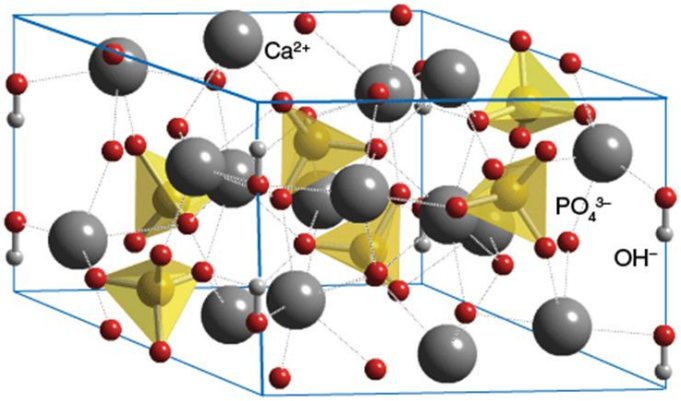

Fig. 1-10. *Schematic representation of hydroxyapatite structure.*

HAp composites scaffolds have largely been used in bone repair applications, being demonstrated very good osteoconductor and osteoinducer behaviors.[61, 62] These scaffolds are consequently able to increase the concentration of osteoblast cells when compared with the neat polymer scaffolds.[63] Moreover, the presence of HAp improves adhesion by absorption of proteins and enables the differentiation and gene expression of osteoblasts.[64].

HAp composites can be prepared by several processes such as induced phase separation,[65, 66] *in situ* polymerization,[67, 68] mechanical dispersion, melt blending,[69] *in situ* precipitation and ultrasound methods.[70]

1.4. Composites and Nanocomposites

A composite material consists in a mixture or two or more components with different physical and chemical properties. The components of the composite are maintained separated and can be distinguished in the final material, which differs from alloys or solution materials. These materials present enhanced properties in comparison with the pure material or even show some characteristics not seen in the individual compounds. Composites can perform excellent mechanical resistance with reduced weight and price. Moreover, these can provide specific properties such as fire retardant, conductivity or corrosion resistance.

Synthetic composites have been used from thousands of years, like cartonnage or polywood. Cartonnage was used in the first period of Egypt (2181-2055 BC) to the fabrication of death mask (**Fig. 1-11**). Polywood was used for building and furniture construction in Ancient Mesopotamia, 3400 BC[71]. One of the more popular ancient synthetic composite used as a building material is the abode, a combination of mud and straw (**Fig. 1-11**). Mud can be dried out into a brick shape for construction purposes; it has good compressive strength but it breaks quite easily if you try to bend it (poor tensile strength). On the other hand, straw brings stretch strength and water absorption. By combination of

these materials, mudbricks are resistant to both squeezing and tearing and make excellent building blocks[72]. It has been used for more than 6000 years and, though nowadays the use of mudbrick has been substituted for modern composites such as concrete or reinforced concrete, it is still an important method in many parts of the world. Concrete is also a composite used widely around the world, about 7.5 billion cubic metres of concrete are made each year[73]. Its use dates from 25 BC and consists in a mixture of fine and big aggregates bonded together with fluid cement.

Fig. 1-11. *Anubis death mask made of cartonnage (up left), mudbricks made of adobe (down left) and Ksar construction done with adobe bricks (right).*

Composites have evolved from this simple mixture base on mud, wood or aggregate to an enginery material which exceptional performances. Around 1930s what is known as fibre-reinforced polymer (FRP) was launched and, in the second half or 20th century, the use of FRP increased in a lot of commercial sectors with a wide range of applications[74]. The versatility of polymer to adapt to several kind of application and their low cost production made them attractive to their use as composite matrix. Global polymer production surpassed steel production in 1970s.

FRP are composites based on polymer matrixes reinforced by glass, carbon or aramid fibers. These composites are characterized by excellent mechanical properties with extremely low weight and reduced cost production. FRP are the best suited for any design that demands weight savings, precision engineering, definite tolerances, and the simplification of parts in both production and operation. To mold a polymer is cheaper, faster, and easier to manufacture than a cast aluminum or steel product. Therefore, polymer composites are mainly used in automobile sector. Some examples are shown in **Fig. 1-12**.

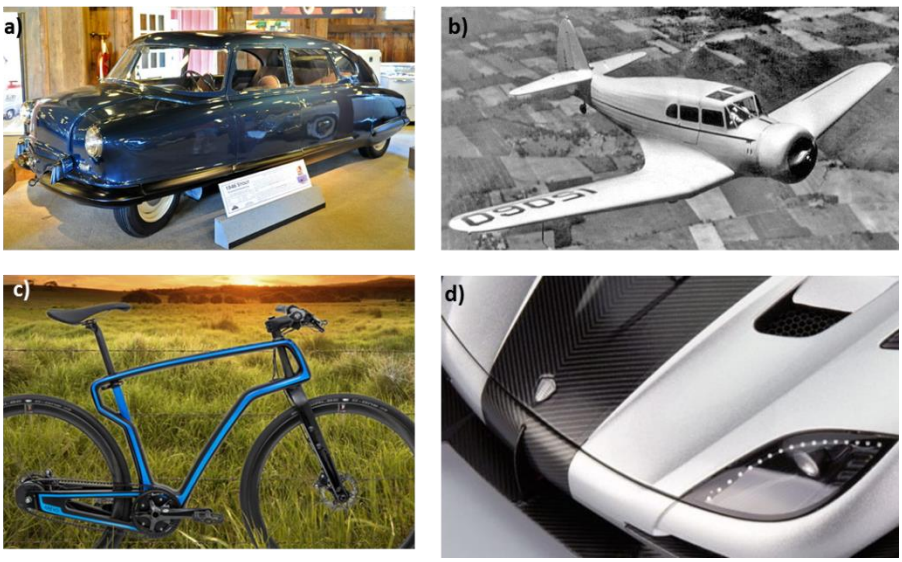

Fig. 1-12. *Examples of polymer reinforced fiber applications: Stout Scarab 1946 first car to have fiberglass body (**a**), Fairchild F-46 light aircraft built using composites (**b**), bike (**c**) and front hood of race care (**d**) made of carbon fiber.*

Composites also exist in natural way such as wood or bone. Wood is a composite made of long fibers of cellulose held together by lignin and bone is based on a polymer matrix (collagen) reinforced with hydroxyapatite particles. Indeed, bone is a nanocomposite.

Nanocomposites are an especial type of composite which use has grown in the recent decades. The enhanced properties of composites are mainly based on the interphase interaction between the composite components. In the case of nanocomposites the dimensions of the reinforcing material are in range of nanometres, increasing in that way (higher specific surface) the interphase interaction bringing even better properties and the possibility to perform in the same way with less amount of reinforced material.[75]

Due to their easy processability, low cost and tuneable properties, polymer nanocomposites are versatile material whose use nowadays is significant in many industries, especially in medicine, biotechnology, electronic and engineering materials. Typical reinforcing materials such as glass nanoparticles, tubular nanotubes or laminar clays have been used in order to improve mechanical and thermal properties of polymer matrix. [76, 77] In the search of specific properties extended number of studies has been done, some examples are following listed and shown in **Fig. 1-13**.

- Antibacterial polypropylene filled with nano-seized silver particle [78]
- Oxygen barrier coating for food packing base on Poly (ethylene terephthalate)/ organoclays dispersion. [79]
- Nylon 6 with improved electric conductivity by loading of multiwall carbon nanotubes[80]
- Flame retardant nylon 6/clay nanocomposites[81]
- PLA/HAP scaffolds with improved biocompatibility and osteoconductivity for tissue engineering.[82]
- PMMA/HAP nanocomposite as provisional dental implant.[83]

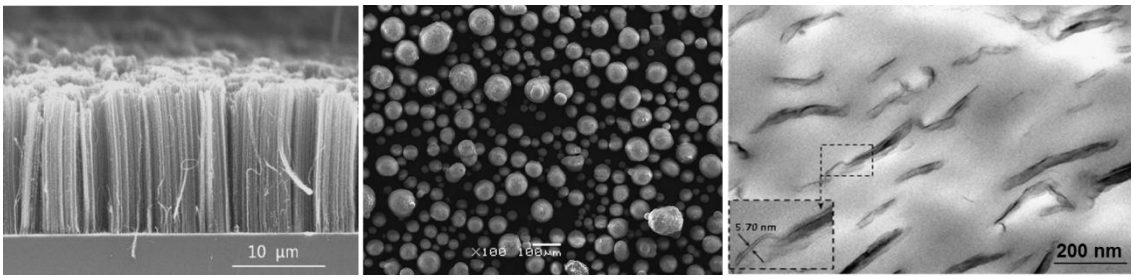

Fig. 1-13. *SEM scans of nano-reinforcing materials; forest of carbon nanotubes and nano-scale particles of hydroxyapatite, and a nanocomposite: Nylon6/MMT (left to right).*

1.4.1. Multiwall carbon nanotubes (MWCNT) nanocomposites

Carbon nanotubes (CNT) were discovered in 1991 by Sumio Iijima.[84] CNTs are rolled up graphene sheets into cylindrical shape and normally are capped with half shape of fullerene structure. These CNTs can be classified as single walled carbon nanotubes (SWCNT) or multi walled carbon nanotubes (MWCNT). SWCNT consist in a single rolled sheet of graphene whilst MWCNT are based on a staking of concentric layers of several rolled graphene sheets (**Fig. 1-14a** and **b**). CNTs have excellent mechanical properties such as high tensile strength and Young's modulus, high aspect ratio and low density.[85] Such properties are highly depending of morphology, size and diameter. CNTs can also perform as metallic or semiconductors, depending on the atomic arrangement. According to the atomic arrangement, rolling angle of the graphene sheets, there are three types of structure zigzag, armchair and chiral structures (**Fig. 1-14c**).

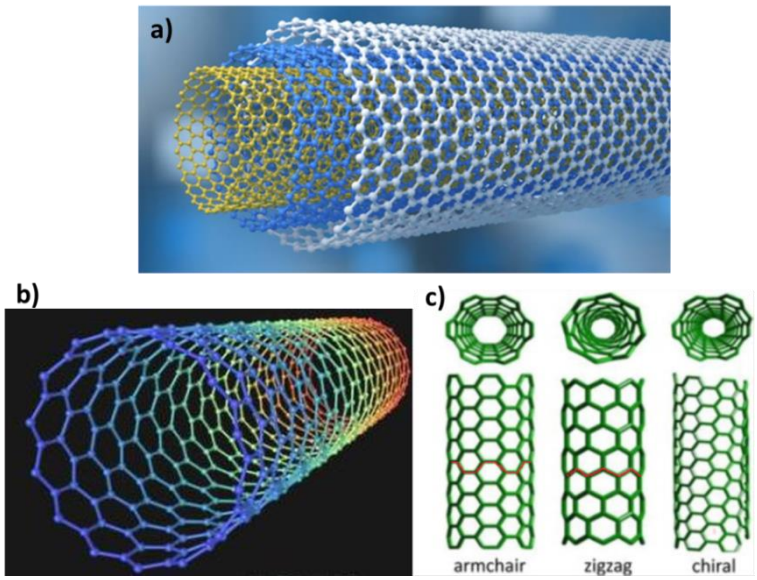

Fig. 1-14. *Model representations of MWCNT (**a**) and SWCNT (**b**) and its possible forms (**c**).*[86]

Ajayan *et al.* reported the first carbon nanotube reinforced polymer in 1991[87] and nowadays its use has extended in a vast range of applications. Reinforced polymer/CNT systems are used in industrial application such as sporting goods and automobile engineering due their improved

mechanical properties.[88] These can also be used as flame retardant and anticorrosion protections.[89] In the recent years, the most of the studies were focused in the use of CNT/polymer nanocomposites for electronic application. These are mainly used as field-emission devices[90, 91], in solar panel to produce light and flexible layers[92] and in aerospace engineering as anti-radar and antistatic paints.[93, 94]

Although melt processing, in-situ polymerization and solution mixing are well established methods to produce nanocomposites they still have to deal with the trend of carbon nanotubes to render high agglomerations. A wide range of polymers like PMMA, PVA, polystyrene has been processed by solution mixing and is the most suitable method for mass production.[95, 96] In order to improve CNTs dispersion many variations of this technique have been studied; for example the use of surface modified CNTs[97] ,ultrasonic agitation within the CNTs dispersion or by using spin casting or electrospinning to avoid agglomeration after solvent evaporation.[98, 99]

1.4.2. Clay Nanocomposites: structure and preparation methods.

Polymer nanocomposites based on reinforcing clay have received a great attention in the last two decades from science and technology point of view, especially the ones based on layered silicates.[100, 101] Early nanocomposites were nylon 6 matrix reinforced with organo-modified montmorillonite, this nanocomposite showed a clear improvement in thermal and mechanical properties.[102-104] Numerous studies describe the benefits of using montmorillonites (MMT) for a wide combination of polymer matrixes. As already mentioned it enhances the mechanical and thermal properties, additionally it could bring special properties such as flame retardant, heat resistance, dimensional stability, optical and barrier properties. The properties presented and the grades of enhancement are directly linked to the degree of delamination and dispersion, which depend on the chemical modified and the obtaining process.

MMT are a kind of phyllosilicate whose crystalline structure consists in two tetrahedral sheets coordinates by oxygen and silicon atoms, symmetrical and fused by an octahedral sheet form by magnesium or aluminium atoms. These 2:1 layers are bonded each other by van der Waals forces (**Fig. 1-15**). On contrary of the more common clay minerals used as fillers, talc or mica, MMT can be delaminated and dispersed in individual layer, the relatively weak forces between layers make possible the penetration of polymer chain in the gallery (gap between layers) and the subsequent clay delamination. The thick of these layers are usually around 1nm while the length can vary between 30 nm and several millimetres. Thus, the MMT layers present extremely high aspect ratio and high specific surface, which bring the huge properties improvement. In addition, it is environmentally friendly, naturally occurring, and readily available in large quantities.

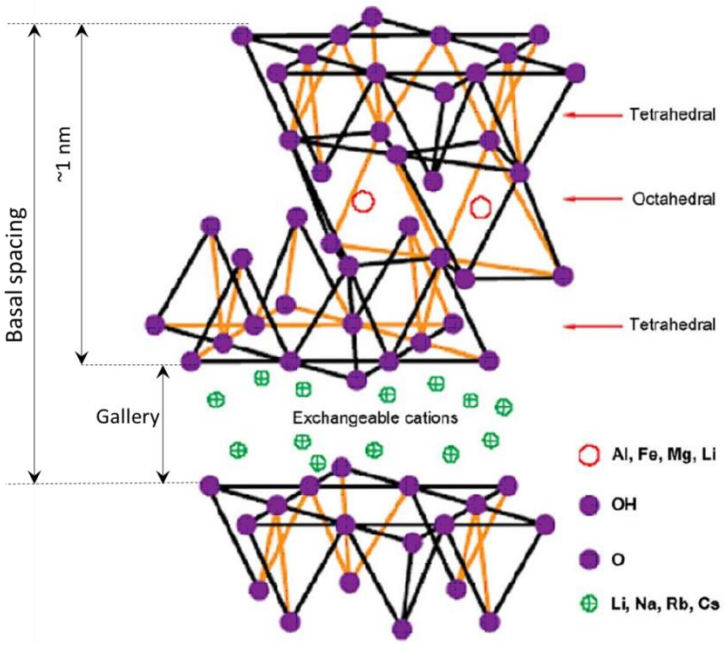

Fig. 1-15. *Schematic representation of MMT structure.*

Although the penetration of polymer chain into the layers gap is theoretically possible, the inorganic character of the mineral clay hinders it, leading to unappropriated clay dispersion with negligible properties enhancement. In order to improve the compatibility between clays and polymer matrixes the clays are usually modified to produce what is known as organo-modified clay or organoclays. In this process the alkaline counter ions (e.g. Li or Na), placed in the gap between layers, are exchanged with alkyl ammonium ions.[105] These alkyl ammoniums reduce the surface tension and increase the hydrophobicity of the inorganic layers. Moreover, some of the organic ions can have functional groups, such as amine or hydroxyl, which also improve the polymer/clay interaction. Organic ions are bigger than the inorganic counter ions, and consequently the gap between layers increases (**Fig. 1-16**) which helps in the nanocomposite formation.

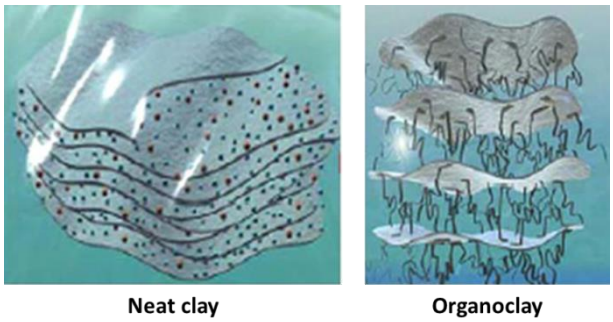

Fig. 1-16. *Schematic representation of the gallery wide increase of an organo-modified clay.*

The nanocomposite structure can be classified as phase separation, intercalated or exfoliated accordingly to how clay's layers are distributed within the polymer matrix.[106, 107] Phase separation occurs when the polymer cannot penetrate into the gallery of the silicate, the degree of improvement in performance is not huge, is closer to a composite rather than nanocomposite. Intercalated

nanocomposites present an increase of the gallery wide in a crystallographically regular way, not linked to the clay amount. The properties of these ones are close to ceramic materials. In the case of exfoliated nanocomposites, the silicate layers are isolates and homogeneously spread through the whole polymer matrix. In this type of nanocomposite the clay-polymer interaction has exponentially been extended, thus the properties can be improved in high level with minimum amount of clay. For this reason, exfoliated structures are the preferred ones. Schematic representations of the above-mentioned structures are displayed in the ***Fig. 1-17***.

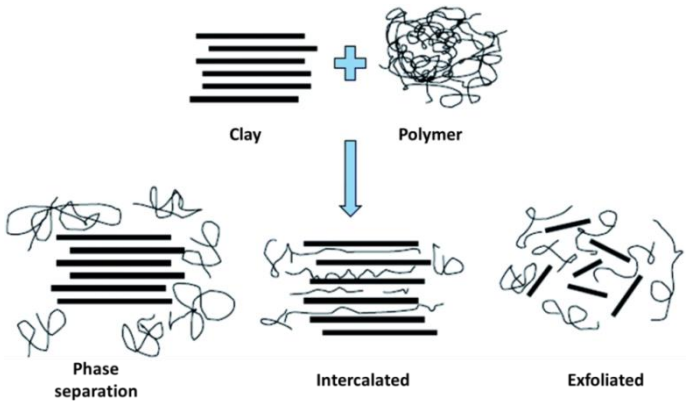

Fig. 1-17. *Schematic representation of the three thermodynamically possible structures of clay-polymer nanocomposites.*

There are several methods to prepare polymer nanocomposites based on MMT, but commonly the following three are used (**Fig. 1-18**):[107]

- *In situ* polymerization: In this method, the silicate layers are swollen by a liquid monomer or monomer solution. Then the polymerization occurs between the phyllosilicate layers leading to an intercalated nanocomposite. Under specific conditions an exfoliate nanocomposite can be obtained. The polymerization can be initiated by heat or radiation, by the diffusion of a suitable initiator, or by an organic initiator or catalyst fixed through cation exchange inside the interlayer before the swelling step. Although this method is very limited due to the need of compatibility between monomers and the inorganic clays, it is possible to obtain a nanocomposite based on a thermostable polymer, which is not possible by solution or melting method.
- Solution intercalation: this method is based on a solvent system where the polymer (or prepolymer) is dissolved while the silicate layers are dispersed. The silicate dispersion is mixed with the polymer solution, then the polymer chains displace the solvent and intercalate within the interlayer of the silicate. Additionally to the need of a compatible solvent/polymer/silicate system this process also need a posttreatment to remove the solvent which increases the cycle time and cost.
- Melt mixing: In this process the silicate is mixed with the molten polymer and depending on the layer-polymer interaction it will render intercalated or exfoliated nanocomposite. This is the most used process in industrial scale nowadays. This method presents great advantages over those above mentioned. Firstly, it is environmentally benign due the absence of organic solvents and the posterior treatment to get rid of them. Second, it can easily adapted to the current manufacturing procedure (i.e. injection molding). Moreover, this method allows the production use of polymers, which are not suitable for solvent intercalation or polymerization *in situ*.

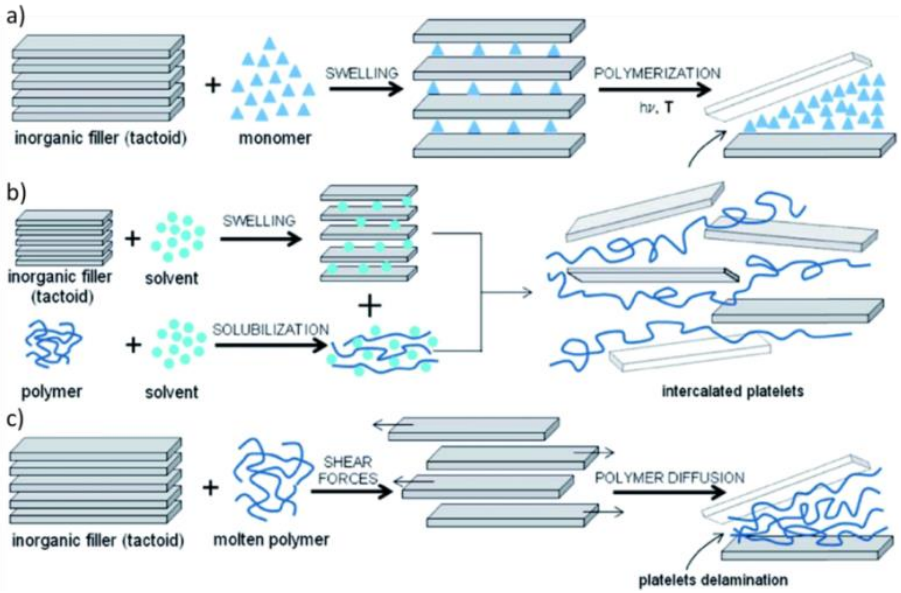

Fig. 1-18. *Schematic illustration of the conventional method to produce silicate nanocomposites: In situ polymerization (**a**), solution intercalation (**b**) and melt mixing (**c**).*

1.4.2.1. Dispersion of clay by means of ultrasound

Although there are several methods to produce MMT nanocomposites which, under specific condition, can render exfoliated structures it is difficult to achieve a fully exfoliation of nanosheets. Commonly a mixture of intercalated and exfoliated structure is attained. Moreover the organic modification of the MMT is always necessary if an exfoliated structure is wanted to be obtained, and in most of the polymers is mandatory to achieve good compatibility. Therefore efforts focused to prepare completely exfoliated polymer-clay nanocomposites without the necessity of chemical modifications appear nowadays highly interesting and necessary in academic and industrial fields.

Several studies were carried out to this purpose; the most promising approach is the combination of ultrasound energy with conventional method. Application of an ultrasound field could improve the dispersity of the nanosheets and render nanocomposite structure with increased polymer-clay interactions.

In the case of *in situ* polymerization, huge improvement has been seen when this procedure is assisted with an ultrasound field. Ultrasound assisted *in-situ* emulsion polymerization is a well-known technology. Ultrasound field is found to be highly efficient method to stable monomer droplets and for achieve a fine dispersion of the inorganic particle in polymer nanocomposites.[108-110] Solution process can also be ultrasound assisted, in that process the use of ultrasound helps in the dispersion of nanofiller. Sonication leads to uniform nanofiller dispersion with significantly improvement of the mechanical and thermal properties in comparison with a nanocomposite obtained by the conventional method.[111]

As above mentioned melt mixing is the preferred one for mass production. The use of ultrasound has also been proved to be highly profitable in this process, this is an effective method to

achieve breakup of the clay agglomerates and increase the layer exfoliation yield.[112] Several studies have demonstrated that the use of ultrasound assisted in the melt mixing process brings a uniform distribution of silicate layer and an enhanced degree of intercalation.[113] Moreover, it has been successfully employed for the preparation of exfoliated nanocomposites, even without organo modified clays.[114, 115]

The possibility of obtaining exfoliated nanocomposite pieces by ultrasound melt mixing in one step is the main focus to explore in this work. Within this new procedure the polymer is also heated up by the ultrasound energy while the silicate layers are sonicated and being dispersed through the molten polymer. This work explores the possibility to obtain nanocomposite in one step by simple feeding of polymer/clay mixture by means of ultrasound micromolding technique.

1.5. Aliphatic polyamides

Polyamides are an important type of polymers characterized by the presence of amide group, -CONH-. This group has the ability to form extremely strength hydrogen bonds, which bring excellent mechanical and resistance properties. These properties are directly linked to the rate between number of amides group and the length of aliphatic chain and the ability to stablish the hydrogen bonds network. Some of them have very low density of amide group, whose properties are similar to polyolefins (such as polyethylene or polypropylene) because of the low amount of hydrogen bonds formed. Others with short aliphatic chain, just one group -CHR- or -CH_2-, and high density of amide groups, as proteins, present a high stable structure formed by the network of hydrogen bonds.

The first produced aliphatic polyamide was the polyamide 6 6. It was commercialized by DuPont under the brand Nylon®, name commonly used nowadays for all aliphatic polyamides, in 1938. The first product launched base on it was a toothbrush with nylon strands, but it was worldwide known for its use to produce tights. During the World War II it gained popularity with its use as ropes, parachutes and some other war stuff. Another commonly known nylon was the polyamide 6, commercialized under several trade names such as Perlon (Germany), Dederon (former East Germany), Nylatron, Capron, Ultramid, Akulon, Kapron (former Soviet Union and satellite states) and Durethan. This nylon was born to imitate the properties of nylon 6 6 without violation the patent. Although both nylons present similar properties and nylon 6 is being used in a lot of daily product, nylon 6 6 is a better choice for high-performing product. Some examples of nylon 6 and 6 6 application are shown in **Fig. 1-19**.

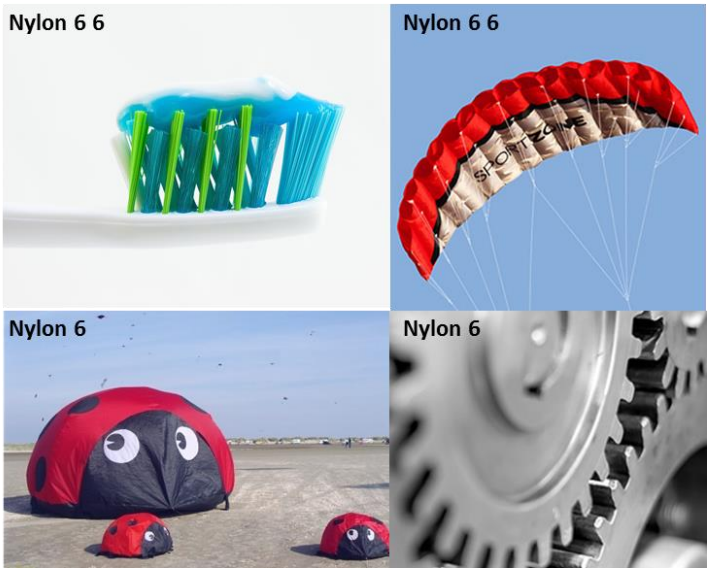

Fig. 1-19. *Some application of nylon 6 6 (toothbrush strings and parachute) and 6 (toys and gears for car).*

These polymers are clear examples of the two types of nylon: nylon *n* (*n* indicates the number of carbon atoms in the repeating unit), synthetized by condensation of ω-amino acids (ring opening of ε-caprolactam in case of nylon 6); and nylon *m, n* produced by polycondensation of one diamine and one dicarboxylic acid or dihalide (where *m* indicates the number of carbon atoms in the diamine chain and *n* the number of carbon atoms of the diacid). The representative repetitive unit of the two types are shown in **Fig. 1-20**.

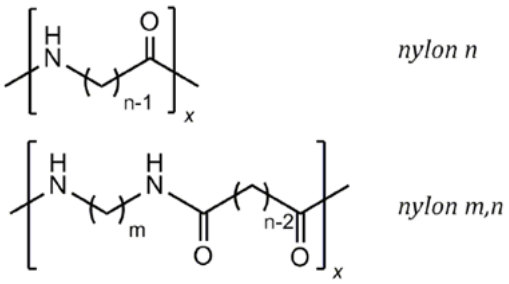

Fig. 1-20.*Schematic representation of nylon n and nylon m,n.*

In general nylons present excellent mechanical properties, such as good abrasion resistance and high tensile strength, also have elevated melting point, good thermal stability and high water absorption. As already mentioned the hydrogen bond network formed by the amide groups is providing these good properties, hence the final properties in nylons are directly linked to the availability to form this structure and how hydrogen bonds are distributed. How these networks are established and which final structures the nylon will present are affected by several parameters such as molecular weight, number and parity of methylene groups, distance between amide groups, the presence of comonomers, thermal history and product preparation process.[116, 117]

1.5.1. Crystalline structure of polyamides: α/β and γ

As mentioned above polyamides can present several crystalline structures. These structures should correspond to a minimum of the packing energy and it is governed by the formation of hydrogen bonds. In order to favour the formation of all hydrogen bonds between all constitutive amide groups the polyamide chains keep a practically linear geometry.

As mentioned above nylons can be produced from ω-amino acid or polycondensation of diamine and dicarboxylic acid (or dihalide), this has a clear effect on the nylon structure. Moreover, these monomers have a number of methylene groups that can be even or odd leading to *even* or *odd* nylons (*n* type) and *even-even*, *odd-odd*, *even-odd* or *odd-even* (*m*, *n type*). It also has a big influence in the hydrogen bond network conformations and the nylon structure.

Even or even-even, such as nylon 6[118] or nylon 6 6[119], are typical examples of commercial nylons that present α or β structures. These structures are based on a stacking of sheets composed of molecular chains with a planar zig-zag conformation. These chains are linked each other by hydrogen bonds. [118-120]Odd nylons can also present these structures. In odd nylons antiparallel chains arrangement is preferred while for even-even nylons both arrangements are likely possible, in both cases chains are fully extended with torsion angles close to 180º and practically all trans configuration.[121, 122] While hydrogen bonds keep these sheets structure, weak van der Waals forces hold the sheets together. Also in order to optimize the packaging energy, sheets are staked each other in a distance close to the half of hydrogen bond distance and the sheets are shifted along chain axis direction. A recuperative displacement is present in α structure, whereas if it is progressive the structure is named as β (***Fig. 1-21***).[123]

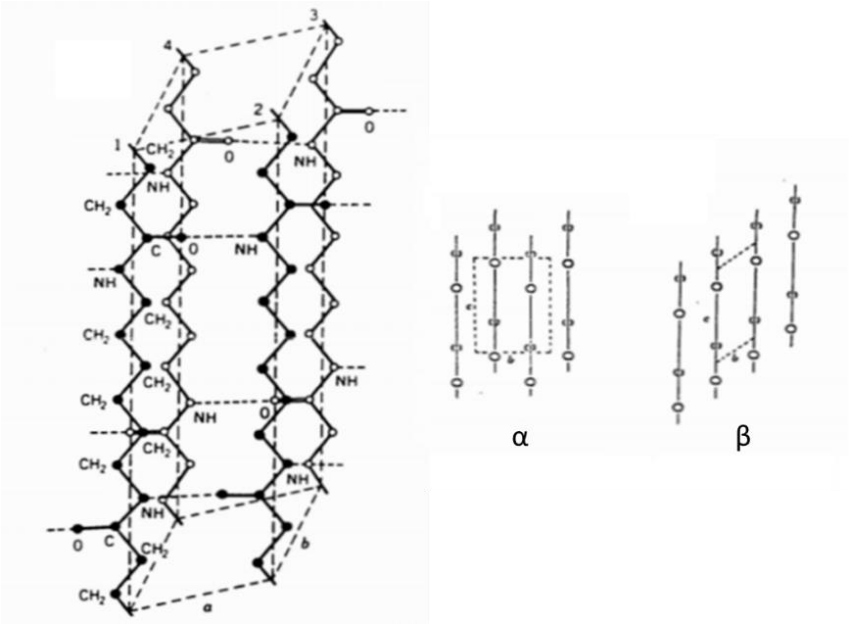

Fig. 1-21. *Representative unit cell for α structure of nylon 6 6. Schematic representation of sheets displacement, α and β structure.*

Nylons *m*, *n* with odd diamines and/or odd dicarboxylic acids are not able to establish all possible hydrogen bonds in a fully extended conformation. In that case, a variation of torsion angle of methylene-amide bonds to ±120º and a twist of 60º of the amide group respect to the plane defined by the methylene carbon atoms, allow the formation of hydrogen bonds in other direction. In this structure, named as γ, the hydrogen bonds are established in a single direction towards adjacent chain belonging to different sheets. The variation from intrasheet hydrogen bonding (α and β structures) to intersheet bonding match the distance between chain of same sheet and adjacent sheets, so the γ-form is defined by a pseudohexagonal structure (**Fig. 1-22**).[124]

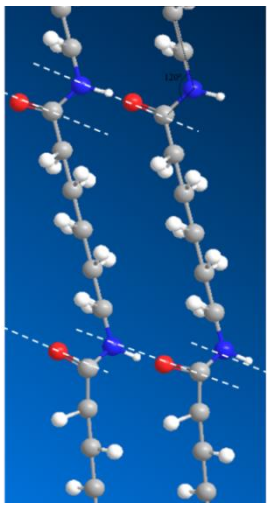

Fig. 1-22. *Illustration of the chain variation to arrange the H-Bond (dashed white line) in γ structure.*

The γ structure is mainly present in nylons with odd segments unable to form hydrogen bonds in *all trans* conformation, but it is also found in nylons with the availability to stablish the hydrogen bonds in a fully extended conformation. For example, it is present as a polymorphic form in *even* nylons with medium length of polymethylene segments (such as nylon 6) as illustrated in **Fig. 1-23**[125] and in some nylons with low density of amide groups and long polymethylene segments.[126] Moreover it is also found in nylons with special units like glycine (nylon 2 3 and 2 6) [127, 128] or malonic acid (nylon n 3) [129]

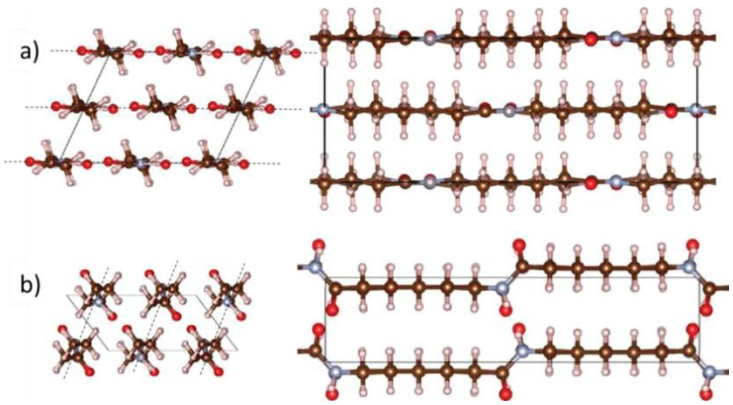

Fig. 1-23. *Schematic comparison of structure α (**a**) and γ (**b**) for nylon 6.*[130]

Both structures can easily be distinguished by their X-ray diffraction patterns (**Fig. 1-24**). Forms α/β are characterized by two strong equatorial reflections around 0.44 and 0.38 nm (corresponding to inter and intra sheets spacing, respectively), whereas X-ray profile of γ form is defined by one signal close to 0.415 nm. [120, 124]

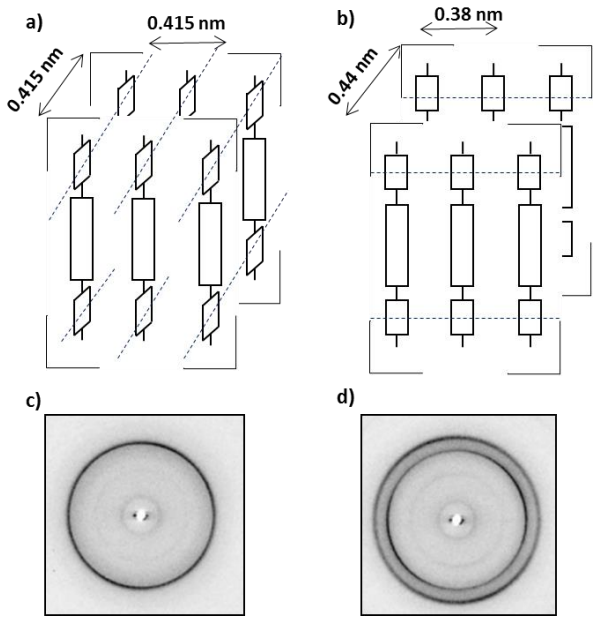

Fig. 1-24. *Schematic representation of unit cells for γ (**a**) and α (**b**) structures and representative X-ray pattern for γ (**c**) and α (**d**) structures. Dashed blue lines indicates de hydrogen bonds directions.*

1.5.2. Structures with two Hydrogen Bond directions

Although the majority of nylons fall into the two structures mentioned above, recently have been postulated a particular structure based on hydrogen bonds stablished in two directions.[131, 132]. This structure has been observed in several nylons derived from diamine or dicarboxylic acid with different parity (e.g. nylons 5 6[132], 5 10[133], 11 10[134], 11 12[135], 4 7[136], 12 5[137], 6 5[138] , 6 9[139], 8 9[140] and 12 9[140]). These nylons are unable to stablish correct hydrogen bonding interaction in a fully extended conformation, as shown for nylon 8 8 and 8 9 in **Fig. 1-25**. However, they show X-ray diffraction patterns closer to α/β than γ form, showing two strong equatorial reflections at 0.43 and 0.375 nm. As shown for nylon 4 7 in **Fig. 1-26a** the hydrogen bonds network is stablished with four neighbouring chains, conveniently shifted along the chain direction, defining a sheets based structure with the hydrogen bonds across the two diagonal of the unit cell (**Fig. 1-26b**). The molecular conformation is close to *all trans*, just a slight deviation towards ±150º two CH_2CH_2-CONH is necessary to face all NH and CO groups. This conformation forces the amide groups to rotate in opposite sense respect to plane defined by the polymethylene segments, allowing the formation of hydrogen bonds in two directions (**Fig. 1-26**)[132, 133, 141]

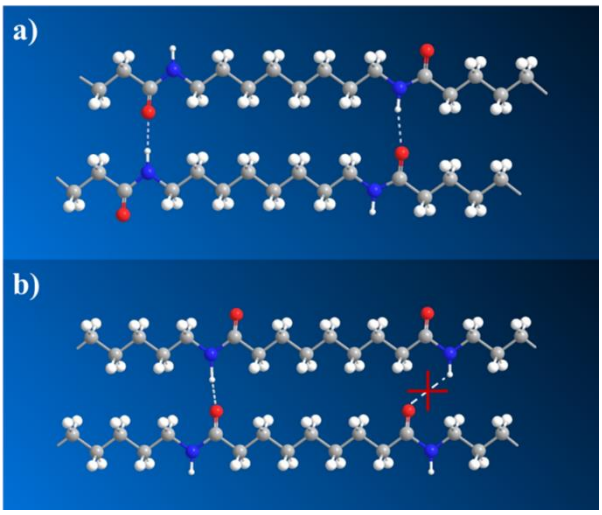

Fig. 1-25. Scheme comparing the hydrogen bonding geometry that could be established between nylon 8 8 (**a**) and nylon 8 9 (**b**) chains having an all trans conformation.

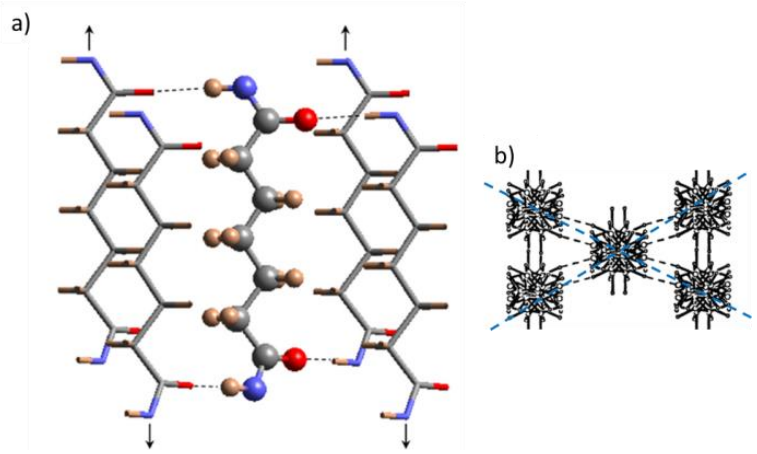

Fig. 1-26. ***a)*** *Scheme showing how hydrogen bonds could be established in nylon 4 7 along two directions when the two amide planes of the amide unit rotate in opposite directions from the plane defined by its methylene carbons.* ***b)*** *Representation of the unit cell with the hydrogen bonds stablish along the two diagonals.*

The commercial interest of nylons based on odd derivatives is recently increasing, mainly based on the possibility to produce bio-based polyamides from renewal source.[142, 143] Dicarboxylic acids can be obtained by the oxidation of unsaturated fatty acid content in plant oil.[144] The majority of them obtained from renewal source are odd, such as acelaic acid (nine carbon) whose can be obtained from plant oil with high content of oleic acid or brassylic acid (thirteen carbons) that can be derived from plant oils that contain significant levels of erucic acid esters, such as crambe and rapeseed oil.[145, 146] Also diamines commonly used in nylon production can be obtained from renewal source. Cadaverine (1,5-diaminopentane) and putrescine (1,4-diaminobutane) are products of the decomposition of dead, rotting animal flesh. The first one is produced by the enzyme-catalyzed decarboxylation of lysine, one of the amino acids found in proteins, during the decomposition process of dead flesh and putrescine is produced biologically by decarboxylation of the amino acid ornithine.[147]Some examples of polyamides based on plant oil-derived dicarboxylic acids that have been

studied include nylon 6 10, 4 10, 6 9, 5 6 or 13 13[148, 149]. **Fig. 1-27** illustrates the evolution of bio plastic production in the world, where polyamides represent the 11.6 % of the global production capacity.

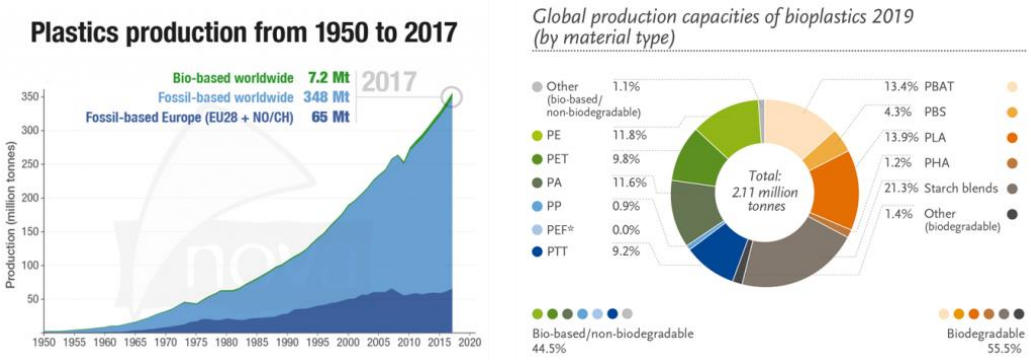

Fig. 1-27. *Evolution of plastic production source and global view of bio-based and biodegradable polymer use in 2019. Source: Bioplastic, nova-Institute (2019).*[150]

1.5.3. Structural transition: Brill temperature.

Polyamides with α or β structure can perform structural transition when heating. This phenomenon is known as Brill transition and was discovered originally for nylon 6 6 in 1942 and after confirmed for almost the majority of aliphatic polyamides displaying α or β structures. It is known that as nylon 6 6 crystals are heated, the two characteristic diffraction signals of α/β structures move together and meet at the Brill temperature. The high temperature phase of Nylon 6 6 above the Brill temperature is pseudohexagonal and it is noted as γ' or Brill's γ. The process occurs in a wide range of temperature through graduals crystallographic changes until reaching the Brill temperature, when the structure transition is done.

The Brill temperature is highly dependent on numerous factors such as material condition, composition, crystallization condition, thermal history or heating rate. For example even-even nylons with extremely large polymethylene segments present T_B close to melting point while for the ones with short aliphatic chains it occurs below melting temperature.[151] For nylon 6 6 T_B vary between 139 and 230 ºC depending on the crystallization condition. If it comes from melting T_B is in a range between 160-225 ºC (higher crystallization temperature higher T_B), whereas nylon 6 6 obtained by solvent crystallization has T_B values around 200-220 ºC. [152-154]

The Brill transition is a reversible process. Thus, nylons crystalize at high temperature in the pseudohexagonal structure, but crystals revert to the higher density room temperature structure (triclinic or monoclinic) on cooling.[151, 155]

Although the full process can easily be monitored by wide angle X ray diffraction (WAXD), since the two equatorial reflections at 0.44 and 0.38 nm merge each other until a single reflection around 0.42-0.415 nm (or vice versa for cooling run) (**Fig. 1-28**), the nature of Brill transition is not completely understood.

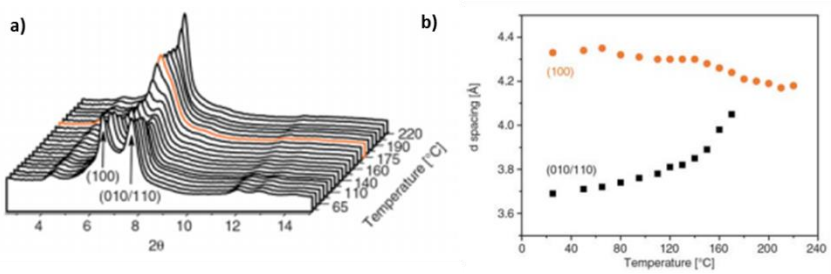

Fig. 1-28. *3D X-ray diffraction profile (**a**) and d spacing (**b**) evolution during heating of a nylon 6 6 film.*[156]

Ramesh et al.[155] postulated that the transition is a first-order process based on the hysteresis effect usually detected, higher T_B on heating than on cooling. However, an endothermic peak has never been identified in calorimetric assays at T_B to collaborate that point.[157] Some researchers thought that the hydrogen bonds break during the transition and a new hydrogen bonding network is set up.[158] However, recent studies focused in the analysis of this transition by mean of infrared spectrums, determined that the hydrogen bonds become weaker but keep intact until the melting point, while the mobility of the polymethylene segment increase with the temperature. These works conclude that the root cause of structural changes is probably based on the conformational disordering experimented by these segments rather than a breakage of the hydrogen bond network.[152, 159] A schematic representation of these processes based on that concept is shown in **Fig. 1-29**.

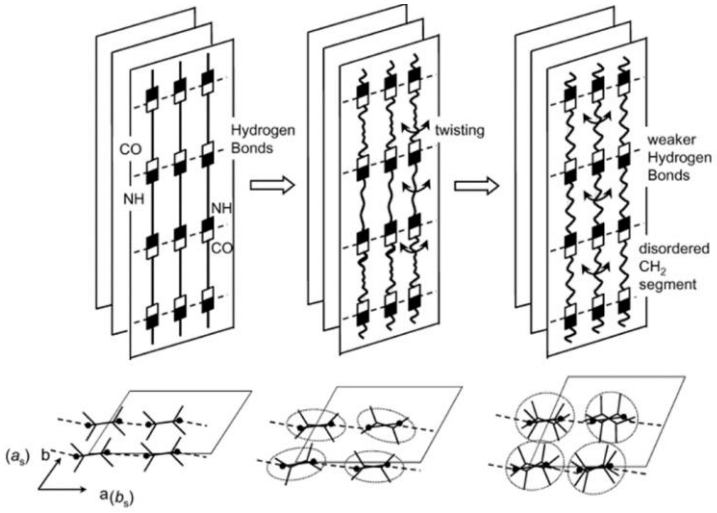

Fig. 1-29. *Schematic illustration of Brill transition for nylon 10 10.* [152]

Even though further studies need to be done the following statements can be stablished:

- The Brill temperature depends on several parameters, even within the same nylon.
- The Brill transition is reversible and a hysteresis effect is observed.
- The structural transition (in heating or cooling run) is preceded by gradual crystallographic change, which can be detected by X-ray diffraction patterns.
- The structural transition at T_B cannot be corroborated by DSC experiments or optical microscopy observation.
- The hydrogen bonds do not break even in the Brill transition region.
- Polymethylene segments show remarkable conformational disordering in Brill transition.

Similar trend was found for even-odd nylons with the described structure based on a hydrogen bonds network stablished along two directions. As was observed in the heating run of nylon 6 9[139] the two reflections at 0.435 and 0.376 nm (noted in this case as form I) merged gradually together until a peak at 0.423 nm related to the typical pseudohexagonal arrangement seen after Brill transition (hereafter named as form III) (**Fig. 1-30a**). A more complex transition was observed for nylon 6 5[138] and 4 7[136] where a new intermediate structure appears before the complete transition to form III. X-ray pattern of this structure, named as form II, differs from ones of initial form I in the closeness of the two reflections (~0.420 and 0.402 nm) which indicates a less compact structure. The nature of the transitions to this form II is not well understood. On heating nylon 6 5 it seems clear that the form II comes from a conversion from form I, were the two reflections of form I get closer towards the form II and then merge to form III (**Fig. 1-30b**). For nylon 4 7 it seems that form II appears independent to form I, between 60 and 120 ºC, and reflections of form I became lower in intensity whereas those related to form II became higher (**Fig. 1-30c**). Also, on cooling the transition is complex and unclear. In the case of nylon 4 7, it does not revert totally to form I at cooling. The transition from form II to I was not completed at room temperature, so form I and II coexist. Nylon 6 9, where form II was not present, transforms to form II during cooling after be crystalized in form III (**Fig. 1-30d**). Similar trend was observed in nylon 6 5 with both structures also present at room temperature.

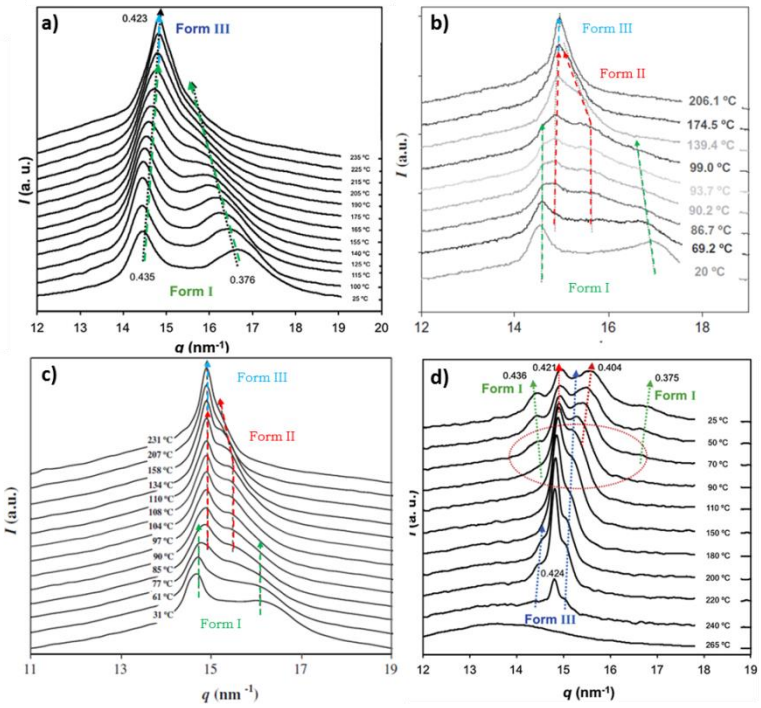

Fig. 1-30. *One-dimensional X-ray profiles of nylon 6 9 (**a**), 6 5 (**b**) and 4 7 (**c**) taken at selected temperature during the heating scan and during the cooling scan from melting of nylon 6 9 (**d**). Dashed lines indicate the evolution of the main diffraction signals for each form: Green for form I, red form II, and blue form III.*

The ratio between form II and I is dependent of the cooling process and the nylon composition. In order to understand the different behaviour experimented for these nylons, even

though having the same initial structure, several studies by DSC, FTIR or optical microscopic observations were carried out. Nevertheless the full process is really complex and further studies are needed.

With the aim to complete the understanding of this series of nylons and having a clear picture on the structural transition process new even-odd polyamides based on azelaic acid (nylons 8 9, 12 9 and 4 9) and glutaric acid (nylon 4 5) have been studied in this thesis. In order to have a further understanding on the structural transitions of random copolyamides copolymers of the latter two were also added to the study. This point is highly interesting due to the additional difficulty to incorporate foreign units in a crystal lattice, especially when the structure is governed by the formation of energetically favoured H-bonds.

The idea of this new series of nylons is to understand the effect of the length of polymethylene segments in dicarboxylic acid and diamine in the transition process, how sample preparation method affects the initial form, the types of transitions depending on this initial structure and how chemical variation in the composition (presence of comonomers) influences on the structures and their transitions. An accurate analysis of X-ray diffraction patterns recorded by real-time synchrotron during heating and cooling runs will be performed. To support the obtained results and study the crystallization kinetic several experiments by means DSC, FTIR and optical microscope were also done.

1.6. References

1. Hynynen, K. Methods and technologies of ultrasound heating. *Ultrasonics* (1992), *30*, 114.

2. Truckenmuller, R.; Ahrens, R.; Chenga, Y.; Fischer, G..Saile, V. *An ultrasonic welding based process for building up a new class of inert fluidic microsensors and -actuators from polymers*. *Sensors and Actuators A* (2006), *132*, 385-392.

3. Li, J.; Xu, K.; Lin, X.; Wu, X..Gao, G. *Research on the Flow Characteristics of Polymer Injection Molding Under Ultrasonic Vibration and Plastics' Mechanical Strength*. *Applied Mechanics and Materials* (2010), *37-38*, 1092-1100.

4. Michaeli, W..Opferman, D. *Ultrasonic plasticising for micro injection moulding*. *4M 2006 - Second International Conference on Multi-Material Micro Manufacture* (2006), 345-348.

5. Giboz, J.; Copponnex, T..Melé, P. *Microinjection molding of thermoplastics polymer: a review*. *J. of Micromechanics and Microengineering* (2007), *17*, R96-R109.

6. Michaeli, W.; Spennemann, A..Gärtner, R. *New plastification concepts for micro injection moulding*. *Microsystem Technologies* (2002), *8*, 55-57.

7. Whiteside, B.; Babenko, M.; Tuinea-Bobe, C.; Brown, E..Coates, P. Ultrasonic injection moulding: A study of thermal behaviour and nanofeature replication. *Proceedings of the 16th International Conference of the European Society for Precision Engineering and Nanotechnology, Nottingham, UK* (2016).

8. Sacristán, M.; Puiggalli, J.; Planta, X..Morell, M. *Effects of ultrasonic vibration on the micro-molding processing of polylactide*. *Ultrasonics Sonochemistry* (2014), *21*, 376-386.

9. Frech, C.B. *Green Plastics: An Introduction to the New Science of Biodegradable Plastics (Stevens, E. S.)*. *Journal of Chemical Education* (2002), *79*, 1072.

10. Jiang, L..Zhang, J., *Biodegradable Polymers and Polymer Blends*, in: S. Ebnesajjad (Ed.), Handbook of Biopolymers and Biodegradable Plastics, William Andrew Publishing, Boston, (2013), pp. 109-128.

11. Zhang, Z.; Ortiz, O.; Goyal, R..Kohn, J., *Biodegradable Polymers*, in: K. Modjarrad, S. Ebnesajjad (Eds.), Handbook of Polymer Applications in Medicine and Medical Devices, William Andrew Publishing, Oxford, (2014), pp. 303-335.

12. Turng, L.-S..Kramschuster, A., Fabrication of tissue engineering scaffolds, in: S. Ebnesajjad (Ed.), Handbook of biopolymers and biodegradable plastics William Andrew Boston, (2012), pp. 427-446.

13. Rai, B.; Teoh, S.H.; Hutmacher, D.W.; Cao, T..Ho, K.H. Novel PCL-based honeycomb scaffolds as drug delivery systems for rhBMP-2. *Biomaterials* (2005), *26*, 3739-3748.

14. Alexandre, M..Dubois, P. Polymer-layered silicate nanocomposites: preparation, properties and uses of a new class of materials. *Materials Science and Engineering: R: Reports* (2000), *28*, 1-63.

15. Usuki, A.; Hasegawa, N.; Kato, M..Kobayashi, S., Polymer-Clay Nanocomposites, Advances in Polymer Science Springer, Berlin, (2005), p. 135.

16. Auras, R.; Lim, L.-T.; Selke, S.E.M..Tsuji, H., *Poly(lactic acid): Synthesis, Structures, Properties, Processing, and Applications*, (2010).

17. Williams, D.F. *Biocompatibility of clinical implant materials*, CRC Press:Boca Raton, Fla., (1981).

18. Ikada, S.S.Y., Medical Applications, in: R.A.L.T.L.S.E.M.S.H. Tsuji (Ed.), Poly(Lactic Acid) (2010).

19. Conn, J.; Oyasu, R.; Welsh, M..Beal, J.M. Vicryl (polyglactin 910) synthetic absorbable sutures. *The American Journal of Surgery* (1974), *128*, 19-23.

20. Burger, C.; Kabir, K.; Rangger, C.; Mueller, M.; Minor, T..Tolba, R.H. Polylactide (LTS) causes less inflammation response than polydioxanone (PDS): a meniscus repair model in sheep. *Archives of Orthopaedic and Trauma Surgery* (2006), *126*, 695-705.

21. Armentano, I.; Bitinis, N.; Fortunati, E.; Mattioli, S.; Rescignano, N.; Verdejo, R.; Lopez-Manchado, M.A..Kenny, J.M. Multifunctional nanostructured PLA materials for packaging and tissue engineering. *Progress in Polymer Science* (2013), *38*, 1720-1747.

22. Tyler, B.; Gullotti, D.; Mangraviti, A.; Utsuki, T..Brem, H. Polylactic acid (PLA) controlled delivery carriers for biomedical applications. *Advanced Drug Delivery Reviews* (2016), *107*, 163-175.

23. Tuan-Mahmood, T.-M.; McCrudden, M.T.C.; Torrisi, B.M.; McAlister, E.; Garland, M.J.; Singh, T.R.R..Donnelly, R.F. Microneedles for intradermal and transdermal drug delivery. *European Journal of Pharmaceutical Sciences* (2013), *50*, 623-637.

24. Park, S.C.; Kim, M.J.; Baek, S.-K.; Park, J.-H..Choi, S.-O. Spray-Formed Layered Polymer Microneedles for Controlled Biphasic Drug Delivery. *Polymers* (2019), *11*, 369.

25. An, J.; Jia, P.; Zhang, Y.; Gong, X.; Han, X..He, Y. Application of biodegradable plates for treating pediatric mandibular fractures. *Journal of cranio-maxillo-facial surgery : official publication of the European Association for Cranio-Maxillo-Facial Surgery* (2015), *43*, 515-20.

26. M. Allen Theresa.Pieter, R.C. *Drug Delivery Systems: Entering the Mainstream*. *Science* (2004), *303*, 1818-1822.

27. Pang, X.; Du, H.-L.; Zhang, H.-Q.; Zhai, Y.-J..Zhai, G.-X. *Polymer–drug conjugates: present state of play and future perspectives*. *Drug Discovery Today* (2013), *18*, 1316-1322.

28. Garnett, M.C. *Targeted drug conjugates: principles and progress*. *Advanced Drug Delivery Reviews* (2001), *53*, 171-216.

29. Bajpai, A.K.; Shukla, S.K.; Bhanu, S..Kankane, S. *Responsive polymers in controlled drug delivery*. *Progress in Polymer Science* (2008), *33*, 1088-1118.

30. Kellomaki, M..Tormala, P. Ultrasonic moulding of bioabsorbable polymers and polymer/drug composites. *Journal of Materials Science Letters* (1997), *16*, 1786-1789.

31. Zema, L.; Loreti, G.; Melocchi, A.; Maroni, A..Gazzaniga, A. Injection Molding and its application to drug delivery. *Journal of Controlled Release* (2012), *159*, 324-331.

32. Bonassar, L.J..Vacanti, C.A. Tissue engineering: The first decade and beyond. *Journal of Cellular Biochemistry* (1998), *72*, 297-303.

33. Atala, A. Tissue Engineering and Regenerative Medicine: Concepts for Clinical Application. *Rejuvenation Research* (2004), *7*, 15-31.

34. Marler, J.J.; Upton, J.; Langer, R..Vacanti, J.P. Transplantation of cells in matrices for tissue regeneration. *Advanced Drug Delivery Reviews* (1998), *33*, 165-182.

35. A.J. Salgado, O.P.C., and R.L. Reis Novel Starch-Based Scaffolds for Bone Tissue Engineering: Cytotoxicity, Cell Culture, and Protein Expression. *Tissue Engineering* (2004), *10*, 465-474.

36. Walsh, D.; Furuzono, T..Tanaka, J. Preparation of porous composite implant materials by in situ polymerization of porous apatite containing ε-caprolactone or methyl methacrylate. *Biomaterials* (2001), *22*, 1205-1212.

37. Su, Z.; Ma, H.; Wu, Z.; Zeng, H.; Li, Z.; Wang, Y.; Liu, G.; Xu, B.; Lin, Y.; Zhang, P..Wei, X. Enhancement of skin wound healing with decellularized scaffolds loaded with hyaluronic acid and epidermal growth factor. *Materials Science and Engineering: C* (2014), *44*, 440-448.

38. Guo, T.; Zhao, J.; Chang, J.; Ding, Z.; Hong, H.; Chen, J..Zhang, J. Porous chitosan-gelatin scaffold containing plasmid DNA encoding transforming growth factor-β1 for chondrocytes proliferation. *Biomaterials* (2006), *27*, 1095-1103.

39. Li, X.; Wang, Y.; Guo, M.; Wang, Z.; Shao, N.; Zhang, P.-b.; Chen, X..Huang, Y. Degradable 3D printed PLA scaffold with long-term antibacterial activity. *ACS Sustainable Chemistry & Engineering* (2017), *6*.

40. Wu, J.C.-C.; Ray, S.; Gizdavic-Nikolaidis, M.; Uy, B.; Swift, S.; Jin, J..Cooney, R.P. Nanostructured bioactive material based on polycaprolactone and polyaniline fiber-scaffolds. *Synthetic Metals* (2014), *198*, 41-50.

41. Velasco, M.A.; Narv; ez-Tovar, C.A.; Garz.n-Alvarado, D.A. Design, Materials, and Mechanobiology of Biodegradable Scaffolds for Bone Tissue Engineering. *BioMed Research International* (2015), *2015*, 21.

42. Jeong, D.; Yun, A..Kim, J. Mathematical model and numerical simulation of the cell growth in scaffolds. *Biomechanics and Modeling in Mechanobiology* (2012), *11*, 677-688.

43. Liu, X.; Holzwarth, J.M..Ma, P.X. Functionalized Synthetic Biodegradable Polymer Scaffolds for Tissue Engineering. *Macromolecular Bioscience* (2012), *12*, 911-919.

44. Rezwan, K.; Chen, Q.Z.; Blaker, J.J..Boccaccini, A.R. Biodegradable and bioactive porous polymer/inorganic composite scaffolds for bone tissue engineering. *Biomaterials* (2006), *27*, 3413-3431.

45. Mikos, A.G.; Bao, Y.; Cima, L.G.; Ingber, D.E.; Vacanti, J.P..Langer, R. Preparation of poly(glycolic acid) bonded fiber structures for cell attachment and transplantation. *Journal of Biomedical Materials Research* (1993), *27*, 183-189.

46. Díaz, A.; del Valle, L.J.; Tugushi, D.; Katsarava, R..Puiggalí, J. New poly(ester urea) derived from l-leucine: Electrospun scaffolds loaded with antibacterial drugs and enzymes. *Materials Science and Engineering: C* (2015), *46*, 450-462.

47. Sin, D.; Miao, X.; Liu, G.; Wei, F.; Chadwick, G.; Yan, C..Friis, T. Polyurethane (PU) scaffolds prepared by solvent casting/particulate leaching (SCPL) combined with centrifugation. *Materials Science and Engineering: C* (2010), *30*, 78-85.

48. Oh, S.H.; Kang, S.G..Lee, J.H. Degradation behavior of hydrophilized PLGA scaffolds prepared by melt-molding particulate-leaching method: Comparison with control hydrophobic one. *Journal of Materials Science: Materials in Medicine* (2006), *17*, 131-137.

49. Widmer, M.S.; Gupta, P.K.; Lu, L.; Meszlenyi, R.K.; Evans, G.R.D.; Brandt, K.; Savel, T.; Gurlek, A.; Patrick, C.W..Mikos, A.G. Manufacture of porous biodegradable polymer conduits by an extrusion process for guided tissue regeneration. *Biomaterials* (1998), *19*, 1945-1955.

50. Bakar, Z.A.; Hussein, B.F..Mustapha, N.M., Clockle Shell-based Biocomposite Scaffold for Bone Tissue Engineering, in: D. Eberli (Ed.), Regenerative Medicine and Tissue Engineering - Cells and Biomaterials, InTech (2010).

51. Maquet, V..Jerome, R. Design of Macroporous Biodegradable Polymer Scaffolds for Cell Transplantation. *Materials Science Forum* (1997), *250*, 15-42.

52. David, D..Silverstein, M.S. Porous polyurethanes synthesized within high internal phase emulsions. *Journal of Polymer Science Part A: Polymer Chemistry* (2009), *47*, 5806-5814.

53. Utela, B.; Storti, D.; Anderson, R..Ganter, M. A review of process development steps for new material systems in three dimensional printing (3DP). *Journal of Manufacturing Processes* (2008), *10*, 96-104.

54. Bergmann, C.; Lindner, M.; Zhang, W.; Koczur, K.; Kirsten, A.; Telle, R..Fischer, H. 3D printing of bone substitute implants using calcium phosphate and bioactive glasses. *Journal of the European Ceramic Society* (2010), *30*, 2563-2567.

55. McMurry, L.M.; Oethinger, M..Levy, S.B. Triclosan targets lipid synthesis. *Nature* (1998), *394*, 531-532.

56. Martin, I.; Wendt, D..Heberer, M. The role of bioreactors in tissue engineering. *Trends Biotechnol* (2004), *22*, 80-6.

57. Zhang, Y..Lu, J. A simple method to tailor spherical nanocrystal hydroxyapatite at low temperature. *Journal of Nanoparticle Research* (2007), *9*, 589-594.

58. Ioku, K.; Yamauchi, S.; Fujimori, H.; Goto, S..Yoshimura, M. Hydrothermal preparation of fibrous apatite and apatite sheet. *Solid State Ionics* (2002), *151*, 147-150.

59. Li, X.; Feng, Q.; Liu, X.; Dong, W..Cui, F. Collagen-based implants reinforced by chitin fibres in a goat shank bone defect model. *Biomaterials* (2006), *27*, 1917-1923.

60. Wei, J..Li, Y. Tissue engineering scaffold material of nano-apatite crystals and polyamide composite. *European Polymer Journal* (2004), *40*, 509-515.

61. Yun, Y.-P.; Kim, S.-J.; Lim, Y.-M.; Park, K.; Kim, H.-J.; Jeong, S.-I.; Kim, S.E..Song, H.-R. The Effect of Alendronate-Loaded Polycarprolactone Nanofibrous Scaffolds on Osteogenic Differentiation of Adipose-Derived Stem Cells in Bone Tissue Regeneration. *Journal of Biomedical Nanotechnology* (2014), *10*, 1080-1090.

62. Zhou, H.; Lawrence, J.G..Bhaduri, S.B. Fabrication aspects of PLA-CaP/PLGA-CaP composites for orthopedic applications: A review. *Acta Biomaterialia* (2012), *8*, 1999-2016.

63. Elgendy, H.M.; Norman, M.E.; Keaton, A.R..Laurencin, C.T. Osteoblast-like cell (MC3T3-E1) proliferation on bioerodible polymers: an approach towards the development of a bone-bioerodible polymer composite material. *Biomaterials* (1993), *14*, 263-269.

64. Hench, L.L. Bioceramics. *Journal of the American Ceramic Society* (1998), *81*, 1705-1728.

65. Wei, G..Ma, P.X. Structure and properties of nano-hydroxyapatite/polymer composite scaffolds for bone tissue engineering. *Biomaterials* (2004), *25*, 4749-4757.

66. Zhang, R..Ma, P.X. Poly(α-hydroxyl acids)/hydroxyapatite porous composites for bone-tissue engineering. I. Preparation and morphology. *Journal of Biomedical Materials Research* (1999), *44*, 446-455.

67. Cool, S.M.; Kenny, B.; Wu, A.; Nurcombe, V.; Trau, M.; Cassady, A.I..Grøndahl, L. Poly(3-hydroxybutyrate-co-3-hydroxyvalerate) composite biomaterials for bone tissue regeneration: In vitro performance assessed by osteoblast proliferation, osteoclast adhesion and resorption, and macrophage proinflammatory response. *Journal of Biomedical Materials Research Part A* (2007), *82A*, 599-610.

68. Ren, J.; Zhao, P.; Ren, T.; Gu, S..Pan, K. Poly (d,l-lactide)/nano-hydroxyapatite composite scaffolds for bone tissue engineering and biocompatibility evaluation. *Journal of Materials Science: Materials in Medicine* (2008), *19*, 1075-1082.

69. Diao, H.; Si, Y.; Zhu, A.; Ji, L..Shi, H. Surface modified nano-hydroxyapatite/poly(lactide acid) composite and its osteocyte compatibility. *Materials Science and Engineering: C* (2012), *32*, 1796-1801.

70. Zhang, C.Y.; Zhang, C.L.; Wang, J.F.; Lu, C.H.; Zhuang, Z.; Wang, X.P..Fang, Q.F. Fabrication and in vitro investigation of nanohydroxyapatite, chitosan, poly(L-lactic acid) ternary biocomposite. *Journal of Applied Polymer Science* (2013), *127*, 2152-2159.

71. O'Halloran, M.R., Wood: Structural Panels, in: A. Mortensen (Ed.), Concise Encyclopedia of Composite Materials, ELSEVIER, The Netherlands, (2007), pp. 917-921.

72. Shaffer, G.D. An Archaeomagnetic Study of a Wattle and Daub Building Collapse. *Journal of Field Archaeology* (1993), *20*, 59-75.

73. United States Geological Survey, (2007). https://www.usgs.gov/centers/nmic/cement-statistics-and-information.

74. *Synthetic Resin – Use in Aircraft Construction*, London England, Monday 5 October 1936;p. 14, Iss. 47497

75. Paul, D.R..Robeson, L.M. Polymer nanotechnology: Nanocomposites. *Polymer* (2008), *49*, 3187-3204.

76. Layachi, A.; Frihi, D.; Satha, H.; Seguela, R..Gherib, S. Non-isothermal crystallization kinetics of polyamide 66/glass fibers/carbon black composites. *Journal of thermal analysis and calorimetry* (2016), *124*, 1319-1329.

77. Zhao, W.; Li, T.; Li, Y.; O'Brien, D.J.; Terrones, M.; Wei, B.; Suhr, J..Lucas Lu, X. Mechanical properties of nanocomposites reinforced by carbon nanotube sponges. *Journal of Materiomics* (2018), *4*, 157-164.

78. Jeong, S.H.; Yeo, S.Y..Yi, S.C. The effect of filler particle size on the antibacterial properties of compounded polymer/silver fibers. *Journal of Materials Science* (2005), *40*, 5407-5411.

79. Frounchi, M..Dourbash, A. Oxygen Barrier Properties of Poly(ethylene terephthalate) Nanocomposite Films. *Macromolecular Materials and Engineering* (2009), *294*, 68-74.

80. Chayad, F.A.; Jabur, A.R..Jalal, N.M. Effect of MWCNT addition on improving the electrical conductivity and activation energy of electrospun nylon films. *Karbala International Journal of Modern Science* (2015), *1*, 187-193.

81. Hu, Y.; Wang, S.; Ling, Z.; Zhuang, Y.; Chen, Z..Fan, W. Preparation and Combustion Properties of Flame Retardant Nylon 6/Montmorillonite Nanocomposite. *Macromolecular Materials and Engineering* (2003), *288*, 272-276.

82. Tanodekaew, S.; Channasanon, S.; Kaewkong, P..Uppanan, P. PLA-HA Scaffolds: Preparation and Bioactivity. *Procedia Engineering* (2013), *59*, 144-149.

83. Zhang, J.; Liao, J.; Mo, A.; Li, Y.; Li, J..Wang, X. Characterization and human gingival fibroblasts biocompatibility of hydroxyapatite/PMMA nanocomposites for provisional dental implant restoration. *Applied Surface Science* (2008), *255*, 328-330.

84. Iijima, S. Helical microtubules of graphitic carbon. *Nature* (1991), *354*, 56-58.

85. Yu, M.-F.; Lourie, O.; Dyer, M.J.; Moloni, K.; Kelly, T.F..Ruoff, R.S. Strength and Breaking Mechanism of Multiwalled Carbon Nanotubes Under Tensile Load. *Science* (2000), *287*, 637-640.

86. Terrones, M. Science and Technology of the Twenty-First Century: Synthesis, Properties, and Applications of Carbon Nanotubes. *Annual Review of Materials Research* (2003), *33*, 419-501.

87. Ajayan, P.M.; Stephan, O.; Colliex, C..Trauth, D. Aligned Carbon Nanotube Arrays Formed by Cutting a Polymer Resin—Nanotube Composite. *Science* (1994), *265*, 1212-1214.

88. Kang, I.; Khaleque, M.A.; Yoo, Y.; Yoon, P.J.; Kim, S.-Y..Lim, K.T. Preparation and properties of ethylene propylene diene rubber/multi walled carbon nanotube composites for strain sensitive materials. *Composites Part A: Applied Science and Manufacturing* (2011), *42*, 623-630.

89. Jeon, H.; Park, J..Shon, M. Corrosion protection by epoxy coating containing multi-walled carbon nanotubes. *Journal of Industrial and Engineering Chemistry* (2013), *19*, 849-853.

90. Connolly, T.; Smith, R.C.; Hernandez, Y.; Gun'ko, Y.; Coleman, J.N..Carey, J.D. Carbon-Nanotube–Polymer Nanocomposites for Field-Emission Cathodes. *Small* (2009), *5*, 826-831.

91. Jin, Y.W.; Jung, J.E.; Park, Y.J.; Choi, J.H.; Jung, D.S.; Lee, H.W.; Park, S.H.; Lee, N.S.; Kim, J.M.; Ko, T.Y.; Lee, S.J.; Hwang, S.Y.; You, J.H.; Yoo, J.-B..Park, C.-Y. Triode-type field emission array using carbon nanotubes and a conducting polymer composite prepared by electrochemical polymerization. *Journal of Applied Physics* (2002), *92*, 1065-1068.

92. Maciej, S.; Malgorzata, J.; Katarzyna, Z.; Marcin, S..Bartlomiej, G. Carbon nanotube transparent conductive layers
for solar cells applications. *Optica Applicata* (2011), 375–381.

93. Dinca, I.; Ban, C.; Stefan, A..Pelin, G. Nanocomposites as Advanced Materials for Aerospace Industry. *Incas Bulletin* (2012), *4*, 73.

94. Kim, Y.-Y.; Yun, J.; Kim, H.-I..Lee, Y.-S. Effect of oxyfluorination on electromagnetic interference shielding of polypyrrole-coated multi-walled carbon nanotubes. *Journal of Industrial and Engineering Chemistry* (2012), *18*, 392-398.

95. Shaffer, M.S.P..Windle, A.H. Fabrication and Characterization of Carbon Nanotube/Poly(vinyl alcohol) Composites. *Advanced Materials* (1999), *11*, 937-941.

96. Safadi, B.; Andrews, R..Grulke, E.A. Multiwalled carbon nanotube polymer composites: Synthesis and characterization of thin films. *Journal of Applied Polymer Science* (2002), *84*, 2660-2669.

97. Gong, X.; Liu, J.; Baskaran, S.; Voise, R.D..Young, J.S. Surfactant-Assisted Processing of Carbon Nanotube/Polymer Composites. *Chemistry of Materials* (2000), *12*, 1049-1052.

98. Andrews, R.; Jacques, D.; Qian, D..Rantell, T. Multiwall Carbon Nanotubes: Synthesis and Application. *Accounts of Chemical Research* (2002), *35*, 1008-1017.

99. Lobo, A.O.; Zanin, H.; Siqueira, I.A.W.B.; Leite, N.C.S.; Marciano, F.R..Corat, E.J. Effect of ultrasound irradiation on the production of nHAp/MWCNT nanocomposites. *Materials Science and Engineering: C* (2013), *33*, 4305-4312.

100. LeBaron, P.C.; Wang, Z..Pinnavaia, T.J. Polymer-layered silicate nanocomposites: an overview. *Applied Clay Science* (1999), *15*, 11-29.

101. Pinnavaia, T.J..Beall, G.W. *Polymer-clay nanocomposites*, Wiley:Chichester, England; New York, (2000).

102. Lysek, L.A.G.S.J.A., Process to prepare a polymer nanocomposite composition, European, (1999).

103. O, E.G., Process for chemically modifying nylon with montmorillonite, United States, (1962).

104. Si-Min, K.; Jeong-Hyeon.Gi-il, J.H., Nanocomposite of Nylon 6, South Korea, (2001).

105. Fornes, T.D.; Yoon, P.J.; Hunter, D.L.; Keskkula, H..Paul, D.R. Effect of organoclay structure on nylon 6 nanocomposite morphology and properties. *Polymer* (2002), *43*, 5915-5933.

106. Chen, G.-X.; Choi, J.B..Yoon, J.S. The Role of Functional Group on the Exfoliation of Clay in Poly(L-lactide). *Macromolecular Rapid Communications* (2005), *26*, 183-187.

107. Sinha Ray, S..Okamoto, M. Polymer/layered silicate nanocomposites: a review from preparation to processing. *Progress in Polymer Science* (2003), *28*, 1539-1641.

108. Sharma, S.; Kumar Poddar, M..Moholkar, V.S. Enhancement of thermal and mechanical properties of poly(MMA-co-BA)/Cloisite 30B nanocomposites by ultrasound-assisted in-situ emulsion polymerization. *Ultrasonics Sonochemistry* (2017), *36*, 212-225.

109. Henglein, A. T. J. Mason, J. P. Lorimer: Sonochemistry (Theory, Applications and Uses of Ultrasound in Chemistry), Ellis Horwood Limited. Chichester, and John Wiley and Sons, New York 1988. 252 Seiten, Preis: £ 38.50. *Berichte der Bunsengesellschaft für physikalische Chemie* (1989), *93*, 1150-1151.

110. Liu, S.; Ying, J.; Zhou, X..Xie, X. Core-shell magnesium hydroxide/polystyrene hybrid nanoparticles prepared by ultrasonic wave-assisted in-situ copolymerization. *Materials Letters* (2009), *63*, 911-913.

111. Anand K, A.; Agarwal, U.S.; Nisal, A..Joseph, R. PET-SWNT nanocomposites through ultrasound assisted dissolution-evaporation. *European Polymer Journal* (2007), *43*, 2279-2285.

112. Isayev, A.I.; Kumar, R..Lewis, T.M. Ultrasound assisted twin screw extrusion of polymer–nanocomposites containing carbon nanotubes. *Polymer* (2009), *50*, 250-260.

113. Swain, S.K..Isayev, A.I. Effect of ultrasound on HDPE/clay nanocomposites: Rheology, structure and properties. *Polymer* (2007), *48*, 281-289.

114. Ryu, J.G.; Kim, H..Lee, J.W. Characteristics of polystyrene/polyethylene/clay nanocomposites prepared by ultrasound-assisted mixing process. *Polymer Engineering & Science* (2004), *44*, 1198-1204.

115. Lapshin, S..Isayev, A.I. Continuous process for melt intercalation of PP–clay nanocomposites with aid of power ultrasound. *Journal of Vinyl and Additive Technology* (2006), *12*, 78-82.

116. Marchildon, K. Polyamides – Still Strong After Seventy Years. *Macromolecular Reaction Engineering* (2011), *5*, 22-54.

117. Bennett, C.; Kaya, E.; Sikes, A.M.; Jarrett, W.L..Mathias, L.J. Synthesis and characterization of nylon 18 18 and nylon 18 adamantane. *Journal of Polymer Science Part A: Polymer Chemistry* (2009), *47*, 4409-4419.

118. Holmes, D.R.; Bunn, C.W..Smith, D.J. The crystal structure of polycaproamide: Nylon 6. *Journal of Polymer Science* (1955), *17*, 159-177.

119. Bunn, C.W.; Garner, E.V..Bragg, W.L. The crystal structures of two polyamides ('nylons'). *Proceedings of the Royal Society of London. Series A. Mathematical and Physical Sciences* (1947), *189*, 39-68.

120. Kohan, M.I. *Nylon plastics handbook*, Hanser Publishers ; Distributed in the USA and in Canada by Hanser/Gardner Publications:Munich; New York; Cincinnati, (1995).

121. Muñoz-Guerra, S.; Prieto, A.; Montserrat, J.M..Sekiguchi, H. Structural studies of odd-nylon crystals grown from solution. *Journal of Materials Science* (1992), *27*, 89-97.

122. Jahnke, T.S. Nylon Plastics Handbook Edited by Melvin I. Kohan (MIK Associates). Hanser: Cincinnati, OH. 1995. xii + 631 pp. $198.00. ISBN 1-56990-189-9. *Journal of the American Chemical Society* (1996), *118*, 8186-8186.

123. Kinoshita, Y. An investigation of the structures of polyamide series. *Die Makromolekulare Chemie* (1959), *33*, 1-20.

124. Arimoto, H.; Ishibashi, M.; Hirai, M..Chatani, Y. Crystal structure of the γ-form of nylon 6. *Journal of Polymer Science Part A: General Papers* (1965), *3*, 317-326.

125. Puiggali, J.; Munoz-Guerra, S..Lotz, B. Extended-chain and three-fold helical forms of poly(glycyl-β-alanine). *Macromolecules* (1986), *19*, 1119-1124.

126. Arabnejad, S..Manzhos, S. Defects in alpha and gamma crystalline nylon6: A computational study. *AIP Advances* (2015), *5*, 107123.

127. Puiggali, J.; Muñoz-Guerra, S..Subirana, J.A. Morphology and crystalline structure of nylon-2/6. *Polymer* (1987), *28*, 209-212.

128. Puiggalí, J.; Aceituno, J.E.; Navarro, E.; Campos, J.L..Subirana, J.A. Structure of n,3 Polyamides, a Group of Nylons with Two Spatial Hydrogen-Bond Orientations. *Macromolecules* (1996), *29*, 8170-8179.

129. Aharoni, S.M. *n-Nylons: their synthesis, structure and properties*, John Wiley and Sons:New York, (1997).

130. Navarro, E.; Aleman, C..Puiggali, J. Folding of Methylene Groups in Linear Glutaramide Analogs. *Journal of the American Chemical Society* (1995), *117*, 7307-7310.

131. Aleman, C.; Navarro, E..Puiggali, J. Conformational analysis of succinamide analogs. *The Journal of Organic Chemistry* (1995), *60*, 6135-6140.

132. Morales-Gámez, L.; Soto, D.; Franco, L..Puiggalí, J. Brill transition and melt crystallization of nylon 56: An odd–even polyamide with two hydrogen-bonding directions. (2010), *51*, 5788-5798.

133. Villaseñor, P.; Franco, L.; Subirana, J.A..Puiggalí, J. On the crystal structure of odd–even nylons: Polymorphism of nylon 5,10. *Journal of Polymer Science Part B: Polymer Physics* (1999), *37*, 2383-2395.

134. Nakagawa, T.; Nozaki, K.; Maeda, S..Yamamoto, T. Polymorphism of poly(nonamethyleneoxamide) crystal. (2015), *57*, 99-104.

135. Cui, X..Yan, D. Preparation, characterization and crystalline transitions of odd–even polyamides 11,12 and 11,10. (2005), *41*, 863-870.

136. Morales-Gámez, L.; Casas, M.T.; Franco, L..Puiggalí, J. Structural transitions of nylon 47 and clay influence on its crystallization behavior. *European Polymer Journal* (2013), *49*, 1354-1364.

137. Navarro, E.; Subirana, J.A..Puiggali, J. The structure of nylon 12,5 is characterized by two hydrogen bond directions as are other polyamides derived from glutaric acid. *Polymer* (1997), *38*, 3429-3432.

138. Navarro, E.; Franco, L.; Subirana, J.A..Puiggali, J. Nylon 65 has a Unique Structure with Two Directions of Hydrogen Bonds. *Macromolecules* (1995), *28*, 8742-8750.

139. Franco, L.; Cooper, S.J.; Atkins, E.D.T.; Hill, M.J..Jones, N.A. Nylon 6 9 can crystallize with hydrogen bonding in two and in three interchain directions. *Journal of Polymer Science Part B: Polymer Physics* (1998), *36*, 1153-1165.

140. Olmo, C.; Rota, R.; Carlos Martínez, J.; Puiggalí, J..Franco, L. Temperature-induced structural changes in even-odd nylons with long polymethylene segments. *Journal of Polymer Science Part B: Polymer Physics* (2016), *54*, 2494-2506.

141. Franco, L.; Subirana, J.A..Puiggalí, J. Structure and Morphology of Odd Polyoxamides Nylon 9,2. A New Example of Hydrogen-Bonding Interactions in Two Different Directions. *Macromolecules* (1998), *31*, 3912-3924.

142. van Velthoven, J.L.J.; Gootjes, L.; Noordover, B.A.J..Meuldijk, J. Bio-based, amorphous polyamides with tunable thermal properties. *European Polymer Journal* (2015), *66*, 57-66.

143. Jasinska, L.; Villani, M.; Wu, J.; van Es, D.; Klop, E.; Rastogi, S..Koning, C.E. Novel, Fully Biobased Semicrystalline Polyamides. *Macromolecules* (2011), *44*, 3458-3466.

144. Nieschlag, H.J..Wolff, I.A. Industrial uses of high erucic oils. *Journal of the American Oil Chemists Society* (1971), *48*, 723-727.

145. Zuo, J.; Li, S.; Bouzidi, L..Narine, S.S. Thermoplastic polyester amides derived from oleic acid. *Polymer* (2011), *52*, 4503-4516.

146. Neischlag, H.J.; Wolff, I.A.; Manley, T.C..Holland, R.J. Brassylic Acid from Ozonolysis of Erucic Acid. *I&EC Product Research and Development* (1967), *6*, 120-123.

147. Li, N.; Chou, H.; Yu, L..Xu, Y. Cadaverine production by heterologous expression of Klebsiella oxytoca lysine decarboxylase. *Biotechnology and Bioprocess Engineering* (2014), *19*, 965-972.

148. Koning, C.; Teuwen, L.; de Jong, R.; Janssen, G..Coussens, B. Polyamides 4.10 and 4.12 and their Isomers. *High Performance Polymers* (1999), *11*, 387-394.

149. Van Dyne, D.L..Blase, M.G. Process Design, Economic Feasibility, and Market Potential for Nylon 1313 Produced from Erucic Acid. *Biotechnology Progress* (1990), *6*, 273-276.

150. https://www.european-bioplastics.org/market/, (2020).

151. Jones, N.A.; Atkins, E.D.T..Hill, M.J. Comparison of Structures and Behavior on Heating of Solution-Grown, Chain-Folded Lamellar Crystals of 31 Even−Even Nylons. *Macromolecules* (2000), *33*, 2642-2650.

152. Yoshioka, Y..Tashiro, K. Structural change in the Brill transition of Nylon m/n (1) Nylon 10/10 and its model compounds. *Polymer* (2003), *44*, 7007-7019.

153. Jones, N.A.; Atkins, E.D.T.; Hill, M.J.; Cooper, S.J..Franco, L. Chain-Folded Lamellar Crystals of Aliphatic Polyamides. Comparisons between Nylons 4 4, 6 4, 8 4, 10 4, and 12 4. *Macromolecules* (1996), *29*, 6011-6018.

154. Jones, N.A.; Atkins, E.D.T.; Hill, M.J.; Cooper, S.J..Franco, L. Chain-folded lamellar crystals of aliphatic polyamides. Investigation of nylons 4 8, 4 10, 4 12, 6 10, 6 12, 6 18 and 8 12. *Polymer* (1997), *38*, 2689-2699.

155. Ramesh, C.; Keller, A..Eltink, S.J.E.A. Studies on the crystallization and melting of nylon-6,6: 1. The dependence of the Brill transition on the crystallization temperature. *Polymer* (1994), *35*, 2483-2487.

156. Wolanov, Y.; Feldman, A.Y.; Harel, H..Marom, G. Amorphous and crystalline phase interaction during the Brill transition in nylon 66. *Express Polym. Lett.* (2009), *3*, 452-457.

157. Xenopoulos, A..Wunderlich, B. Conformational motion and disorder in aliphatic nylons The case of nylon 6.6. *Colloid and Polymer Science* (1991), *269*, 375-391.

158. Cojazzi, G.; Fichera, A.M.; Malta, V..Zannetti, R. Phase transitions in Nylons 8, 10 and 12 crystallized from solutions. *Die Makromolekulare Chemie* (1991), *192*, 185-190.

159. Hirschinger, J.; Miura, H.; Gardner, K.H..English, A.D. Segmental dynamics in the crystalline phase of nylon 66: solid state deuterium NMR. *Macromolecules* (1990), *23*, 2153-2169.

2. OBJECTIVES

Taking into account the potential of ultrasound micromolding as a new technique to produce microsized pieces in terms of energy and material efficiencies, the main goal of this work is to explore further possibilities of this technique to produce polymer specimens with added values.

From a contextualizing point of view, this PhD work is divided in two main blocks. First block (**Chapter 3**) focusses in biomedical applications, it explores the use of biodegradable polymers (i.e. polylactide) to produce drug loaded pieces and scaffolds with antibacterial activity or increased osteoconductivity. The specific objectives of this block are listed below:

- To explore the use of ultrasound micromolding technique in the production of controlled drug release polymer systems.
- To evaluate the effect of ultrasound waves in the bioactivity of different drugs.
- To investigate the use of ultrasound micromolding technique to produce biodegradable scaffolds with high shape resolution.
- To study the use of ultrasound micromolding technique to obtain polymer hybrids loaded with inorganic compounds.
- To evaluate the possibility of having scaffolds with antibacterial activity or increased osteoconductivity by the incorporation of hydroxyapatite.

The second block of the work exposed in this thesis (**Chapter 4**) is focused on the manufacturing of nanocomposites reinforced with carbon nanotubes and clays in a single step. Additionally, an exhaustive study on the effect of the incorporation of these external agents in the polymeric matrix on the crystallization and polymorphic transition behavior has centered our attention. To this end nylon 12 and polycaprolactone are considered as examples of polymers with high mechanical performance or high biodegradability. The specific objectives of this block are:

- To evaluate the possibility to obtain nanocomposites based on nylon 12 and polycaprolactone by means of ultrasound micromolding technique.
- To compare conventional method to obtain nanocomposites with ultrasound micromolding technique.
- To evaluate the possibility of having PLC/MWCNT with a proper nanotubes distribution
- To evaluate the possibility of having nylon 12 based exfoliated clay-nanocomposite without the use of organo modified clays.
- To study the effect of the incorporation of external agents (e.g. clays and CNTs) on the crystalline behavior and structural transitions of the corresponding polymer matrices.

A final goal (**Chapter 5**) tries to provide deeper knowledge of structural transitions observed for the even-odd family of polyamides. Specifically, nylons 4 9, 8 9, 12 9 and the copolyamides 4 5+9_X (polyamides with different ratios of glutaric and azelaic acid), will be considered. The specific objectives of this block are below listed:

- To study the effect of amine polymethylene length and amide density in the crystalline structure and polymorphic transitions.
- To understand the effect of processing condition in the final crystalline structure of even-odd polyamides.
- To evaluate the effect of chemical modification in the nylon structures by the incorporation of comonomers in the main polyamide chain.

3. Ultrasound Micromolding: Biomedical Application

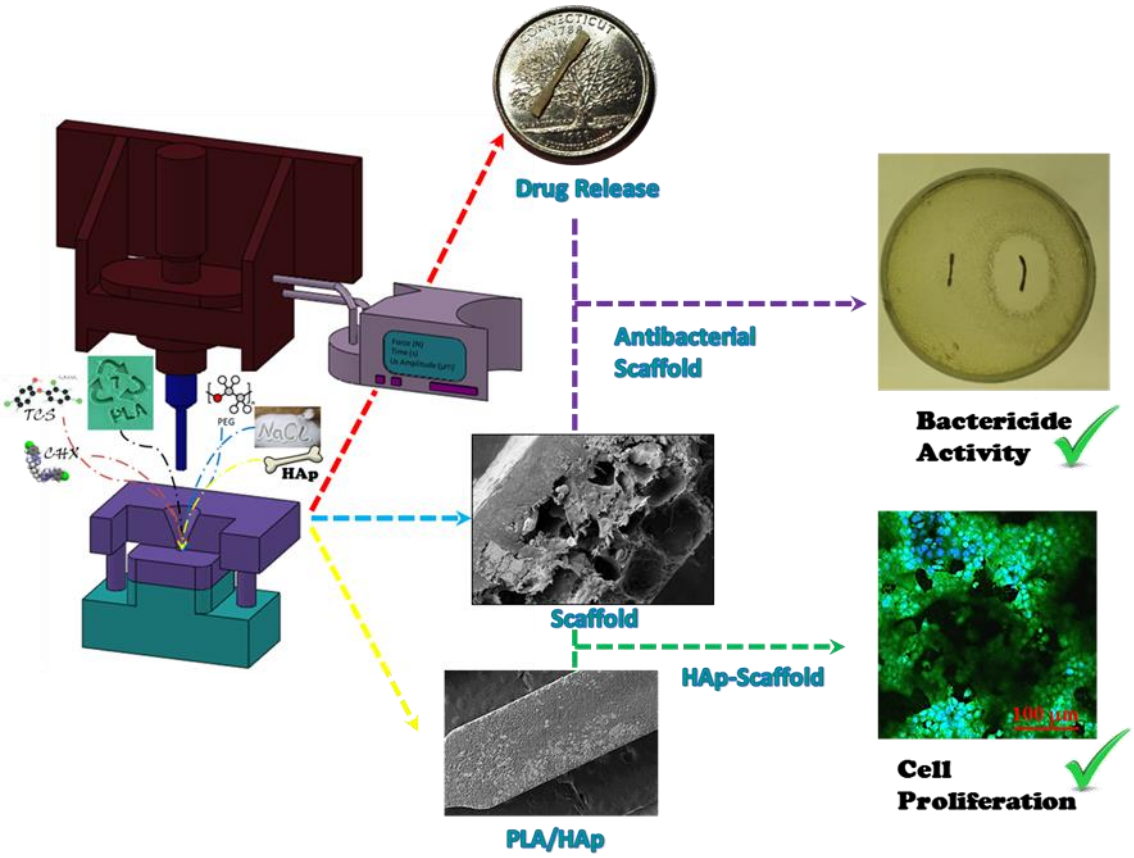
Drug Release
Antibacterial
Scaffold
Bactericide
Activity
TCS
PLA
CHX
PEG
NaCl
HAp
Scaffold
HAp-Scaffold
100 µm
Cell
Proliferation
PLA/HAp

A technology based on the application of ultrasounds as a heating energy source was applied to get polylactide (PLA) micropieces with minimum degradation and processing time. This requirement could be even shorter than 1.5 seconds. The ultrasound technology was also demonstrated to be efficient for the incorporation of drugs with a pharmacological activity and inorganic compound such as NaCl and HAp.

Loading of two representative bactericide agents, triclosan (TCS), and chlorhexidine, (CHX), having differentiated chemical properties was evaluated. Typical physicochemical characterization included mechanical and thermal properties together with the evaluation of molecular degradation during processing for both unloaded and loaded specimens were carried out. Results pointed out that thermally stable specimen could be attained without any problem when working with TCS but cautions should be taken into account for CHX. Nevertheless, degradation could in this case be avoided when the drug load was lower than 3 wt-%, a result that contrasts with the significant decomposition attained by using conventional melting processes, which required long processing times at high temperatures. Morphologic analyses of loaded specimens did not reveal significant defects and spectroscopic analyses showed that a good dispersion of drugs inside pieces could be attained. Drugs were slowly released from micropieces with a rate that was dependent on their hydrophilic character. A clear bactericide effect against both Gram-positive and Gram-negative bacteria was achieved at the beginning of exposure to the corresponding culture media, while a bacteriostatic effect was interestingly still detected after long exposure times.

Microporous polylactide scaffolds have been produced from the subsequent leaching of incorporated NaCl salts. NaCl was a suitable salt for ultrasound processing since cavitation problems could be avoided and a minimum change of the optimized parameters determined for the neat PLA was required. A small amount of water soluble polyethylene glycol was required in order to improve the leaching process and get compact pieces with interconnected pores; PEG could also be micromolded without a significant degradation. Distribution of polymers in the processed specimens was rather homogeneous due to the small PEG content, although it was more concentrated in the regions close to the feeding channels due to its higher viscosity. Hydrophobic drugs like triclosan could be incorporated suffering an insignificant solubilization during the leaching step. Final scaffolds showed clear bactericide or bacteriostatic effects before and after 10 h of exposure. Cell proliferation of MDCK epithelial cells was higher for TCS loaded porous scaffolds (200%) than for unloaded samples (170%) and non-porous PLA specimens (100%, control). Micrographs showed the absence of non-inhibition areas in both the specimens and the container, confirming the biocompatibility of PLA specimens.

Preparation of hybrid scaffolds based on polylactide (PLA) and hydroxyapatite (HAp) particles has also been evaluated. In order to avoid cavitation and decomposition problems during micromolding, it was necessary to use HAp absolutely free of typical synthesis impurities like carbonate and nitrate compounds. Compact PLA/HAp pieces allowed a maximum HAp load of 60 wt-%, while

porous specimens could be obtained with a maximum load of 38 wt-%. Results indicated that a degree of porosity of 35% can be achieved with relatively good mechanical properties (i.e., 580 MPa, 4% and 15.6 MPa for the Young modulus, elongation at break and tensile strength, respectively). Incorporation of HAp increased the thermal stability and the hydrophilicity with respect to neat PLA specimens. Processed scaffolds showed a positive effect of HAp and porosity on cell proliferation, which resulted 40% higher than that detected for non-porous PLA specimens. Furthermore, cell colonization of specimens was clearly evidenced by confocal microscopy.

3.1. Materials and Methods

3.1.1. Materials

A commercial PLA powder grade (Ecorene® NW30 from NatureWorks, Naarden, The Netherlands) with number average molecular weight of 43,000 g/mol and a degree of crystallinity of 35% was employed.

Polyethylene glycol (PEG) samples with weight average molecular weights of 35,000 and 100,000 g/mol were purchased from Sigma-Aldrich®.

Porogenic agents (i.e. Na_2CO_3), $NaHCO_3$, NaCl), and antimicrobial Clorhexidine and Triclosan® were also provided by Sigma-Aldrich®. ®. NaCl was sieved in order to get particles with sizes lower than 100 μm.

CHT ceramic hydroxyapatite type I was provided by Bio-Rad. This HAp was constituted by highly homogeneous particles with sizes lower than 200 μm.

3.1.1.1. Synthesis of hydroxyapatite

HAp in form of amorphous calcium phosphate was synthetized by precipitation at room temperature following the procedure described by Zhang and Lu [1]. 500 mM of $Ca(NO_3)_2 \cdot H_2O$ in ethanol and 500 mM of NH_4PO_4 in water (pH<10), were vigorously stirred at room temperature for 1 h. Reagent volumes were determined to get a Ca/P ratio of 1.67, which is the typical value for natural HAp [2]. The pH of the medium was adjusted by using NH_4OH.The mixture was kept at 37 ºC for 24 h, and after that, the product was washed with milli-Q water and centrifuged four times at 5000 rpm. The precipitated extract was frozen overnight at -80 ºC, then it was dried at low temperature for 48 h. The HAp obtained was ground and filtered.

3.1.2. Specimen characterization

Molecular weight was determined by size exclusion chromatography (GPC) using a liquid chromatograph (Shimadzu, model LC-8A) equipped with an Empower computer program (Waters). The polymer was dissolved and eluted in 1,1,1,3,3,3-hexafluoroisopropanol (HFIP) containing CF_3COONa (0.05 M). The flow rate was 1 mol/min, the injected volume 20 μL, and the sample concentration 2 mg/ml. A PL HFIP gel column (Polymer Lab) and a refractive index detector (Shimadzu RID-10A) were employed. The number and weight average molecular weights were determined using polymethyl methacrylate standards.

Infrared spectra (ATR-FTIR) were recorded at a resolution of 4 cm^{-1}, with a Fourier transform FTIR 4100 Jasco spectrometer dotted with a Specac MKII Golden Gate Single Reflection Diamond ATR system.

SEM micrographs of micromolded specimens were taken by using a Focused Ion Beam Zeiss Neon40 microscope (Zeiss, Oberkochen, Germany) operating at 5 kV. Samples were mounted on a double-side adhesive carbon disc and sputter-coated with a thin layer of carbon by using a Mitec K950 Sputter Coater (Quorum Technologies Ltd., Ashford, UK).

Tensile deformation tests were performed using the Universal Testing Machine Zwick Z 2.5 equipped with a cell charge of 100 N and testXpert 8.1 software. Gauge length was 5 mm and test crosshead speed was 1 mm/min. Fifteen specimens (1.5 x 0.1 x 0.1 cm^3) were tested for each processing condition. The width of each one was accurately measured with a width measurement equipment Uno-Check Fe.

Contact angles (CA) were measured at room temperature with sessile drops using an OCA-15 plus Contact Angle Microscope (Dataphysics, USA) and SCA20 software. Contact angle values of the right and left sides of distilled water drops were measured and averaged. Measurements were performed 10 s after the drop (0.5 μL) was deposited on the sample surface. All CA data were an average of six measurements on different surface locations.

Calorimetric data were obtained by differential scanning calorimetry with a TA Instruments Q100 series (TA instruments, New Castle, DE, USA) with Tzero technology and equipped with a refrigerated cooling system (RCS, TA instruments, New Castle, DE, USA). Experiments were conducted at a heating rate of 10 °C/min and under a flow of dry nitrogen. The sample weight was approximately 5 mg, and calibration was performed with indium.

Thermogravimetric (TGA) and differential thermogravimetric (DTGA) data were acquired with a Q50 thermogravimetric analyzer of TA Instruments (New Casttle, DE, USA) under a flow of dry nitrogen with approximately 5 mg samples and at a heating rate of 20 ºC/min.

^{1}H NMR spectra were recorded with a Bruker AMX-300 spectrometer operating at 300.1 MHz and 25 ºC. Samples were dissolved in deuterated chloroform and spectra were internally referenced to tetramethylsilane (TMS).

Real-time synchrotron studies at variable temperatures were carried out on beamline BL11-NCD at ALBA Synchrotron (Cerdanyola del Vallès, Barcelona, Spain) by using a wavelength of 0.100 nm and a WAXD LX255-HS detector from Rayonix. Polymer samples were confined between Kapton films and then held on a Linkam hot stage with temperature control within ± 0.1 °C. WAXD profiles were acquired during heating and cooling runs in time frames of 20 s and rates of 10 °C/min. WAXD diffraction patterns were calibrated by means of a geometrical calibration process of a well-known sample (standard Cr_2O_3). Diffraction profiles were normalized to the beam intensity and corrected considering the empty sample background.

3.1.3. Micromolding equipment and sample preparation

The main parts of the USM equipment (Sonorus®, Ultrasion S.L., Barcelona, Spain) are schematized in **Fig. 3-1**. The USM process requires a digital ultrasound generator (1000 W–30 kHz), a controller (3010 DG digital system, Mecasonic, Barcelona, Spain), a focused piezoelectric transducer (Mecasonic, Barcelona, Spain), which converts electrical energy into kinetic energy and creates undulatory movement, and an acoustic unit constituted by a booster and a sonotrode that operates in longitudinal vibration. The first element amplifies or reduces the wave amplitude (0–137.5 μm) while the second transfers vibration energy to the material and provides the pressure/force required to transfer it into the mold.

The equipment is also provided with an electric servomotor control (Berneker and Rainer, Barcelona, Spain) fitted with software from Ultrasion S.L. (Barcelona, Spain), a little plasticizing camera and a mold capable to prepare 8 test specimens of dimensions 1.5 cm × 0.1 cm × 0.1 cm, and upgraded with an automatic ejection system.

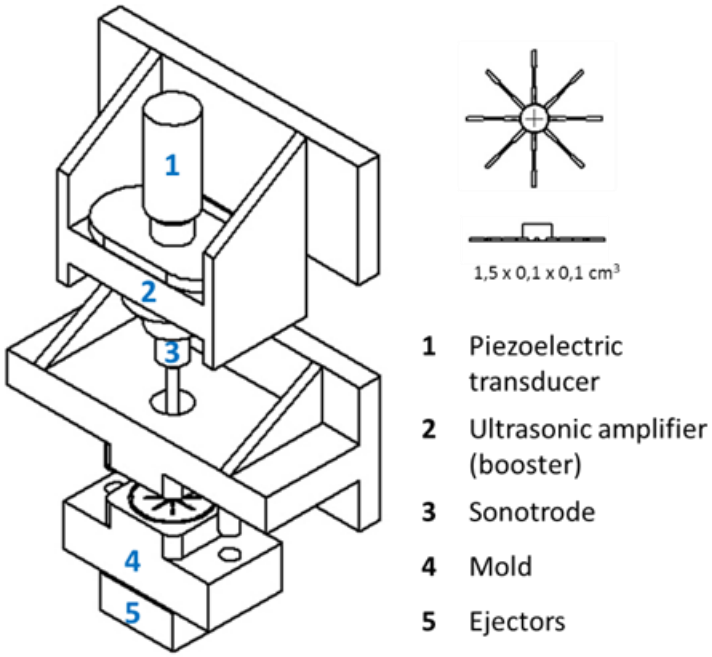

Fig. 3-1. *Diagram of the main parts of the micro-molding equipment.*

In the first stage, the sonotrode compacted the powdered sample and then the transducer converted the electric energy to a vibration movement regulated by the booster, according to the wave amplitude previously set up. This cycled vibration was able to melt and mold the polymer, and facilitated its flow. Once the vibration was stopped, the mold was cold down at constant pressure and the specimen was released with the ejection system. The full process is summarized in the **Fig. 3-2.**

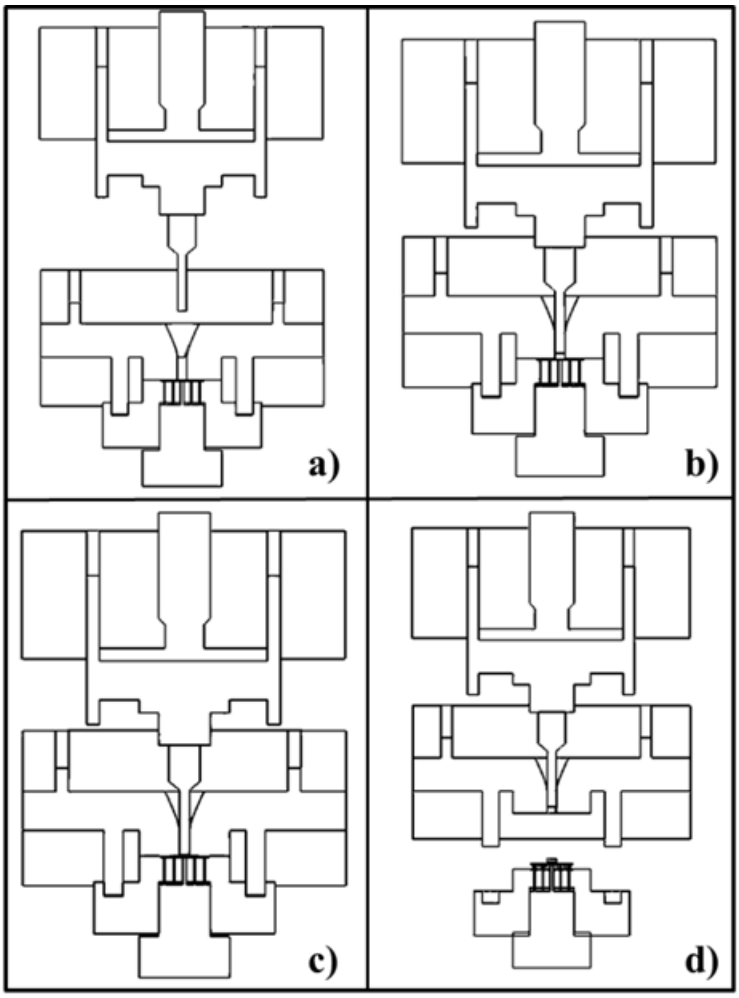

Fig. 3-2. *Schematic representation of the molding process: (**a**) Feed position, (**b**) Compression of sample, (**c**) Ultrasound turn on and molding, and (**d**) Ejection.*

Each micromolding experiment was performed with around 380 mg of powdered material that was loaded directly to the feeding/plasticizing camera of the USM equipment. When mixtures were employed (e.g. those involving PLA, TCS, PEG, HAp and/or drugs), the appropriate amounts of each powdered component were externally mixed. In the case of porous specimens (scaffolds), a subsequent washing for 24 h was needed to remove the added water soluble NaCl and PEG components.

3.1.4. Leaching of NaCl: Mass extraction yield and porosity calculations

NaCl extraction was calculated by measuring the conductivity of the washing water with a SX-650 Sanxin electrical conductivity meter (0-50 mS/cm). Calibration was performed with standard NaCl solutions at 21 °C. Values were averaged from three measurements. The weight of the removed salt, W_r, was calculated according to equations (1) and (2):

$$W_r^{NaCl} = V \cdot \frac{\sigma - b}{\sigma} \quad (1)$$

$$\%NaCl_{Extracted} = \frac{W_l^{NaCl} - W_r^{NaCl}}{W_l^{NaCl}} \quad (2)$$

where, W_l^{NaCl} is the theoretical weight loaded; W_r^{NaCl} is the weight of the removed NaCl; *a* and *b*, are calibration curve constants; *V*, volume of washing water (mL); σ, medium conductivity (S/m).

In the case of porosity and mass extraction of the PLA-NaCl-PEG systems, the samples were weighted before being washed (W_o), after staying in water for 24 h (W_w) and once the washed specimens were dried (W_d). Porosity and mass extraction were calculated according to the following equations (3) and (4):

$$\%Mass_{extr.} = \frac{W_o - W_d}{W_{theo.}^{PEG+NaCl}} \quad (3)$$

$$Porosity\ [\%] = \frac{|W_w - W_o| \,/\, \delta_{water}}{\Sigma\ {}^{W_i}/_{\delta_i}} \quad (4)$$

where, i refers to the components of the mixture (e.g., PLA, NaCl and PEG).

3.1.5. Release and quantification

Quantification analysis of the loaded drugs was done by means of a spectrophotometer SHIMADZU UV-3600. Calibration curves were done with pure drugs dissolved in ethanol and measuring absorbances at 292 nm and 259 nm for TCS and CHX, respectively.

Studied specimens were cut in three different sections. These as well as the sprue were dissolved in 100 µl of chloroform and then the drug was extracted with 900 µl of ethanol. For each part the percentage of drug was calculated by the use of the calibrations curve previously done, each measurement was performed in triplicate.

Release experiments were performed with specimens exposed in 10 mL of the selected release media, keeping the specimen under a moderate stirring (80 rpm) and constant temperature of 37ºC for one week. In this period, aliquots of 1 mL were taken out of the media and analyzed by UV spectroscopy to quantify the amount of drug released. After each extraction the media were renewed with fresh solutions.

3.1.6. Inhibition of bacterial growth

Escherichia coli (*E. coli*) and *Staphylococcus Epidemidis* (*S. epidermidis*) were selected to evaluate the antibacterial activity of drugs loaded in PLA. The bacteria were previously grown aerobically to exponential phase in lysogeny broth (LB) (Lennox) (tryptone 10 g; yeast extract 5 g, NaCl 5 g, pH 7.2). Growth experiments were performed placing three specimens (1.5 x 0.5 x 0.5 cm3) of each sample in tubes of 15 ml; neat PLA, PLA-CHX 3wt-% and PLA-TCS 3wt-%. After this, 2 ml of broth culture containing 1×10^3 colony forming units (CFU) was seeded in each sample-containing tube. The

cultures were incubated at 37°C and agitated at 80 rpm. Aliquots of 100 µL were taken at predefined time intervals for absorbance measurement at 650 nm in a reader plate. Thus, turbidity was directly related to bacterial growth. The bacterial growth in broth culture with neat PLA specimen was considered as the maximum growth (control) and it was used to calculate the relative growth of the bacteria in presence of the samples. Values were averaged considering the three replicas. Agar diffusion tests were performed in Petri dishes of 90 mm and seeded separately with 1.5×10^8 CFU/mL of each bacterium. Four sample were placed on each Petri plate; neat PLA (as negative control) and samples loaded with 1.5wt-%, 3wt-% and 6wt-% of each drug. The assay was carried on for two drugs in both bacterial media in triplicate. Inhibition halo images were taken after incubation of samples with bacteria for 24 h at 37°C.

3.1.7. Cell proliferation assay

MDCK cells (Madin-Darby Canine Kidney epithelial-like cell line) (ATCC, USA) were thawed at step subcultivation #45 and used for the proliferation assay at step #47). The cells were cultured in Dulbecco's modified Eagle's medium (DMEM with 4500 mg/L of glucose, 110 mg/L of sodium pyruvate and 2 mM of L-glutamine) supplemented with 10% fetal bovine serum (FBS), 50 U/cm^3 penicillin, 50 mg/mL streptomycin and L-glutamine 2 mM at 37 ºC in a 10% humidified atmosphere of 5% CO_2 and 95% air. Culture media were changed every two days. For sub-culture, cell monolayers were rinsed with PBS and detached by incubating them with 0.25% trypsin/EDTA for 2-5 min at 37 ºC. The incubation was stopped by resuspending in 5mL of fresh medium and the cell concentration was determined by counting with Neubauer camera and using 4% trypan blue as dye vital.

PLA scaffold, antibacterial PLA scaffold and PLA specimens (380mg) were previously washed in water to remove the salt used as a porogenic agent and to avoid hypo-osmotic damage of cultured cells. Then, the specimens were placed in tissue culture plates of 24-well, sterilized by exposed to UV light for 15min. 100 µL containing $5x10^4$ cells were deposited in each well and incubated for 60 minutes. 1 mL of culture media was then added to each well. Controls were conducted by cell culture on the wells without any material. Quantification of proliferated cells was performed after one week.

The percentage of cells adhered and proliferated was determined through the MTT (3-(4,5-dimethylthiazol-2-yl)-2,5-diphenyltetrazolium bromide) assay [3]. After a week, 50 µL of MTT (3 mg/mL) were added to each well in the plates and incubated for 4h. After that, samples were washed twice with PBS and the specimens deposited in a new plate. 1mL of dimethyl sulfoxide (DMSO) was subsequently added and the absorbance was measured at 540 nm in a microplate reader (Biochrom EZ-Read 400) after 15min of gentle stirring. Three replicas were evaluated and the corresponding values were averaged. The statistical analysis was performed by one-way ANOVA followed by Tukey test. The analyses were performed with a confidence level of 95% ($p < 0.05$).

To obtain representative fluorescence images of samples coming from proliferation assay, samples were fixed in glutaraldehyde 2.5% in PBS overnight at 4 °C, and then dehydrated by extensive washing in an alcohol battery. Finally, samples were dried in air and sequentially stained with green-fluorescent Alexa Fluor Atto-488 phalloidin dye and DAPI for labeling actin and nucleus, respectively. The images were obtained with a confocal laser scanning microscope (LSM 900 Zeiss) controlled by ZEN 2.6 software (blue edition) (Carl-Zeiss Microscopy GmbH, Jena, Germany).

3.2. Preparation of Medicated Polylactide Micropieces by Means of Ultrasonic Technology

3.2.1. Introduction

Nowadays the use of pieces with reduced dimensions has increased widespread in several commercial sectors, especially in electronic and medicine fields. Some examples of these devices are microchips, nanoneedles or pumps for microfluidics [4-6]. The wide range of applications and the high resolution required for the final performance have enhanced the interest towards the use of polymers for these purposes due to their versatility. However, the technology to produce them in a large scale is still under development.

There are some techniques to mold polymers in a microsize scale as hot embossing, thermoforming or microinjection [7, 8]. The former ones are mainly employed in a laboratory scale, being limited their interest for a large scale processing. On the other hand, microinjection equipment has been introduced in the market and is widely used to get microsamples in a commercial way. However, production cost is high due to the procedure itself and consequently microinjection application is somehow restricted. Microinjection equipment is a simple adaptation of conventional injection equipment where a microsized mold is connected by an adapted pipe. For this reason, the dosage of the material is really poor, the feeding is excessive, and the amount of non-useful material is huge, in some cases even more than 90%. Moreover, the produced molten material is more than required leading to an elevated energy cost and a large cycle time process [9, 10].

In the search of new technologies to obtain small pieces, some studies come up with the development of processing techniques based on the use of ultrasounds as a heating source. This technique has been applied for over 40 years as standard assembly procedure [11] where ultrasonic welding is based on a local melting in a thermoplastic surface. The polymer heating is generated from inside to outside the material as a result of internal polymer chain friction. This heating technique is highly efficient and accurate, moreover, ultrasound vibration increases the motion of molecular chain dropping the polymer viscosity and facilitating the molten polymer flow [12]. Some prototypes have been launched based on this heating concept combined with direct injection to plasticize material [13]. This process also offers a high efficient dosage system, delivering just the amount of material required. The potential applications of this methodology are clear, being up to now different studies conducted to improve knowledge about the effect of ultrasounds in the melting process of some commodities, as polyethylene or polystyrene [14, 15]. Also this technology is being considered for biodegradable polymers with biomedical applications, such as polylactide (PLA) [10]

PLA is an aliphatic polyester (i.e. a poly α-hydroxyacid), that can be obtained from renewal sources, such as sugar cane and starch. PLA is a biocompatible polymer which can be biodegraded into

lactic acid, has low immunologic toxicity and good mechanical properties. Furthermore, PLA has been approved by FDA for clinical assays[16] Currently, the use of PLA in the biomedical field is much extended. Specifically, it is employed in medical implants such as screws, pins or meshes[17, 18], bioabsorbable sutures [19, 20], tissue engineering [21-23] and drug-delivery system [24, 25].

One of the potential applications of ultrasonic micromolding is the possibility to incorporate drugs inside the polymer matrix and perform the molding process in a single step. Considering the prolonged cycle time and the mechanical stress suffered by the polymer, conventional injection process is not suitable for the direct loading of drugs. In most cases, drug degrades and turns biologically inactive. On the contrary, ultrasonic micromolding presents shorter cycles and a high effective heating. Hence, it seems a proper procedure to produce drug-delivery pieces with its final shape in one step.[26] A promising application could be mass production of medical screws or other implants loaded with antibacterial drugs. In this way, drug effectiveness would be improved by reducing the drug amount and targeting the effect, possible infections and facilitating the implant incorporation.[27]

The main goal of this work is centered on the evaluation of the possibility of getting PLA microspecimens with a biomedical added value. The aim is to incorporate antibacterial drugs in a PLA matrix by ultrasonic micromolding, study the effect of representative drugs (Scheme 1) in the final piece, evaluate the release kinetics of the loaded drugs, and determine if the ultrasonic heating affects the antibacterial function.

Triclosan and chlorhexidine are two well-known bactericide agents with differentiated size, physical properties (e.g. solubility) and functional groups (i.e. hydroxyl for TCS and biguanidine for CHX) (**Fig. 3-3**). These different characteristics have prompted us to select them as representative examples.

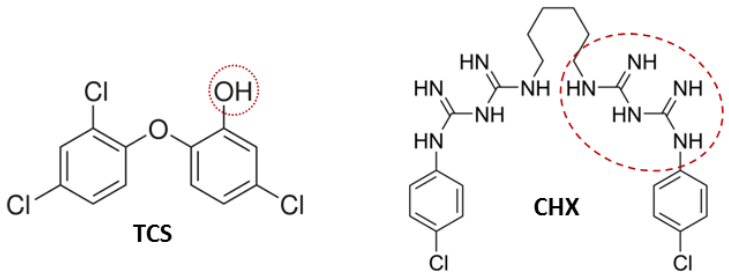

Fig. 3-3. *Chemical formulas of the selected antibacterial drugs. Dashed red circles point out distinctive functional.*

3.2.2. Results and Discussion

3.2.2.1. Set up of molding conditions

As mentioned before, this new processing technique is based on the use of ultrasounds as a heating source. Hence, molding parameters such as ultrasound intensity or wave amplitude have not a clear correlation with physical characteristics of processed specimens compared with the well-established knowledge concerning conventional micromolding machines. In this case, polymer

properties such as melting point or flow index, are easily related to heating and pumping intensity, whereas ultrasound micromolding needs further research to arrive to a similar know how.[10] Therefore an empirical study has been done to determine correct molding conditions for neat PLA before starting to work with drug blends. The aims of these assays are the following points:

a) To find appropiate energy and molding force are enough to fill the whole mold. With a previous prescreening made with neat PLA, a clear relation between ultrasonic intensity and molding force with the capability to fill the whole mold was found. Through a visual inspection (the 8 specimens were fully molded or not) could be concluded that working with an amplitude lower than 24 µm was not enough to reach the flowing state of PLA. In reference to the molding force, a value above 300 N was needed to the get the 8-specimen full. However, cautions should be taken into account since forces around 500-600 N were not stable since in some cases the sonotrode was overload (i.e. it cannot vibrate) due a high compaction of PLA.

b) To compare the molecular weight of molded sample with the original polymer. One of the main issues of this process is the possibility of polymer degradation, rupture of the polymer chain in oligomers, compromising the final physical properties of the molded specimen [12]. GPC measurements of samples processed under different conditions are summarized in **Table 3-1**. PLA seems very flexible with the molding condition in comparison with other polymers.[28] Molecular weight variation was not detected for the applied range of force. However, the increase of the molding time caused a significant degradation. It can be assumed that a molding time equal or lower than 1.2 s may cause a minimum degradation of PLA.

Table 3-1. *Molding efficiency and molecular weight of a PLA sample molded under several conditions.*[a]

Molding[b]	Efficiency[c] (%)	M_n (g/mol)	M_w (g/mol)	PDI
Raw	-----	43,00	69,100	1.64
24-200-1.5	40	35,400	69,700	1.96
24-300-1	100	34,500	68,600	1.98
24-300-1.2	**100**	**38,800**	**72,200**	**1.88**
24-400-1	80	-----	-----	-----
24-400-1.5	100	37,700	71,300	1.89
24-500-1.5	-Ovl-	33,900	67,500	1.99
24-600-1.5	-Ovl-	-----	-----	-----

(a) Optimized conditions use in this work are highlighted.
(b) Micro-molding conditions: Amplitude (µm), Force (N) and Time (s)
(c) Mold filling, qualitative evaluation (i.e. 8 half pieces or 4 full correspondedto 50%. –Ovl- Sonotrode overload

c) To confirm that chemical structure of the polymer molded keeps unaltered the FTIR spectrum of a PLA specimen molded at the optimized condition of 300N 1.2s 24 µm, according to the filling efficiency and GPC assay, were compared with the spectrum of commercial powdered PLA (**Fig. 3-4**). It is clear that the ultrasonic source has not given rise to any significant modification of the chemical structure of the polymer. The typical bands of ester (1745, 1266 and 1108 cm^{-1}) and methylene groups (1455 and 1380 cm^{-1}) remained unchanged.

d) To check the presence of fissures, cracks or cavitation inside the processed samples, features that may affect the final mechanical properties of specimens. **Fig. 3-5** shows SEM micrographs of the processed sample under optimal parameters where significant physical defects cannot be detected.

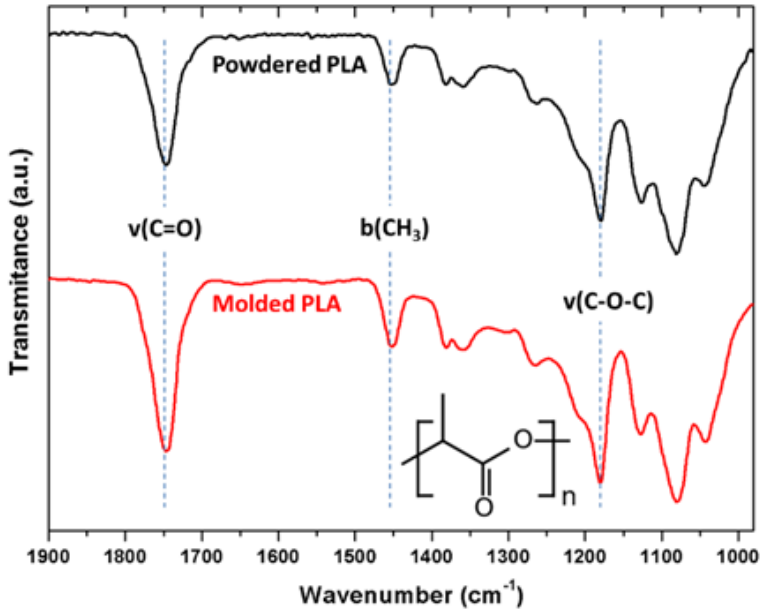

Fig. 3-4 *FTIR spectrum of PLA before (black) and after (red) being molded.*

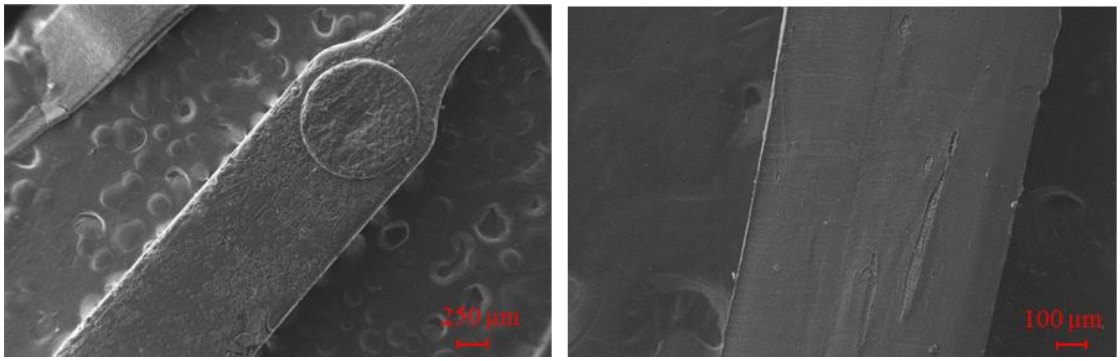

Fig. 3-5 *SEM micrographs of a PLA specimen molded at 24-300-1.2 condition.*

3.2.2.2. Characterization of PLA specimens loaded with drugs

The influence of the incorporation of different amounts of TCS and CHX on the ultrasound micromolding processing of PLA was followed by FTIR spectroscopy and GPC measurements.

Fig. 3-6 shows that CHX can be detected in the FTIR spectra of specimens even for the lowest load. Thus, bands related to the biguanide compound appearing at 1640 cm^{-1}, 1530 cm^{-1} and 1490 cm^{-1} could be seen, even for a load of only 1%-wt. Logically, the intensity of those bands get higher with the increase of the CHX amount. On the contrary, the infrared spectrum of TCS loaded samples did not show any characteristic band associated to the drug (i.e. those appearing at 1598, 1579, 1507, 1471, 1417 and 1,392 cm^{-1}) and only the spectra of PLA was detected (not shown). A potential explanation is the lower intensity of TCS bands but also to the hydrophobic character of TCS that

could improve its dispersion in the PLA hydrophobic matrix. On the contrary, the high hydrophilicity of CHX may favor its disposition onto the PLA specimen surface, its detection by ATR measurements being increased.

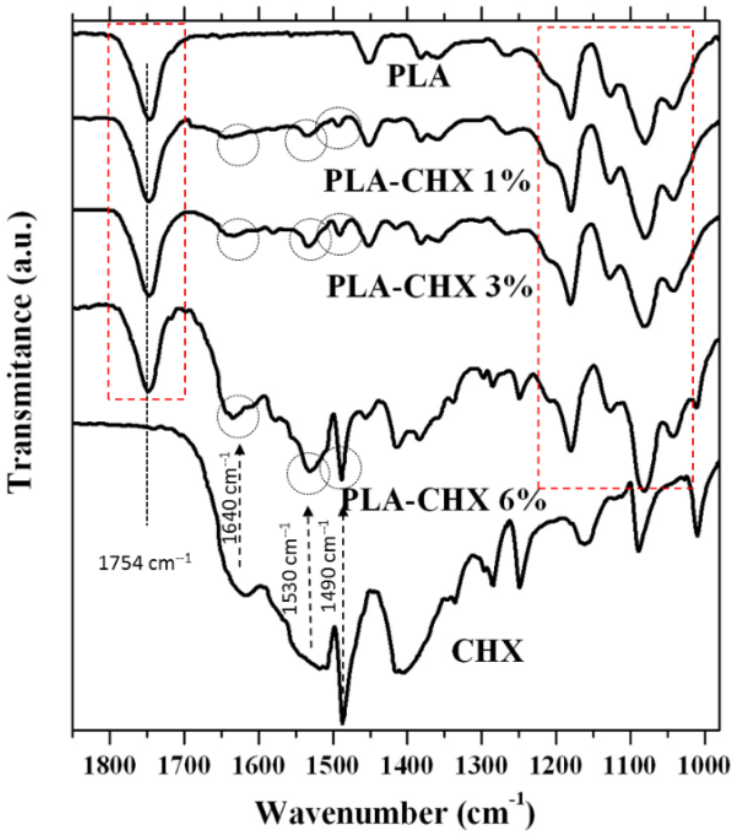

Fig. 3-6. *FTIR spectrum of PLA, PLA samples loaded with different amount of CHX and pure CHX. Dashed red boxes indicated bands associated to PLA.*

GPC curves were recorded for specimens loaded with different percentages of TCS and CHX and processed under the conditions optimized for the PLA matrix (24 μm-300 N-1.2 s). In this way, the effect of the type of drug and percentage can be determined, it being possible in a subsequent work to change the ultrasound parameters in order to improve processing.

Fig. 3-7a shows similar GPC curves for the neat PLA, the ultrasound processed unloaded PLA sample and that loaded with the maximum amount of TCS (i.e. 6 wt-%). Basically, the maximum appeared at practically the same elution time (see dashed blue box) and differences can mainly be seen in the tail corresponding to higher elution times (i.e. fraction of low molecular weight chains) that slightly increased for the ultrasound processed samples (see dashed red box). Analyses indicated a slight decrease from an initial M_n value of 43,000 g/mol to 40,000-38,800 g/mol after processing.

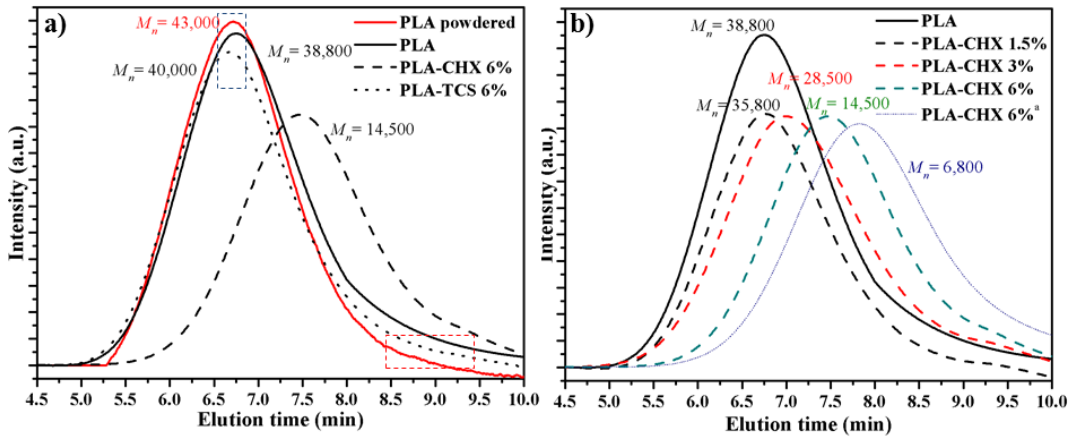

*Fig. 3-7. (**a**) GPC curves determined of initial powdered PLA, the molded PLA and its mixtures with the maximum assayed amounts of TCS and CHX. (**b**) Comparison between GPC curves of processed PLA and PLA mixtures with the indicated percentages of CHX. For the sake of completeness, the curve corresponding to a molten PLA film loaded with 6 wt-% of CHX is also drawn (dotted curve).*

By contrast, incorporation of CHX caused a clear degradation at the percentage of 6 wt-% (**Fig. 3-7b**) as evidenced by the decrease of M_n from 43,000 g/mol to 14,500 g/mol. Furthermore, **Fig. 3-7b** demonstrated a correlation between the CHX load and the molecular weight decrease. Nevertheless, it is interesting to note that degradation becomes minimum for a load of 1.5 wt-% (i.e. M_n decreased from 38,800 g/mol to 35,800 g/mol which means a loss less than 5%). In order to verify if degradation was a direct consequence of the exposition to the ultrasonic source, we have also evaluated CHX loaded samples only submitted to the high temperature required to melt the PLA matrix. ***Fig. 3-7b*** shows the GPC curve of a PLA film loaded with 6 wt-% of CHX by solvent casting and then heated at a rate of 10 °C/min to 180 °C (i.e. over the melting temperature of PLA). In this case, degradation was the highest since the molecular weight decreased up to 6,600 g/mol. Thus, the presence of CHX molecules having a great proportion of amine groups (i.e. those belonging to the characteristic biguanide entities) accelerated the thermal degradation of PLA as was reported more explicitly in previous works [29, 30]. Results pointed also out the great advantage of the new ultrasound technique. Probably, the low processing time that is in this case required allows reducing significantly the degradation effect in such way that it could not be detected for reduced loads.

Applications of microspecimens would need some mechanical requirements, such as elasticity or physical resistance. To this end typical stress-strain measurements were performed to evaluate both the effect of processing and the incorporation of drugs. Representative plots are shown in **Fig. 3-8a** and the corresponding mechanical parameters are summarized in **Table 3-2. Fig. 3-8b** shows the specific variation of the Young modulus and the deformation with the amount of loaded drug.

Samples loaded with chlorhexidine followed the same trend of the GPC assay. Thus, both properties clearly decreased for a load higher than 1.5 wt-% as consequence of degradation. Moreover, when the load was 2.5 wt-% a sudden decrease was observed. Logically the most sensitive property was the elongation at break, which decreased from an 8.5% to 4% for PLA-CHX 6 wt-%. It should be indicated that high standard deviations were observed since this property is highly affected by the presence of minimum defects (e.g. fissures, cracks, etc) in the processed specimen. By contrast, the

behavior of samples loaded with TCS is clearly different as expected from their minimum molecular degradation. Thus, Young modulus was practically constant for all TCS loaded specimens, while the elongation at break tended to increase (i.e. from 9% to 11%) due to a plasticization effect of TCS.

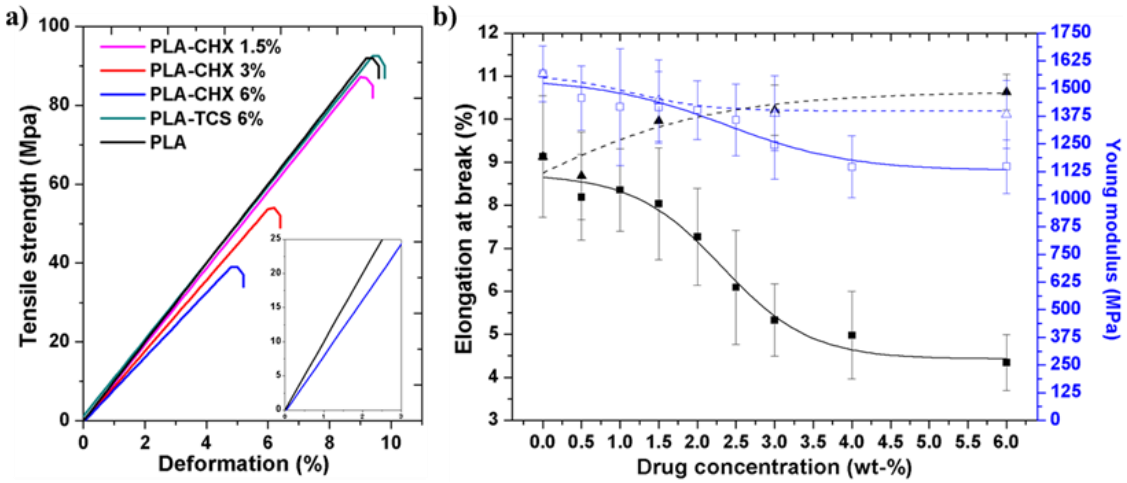

Fig. 3-8. ***(a)*** *Stress-strain plots obtained from the representative indicated samples.* ***(b)*** *Variation of the elongation at break (black curves) and the Young modulus (blue curves) with the TCS (dashed lines) or CHX (solid lines) load. All samples were processed under the optimized conditions of 24-300-1.2.*

Table 3-2. *Mechanical parameters extracted from stress-strain assays.*

Drug %-wt	Chlorhexidine		Triclosan	
	Elongation at Break (%)	Young Modulus (MPa)	Elongation at Break (%)	Young Modulus (MPa)
0	9.13 ± 1.4	1,565 ± 127	9.13 ± 1.4	1,565 ± 130
0.5	8.19 ± 1.0	1,456 ± 145	9.11 ± 1.0	1,558 ± 120
1	8.35 ± 0.9	1,416 ± 264	9.61 ±0.8	1,510 ± 135
1.5	8.03 ± 1.3	1,414 ± 161	9.95 ± 0.5	1,445 ± 190
2	7.26 ± 1.1	1,401 ± 132	10.01 ± 0.7	1,411 ± 160
2.5	6.09 ± 1.3	1,357 ± 161	10.19 ± 0.8	1,393 ± 110
3	5.33 ± 0.8	1,243 ± 152	10.21 ± 0.6	1,388 ± 170
4	4.97 ± 1.0	1,145 ± 139	10.50 ± 0.4	1,380 ± 140
6	4.34 ± 0.7	1,146 ± 120	10.62 ± 0.4	1,383 ± 150

Micrographs shown in **Fig. 3-9** show the more irregular section surfaces of samples loaded with CHX as consequence of some evidences of degradation. Note that despite the major irregularities were caused by the blade cut some imperfections can be evidenced in the chlorhexidine specimen (dashed circle). The observed erosion may also be induced by cavitation. Although this is not a goal of the present work, a correlation between cavitation events with damaged areas will provide useful information.[31, 32]

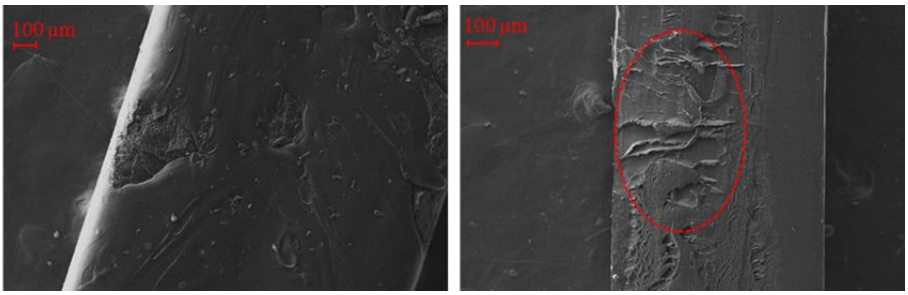

Fig. 3-9. *SEM micrographs of a PLA specimen loaded with 6 wt-% of TCS (left) and CHX (right) molded at 24-300-1.2 condition.*

3.2.2.3. Calorimetric characterization

DSC scans were performed in order to compare thermal properties of ultrasound micromolded pieces and melt crystallized samples, and also to study the influence of the loaded drug in the thermal properties. **Fig. 3-10** compares the DSC runs obtained directly from micromolded pieces (**Fig. 3-10a**) and those registered from samples after being cooled (10 ºC/min) from the melt state (**Fig. 3-10b**).

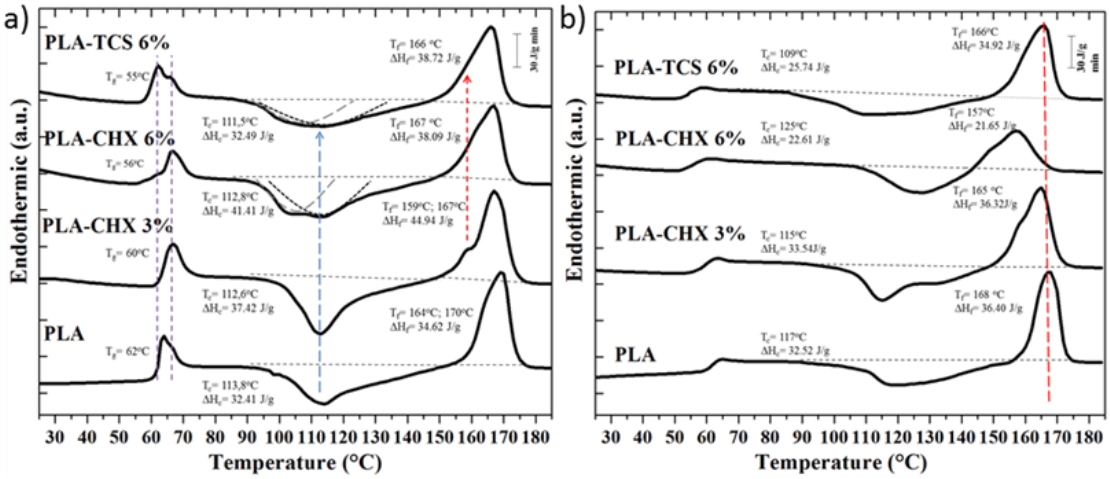

Fig. 3-10. *DSC curves corresponding to the first heating (**a**) and second heating (**b**) runs of neat PLA, PLA loaded with 3% and 6% of CHX and PLA loaded with 6% of TCS. Both heating runs were performed at 10 ºC / min.*

Main characteristic are the followings:

a) Specimens prepared by ultrasound micromolding showed relaxation endothermic overshoots over T_g, which indicated that the heating rate in DSC scan was higher than the previous cooling rate during glass formation. The observed peaks are complex but were minimized in the second heating run. It should be pointed out that relaxation peaks were not associated with a potential fusion of loaded drugs (55 ºC for TCS and 134 ºC for CHX) since were also detected for unloaded PLA.

b) All samples showed exothermic cold crystallization peaks, which were higher for the micromolded specimens as a consequence of their higher amorphous content. The associated

enthalpy clearly increased also when drugs were loaded and even were split in two peaks for loads around 6 wt-%.

c) The melting process was similar for all PLA samples and those loaded with 3 wt-% of CHX. This fusion was characterized by a complex melting peak with a shoulder at 164 ºC and a main peak at 170 ºC as it is well described. The melting enthalpy was also comparable, indicating that a similar degree of crystallinity was achieved after cold crystallization. Nevertheless, the second heating run of the sample loaded with 6 wt-% of CHX showed a melting peak with a clearly lower enthalpy (i.e. 21.65 J/g with respect to 38.09 J/g measured for the melt crystallized PLA sample), lower melting peak temperature (157 ºC with respect to 168-170 ºC) and a higher temperature for the cold crystallization peak (i.e. 125 ºC with respect to 114-118 ºC). The different behavior of such sample is in agreement with the above mentioned degradation process that should be maximum at the end of the second heating run due to the considerable exposure to high temperatures (i.e. during the performed heating and cooling runs) and demonstrates also the clear loss of properties.

Thermogravimetric analyses to see the influence of the loaded drugs on the thermal stability of processed samples were also carried out and are shown in **Fig. 3-11.**

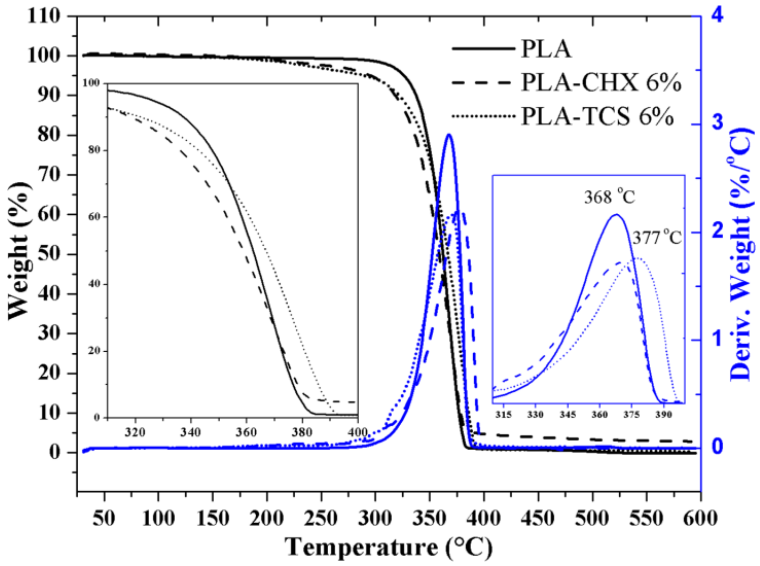

Fig. 3-11. *TGA and DTGA profiles of ultrasound processed specimens of PLA and PLA loaded with 6wt-% of each drug. Magnification of onset temperature region and DTGA peaks are shown in the insets.*

Fig. 3-11 shows the typical TGA and DTGA curves of PLA with a main decomposition step at 370 ºC, a small shoulder at lower temperature and an onset degradation temperature of 345 ºC. Both TCS and CHX loaded samples gave rise to a reduction of the onset temperature to around 200 ºC, which mean that cautions should be taken to avoid the exposure to such high temperature. Fortunately, this onset temperature is clearly higher than the PLA melting temperature in such a way that TCS processed samples did not shown any evidence of degradation. Similar TGA and DTGA curves were

detected for CHX loaded curves but degradation cannot be discarded as evidenced by the previous analyses. It seems that molecular scission took place without rendering small volatile fragments that could be detected in the TGA profiles. Degradation rate was also different between neat PLA and drug loaded samples since peak temperature slightly increased for TCS and CHX loaded specimens. Minimum differences were also found in the char yield, which was higher for CHX loaded samples probably as a consequence of its higher aromatic content.

3.2.2.4. Drug load and release

The study of the drug loading process was done considering two points: the amount of drug loaded in the specimen and its homogeneity (i.e. the drug can be distributed in a non-homogeneous way along the flow direction). Note also that some amount of drug should rest in the sprue and consequently the drug effectively incorporated in the specimen is different to the amount of drug loaded in the processing chamber. Therefore, results will be always referred as the percentage of drug in each evaluated specimen. In order to determine the uniformity of the drug distribution, the specimen was cut in three parts along the flow direction as shown in **Fig. 3-12a**. The percentage of drug incorporated in each section was determined by UV measurements of three replicas. Comparison between the average values determined for each one of the three parts allowed for getting an idea about the homogeneity of the sample

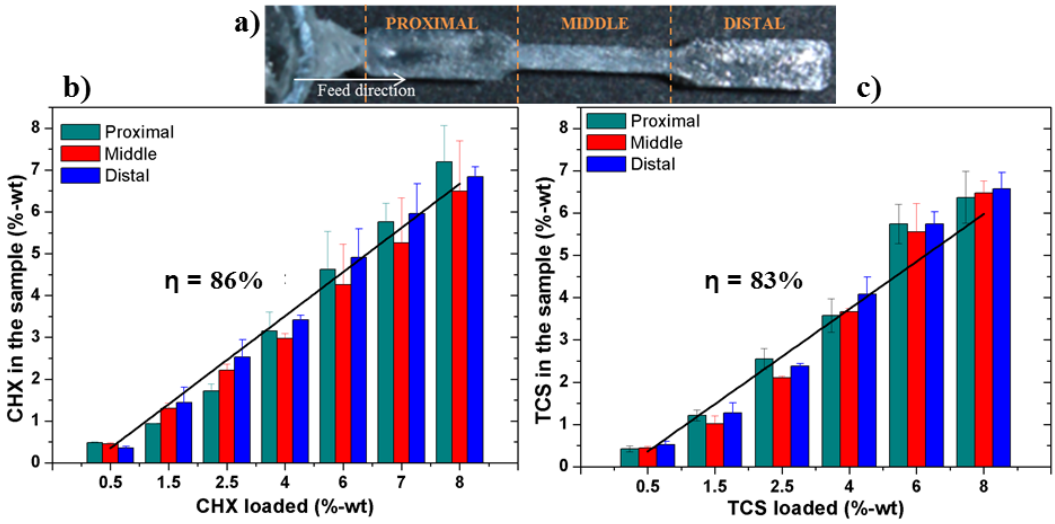

Fig. 3-12. *Schematic representation of the three selected sections for each specimen (**a**). Percentage of loaded CHX (**b**) and TCS (**c**) drugs for the three specimen sections with respect to the percentage introduced in the processing chamber.*

Fig. 3-12b and **12c** compare the theoretical percentage that should be loaded and the real percentage incorporated in each analyzed section. The loading efficiency was around 83-86% for both drugs, independently of the total load. A relatively good distribution along the flow direction was found, although the proximal region (i.e. that closest to the sprue) tended to have a slightly higher

percentage. Results attained with CHX and TCS were similar despite the great differences on molecular size and even in their hydrophobic character.

Release studies were performed in static conditions, which are obviously di_erent to the continuous renewal of the medium that occurs in the human body. The performed study tries to use media with different polarity (i.e., by controlling the PBS:ethanol ratio) in order to evaluate drug retention and compare kinetic data. Specifically, the release assays were carried out in two types of media: ethanol and a PBS-ethanol mixture with 70% of PBS. Ethanol was selected in order to favor the drug release due to its capability to swell the PLA matrix. The second medium kept a certain content of ethanol and had a similar hydrophobicity of a typical serum medium as has previously been reported.[33, 34]

The release profiles of both drugs in the PBS-ethanol medium are shown in ***Fig. 3-13*** (dashed lines). These releases follow a first order kinetic without a significant burst effect. The release rate was slow and specifically 155 h were required for a delivery of 50%. This release was faster for the more hydrophilic CHX drug (i.e. k_1 values of 0.0356 h^{-1} and 0.027 h^{-1} for CHX and TCS, respectively). The specimens were clearly too wide and compact to get a complete release in the limited exposure time of 155 h

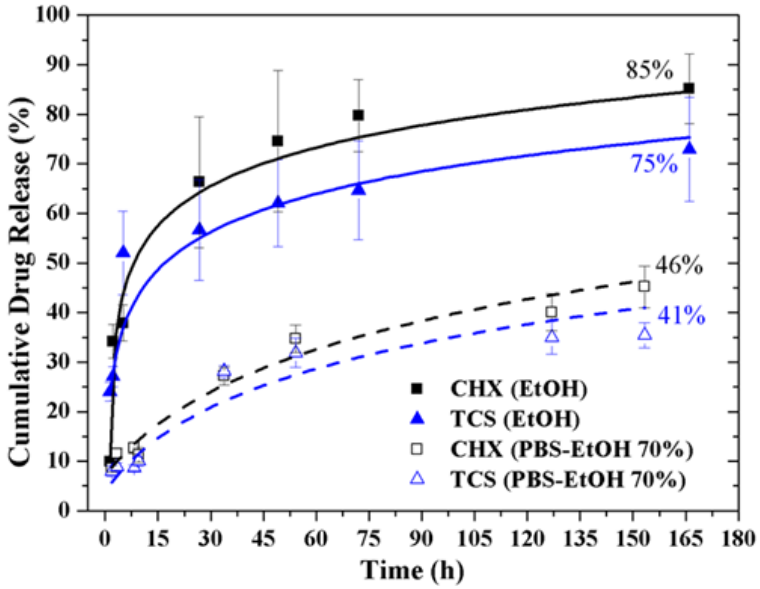

Fig. 3-13. *Release profile of PLA samples loaded with 3 wt-% of TCS (blue) and CHX (black) in absolute ethanol (solid lines) and PBS-EtOH 70% (dashed lines).*

Ethanol media increased the release rate and allowed the release of drugs located in the inner part. Specifically, release percentages of 85% and 75% were achieved after 165 h. This release was characterized by a clear burst effect (40-45% after only 8 h of exposure) of drugs located near the outer layer of microspecimens followed by a first order kinetic process with values of the same magnitude order of those found in the PBS containing medium (i.e. 0.0367 h^{-1} and 0.0297 h^{-1} for CHX and TCS, respectively).

3.2.2.5. Antibacterial properties of CHX and TCS loaded micromolded pieces

The results of agar tests for representative Gram-negative (*E. coli)* and Gram-positive (*S. epidermidis*) bacteria are shown in **Fig. 3-14**. The presence of an inhibition halo in the loaded samples, not observed around the neat PLA, reflects the drug antibacterial activity. Therefore, the ultrasound heating source has not a negative effect in the antibacterial activity of the evaluated drugs. These results show that the drugs maintain their molecular structure intact and consequently their activity during the micromolding process.

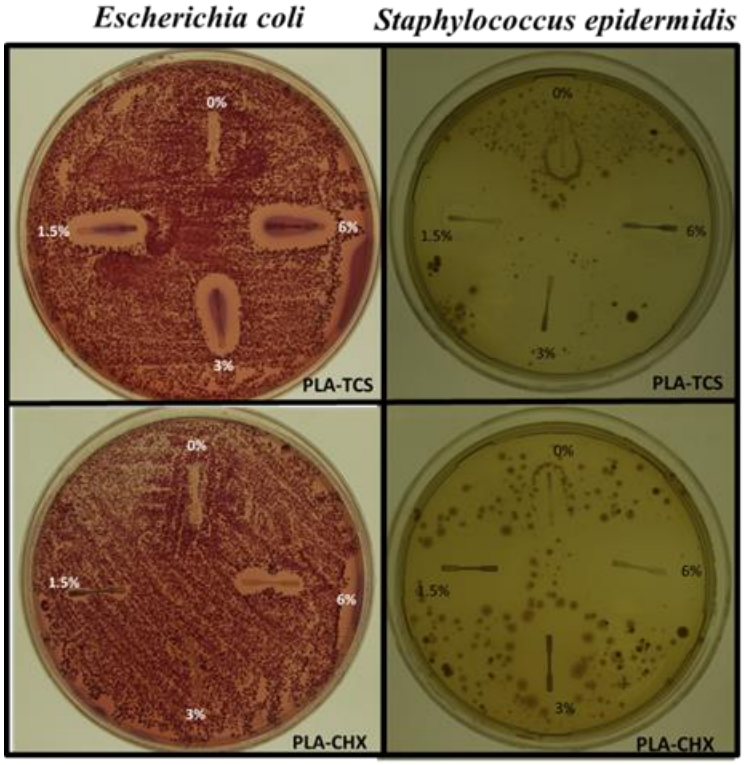

Fig. 3-14. *Agar tests performed with PLA samples loaded with 1.5/3/6 wt-% of each drug (TCS or CHX) for E. coli and S. epidermidis. For the sake of completeness PLA unloaded samples are also evaluated.*

The sizes of the inhibition halo are directly linked with antibacterial activity level. Accordingly, the activity of both drugs against *S. epidermidis* was much higher than for *E. coli*. Comparing the CHX and TCS response, a greater effect was observed for TCS loaded samples despite its smaller release rate, being its greater inherent bactericide activity demonstrated as discussed below. Differences in the size of the inhibition halo were nevertheless minimized when high drug concentrations were used. The previously indicated small release rate, which is derived from the high specimen compaction, suggests that the initial bactericide effect was caused by the drug located at the specimen surface, which needs a minimum loading concentration to be significant.

These results shown in **Fig. 3-14** can be explained taking into account the different antibacterial mechanisms of both drugs. TCS diffuses through the bacterial cytoplasmic membrane and interferes with its lipid metabolism, leading to clear inhibition halos for both bacteria. By contrast,

CHX salts are dissociated at physiologic pH and consequently positively charged CHX cations become the delivered agents. The bactericidal effect of CHX is a result of the binding of this cationic molecule with the negatively charged bacterial cell walls. Responses are consequently dependent on the structure of the bacterial walls, which are only constituted by peptidoglycans (PGs) in the case of Gram-positive bacteria, while these PGs are coated by proteins, phospholipids and lipopolysaccharides in Gram-negative bacteria. Coatings provide a protective effect to the action of CHX cationic molecules. Therefore, halos produced by TCS (large-medium sizes) and CHX (reduced size) can be well-differentiated in an *E. coli* medium.

Both TCS and CHX act as biocides at high concentrations and at lower concentrations have a bacteriostatic effect. Drug effects can be analyzed through the broth culture quantification assay. **Fig. 3-15** compares the bacterial growth curves of unloaded (solid lines) and loaded (dashed and dotted lines for CHX and TCS, respectively) PLA processed specimens. Both drugs had a clear bactericidal and bacteriostatic effect in the two studied bacterium media. Thus, bacterial growth was reduced to near 20 %, related to the 100 % of neat PLA. PLA loaded with 3 wt-% of CHX firstly had a high bactericidal effect, suppressing the bacterial growth up to 24h, and subsequently a bacteriostatic activity that kept the total bacterial growth under 20%. For the samples loaded with TCS the bactericidal effect was a little less effective since a delay of the growth around 10-15 h was observed with respect to CHX. Nevertheless, the bacteriostatic effect was active for the whole assay, allowing reaching similar growth levels in both bacterium media than those observed for CHX loaded specimens. These results are very interesting because they firstly show that loaded micromolded pieces provide enough bactericidal concentration in the medium, and secondly that drugs are released in a continuous way to guarantee clear bacteriostatic effects. In summary, the studied micromolded pieces loaded with TCS or CHX remain efficiently protected against eventual bacterial infections over time.

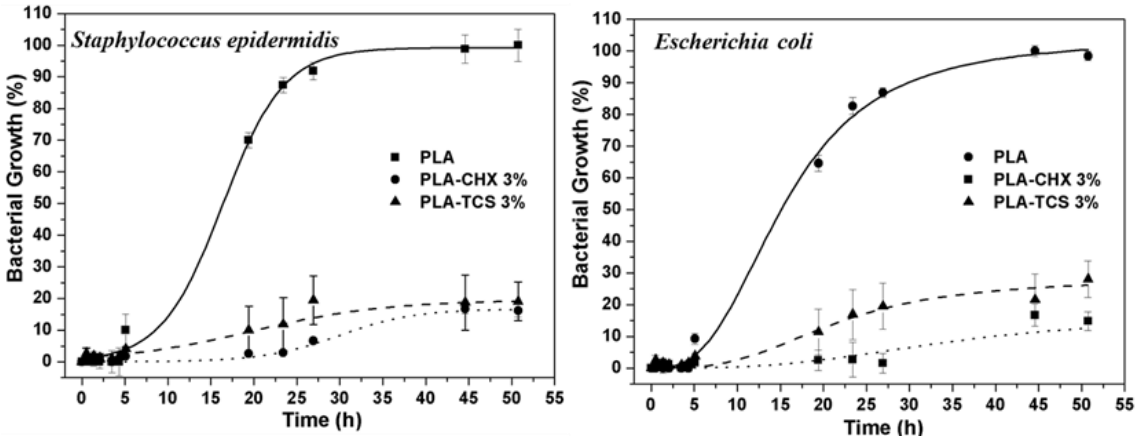

Fig. 3-15. Bacterial growth in presence of PLA samples and PLA loaded with 3 wt-% of TCS and CHX.

3.2.3. Conclusions

Micromolded specimens loaded with bactericide agents could be effectively processed using ultrasound as an effective energy source. Results supported the potential of this new processing technology for producing micropieces from biodegradable and biocompatible polymers such as polylactide, and pharmacological drugs. Specimens with minimum degradation and a uniform drug distribution could be easily obtained. More interestingly, the low processing time required for the ultrasound technology appears highly advantageous when compounds that enhance thermal degradation should be incorporated into the polymer matrix. In this sense, the decrease in the final degradation of pieces loaded with CHX is notable with respect to specimens obtained by classical melt processing. CHX and TCS loaded microspecimens retained the activity of TCS and CHX after ultrasound processing. Specifically, drugs were slowly released from the micropieces with a rate that was slightly dependent on their hydrophilicity. The release in a PBS-ethanol medium (70% of PBS) followed a first order kinetics with constants of 0.0356 h^{-1} and 0.027 h^{-1} for CHX and TCS, respectively. Bactericide and bacteriostatic effects against both Gram-positive and Gram-negative bacteria were detected for the two drugs at the beginning and at the final step of exposure to the bacterium media, respectively. Bacterial growth could be reduced to close to 20% when micropieces were loaded with only 3 wt-% of any of the selected CHX and TCS drugs.

3.3. Biodegradable polylactide scaffolds with pharmacological activity by means of ultrasound micromolding technology

3.3.1. Introduction

The regeneration and repair of biological tissues usually require a temporal or permanent support to provide at least structural and mechanical properties. Tissue engineering appears as a new research discipline [35-37] that is addressed to develop new materials with appropriate properties and features that can also improve their final performance with additional functions. Efforts are mainly focused to accelerate the regeneration and reparation of tissues, to guide cell growth [38], to increase the biodegradability of temporal supports, to decrease cytoxicity [39, 40], to produce nanocomposites reinforced with particles or fibers in order to improve adhesion and cell proliferation [41-43], to incorporate growth factors and other bioactive agents in order to stimulate cell growth [44, 45], to give an antimicrobial response or other effects such as radical scavenging [46], and finally to develop materials with electroconductive properties that make feasible an electrical stimulation or a controlled drug release [47].

Tissue engineering has developed the so-called scaffolds, which are biomaterials that mimic the extracellular matrix of tissues. Scaffolds are usually porous supports with a three-dimensional structure that allows increasing the number of adhered cells and the cell growth [48]. Furthermore, porous scaffolds may also enhance cell transit and diffusion of nutrients and growth factors [49, 50]. Biodegradable polymers are usually employed when scaffolds should have a temporary function and act as templates for tissue repair and regeneration. Extensive reviews have been focused on the selection of appropriate polymeric materials since degradation rate and maintenance of properties should be in agreement with the time required for tissue regeneration [51-53].

Scaffolds can also be considered as drug releasing systems since the polymer matrix can be loaded with the appropriate active agents. Scaffolds increase their surface due to their porous structure and therefore the amount of drug released could be tuned depending on this surface. In most cases, scaffolds have been developed as temporary supports based on biodegradable materials, having some of the above indicated specific properties (e.g., antibacterial activity). Triclosan (TCS), is for example. usually employed as biocide in both home and hospital settings for disinfection. TCS has a clear hydrophobic character and basically acts as an inhibitor of the bacterial lipid biosynthesis [54].

There are several methods to obtain a porous polymeric scaffold; some of them can directly generate the pores while in other cases a secondary treatment is needed. Deposition and assembly of micro/nanofibers is a common one step process. These meshes can be produced by the bonding of different fibers, where some of them (with lower melting point) act as a reticulation point, or by electrospinning. The binding process is simpler but the porosity grade is not under such accurate

control as could be achieved through electrospinning [55, 56]. Most of direct processes developed for scaffold production are limited to a laboratory scale and are not widely applied in the industrial field.

By contrast, indirect procedures are more common in big mass production and also they allow a fabrication with the desired final shape [57]. Conventional industrial procedures, such as extrusion or injection can be applied when are combined with the salt leaching technique. In this case, the polymer is mixed with a water soluble salt and then molded. Porosity is created after removing the salt by water immersion. Porous size and density can be accurately controlled through the selection of both particle size and the incorporated amount of salt [58, 59].

Nowadays, the market is demanding high resolution scaffolds able to produce shape profiles with nanosized ending to mimic fissures and textures of naturally occurring tissues. Despite 3D printing can reach this scale with high accurate ending, it is still high cost production to be used for mass production [60, 61].

The use of pieces with reduced dimensions has increased in the last years through several markets. Microinjection is being used in a commercial way and good results have been achieved, this technique is inefficient and the production costs are really high. Microinjection is based in a simplistic adaptation of a conventional injection machine to produce micro samples, and is not optimized to mold samples with nano or microscale features. The material dosage and heating is poor and not well optimized leading to a high amount of non-useful material, long cycle times and an inefficient heating profile [13, 62].

Recently, some studies have been focused on the development of a new promising technique based on ultrasound micromolding [63]. Advantages concern to its good reproducibility, low cost, efficient material dosage, low cycling time and high resolution [10]. The sample is locally heated by the kinetic energy produced by the chain vibration that is induced by an ultrasonic source [9, 14, 64]. Ultrasound heating also increases the flow index of the polymers leading to an effective filling of designed micromold cavities if an appropriate pressure/force is applied [15]. Different studies have been carried out with some commodities, such as polyethylene, polymethylene oxide and polypropylene, [14], commercial biodegradable polymers such as polylactide (PLA) and polybutylene succinate [28], and polymers loaded with exfoliated clays (e.g. PLA) [65] and multiwall carbon nanotubes (e.g. polycaprolactone) [66]. All of them concluded that an accurate selection of amplitude, force and time parameters could lead to minimum polymer degradation, absences of defects in the micromolded pieces and an accurate filling of the mold.

In this work, PLA was selected as the polymer matrix due to its biocompatibility, low immunogenicity and good mechanical properties. PLA is FDA-approved for clinical use, and has the ability to biodegrade in lactic acid into the human body. PLA has already been used to fabricate medical implants like screws and pins [18], scaffolds [67] and drug-delivery systems [68]. Moreover, our previous works have demonstrated that ultrasonic-assisted molding is an adequate process to produce miniature pieces loaded with bactericide agents without activity loss [69]. This is a key point since it is well known

that production methods can influence on the pharmacological activity. The main goal of the present work is the preparation of new biodegradable porous scaffolds through an ultrasonic-assisted micromolding technology as a new indirect method suitable to be employed at an industrial scale with an extremely high resolution. In addition, we have explored the capacity to load the porous scaffolds with a pharmacological agent. In this case, an antibacterial drug able to protect against potential infections been selected. The crucial point concerns the retention of the drug during the necessary salt leaching step. The work involves three main parts: evaluation of the effects caused by the incorporation of porogenic agents, optimization of the leaching process and evaluation of the capacity to load a representative drug. Thus, the achievement of antimicrobial properties for the triclosan (TCS) loaded scaffold could be considered as a good probe of the suitability of the new application of ultrasound technology to prepare porous scaffolds.

3.3.2. Results and Discussion

The different molded samples and the corresponding optimized molding parameters as then will be explained are summarized in **Table 3-3.**

Table 3-3. *Abbreviation, composition and processing parameters of the studied samples.*

Samples	PLA (wt-%)	PEG (wt-%)	NaCl 45nm (wt-%)	TCS (wt-%)	Molding parametres[a]
PLA	100	0	0	0	24/300/1.2
PLA:NaCl-35	65	0	35	0	24/400/1.2
PLA:NaCl-40	60	0	40	0	24/400/1.2
PLA:PEG 85%	85	15	0	0	24/300/1.2
PLA:PEG 70%	70	30	0	0	24/300/1.2
PLA:PEG 60%	60	40	0	0	24/300/1.2
PLA:PEG 50%	50	50	0	0	24/300/1.2
PLA:PEG-10:NaCl-40[b]	50	10	40	0	24/400/1.2
PLA:PEG-8:NaCl-36:TCS-6	50	8	36	6	24/400/1.2

(a) Amplitude (μm)/Force (N) /Time (s) (b) Scaffold (c) Antibacterial Scaffold

3.3.2.1. Micromolding of mixtures of PLA and the porogenic agent

A preliminary study was done to determine the capability of the ultrasound equipment to mold mixtures of PLA and a water soluble salt. Sodium carbonate (Na_2CO_3), sodium bicarbonate ($NaHCO_3$) and sodium chloride (NaCl) were selected due to their low cost, biocompatibility and wide use in salt leaching applications [70-72]. In a first attempt, PLA was mixed with a low percentage (e.g. 10 wt-%) of the selected salt. Both carbonates were decomposed during processing giving rise to carbon dioxide (**Fig. 3-16a** and **17b**) which means that samples could not be successfully molded. Even by varying amplitude, force and time processing parameters the PLA was not able to fill completely the mold and the specimens presented a lot of bubbles, especially for the bicarbonate sample (**Fig. 3-16c**).

Gas bubbles inside the molten polymer hindered the diffusion of molecular chains and led to a bad distribution and an imperfect molded specimen. Moreover, bubbles were responsible of cavitation effects that caused some polymer degradation as evidenced by the observed punctual coloration in some parts of the specimens.

By contrast, sodium chloride (NaCl) with a particle size of 250-100 μm allowed obtaining well molded specimens (**Fig. 3-16d**) without modifying the processing parameters previously determined for the selected commercial PLA [69]. Thus, amplitude, force and time of 24 μm, 300 N and 1.2 s, respectively, were considered optimal and used in the most of the performed tests.

Tests were also carried out considering different NaCl loads and varying also the particle size. The above indicated processing parameters were appropriate to get specimens up to a maximum NaCl load of 40 wt-% when diameters were in the 250-100 □m size range. Higher salt contents lead to an overload signal. When smaller particles (e.g. < 45 μm) were employed, the salt percentage could be increased to 50 wt-% but the applied force should be increased to 400 N. Lower (e.g. 300 N) and higher (e.g. 500 N) forces caused an incomplete filling of the mold (85%) and an overload signal, respectively.

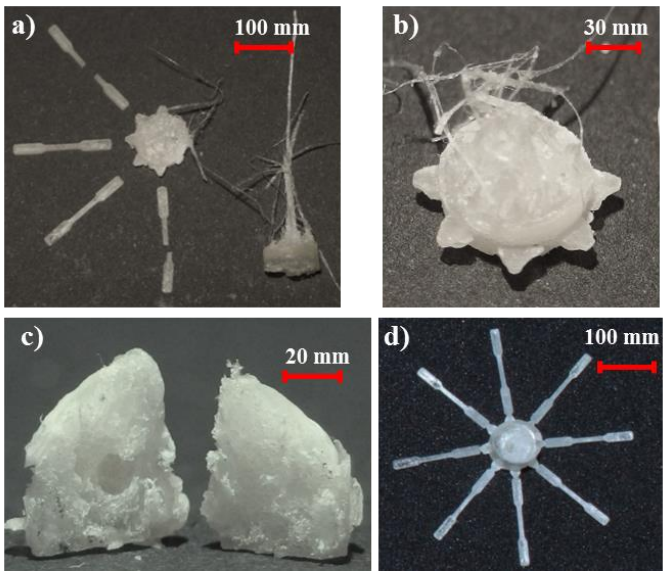

Fig. 3-16. *PLA micromolded samples loaded with 10 wt-% of sodium carbonate (**a**, **b**), sodium bicarbonate (**c**) and sodium chloride (**d**). Processing amplitude, force and time parameters were in this case 24 μm, 300 N and 1.2 s, respectively.*

GPC chromatograms showed that the molecular weight of the neat PLA sample and that processed with 40 wt-% of salt were practically identical (**Fig. 3-17**), although a small decrease on the weight average molecular weight (i.e. from 72,200 g/mol to 68,800 g/mol) was detected, suggesting the occurrence of a small degradation caused by ultrasound processing. This was slightly more significant than that detected in previous works[69], being consequently associated to the increased force that was necessary to process the salt rich specimen. In any case, the observed degradation (decrease on M_n less than 5%) was not significant to compromise final mechanical properties. Note also that the influence

of the molecular weight decrease should be insignificant considering the porosity of the sample once the incorporated salt is removed.

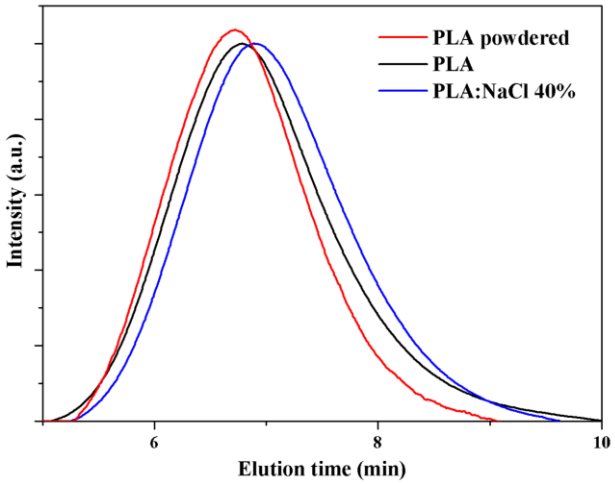

Fig. 3-17. *GPC chromatograms of commercial PLA powder, micromolded PLA, and mixtures of PLA:NaCl at 40 wt-% of salt. Processing parameters were 24 μm-300 N-1.2 s for neat PLA and 24 μm-400 N-1.2 s for PLA:NaCl 40%.*

Fig. 3-18 shows cross sections of a PLA specimen prepared under the chosen optimal conditions (i.e. amplitude, force and time of 24 μm, 400 N and 1.2 s, respectively), the maximum allowed amount of NaCl (i.e. 40 wt-%) for the highest and the lowest particle size, <45 μm (**Fig. 3-18a**) and 100-250 μm (**Fig. 3-18d**).

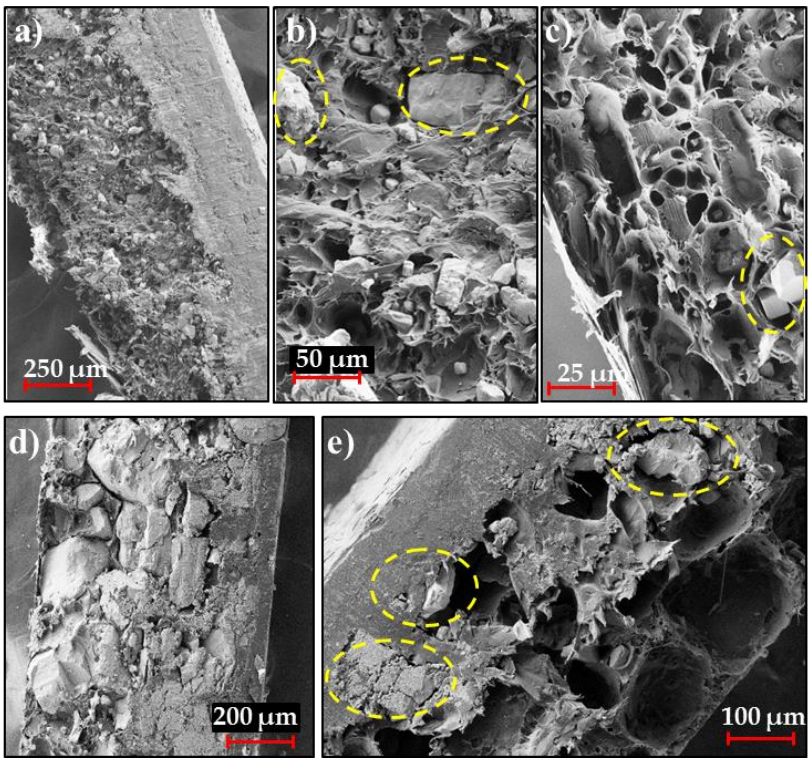

Fig. 3-18. *SEM micrographs of the cross section of PLA specimens loaded with 40 wt-% of NaCl before (**a** for <45 μm and d for 100-250 μm) and after immersion in water (**b** and **c** for< 45 μm and e for 100-250 μm). NaCl particles are marked with yellow ellipsoids.*

Salts were well encapsulated within the specimen with a minimum deposition on the specimen surface. A significant amount of salt was retained inside the specimen after the salt leaching process (**Fig. 3-18b, c** and **e**), even when particles with the smallest dimensions were employed (i< 45μm). Note that lower particles could be faster solubilized and also that they gave rise to the smallest pore size and the maximum internal surface, which should favor the solubilization process. Nevertheless, the highly hydrophobic PLA matrix hindered water penetration and lead to an incomplete solubilization, especially when pores were isolated or not well interconnected.

In order to solve this problem and produce a proper scaffold, the PLA was blended with PEG as a hydrophilic and water soluble polymer. This is a solution currently tested for some injection processes to improve porous interconnection when sodium chloride is used [73].

3.3.2.2. Ultrasound micromolding of PLA/PEG blends

In spite of PEG being employed as a sacrifice polymer and therefore preservation of molecular weight and mechanical properties are not essential, an analysis of the micromolding suitability of PEG and PLA/PEG blends was undertaken, following the protocol previously done for PLA [69].

It should be noticed that the ultrasound processing of PEG and even its blends with PLA had not been previously evaluated. So that, a further study focused in processing, composition, structure and calorimetric properties of the derived micromolded specimens was carried out.

PEG samples with two distinctive molecular weights (i.e. M_w of 100,000 and 35,000 g/mol) were selected. Results pointed out that both polymers could be properly molded with the same set-up that was selected for PLA specimens (i.e. 24 μm-300 N-1.2 s). Nevertheless, specimens produced from PEG with lower molecular weight had not enough mechanical consistency and were shattered in the mold ejection step. This problem persisted even with the blend containing only 15 wt-% of PEG. In order to get perfect specimens for all compositions, the higher molecular weight sample was selected for all assays despite its higher viscosity could cause potential problems for the mixing process. Blends with 15, 30 and 50% of PEG were assayed. These blends will be named as: PLA:PEG 85%, PLA:PEG 70% and PLA:PEG 50% respectively where the percentage refers to PLA content. Molecular weight of molded PEG was compared with that of the original commercial sample (i.e. before to exposition to the US heating source.) As shown in **Fig. 3-19**, both GPC chromatograms were similar and the molecular weight of the molded sample was kept practically unaltered. Specifically, M_n and M_w values were 54,200 and 88,600 g/mol for the powdered PEG and 57,400 and 87,700 g/mol for the micromolded sample. GPC chromatograms were also characterized by a narrow distribution that contrasted with the relatively high polydispersity index (PDI) determined for micromolded PLA (i.e. 1.5 versus 1.9). GPC chromatograms of micromolded blends were logically wider than those observed for individual polymers and for example PDI reached values around 3.1 for a 50 wt-% of PEG.

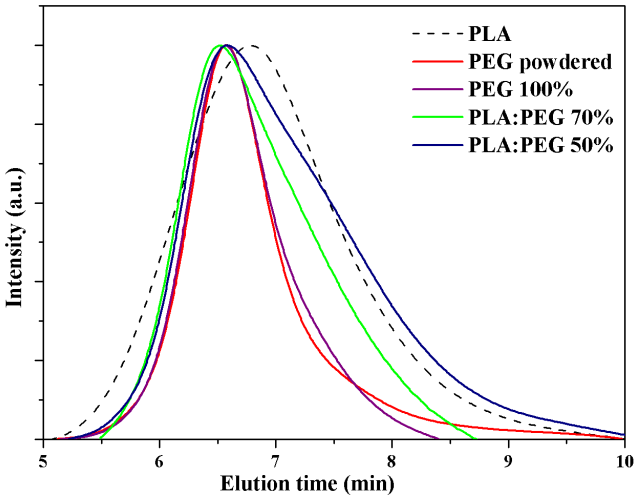

Fig. 3-19. *GPC profiles of powdered PEG, micromolded PEG and PLA/PEG blends having 30 wt -% and 50 wt-% of PEG. The curve of a micromolded PLA specimen (dashed line) is also given for comparison purposes.*

Distribution of PEG and PLA in the processed specimens could not be homogeneous due to the different flow properties of the two involved polymers caused by their different chemical structure and viscosity. This problem was evaluated by analyzing two half parts of each specimen: proximal (P) and distal (D) parts along the flow direction (**Fig. 3-20).**

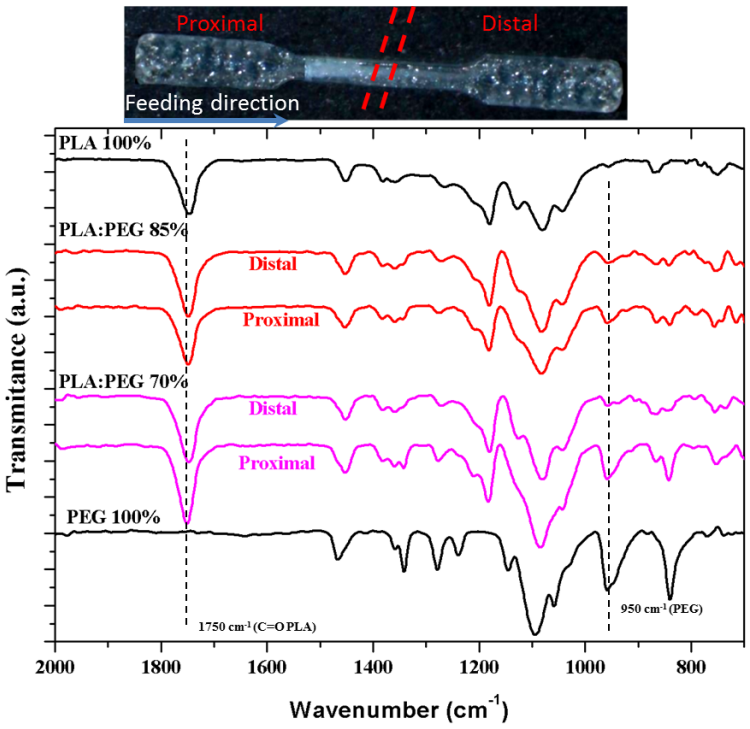

Fig. 3-20. *FTIR spectra of PLA, PEG and selected PLA/PEG (30 and 15 wt-% of PEG) specimens. Spectra corresponding to distal and proximal parts are displayed for the blend specimens.*

Fig. 3-20 compares the FTIR spectra of micromolded specimens of PLA, PEG and representative PLA/PEG blend with 30 wt-% and 15 wt-% of PEG. The PLA spectrum was characterized by the C=O stretching band of the ester group at 1750 cm^{-1}, whereas PEG was characterized by the ether band at 1090 cm^{-1} which is also close to the C(O)-O signal of the ester PLA

group. PEG had also a strong signal at 950 cm^{-1}, which was useful to evaluate its presence since the PLA spectrum was rather clear in the 1000-900 cm^{-1} region.

FTIR spectra clearly demonstrated that PEG tended to be concentrated in the proximal part (i.e. the closest section from the feeding camera) as consequence of its lower fluidity (higher viscosity and higher molecular weight). Differences between proximal and distal parts become enhanced as the total PEG content in the initial blend increased. Note that a relatively homogeneous specimen was obtained for a theoretical PEG content of 15 wt-%, which contrasts with the high heterogeneity detected for the sample containing 30 wt-%.

^{1}H RMN spectra gave more quantitative results about the specimen uniformity as shown in **Fig. 3-21** and **Table 3-4** for representative specimens obtained from mixtures containing 15 wt-%, 30 wt-% and 50 wt-% of PEG. Again, spectra were taken from the P and D parts of each processed sample.

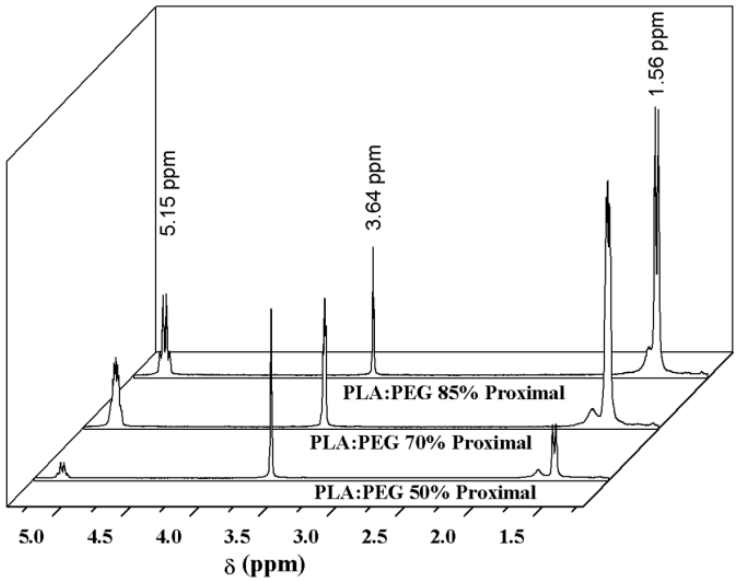

Fig. 3-21. *RMN spectra of proximal sections of PLA:PEG specimens with theoretical PEG content of 15%, 30% and 50 wt-%.*

Spectra were characterized by PLA peaks at 1.56 ppm (-CH_3, d) and 5.15 ppm (-CH-, q) and the PEG peak at 3.64 ppm (-CH_2-, s). **Table 3-4** shows the value of integrated area for a representative peak of each polymer and the deduced PEG content according to equation 5:

$$\text{PEG}\ (\%-\text{wt}) = 100 \cdot \frac{A_{3.64}/_4 \cdot 60}{A_{3.64}/_4 \cdot 60 + A_{1.56}/_3 \cdot 72} \qquad (5)$$

where A refers to the area of the indicated (subscript) NMR peak, 60 and 72 are the molecular weight (g/mol) of ethylene glycol and lactoyl repeat units, respectively.

Table 3-4. *Area of characteristic NMR peaks and calculated PEG content of micromolded PLA/PEG specimens with a theoretical PEG content of 15 wt-%, 30 wt-% and 50 wt-%. P and D in the specimen name are indicated the proximal and distal part, respectively.*

Sample	1.56 ppm ($-CH_3-$)	3.64 ppm ($-CH_2-$)	PEG (wt-%)
PLA:PEG 85% P	4.49	0.62	8.0
PLA:PEG 85% D	4.35	0.54	7.2
PLA:PEG 70% P	3.56	0.96	14.4
PLA:PEG 70% D	3.72	0.77	10.5
PLA:PEG 50% P	1.03	1.66	50.2
PLA:PEG 50% D	1.20	1.47	43.3

Differences between D and P parts were again minimized when the PEG load was low (e.g. 8.0 wt-% and 7.2 wt-% were determined for a load of 15 wt-%), while a difference close to 10 wt-% was observed for a 50 wt-% load. Maximum percentages were always lower than the expected value since the sprue was enriched on the less flowing polymer (i.e. PEG).

Fig. 3-22 shows the calorimetric profiles of the first heating run of the neat PLA and PEG processed specimens, and micromolded blends with different PEG contents. The PEG profile was characterized by a sharp melting peak at 67 ºC with a high melting enthalpy that pointed out the high crystallinity that could be attained (i.e. 89.6 % considering the reported value for a 100% crystalline sample, 196.8 J/g [74]. PLA profile shows a glass transition temperature with a relaxation peak at 62 ºC and a wide cold crystallization peak over a temperature range between 95 ºC and 140 ºC. The enthalpy difference between the melting and cold crystallization peaks was only 0.3 J/g, indicating that PLA was practically amorphous after the micromolding processing.

Features of PEG and PLA were distinguishable in the heating traces of the different blends, being possible to indicate the following points: a) The PEG phase was crystalline being detected minimum changes in the corresponding temperature and enthalpy when the real PEG content was considered. Note that the melting peak appeared overlapped with the relaxation peak of PLA, being measurements more problematic for high PLA contents. b) The temperature of the cold crystallization peak of PLA decreased with respect to that detected for neat PLA (i.e. from 114 ºC to 96-98 ºC), suggesting a nucleating effect of the PEG crystals. c) The final melting enthalpy of PLA was lower than observed for the neat polymer even when the real PLA content in the processed samples was taken into account. This feature suggests that the presence of PEG crystals hindered the growth of PLA crystals and that a limited crystallinity could be achieved. More interestingly, the enthalpy difference between melting and cold crystallization peaks of PLA increased when the real PLA content was taken into account (e.g. 30.3 and 18.3 J/g for samples with 49.8%).This means that an increased percentage of PLA was able to crystallize after processing and specifically crystallinities of 12.7% and 1.9% could be estimated for specimens having PLA contents of 49.8 wt-% and 92 wt-% (i.e. those coming from theoretical blends with 50 wt-% and 85 wt-% of PLA).

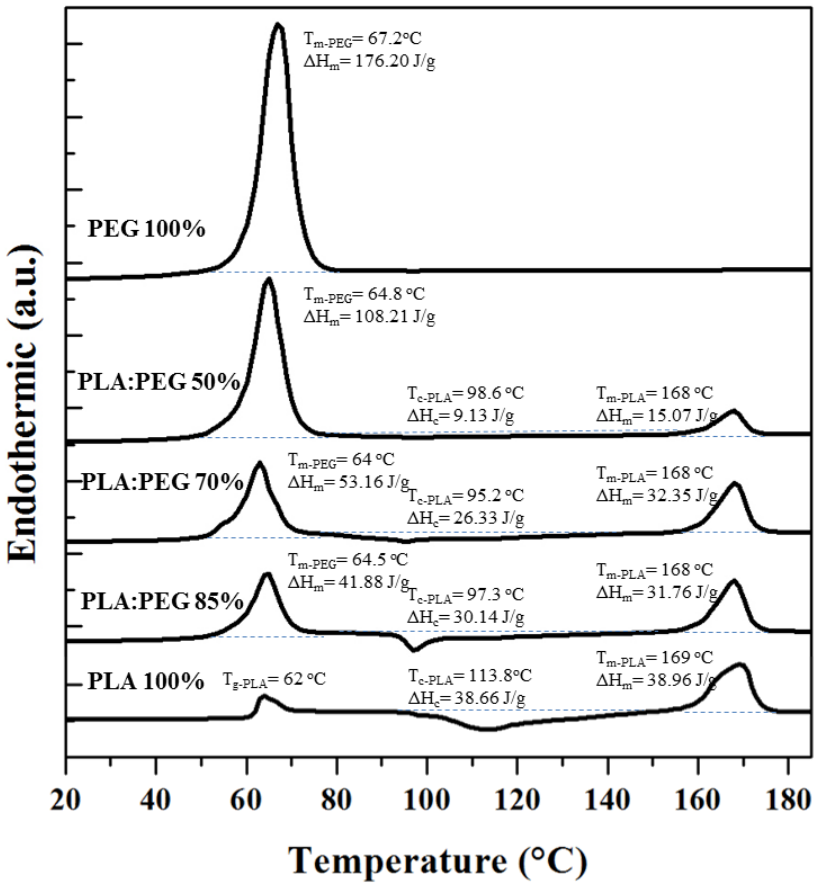

Fig. 3-22. *DSC curves corresponding to the first heating scan (10 °C/ min) of PEG (top), PLA (bottom) and PLA:PEG blends having the indicated theoretical concentrations.*

In order to get a further evaluation of the effect of PEG in the PLA crystallization during processing, micromolded specimens were analyzed by wide angle X ray diffraction (WAXD) in a heating scan performed at a rate of 10 °C/min.

X-ray diffraction profiles of selected samples: PLA:PEG 70% and PLA:PEG 50% were recorded during the heating process and the corresponding graphs of 3D evolution are shown in the **Fig. 3-23**. Peaks around 13.5, 14.8 (low intensity), 15.6 (low intensity) and 16.5 nm^{-1} were related to PEG, and clearly appeared in both cases indicating a high crystallization degree at room temperature. Peaks at 11.5, 13.3 and 15.5 (low intensity) were assigned to PLA. At room temperature PLA is mainly amorphous before cold crystallization in the PLA:PEG 70% sample whereas some degree of crystallization could be observed in the PLA:PEG 50% sample. Note that the main peak of PLA at 11.5 nm^{-1} is observed at room temperature, in agreement with DSC results. The presence of PEG during molding process increased the PLA crystallinity of the as-molded specimen. In both cases the increase in intensity of PLA peaks during the cold crystallization, from 100 °C, and the decrease of PEG peaks during melting process, around 70 °C, could be appreciated.

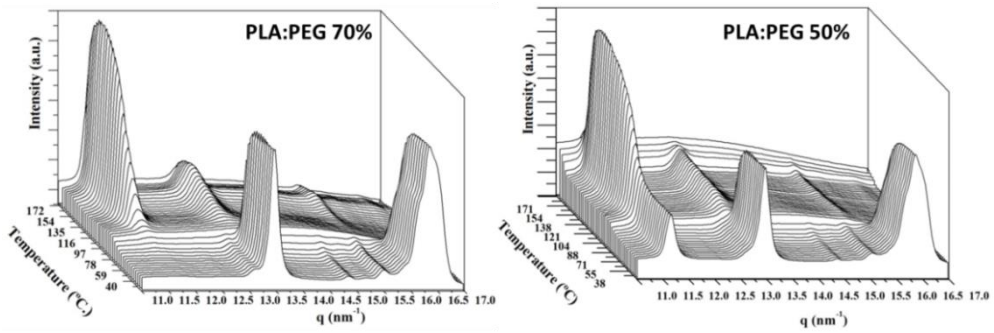

Fig. 3-23. *Three dimensional representation of WAXD profiles of representative micromolded PLA:PEG specimens having theoretical PLA contents of 70 wt-% (left) and 50 wt-% (right). Diffractograms were taken during heating scans at a rate of 10 °C/min from room temperature.*

3.3.2.3. Ultrasound micromolding of PLA:PEG:NaCl mixtures. Salt leaching and scaffold characterization

PLA:NaCl mixtures with salt contents lower that 50 wt-% could be micromolded under the previously determined conditions (i.e. amplitude, force and time of 24 μm, 400 N and 1.2 s, respectively) without a significant degradation. Namely, GPC curves showed only a minor molecular weight loss for the PLA component as above discussed for the PLA:NaCl specimens (**Fig. 3-17**). Scaffolds were therefore prepared with PLA, PEG and NaCl contents of 50 wt-%, 10 wt-% and 40 wt-% (abbreviated as PLA:PEG-10:NaCl-40), respectively, and a NaCl particle size lower than 45 μm in order to favor the leaching process. PEG content was found enough to dissolve the salt as demonstrated by thermogravimetric analyses. Note also that the low PEG percentage (i.e. 10 wt-%) should lead to a relatively homogeneous distribution of both polymers in the specimen. FTIR spectra (**Fig. 3-24**) clearly indicated that PEG could be effectively removed after immersion of micromolded specimens for 1 day into water. Results were positive for both selected PLA:PEG 70% and PLA:PEG-10:NaCl-40 specimens.

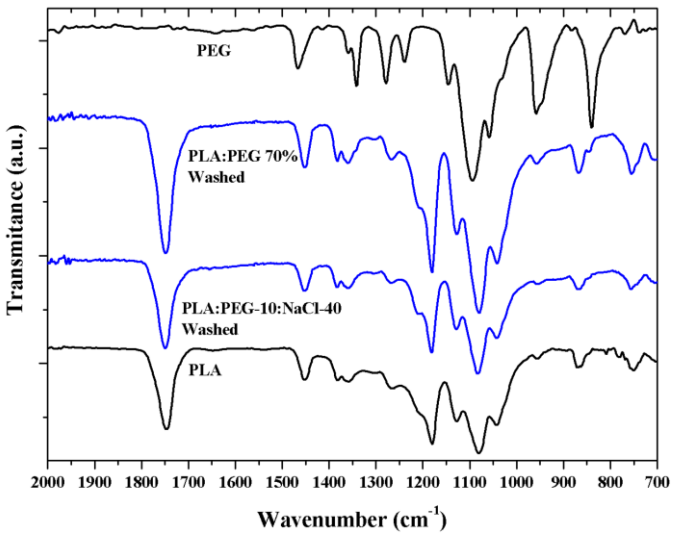

Fig. 3-24. *FTIR spectra of PLA:PEG 70% and PLA:PEG-10:NaCl-40 specimens after immersion in a water medium. For comparison purposes spectra of PLA and PEG micromolded specimens are also given.*

Thermogravimetric (TGA) assays were useful to quantify the amount of NaCl incorporated in the processed specimens, since the residue determined after heating the samples up to 600 ºC should be associated to the salt content due to the expected polymer decomposition. **Fig. 3-25a** shows TGA curves of two representative specimens before and after the washing process. In the case of the PLA:NaCl 35% sample the TGA curve was characterized by a single decomposition step with a maximum at 370 ºC, which is associated to the PLA decomposition [75] and a high residual weight. This is nevertheless lower that the theoretical salt content (i.e. 30.2% with respect to 35%), suggesting that the flow of NaCl was hindered and consequently the salt was preferably located in the sprue. This feature was corroborated also from the 40% char yield determined from TGA experiments performed with the sprue (not shown). Char yield decreased to 18.9% after the washing process, a value that was significant and indicative of a considerable amount of NaCl retained in the specimen. In this case the effectiveness of the leaching process was only 37%.

Fig. 3-25b demonstrates the effectiveness of the leaching process (e.g. 95%) when PEG was incorporated. The TGA curve of the non-washed samples showed two decomposition steps associated to PLA and PEG at 370 ºC and 430 ºC (423 ºC is the value reported in the literature for PEG [76]) and a high residue that was lower, as expected, than the theoretical value. After washing, salt was practically eliminated and a small trace of PEG could still be detected.

In addition to the residue quantification by the TGA assay, a visual inspection of SEM micrographs showed that the internal surface of PLA:PEG-10:NaCl-40 specimens after washing (**Fig. 3-25d**) was rough and porous and practically free of NaCl particles. A clear contrast exists in related specimens where PEG was not incorporated (**Fig. 3-18c** and **Fig. 3-25c**).

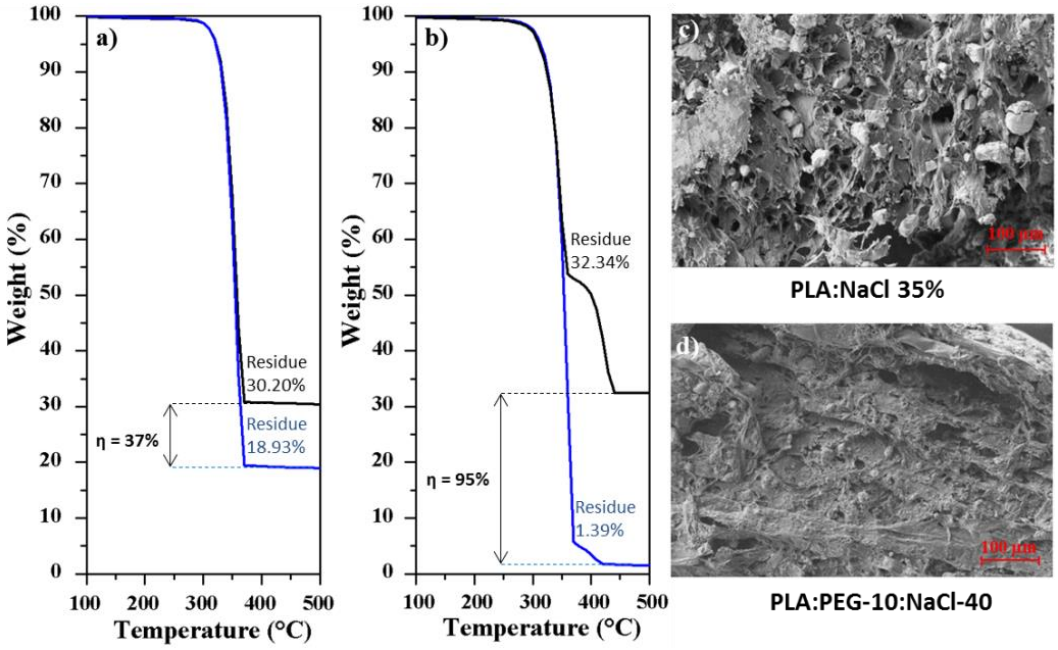

Fig. 3-25. *TGA profiles of PLA:NaCl 35% (a) and PLA:PEG-10:NaCl-40 (b) specimens as molded (black lines), and after being washed (blue lines). (c) and (d) SEM micrographs of cross sections of both samples after being washed.*

Hydrophilicity of the specimen surface is an important factor that favors the salt leaching process to get a porous scaffold. Contact angle measurements of representative ultrasound processed samples are shown in **Fig. 3-26**.

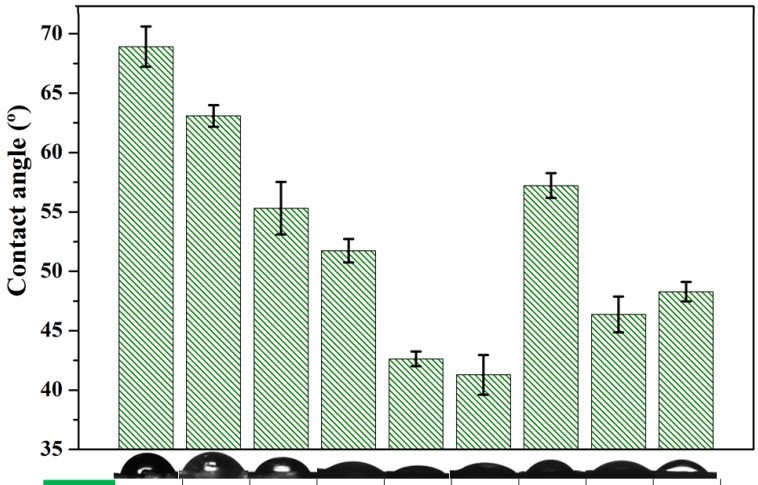

PLA	100	85	70	60	50		65	50	50
PEG		15	30	40	50	100		10	8
NaCl							35	40	36
TCS									6

Fig. 3-26. *Contact angle for representative micromolded specimens. Below the bars are shown the images of the water droplets on the respective material whose composition is shown in the table.*

The initial PLA specimen was characterized by an angle of 69º, which is low probably as a consequence of the relatively low molecular weight of selected PLA (effect of terminal groups) and the smooth surface of processed samples. In fact, angles close to 90-100º are usually determined for PLA due its hydrophobic character, instead higher contact angles of 131.9º were reported for PLA electrospun scaffolds [77]. Recently, it has been discussed that the geometry of the surface can influence the measurements of the contact angles [78]. Incorporation of PEG clearly diminishes the contact angle being observed a regular evolution with the composition. The value of 43º measured for a 50 wt-% content of PEG is close to the asymptotic angle of 41º evaluated for PEG. Results clearly indicated that the specimen was hydrophilic at the selected PEG content, allowing the water penetration. It is also important to note that the incorporation of NaCl caused an important decrease of the contact angle and specifically a decrease from 69º to 57º was determined when the specimen was loaded with a 35 wt-% of NaCl. In summary, selected PLA:PEG-10:NaCl-40 specimens were clearly hydrophilic with a contact angle of 46º that approaches also to the minimum value expected for a PEG sample.

Fig. 3-27 compares the porosity, total mass extraction and NaCl extraction yields of representative samples with and without containing PEG samples. PEG. Samples loaded with the antibacterial drug, PLA:PEG-8:NaCl-36:TCS-6 is also considered. The incorporation of PEG allowed to increase the porosity from 20% to 40-42%, a feature that demonstrates the significant role displayed by the soluble PEG to increase pore connection and enhance NaCl extraction. The extraction yield for

PLA:NaCl-40 samples was lower than 40% while values around 90-98% were found for PLA:PEG-10:NaCl-40 and PLA:PEG-8:NaCl-36:TCS-6. In the case of PLA:PEG-10:NaCl-40 sample the difference between total mass extraction and NaCl extraction was higher than expected considering the amount of PEG. This point suggests that some PLA was lost during the leaching process probably as a consequence of dragging. It should also to be pointed that 2-3.5% of NaCl could still be present in the PLA:PEG-8:NaCl-36:TCS-6 sample according to the extraction yield.

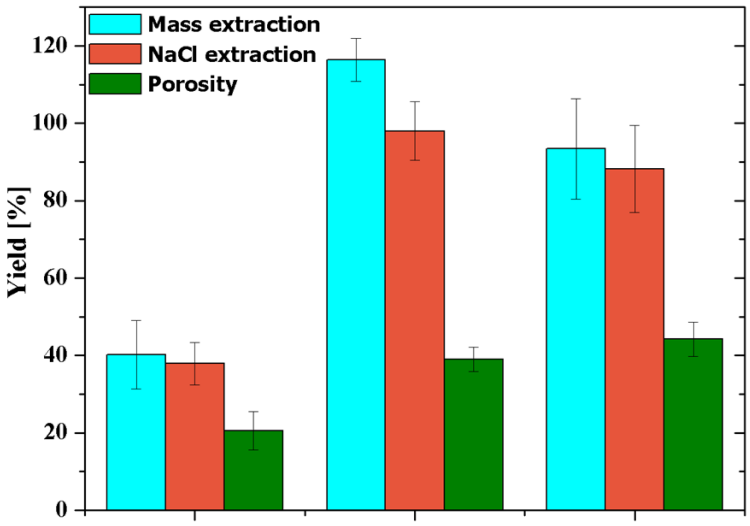

Fig. 3-27. *Extraction yields and porosity for PLA:NaCl-40, PLA:PEG-10:NaCl-40 and PLA:PEG-8:NaCl-36:TCS-6.*

3.3.2.4. Antibacterial micromolded scaffolds

An antibacterial scaffold was produced by introducing 6 wt-% of triclosan (TCS) to the previous formulation found out, namely combining the use of PEG and NaCl to obtain a proper pore interconnection and high porosity density. As concluded in the previous work [69] TCS can be incorporated in the ultrasound micromolding of PLA without causing an appreciable degradation. Antibacterial scaffolds were therefore prepared with a PLA:PEG:NaCl:TCS mixture having 50 wt-%, 8 wt-%, 36 wt-% and 6 wt-% of each component, respectively (abbreviated as PLA:PEG-8:NaCl-36:TCS-6). GPC measurements indicated as previously explained a slight decrease on the PLA molecular weight (i.e. M_n = 39,400g/mol). The porosity achieved after immersion on water was similar to that observed for the evaluated PLA:PEG-10:NaCl-40 scaffold. The incorporation of the hydrophobic TCS was performed through the slight decrease on the content of hydrophilic PEG and NaCl components, which may alter the surface characteristics of the molded specimens. However, contact angle measurements indicated a minimum increase from 46º to 48º (**Fig. 3-26**) and consequently samples showed a good wettability as desired for a delivery application. Drug release, bacterial growth and cell proliferation assays were carried out to evaluate the bactericide and potential tissue engineering applications of the new processed scaffolds.

Release experiments were firstly carried out in a PBS medium. Less than 0.2% of the TCS loaded in the specimen was released (profile not shown) due to the poor solubility of TCS. Therefore a PBS-ethanol mixture having 70% of ethanol was used as a release medium, the presence of ethanol increased the medium hydrophobicity and enhanced the TCS solubility. It has also been reported in previous works that this medium with an ethanol supplement could simulate the release of TCS in a physiological medium with serum supplementation [33, 34].

As show in **Fig. 3-28** the drug release profile of the antibacterial scaffold (black line) was characterized by a first burst release. Thus, 56% of the loaded TCS was delivered in less than 10 h. A sustained release for a period longer than 150 h was subsequently observed. This release was defined for a first order kinetic profile with a k_1 value of 0.019 h^{-1}. As a comparison the release profile of a non-porous PLA specimen with the same TCS load is also shown in **Fig. 3-28** (blue line). A burst release was not observed, indicating that less accessible surfaces for an immediate release were available. Furthermore, only 40% of TCS was released after 150 h of exposure, a value that clearly contrasts with the 84% reached with the porous sample. It is clear that the presence of a high density of pores has a dramatic effect and a considerably improvement of the TCS release, which should led to specimens with bactericide activity [69].

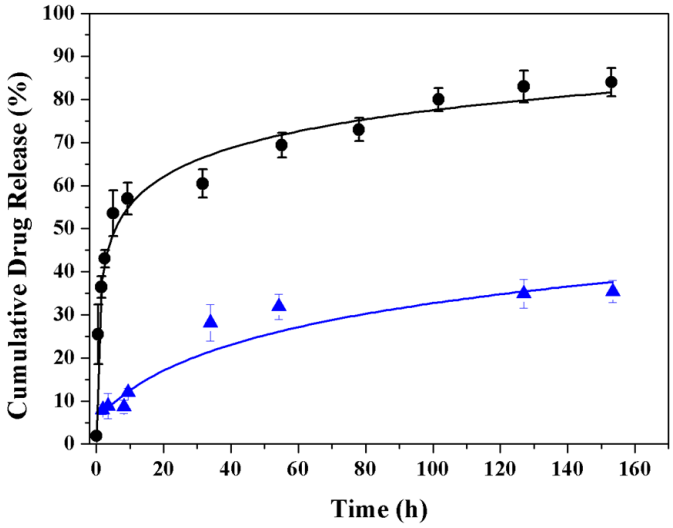

Fig. 3-28. *Release profiles in a PBS-EtOH 70% medium of the antibacterial scaffold (**black**) and non-porous (**blue**) micromolded PLA specimen. Both samples contained 6 wt-% of TCS.*

Fig. 3-29a shows *E. coli* (Gram-negative) and *S. epidermidis* (Gram-positive) bacterial growth curves in presence of micromolded specimens of non-porous PLA (control), PLA porous scaffold (PLA:PEG-10:NaCl-40) and TCS loaded PLA scaffold. The unload scaffold displayed a similar bacterial growth curve than the non-porous PLA sample. Note that in both cases, the bacterial growth required a lag phase close to 4 h. However, bacterial growth in the porous scaffold was subsequently limited to a value around 80-90%. This low inhibition growth effect (in the stationary phase) could be explained taking into account that some NaCl remained in the piece. By contrast, the scaffolds loaded with TCS had a clear bactericide effect during the first 10 h that was followed by a bacteriostatic effect

that kept the bacterial growth around 30-35%. Performance of TCS loaded specimens was similar for both Gram-positive and Gram-negative bacterial cultures. Agar tests showed the presence of inhibition halos, which confirmed the antibacterial activity, only when TCS loaded specimens were assayed (see **Fig. 3-29b**) for an *E. coli* culture).

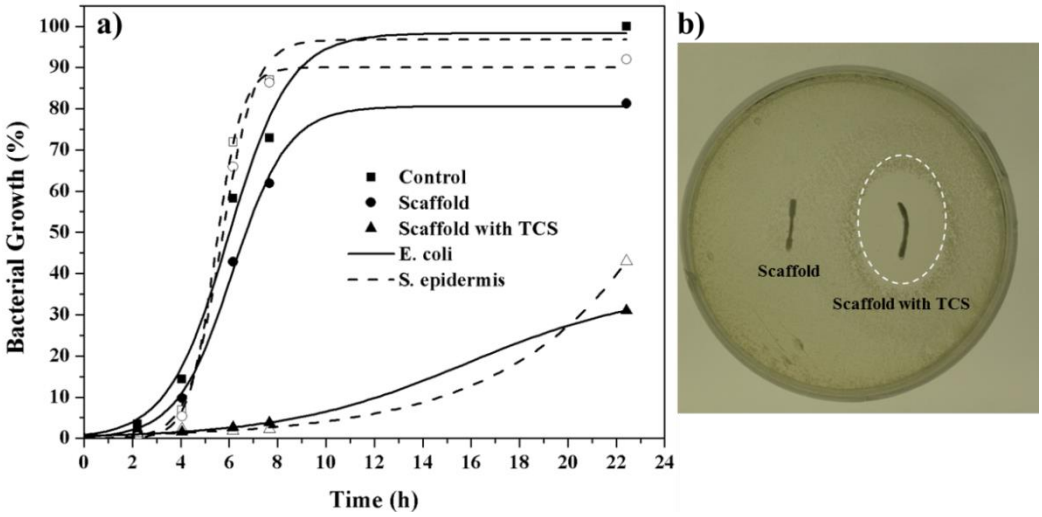

Fig. 3-29. ***(a)*** *S. epidermidis (dashed lines) and E. coli (solid lines) bacterial growth profiles in presence of non-porous PLA control), PLA scaffold and PLA scaffold loaded with 6%-wt of TCS.* ***(b)*** *Agar test for E.coli bacterium using PLA scaffolds with and without the TCS antibacterial drug.*

Fig. 3-30 compares the cell growth of MDCK cells on a non-porous PLA specimen, a PLA scaffold and the TCS loaded PLA scaffold. Specifically, **Fig. 3-30a** shows that cell viability was similar for the different samples (e.g., control well without specimens and wells containing the specimens). These results allow discarding the potential toxicity of TCS and are coherent with the potential use of TCS for sanitizing the specimens, in a similar way as used in different hygiene products (e.g., soaps, deodorants, toothpastes, and others). **Fig. 3-30b** shows that the numbers of cells grown on the porous micro-pieces, with and without TCS, were similar but significantly higher (increase by about 40-60%) than observed for specimens without pores ($p < 0.05$). The reduction in the size of cells in the porous specimens can be a morphological evidence of the increase in the number of cells (**Fig. 3-30c**). The ability of MDCK cells to colonize tubular channels is demonstrated by differences evidences related to their mobility and adherent growth [79-81]. Note that pores in the scaffolds were remained open but covered by cells (see asterisks in **Fig. 3-30c**).

Finally, the cells proliferated similarly in all the cases, confirming the biocompatibility of processed PLA scaffolds. Cell growth percentages demonstrate the increase of cell proliferation in the porous specimens. Moreover, the presence of the TCS has not a cytotoxic effect and as antibacterial drug could prevent bacterial contamination of the micromolded specimen.

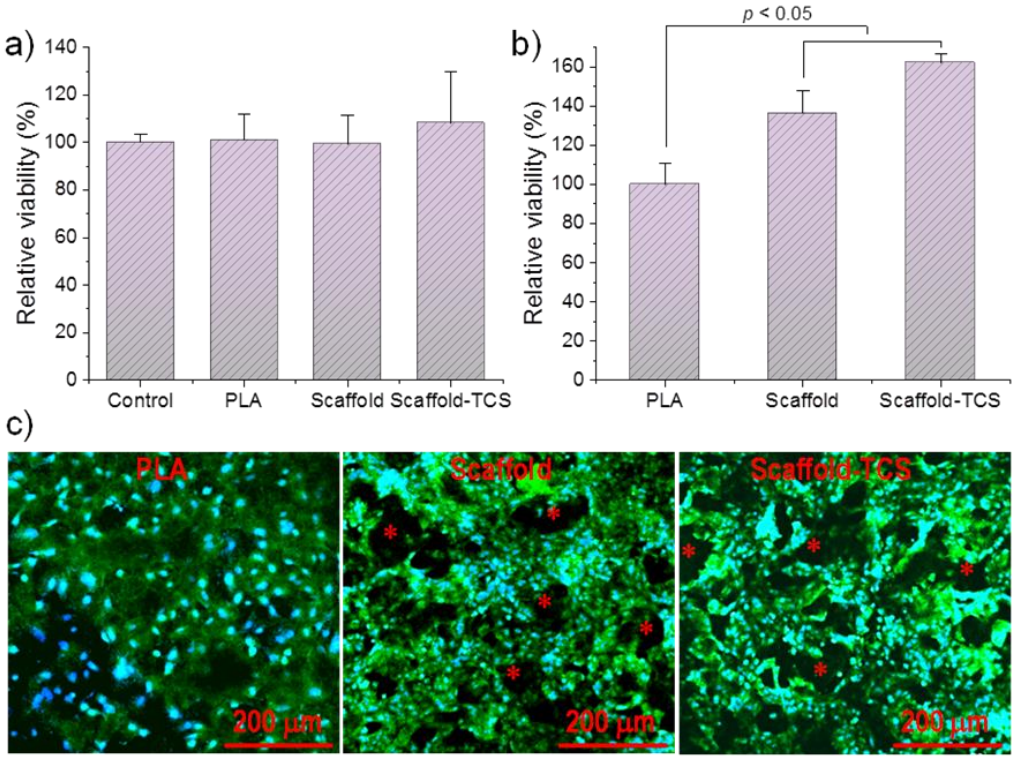

Fig. 3-30. ***(a)*** *Cell viability in the presence of the micro-molded specimens. Control corresponds to cell growth in the absence of any specimen.* ***(b)*** *Relative cell proliferation at 7 days after seeding on non-porous PLA, PLA scaffold and PLA scaffold loaded with 6%-wt of TCS.* ***(c)*** *Fluorescence micrographs of the three indicated samples after the cell proliferation assay. The cells were stained for nuclei (DAPI, blue) and actin (phalloidin, green). Asterisks indicate scaffold porous.*

3.3.3. Conclusions

Porous micromolded PLA scaffolds could be successfully prepared by a combination of ultrasound micromolding and salt leaching techniques. The combined process showed clear advantages with respect to conventional injection methods. Specifically, small polymer degradation due to the short exposure time to the energy source (1.2 s), minimum material loss and the possibility to attain a high precision of details in the processed specimens can be mentioned. NaCl was a suitable salt for ultrasound processing since cavitation problems could be avoided and a minimum change of the optimized parameters determined for the neat polylactide was required. A small addition of water soluble PEG (10 wt-%) was nevertheless necessary to attain a complete solubilization of NaCl particles. Final specimens could be prepared with a relatively homogeneous porous distribution despite the higher fluidity of polylactide. PEG could also be micromolded without a significant degradation. It was found that large amounts of PEG could influence the PLA crystallinity. Micromolded scaffolds with antibacterial properties and a minimum polymer degradation could finally be obtained when triclosan was added to the PLA:PEG:NaCl processing mixture. Porosity of samples was appropriate to favour cell proliferation.

3.4. Ultrasound Micromolding of porous Polylactide/Hydroxyapatite Scaffolds

3.4.1. Introduction

Hybrid materials based on biodegradable polymers are continuously being developed to cover a wide range of biomedical applications such as prostheses (e.g. polylactide (PLA) loaded with silver particles to increase antibacterial activity [82]), dental implants (e.g. polymethymethacrylate (PMMA) reinforced with ceramic materials [41, 83]), dental fixed bridges (e.g. ultra-high molecular weight polyethylene reinforced with glass fibers [83]) or miniscrews for cranial bone repair (e.g. polylactide reinforced with hydroxyapatite (PLA/HAp) [84]). Probably, the development of new materials for tissue regeneration is one of the most promising areas since concentrates great research efforts

In tissue engineering it is important to highlight the use of scaffolds to develop biological substitutes that restore or maintain the tissue function. A biocompatible, biodegradable and cell colonizable material is required for the regeneration of the damaged tissue [35, 36]. Therefore, efforts are focused to develop biocompatible synthetic polymeric systems to build porous matrices that can act as templates for new tissue formation. Matrices can also be seeded with cells or specific grown factors to enhance proliferation, and/or loaded with fibers and particles such as HAp to increase biocompatibility [85].

HAp is usually selected as a component of biomaterials for being the main inorganic constituent of bones, for enhancing cell proliferation and for having a high bioactivity and biocompatibility. HAp is obviously found in nature but it can alternatively be synthesized by precipitation or hydrolysis following well-standardized procedures [1, 86, 87]. The use of HAp alone as a ceramic implant is limited because it is extremely brittle with low mechanical strength and fatigue failure [88, 89]. Thus, HAp is usually employed in a wide variety of biomedical applications in the form of composites. PLA is an ideal polymer matrix due its biocompatibility, relatively low degradation rate and good mechanical properties. Furthermore, PLA biodegrades into non-toxic products and is FDA approved [16, 21, 23].

PLA/HAp scaffolds have largely been used in bone repair applications, being demonstrated very good osteoconductor and osteoinducer behaviors [90, 91]. These scaffolds are consequently able to increase the concentration of osteoblast cells when compared with conventional PLA scaffolds [92]. On the other hand, the presence of HAp improves adhesion by absorption of proteins and enables the differentiation and gene expression of osteoblasts [93]. PLA/HAp scaffolds have already been prepared by several processes such as induced phase separation [94, 95], *in situ* polymerization [96, 97], mechanical dispersion, melt blending [98], *in situ* precipitation and ultrasound methods [99, 100].

Ultrasound micromolding (USM) is a relatively new processing technique that uses ultrasound as a heating source. Specifically, energy is transferred to the polymer through increased vibration of the

molecular chains. This heating process is really accurate and efficient, just melting the amount of material needed. Moreover, ultrasound vibration reduces the polymer viscosity facilitating the material pumping and mold filling [101]. The combination of the accurate energy transfer and dosing systems has made USM suitable for large production of microsized specimens with high spatial resolution [102, 103]. USM seems ideal for producing pieces for biomedical applications where the added value materials are expensive, and an inefficient cost cycle would bring great economic losses as it may be the case of other alternative processes such as microinjection molding[104].

The efficiency of USM has already been proved for the production of microspecimens based on commodities like polyethylene, polypropylene and polystyrene [12, 15] and biodegradable polymers such as polylactide and polybutylene succinate [28]. All these previous studies have concluded that high quality specimens can be produced after an accurate setting up of the wave amplitude, time and pumping force molding parameters. USM has also been probed appropriate to produce nanocomposites (e.g. polylactide or poly(ε-caprolactone) incorporating nanoclays [65] or carbon nanotubes [66], respectively), and even specimens with an added pharmacological activity [69].

The present work is focused on the preparation of PLA/HAp composites by USM, taking into consideration the influence of the origin of the inorganic component and evaluating particle distribution and processing parameters. USM preparation of porous PLA/HAp composites is a second goal of the present work that appears fundamental for applications like tissue engineering where cell colonization is required.

3.4.2. Results and Discussion

3.4.2.1. Ultrasound micromolding of PLA/HAp composites

The ability to prepare uniform PLA/HAp nanocomposites by means of the USM technique has been explored considering the HAp type (i.e. commercial or synthesized), the particle size and the maximum allowed load.

The starting processing parameters were those previously determined for the commercial PLA powder sample: amplitude, force and time of 24 μm, 300 N and 1.2 s. Basically, previous studies indicated that lower amplitudes were not enough to get an appropriate PLA flow and that 300 N was the minimum force that allowed to fill completely the mold cavities. Forces higher than 500 N caused an overloading of the sonotrode (i.e. it could not vibrate as consequence of the high compaction of PLA). A processing time of only 1.2 s was enough and has been kept constant for all experiments since a slight degradation was noticed for times higher than 3 s. GPC measurements indicated a minimum variation of M_n from 43,000 g/mol to 38,800 g/mol (i.e. less than 10%) when PLA was processed under the indicated optimal conditions.

PLA composites were not able to be well-molded when the synthesized HAp was employed. For a load of 50 wt-% the equipment only compacted the powdered mixture, which therefore could not properly flow and fill the mold. Results progressively improved when the load decreased down to 30 wt-%. The fluidization of the material was achieved when the HAp amount was decreased to 20 wt-%, but the whole mold could still not be completely filled and some of the final specimens resulted in being uncompleted (**Fig. 3-31**) despite the force was increased up to 400 N.

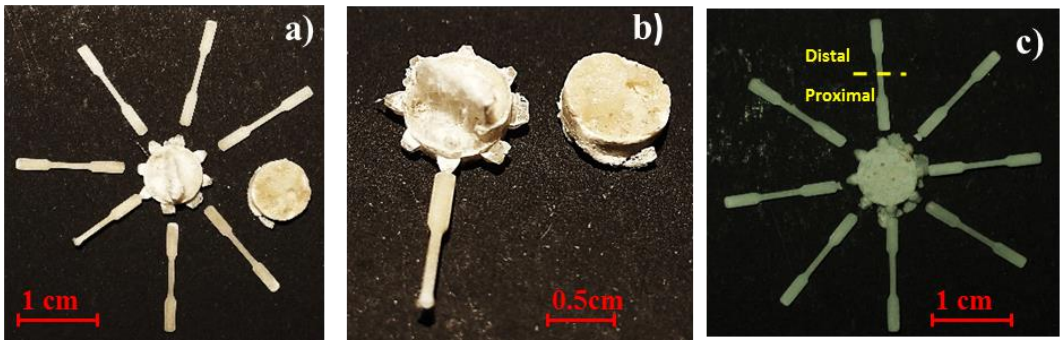

Fig. 3-31. *Molded specimens, with synthesized (**a**,**b**) and commercial grade HAp (**c**). HAp contents were 20 wt-% and 60 wt-% for synthesized and commercial particles, respectively. Proximal and distal parts of a given specimen are indicted in (**c**). Images of processed specimens incorporating synthesized Hap were obtained with sieved granules 100-80 μm size range.*

Synthesized HAp corresponds to nanometrics crystals that, unfortunately, become agglomerated (**Fig. 3-32**), given rise to granules with a broad size distribution. These granules could be sieved into fractions with sizes ranges of 250-125 μm, 100-80 μm, 80-45 μm and < 45 μm, it is, therefore, possible to evaluate the effect of the particle size on the micromolding effectiveness Note that the high dimension of aggregates may difficult the correct flow of the mixture towards the mold when the content of inorganic components is high. The indicated fractions of synthesized HAP were subsequently used in the USM experiments that were carried out with a load of 20 wt-% and parameters of 24 μm, 400 N and 1.2 s. The main observed effect was a lower capacity of HAp to load the mold as its particle size increased, HAp preferably remained in the sprue for increasing sizes. This heterogeneous distribution could be easily evaluated through density measurements of representative parts (i.e., sprue and specimen). Thus, densities determined by the flotation method using water and a KBr saturated aqueous solution were 1.81 g/mL (sprue) and 1.41 g/mL (specimen) when the 250-125 μm fraction was employed and 1.66 g/mL and 1.58 g/mL for the < 45 μm fraction. Note that a value lose to 1.62 g/mL should be expected for a sample with a HAp load of 20 wt-% considering theoretical densities of 1.24 g/mL and 3.16 g/mL for PLA and HAp, respectively.

The inspection of processed samples (**Fig. 3-31**) indicated that the sprue was plenty of bubbles; the material had a slight brown coloration and was very brittle. Observations pointed out the possibility of gas formation, cavitation phenomena and degradation. Therefore, the use of synthetic particles was discarded for the rest of the experiments.

USM of mixtures with commercial HAp was completely different since good results were attained even for a high load of 60 wt-%. In all cases, the applied force should be 400 N in order to get

a perfect specimen (using amplitude and time of 24 μm, and 1.2 s, respectively). Lower forces were inefficient to fill completely the mold even when the HAp content was reduced to 10 wt-%. **Fig. 3-31** shows that eight perfect specimens were obtained for the maximum load. Furthermore, no coloration and degradation evidences could be observed. In addition, cavitation phenomena were not detected since bubbles were absent.

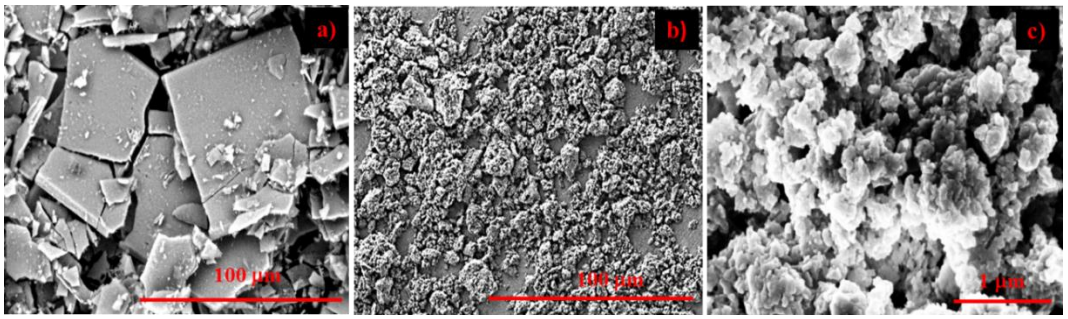

Fig. 3-32. *SEM micrographs showing typical morphologies of commercial (**a**) and synthesized (**b,c**) HAp crystals.*

The morphology of commercial HAp particles was completely different from that observed for the synthesized sample, as shown in **Fig. 3-32**. In this case, HAp crystals had a regular sheet-like morphology with its larger dimension close to 10 μm. The brittle character of HAp caused some breakage of crystals during preparation, as detected in **Fig. 3-32**. Nevertheless, the commercial HAp was rather homogeneous in size and consequently the effect of the particle dimensions on the distribution inside the molded specimen could not be evaluated. Density measurements pointed out again a slight difference between sprue and specimen, which become more significant as the HAp load increased. Thus, densities of 2.46 g/mL (sprue) and 2.27 g/mL (specimen) and 1.64 g/mL (sprue) and 1.60 g/mL (specimen) were found for loads of 60 wt-% and 20 wt-%, respectively. Samples with an intermediate load of 40 wt-% could already be considered practically homogeneous with densities of 2.23 g/mL (sprue) and 2.12 g/mL (specimen). Homogeneity, inside the specimen was also evaluated by analyzing two half parts of each specimen: proximal (P) and distal (D) parts along the flow direction (***Fig. 3-31c***). In this case, minimum differences were found and for example, density values of 2.10 g/mL (distal) and 2.08 g/mL (proximal) were determined for the sample having 40 wt-% of HAp. Finally, it can be pointed out that similar particle distribution was found for samples having a 20 wt% load of synthetic (*i.e.*, densities of 1.66 g/ml (sprue) and 1.58 g/ml (specimen) for the <45 μm fraction) and commercial (*i.e.*, densities of 1.64 g/ml (sprue) and 1.60 g/ml (specimen)) particles. Therefore, USM seems a suitable process to get homogeneous particle dispersion even for high loads and particle sizes in the micrometer range.

SEM micrographs of processed specimens (**Fig. 3-33**) clearly revealed the presence of HAp particles inside the PLA continuous matrix with a rather homogeneous distribution in the inner cross sections (**Fig. 3-33c**) and an irregular distribution on the specimen surface (**Fig. 3-33a** and **b**).

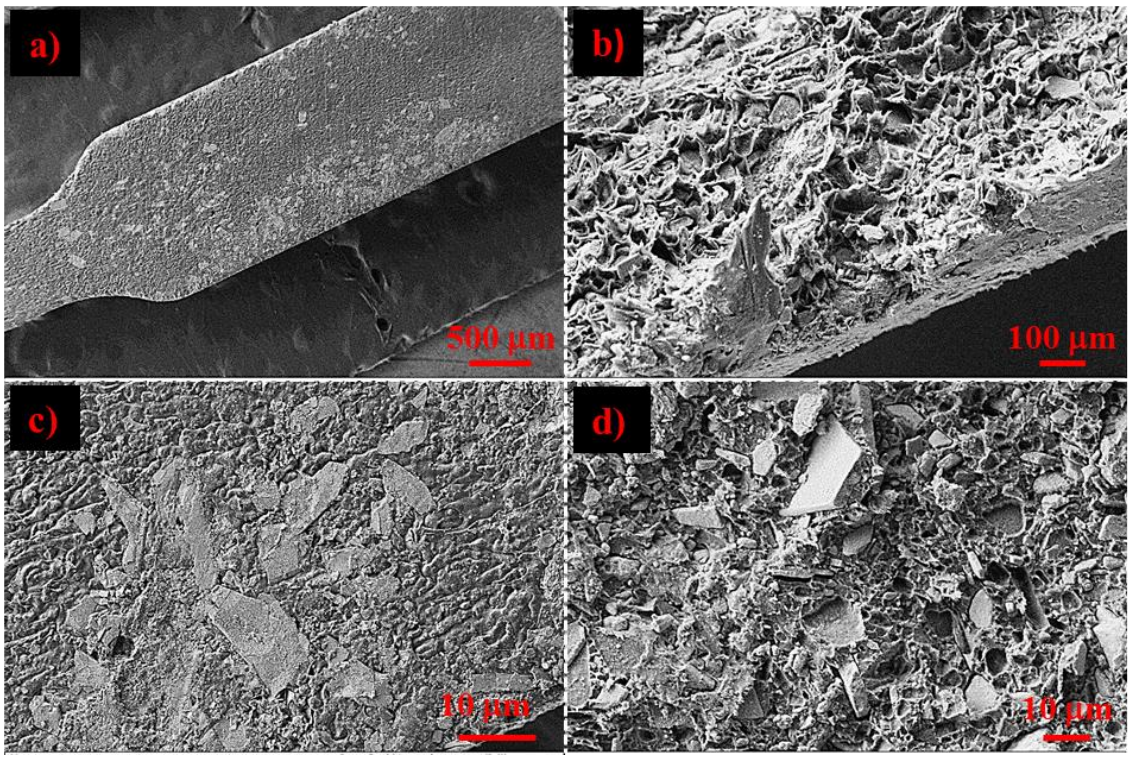

Fig. 3-33. *SEM micrographs showing the surface (**a, c**) and an inner cross section (**b, d**) of a PLA micromolded specimen having 40 wt-% of HAp.*

FTIR analysis allowed explaining the negative effect of synthesized HAp in comparison with the commercial grade sample. Clear differences can be observed between both spectra as shown in **Fig. 3-34**.

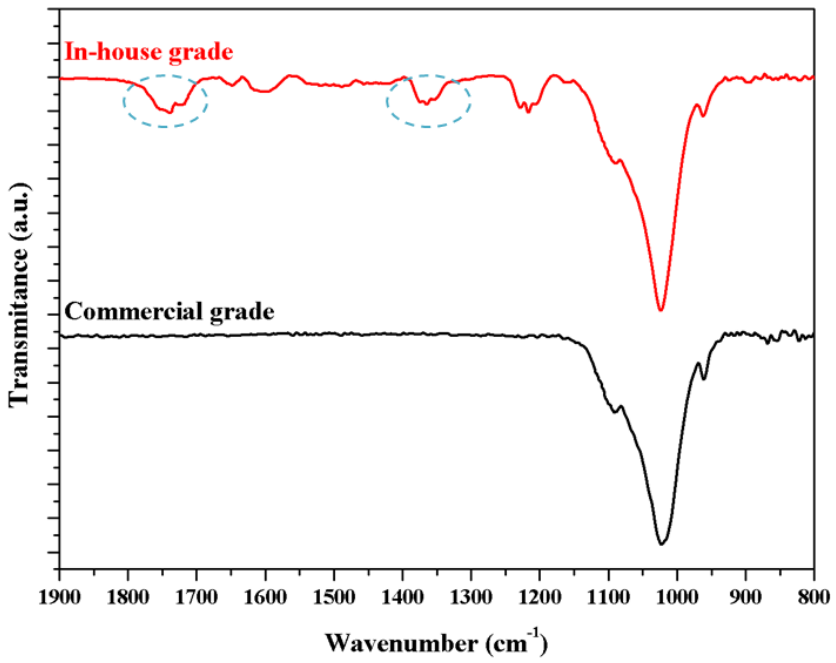

Fig. 3-34. *FTIR spectrum of synthesized HAp (**red line**) and commercial HAp (**black line**).*

Thus, the commercial grade-sample had a high purity and only typical bands for the phosphate compound at 1280, 1090, 1020, 960 cm^{-1} were detected [2, 105, 106]. By contrast, some other minor bands were observed in the synthesized sample. Especially bands around 1740-1600 cm^{-1} that can be associated to carbonyl groups of carbonated HAp [107]. Furthermore, the band at 1360 cm^{-1} can be related to residual nitrates. The CO_2 formation caused by the degradation of carbonate by ultrasound heating lead to internal cracks, enclosed bubbles and poor heating conductivity. The presence of nitrates also affects negatively the characteristics of the molded specimen since heated nitrates burnt and colored the sample.

In summary, the use of synthesized HAp requires exhaustive cleaning and purification steps in order to avoid the presence of carbonated or nitrates byproducts. Despite the fact that HAp nanocrystals are highly interesting for biomedical applications, the rest of the study is performed with commercial sample to avoid the effect of impurities. Finally, a careful drying is essential to reduce the moisture absorbed when hygroscopic salts are added. Moisture can render bubbles and lead to a cavitation phenomenon as also observed for some samples (not shown).

3.4.2.2. Characterization of PLA/HAp micromolded specimens

Micromolded composite specimens were characterized considering the GPC molecular weight, thermal properties, crystalline structure and mechanical properties.

Fig. 3-35 compares the GPC curves of the commercial PLA powder, the processed PLA specimen and the PLA-HAp composite specimen having the maximum load (i.e., 60 wt-%). Specimens were processed using the above indicated optimal parameters (i.e. 24 µm, 300 N and 1.2 s for PLA and 24 µm, 400 N and 1.2 s for the composite). Processing of PLA leads to a small increase of the tail of the curve corresponding to the smallest molecular weight fraction and therefore minor evidences of degradation could be detected through the M_n values. Specifically, M_w and M_n values were 69,100 g/mol and 43,000 g/mol for the commercial sample and 72,200 g/mol and 38,800 g/mol for the processed PLA with a force of 300 N. The incorporation of the commercial and carefully dried HAp lead also to a scarce degradation, which could be mainly attributed to the increase of the applied force [69]. In this case, M_w and M_n values decreased to 69,700 g/mol and 35,900 g/mol. It should also be indicated that for PLA alone, M_n decreased to 37,700 g/mol when the processing force was increased to 400 N. The incorporation of a ratio of HAp so high as 60 wt% had, therefore, a minimum influence on degradation.

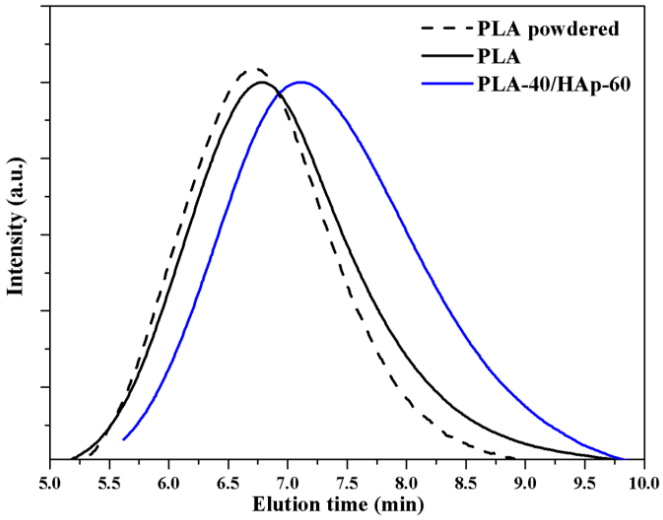

Fig. 3-35. *GPC chromatograms of commercial PLA powder, micromolded PLA and PLA-40/HAp-60. Processing parameters were 24 μm, 1,2 s and 300 N (PLA) and 400 N (PLA/HAp).*

As seen in **Fig. 3-36** incorporation of HAp had a clear nucleation effect, thus the cold crystallization exothermic peak of PLA/HAp composite shifted to a lower temperature. This behavior is not proportional to the HAp amount, at least in this high values 20-60%-wt, all PLA/HAp nanocomposites show a cold crystallization peak 10 ºC lower than neat PLA (i.e. 103.8 ºC with respect to 113.8 ºC). In addition, the melting enthalpy of the composite increased if the real amount of PLA is taken into account (i.e., 25.9 J/g become 43.2J/g for a sample containing only 60 wt% of PLA, a higher value than the enthalpy of 39.1 J/g determined for neat PLA). Samples showed minimum differences between their T_gs and the enthalpic relaxation peak. It is interesting to note that after processing PLA and PLA/HAp-40 remained practically amorphous since cold crystallization and melting (169 ºC) peaks had a similar enthalpy (i.e., 39 J/g for neat PLA and 26 J/g for PLA/HAp-40).

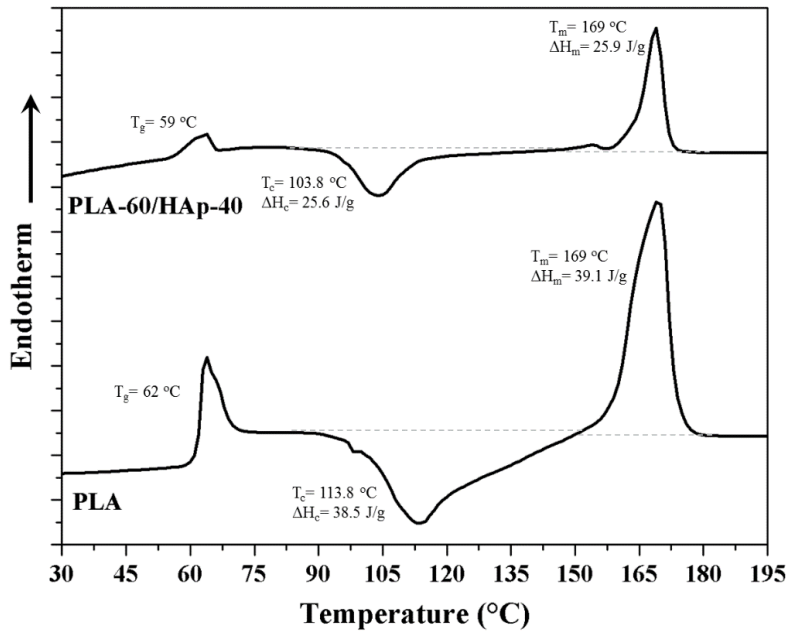

Fig. 3-36. *DSC heating runs of USM specimens of PLA and a representative PLA/HAp composite having 40 wt-% of HAp.*

Dynamic WAXD profiles were also recorded during the heating run of USM specimens (**Fig. 3-37a** and **b**). An amorphous profile was recorded for the PLA specimen at room temperature, but around 94 ºC the cold crystallization of PLA started as evidenced by the apparition of α-form characteristic peaks [108, 109] at scattering vector ($q = 2\pi/d$, d being the Bragg spacing) values of 11.5, 13.3 and 15.5 nm^{-1} (i.e., Bragg spacings of 0.546 nm, 0.472 nm and 0.405 nm that correspond to (200)+(110), (203) and (015) reflections, respectively). These peaks started to appear at a temperature of 104 ºC and reached maximum intensity around 125º C (see **Fig. 3-37c**). Then a partial melting of defective lamellae took place before a complete fusion that ended around 180 ºC. The behavior of the composite was completely similar except the detection of the crystalline peak of HAp at 18.15 nm^{-1} (Bragg spacing of 0.34 nm) [86, 105]. The main difference between PLA reflections of the processed specimens concern to the relative intensity of diffraction peaks and even in their broadness (**Fig. 3-37d**), which suggests the development of smaller PLA crystals in the composite as presumably due its higher nucleation density.

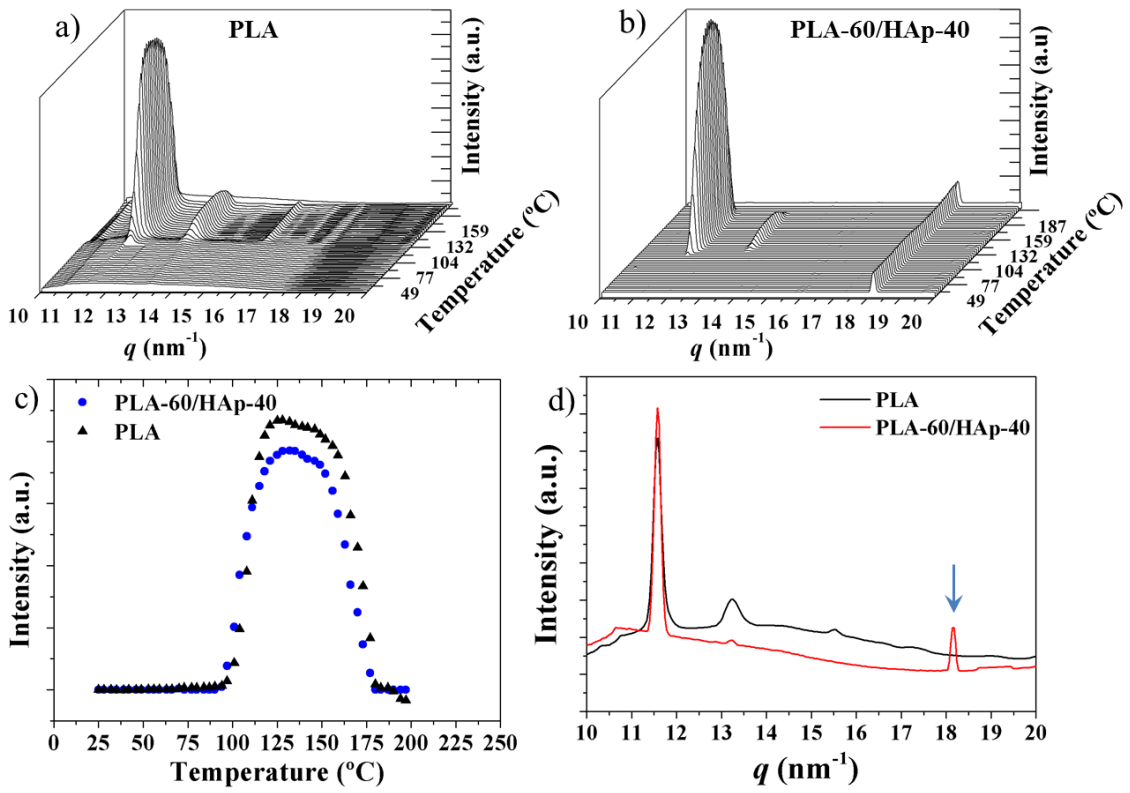

Fig. 3-37. *Three dimensional representations of WAXD profiles of USM PLA (**a**) and PLA-60/HAP-40 (**b**) specimens. **c**) Intensity evolution of the main PLA peak during heating (10 °C/min) from room temperature to fusion. **d**) Comparison of WAXD profiles recorded at 125 ºC of PLA and PLA-60/HAp-40 specimens. Arrow points out the reflection corresponding to the crystalline HAp.*

Incorporation of HAp improved mechanical properties of the composite in terms on the Young modulus, which logically increased due to the higher global crystallinity of the sample and the higher modulus of the HAp component. Thus, values of 847, 800, 780 and 754 MPa were evaluated for specimens with HAp loads of 60 wt-%, 40 wt-%, 35 wt-% and 20 wt-%, respectively, while a modulus of 707 MPa was measured for USM PLA. On the contrary, the elongation at break slightly

decreased as consequence of the lower cohesion between PLA and HAp (i.e., from 11.4% for neat PLA to 11.0, 10 and 9.5% for composites with HAp content of 20, 40 and 60 wt-% respectively). The combination of the two factors led to a practically constant maximum tensile strength (i.e., 58 MPa for PLA and 62, 60 and 59 MPa for composites with HAp contents varying from 60, 40 and 20 wt-% respectively). For the sake of clarity **Fig. 3-38** compare the Stress-Strain profiles of micromolded PLA and PLA-60/Hap-40 specimens.

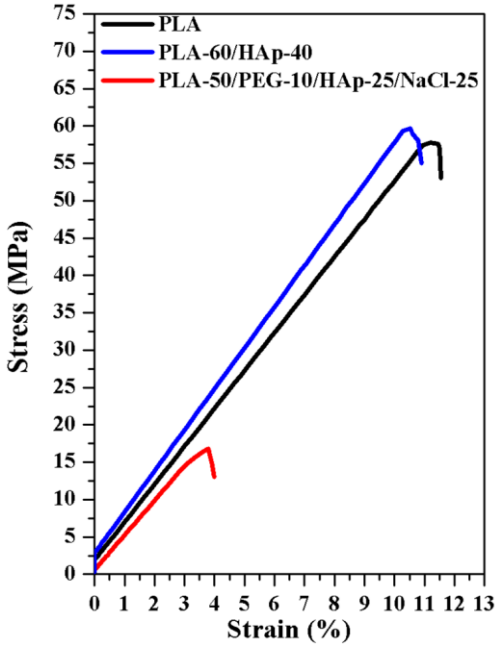

Fig. 3-38. *Stress-strain plots obtained from the representative indicated samples. PLA/PEG-10/Hap-25/NaCl-25 (PLA/Hap Scaffold) is also added to the comparison.*

The incorporation of Hap slightly increased the hydrophobicity of the processed specimen, which is a positive effect to promote cell growth. Thus, the contact angle determined for the USM PLA specimen decreased to 64º and 70º for composites having HAp contents of 60 wt-% and 20 wt-%, respectively (**Fig. 3-39**).

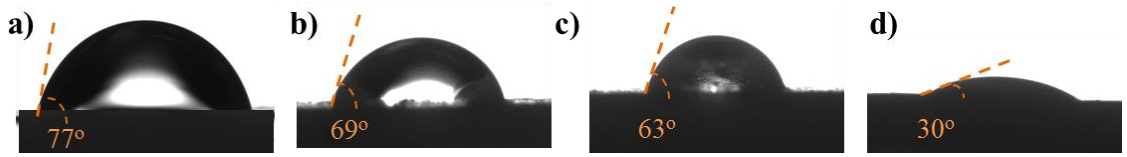

Fig. 3-39. *Water drop contact angle on PLA (**a**), PLA/HAp-20 (**b**) PLA/HAp-60 (**c**) and PLA/PEG-10/HAp-25/NaCl-25 (**d**) surface.*

3.4.2.3. Preparation of porous PLA/HAp scaffolds by ultrasound micromolding

The salt leaching technique has been employed in order to get porous PLA/HAp specimens. To this end, NaCl and PEG have been incorporated in the initial mixture before processing as has recently been reported as a highly effective method to provide porosity .[110] Therefore, NaCl particles

were sieved to get a homogeneous distribution with a small average size that facilitated the solubilization process, and that was appropriate for the subsequent cell colonization. A certain ratio of water-soluble PEG was necessary to increase the hydrophilicity of the specimen and make feasible both the entrance of water inside the processed specimen and the salt removal. According to get a significant porosity, USM was carried out using a mixture of PLA, PEG, NaCl and HAp powdered samples of 40 wt-%, 10 wt-%, 25 wt-% and 25 wt-%, respectively. Note that the final scaffolds should have a composition close to a 40 wt-% (i.e. 38 wt-%).

Processing parameters could be kept at the above selected values of 24 μm, 400 N and 1.2 s since molds were completely filled and specimens without coloration or other apparent degradation signals were obtained. In fact, GPC curves (not shown) of the processed specimens and after NaCl and PEG solubilization allowed estimating M_n and M_w values of 67,100 g/mol and 39,200 g/mol, respectively. SEM micrographs (**Fig. 3-40)** of specimen cross sections revealed the high porosity of the final scaffold and the absence of white and geometrically regular salt particles, which by contrast were still detectable when PEG was not incorporated. In this case, a perfect porous interconnectivity was not attained and therefore some salt particles were not accessible to water.

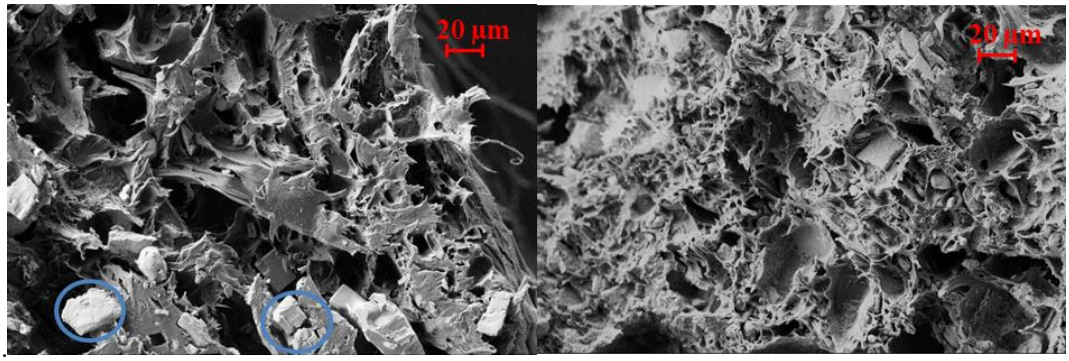

Fig. 3-40. *SEM micrographs of PLA/HAP scaffolds obtained by USM and subsequent washing (24 h) of PLA-50/NaCl-25/HAp-25 (**left**) and PLA-40/PEG-10/NaCl-25/HAp-25 (**right**) specimens. Blue circles pointed out the presence of some NaCl particles.*

3.4.2.4. Characterization of PLA/HAp micromolded porous scaffolds

Table 3-5 summarizes the results attained about weight percentages of total mass extraction (i.e. NaCl + PEG), NaCl extraction and porosity of representative scaffolds after the leaching process in water during 24 h. For comparison purposes values of PLA/NaCl-40 and PLA/PEG-10/NaCl-40 specimens from previous work was also added.[110] These two samples revealed the essential role of PEG to enhance the NaCl extraction. Note that extraction of NaCl was around only a 40% when PEG was not present whereas the addition of a small PEG percentage allowed getting a NaCl extraction close to 100%. Moreover, as consequence of this successful extraction, the porosity degree could be duplicated and attained a value close to 40%.

Table 3-5. *Mass and NaCl extraction percentages and degree of porosity of representative USM specimens.*

Sample[a]	Mass extraction (%)	Mass extraction (%)	Porosity (%)
PLA-60/NaCl-40	40 ± 8	38 ± 3	20 ± 5
PLA-50/PEG-10/NaCl-40[b]	98 ± 6	98 ± 7	39 ± 3
PLA-50/PEG-10/HAp-40[b]	100 ±2	--	16 ± 6
PLA-50/NaCl-25/HAp-25	53 ± 6	41 ± 3	18 ± 4
PLA-40/PEG-10/NaCl-25 /HAp-25	96 ± 13	92 ± 11	35 ± 4

(a) The number after each component correspons to the loaded wt% in the feeding camera.
(b) From previous work.[110]

Looking at the homologous samples loaded with HAp, a similar trend was observed: Incorporation of PEG increased the NaCl extraction yield as well as the porosity percentage.

Mechanical properties of the porous scaffold obviously decreased with respect to those determined for the solid PLA/HAp specimen having a similar composition (i.e. 38.4-40 wt-% of HAp). Specifically, Young modulus, elongation at break and tensile strength decreased to 580 MPa, 4% and 15.6 MPa. (**Fig. 3-38**)

Contact angle measurements showed a change from a value of 30º determined for the processed specimen before the leaching process to 60º after extraction of PEG and NaCl. Note that this angle is slightly lower than measured for the PLA/HAp scaffold having 40 wt-% of HAp (i.e. 70º). The difference suggests the presence of some residual NaCl since probably the increase of the specimen surface roughness and even the presence of voids should lead to a slight contact angle increase. (**Fig. 3-39**)

Fig. 3-41 compares the TGA and DTGA curves of the USM PLA and PLA-40/PEG-10/NaCl-25/HAp-25 specimens after PEG and salt extraction.

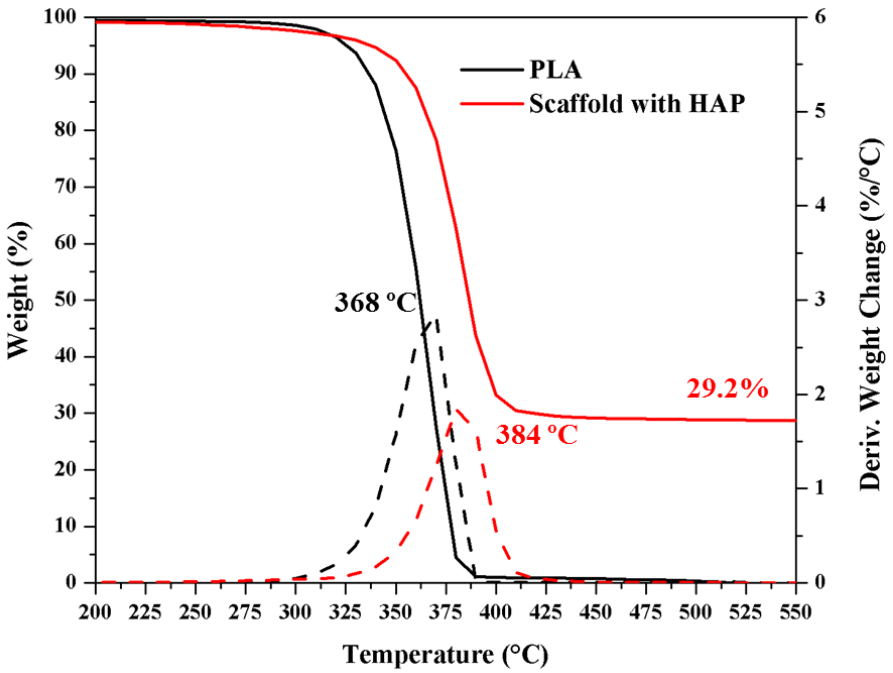

Fig. 3-41. *TGA and DTGA profiles of neat PLA and the porous PLA/HAp scaffold prepared by USM.*

As previously indicated, HAp provided a slight thermal stabilization and increased the onset decomposition temperature (i.e. from 345 ºC to 362 ºC) as well the DTGA peak temperature (i.e. from 368 ºC to 384 ºC). The residue detected at 550 ºC was 29.2%, a value in relatively good agreement with the loaded amount of HAp (25 wt-%). Nevertheless, extraction of NaCl was uncomplete, being the NaCl extraction percentage (84%) slightly worse than that evaluated by conductivity measurements.

The incorporation of HAp in materials used for different biomedical applications has interest in order to improve biocompatibility and favor cell viability[35, 36]. Particular attention merits the enhancement of the growth of bone tissue cells by biomineralization[90-93]. The advantages of HAp incorporation are additive to the porous characteristic of the final scaffold.

Fig. 3-42a compares the growth of MDCK cells onto specimens of neat PLA and representative scaffolds with and without HAp. Results pointed out the absence of cytotoxicity and good biocompatibility of PLA since cell viability was similar to the control. However, a significative higher relative cell viability ($p < 0.05$) was found for the porous samples as consequence of their higher adhesion area. Despite the greatest improvement was seen when compact and porous specimens were compared, it is also clear that the addition of HAp was beneficious, and a small additional increase of cell viability was detected. Therefore, cell proliferation increased by 45% and 30% with respect the control for PLA scaffolds with and without HAp. **Fig. 3-42** also compares the relative viability on the specimen and onto the well once the specimen was removed. Results attained with the well were similar, as expected, to those found with the control.

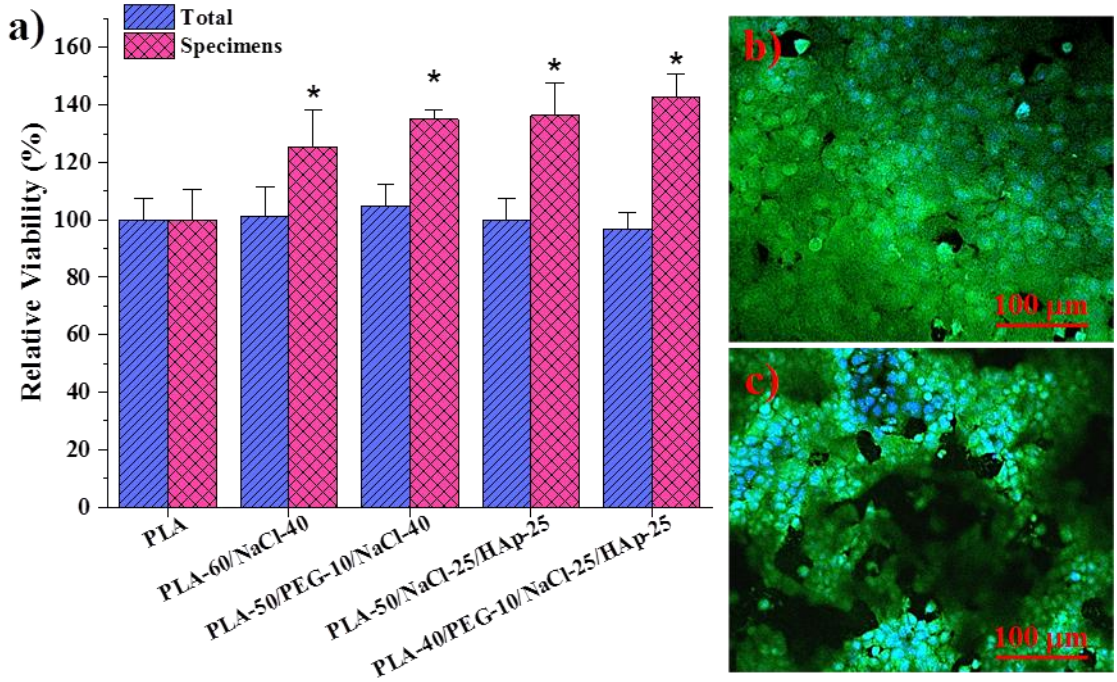

Fig. 3-42. *Bar graphic showing the relative cell proliferation determined at 7 days of culture for USM specimens of the indicated representative specimens (**a**). Asterisks indicate* $p < 0.05$ *vs PLA scaffold (ANOVA-Tukey test). Fluorescence micrographs showing the cell grown are also given for non-porous PLA (**b**) and porous PLA/HAp (i.e. from PLA-40/PEG-10/NaCl-25/HAp-25) (**c**). The cells were stained for nuclei (DAPI, blue) and actin (phalloidin, green).*

Fluorescence micrographs showed the formation of a uniform cell monolayer onto the surface of the PLA specimen. However, cells in the porous scaffold can penetrate the porous surface and fill the voids of the sample as evidenced by their growth in different planes.

3.4.3. Conclusions

Hybrid scaffolds of polylactide and hydroxyapatite can successfully be obtained through a new micromolding technology based on the application of ultrasounds as energy source. Specimens showed a minimum degradation and could be obtained with a processing time so low as 1.2 s and a minimum material loss. Micropieces showed a relatively homogeneous distribution of HAp particles except for their surfaces. The maximum amount of HAp that could be loaded keeping a correct fluency in the feeding channels was 60 wt-%, a content that rendered materials with higher mechanical properties than non-loaded specimens (e.g., Young modulus of 847 MPa in front of 707 MPa). PLA was practically amorphous after processing although micropieces could subsequently been submitted to cold crystallization. The quality of HAp was fundamental to get specimens without degradation and colaration as consequence of cavitation phenomena induced by the decomposition of synthesis byproducts such as carbonate and nitrate salts.

Porous scaffolds of PLA/HAp could also be prepared by adding water soluble compounds (e.g., polyethylene glycol and NaCl salts) in the feeding mixture and performing a subsequent leaching process. The HAp content should be reduced to 38 wt-% to get materials with a porosity of 35%. Young modulus and tensile strength logically decreased with respect to the non-porous PLA samples, but acceptable values of 580 MPa and 15.6 MPa were attained. The presence of HAp provided thermal stability and allowed to increase the hydrophilicity, an interesting feature for biological applications. In the same way, it was found that both porosity and presence of HAp particles favoured cell colonization and specifically an increase of the proliferation of assayed MDCK cells around 40% with respect to the control was found.

3.5. Reference

1. Zhang, Y..Lu, J. A simple method to tailor spherical nanocrystal hydroxyapatite at low temperature. *Journal of Nanoparticle Research* (2007), *9*, 589-594.

2. Berzina-Cimdina, L..Borodajenko, N., Research of Calcium Phosphates Using Fourier Transform Infrared Spectroscopy, in: P.T. Theophile (Ed.), Materials Science, Engineering and Technology., InTech (2011).

3. Mosmann, T. Rapid colorimetric assay for cellular growth and survival: Application to proliferation and cytotoxicity assays. *Journal of Immunological Methods* (1983), *65*, 55-63.

4. Attia, U.M.; Marson, S..Alcock, J.R. Micro-injection moulding of polymer microfluidic devices. *Microfluidics and Nanofluidics* (2009), *7*, 1.

5. Lee, C.-Y.; Wu, G.-W..Hsieh, W.-J. Fabrication of micro sensors on a flexible substrate. *Sensors and Actuators A: Physical* (2008), *147*, 173-176.

6. Besten, C.d.; Hal, R.E.G.v.; Munoz, J..Bergveld, P. Polymer bonding of micro-machined silicon structures. *Proceedings IEEE Micro Electro Mechanical Systems* (1992).

7. Heckele, M.; Bacher, W..Müller, K.D. Hot embossing - The molding technique for plastic microstructures. *Microsystem Technologies* (1998), *4*, 122-124.

8. Heckele, M..Schomburg, W.K. Review on micro molding of thermoplastic polymers. *Journal of Micromechanics and Microengineering* (2004), *14*, R1.

9. Michaeli, W.; Spennemann, A..Gärtner, R. *New plastification concepts for micro injection moulding*. *Microsystem Technologies* (2002), *8*, 55-57.

10. Sacristán, M.; Puiggalli, J.; Planta, X..Morell, M. *Effects of ultrasonic vibration on the micro-molding processing of polylactide*. *Ultrasonics Sonochemistry* (2014), *21*, 376-386.

11. Truckenmuller, R.; Ahrens, R.; Chenga, Y.; Fischer, G..Saile, V. *An ultrasonic welding based process for building up a new class of inert fluidic microsensors and -actuators from polymers*. *Sensors and Actuators A* (2006), *132*, 385-392.

12. Chen, J.; Chen, Y.; Li, H.; Lai, S.-Y..Jow, J. Physical and chemical effects of ultrasound vibration on polymer melt in extrusion. *Ultrasonics Sonochemistry* (2010), *17*, 66-71.

13. Michaeli, W..Opferman, D. *Ultrasonic plasticising for micro injection moulding*. *4M 2006 - Second International Conference on Multi-Material Micro Manufacture* (2006), 345-348.

14. Michaeli, W.; Kamps, T..Hopmann, C. Manufacturing of polymer micro parts by ultrasonic plasticization and direct injection. *Microsystem Technologies* (2011), *17*, 243-249.

15. Chen, G.; Guo, S..Li, H. Ultrasonic improvement of rheological behavior of polystyrene. *Journal of Applied Polymer Science* (2002), *84*, 2451-2460.

16. Auras, R.; Lim, L.-T.; Selke, S.E.M..Tsuji, H., *Poly(lactic acid): Synthesis, Structures, Properties, Processing, and Applications*, (2010).

17. Williams, D.F. *Biocompatibility of clinical implant materials*, CRC Press:Boca Raton, Fla., (1981).

18. Ikada, S.S.Y., Medical Applications, in: R.A.L.T.L.S.E.M.S.H. Tsuji (Ed.), Poly(Lactic Acid) (2010).

19. Conn, J.; Oyasu, R.; Welsh, M..Beal, J.M. Vicryl (polyglactin 910) synthetic absorbable sutures. *The American Journal of Surgery* (1974), *128*, 19-23.

20. Burger, C.; Kabir, K.; Rangger, C.; Mueller, M.; Minor, T..Tolba, R.H. Polylactide (LTS) causes less inflammation response than polydioxanone (PDS): a meniscus repair model in sheep. *Archives of Orthopaedic and Trauma Surgery* (2006), *126*, 695-705.

21. Armentano, I.; Bitinis, N.; Fortunati, E.; Mattioli, S.; Rescignano, N.; Verdejo, R.; Lopez-Manchado, M.A..Kenny, J.M. Multifunctional nanostructured PLA materials for packaging and tissue engineering. *Progress in Polymer Science* (2013), *38*, 1720-1747.

22. Shah Mohammadi, M.; Bureau, M.N..Nazhat, S.N., 11 - Polylactic acid (PLA) biomedical foams for tissue engineering, in: P.A. Netti (Ed.), Biomedical Foams for Tissue Engineering Applications, Woodhead Publishing (2014), pp. 313-334.

23. Lopes, M.S.; Jardini, A.L..Filho, R.M. Poly (Lactic Acid) Production for Tissue Engineering Applications. *Procedia Engineering* (2012), *42*, 1402-1413.

24. Tyler, B.; Gullotti, D.; Mangraviti, A.; Utsuki, T..Brem, H. Polylactic acid (PLA) controlled delivery carriers for biomedical applications. *Advanced Drug Delivery Reviews* (2016), *107*, 163-175.

25. Lassalle, V..Ferreira, M.L. PLA Nano- and Microparticles for Drug Delivery: An Overview of the Methods of Preparation. *Macromolecular Bioscience* (2007), *7*, 767-783.

26. Kellomäki, M..Törmälä, P. *Ultrasonic moulding of bioabsorbable polymers and polymer/drug composites*. *Journal of material science letters* (1997), *16*, 1786-1789.

27. M. Allen Theresa.Pieter, R.C. *Drug Delivery Systems: Entering the Mainstream*. *Science* (2004), *303*, 1818-1822.

28. Planellas, M.; Sacristán, M.; Rey, L.; Olmo, C.; Aymamí, J.; Casas, M.T.; Valle, L.J.d.; Franco, L..Puiggalí, J. Micro-molding with ultrasonic vibration energy: New method to disperse nanoclays in polymer matrices. *Ultrasonics Sonochemistry* (2014), *21*, 1557-1569.

29. Li, S.; Girod-Holland, S..Vert, M. Hydrolytic degradation of poly(dl-lactic acid) in the presence of caffeine base. *Journal of Controlled Release* (1996), *40*, 41-53.

30. Alexis, F. Factors affecting the degradation and drug-release mechanism of poly(lactic acid) and poly[(lactic acid)-co-(glycolic acid)]. *Polymer International* (2005), *54*, 36-46.

31. Pouliopoulos, A.N.; Li, C.; Tinguely, M.; Garbin, V.; Tang, M.-X..Choi, J.J. Rapid short-pulse sequences enhance the spatiotemporal uniformity of acoustically driven microbubble activity during flow conditions. *The Journal of the Acoustical Society of America* (2016), *140*, 2469-2480.

32. Haworth, K.J.; Bader, K.B.; Rich, K.T.; Holland, C.K..Mast, T.D. Quantitative Frequency-Domain Passive Cavitation Imaging. *IEEE Transactions on Ultrasonics, Ferroelectrics, and Frequency Control* (2017), *64*, 177-191.

33. Márquez, Y.; Cabral, T.; Lorenzetti, A.; Franco, L.; Turon, P.; del Valle, L.J..Puiggalí, J. Incorporation of biguanide compounds into poly(GL)-b-poly(GL-co-TMC-co-CL)-b-poly(GL) monofilament surgical sutures. *Materials Science and Engineering: C* (2017), *71*, 629-640.

34. Zurita, R.; Puiggalí, J..Rodríguez-Galán, A. Triclosan Release from Coated Polyglycolide Threads. *Macromolecular Bioscience* (2006), *6*, 58-69.

35. Bonassar, L.J..Vacanti, C.A. Tissue engineering: The first decade and beyond. *Journal of Cellular Biochemistry* (1998), *72*, 297-303.

36. Atala, A. Tissue Engineering and Regenerative Medicine: Concepts for Clinical Application. *Rejuvenation Research* (2004), *7*, 15-31.

37. Peter, S.J.; Miller, M.J.; Yasko, A.W.; Yaszemski, M.J..Mikos, A.G. Polymer concepts in tissue engineering. *Journal of Biomedical Materials Research* (1998), *43*, 422-427.

38. Marler, J.J.; Upton, J.; Langer, R..Vacanti, J.P. Transplantation of cells in matrices for tissue regeneration. *Advanced Drug Delivery Reviews* (1998), *33*, 165-182.

39. A.J. Salgado, O.P.C., and R.L. Reis Novel Starch-Based Scaffolds for Bone Tissue Engineering: Cytotoxicity, Cell Culture, and Protein Expression. *Tissue Engineering* (2004), *10*, 465-474.

40. Heller, C.; Schwentenwein, M.; Russmueller, G.; Varga, F.; Stampfl, J..Liska, R. Vinyl esters: Low cytotoxicity monomers for the fabrication of biocompatible 3D scaffolds by

lithography based additive manufacturing. *Journal of Polymer Science Part A: Polymer Chemistry* (2009), *47*, 6941-6954.

41. Watari, F.; Yokoyama, A.; Saso, F.; Uo, M..Kawasaki, T. Fabrication and properties of functionally graded dental implant. *Composites Part B: Engineering* (1997), *28*, 5-11.

42. Walsh, D.; Furuzono, T..Tanaka, J. Preparation of porous composite implant materials by in situ polymerization of porous apatite containing ε-caprolactone or methyl methacrylate. *Biomaterials* (2001), *22*, 1205-1212.

43. Mizuno, S..Glowacki, J. Three-dimensional composite of demineralized bone powder and collagen for in vitro analysis of chondroinduction of human dermal fibroblasts. *Biomaterials* (1996), *17*, 1819-1825.

44. Su, Z.; Ma, H.; Wu, Z.; Zeng, H.; Li, Z.; Wang, Y.; Liu, G.; Xu, B.; Lin, Y.; Zhang, P..Wei, X. Enhancement of skin wound healing with decellularized scaffolds loaded with hyaluronic acid and epidermal growth factor. *Materials Science and Engineering: C* (2014), *44*, 440-448.

45. Guo, T.; Zhao, J.; Chang, J.; Ding, Z.; Hong, H.; Chen, J..Zhang, J. Porous chitosan-gelatin scaffold containing plasmid DNA encoding transforming growth factor-β1 for chondrocytes proliferation. *Biomaterials* (2006), *27*, 1095-1103.

46. Li, X.; Wang, Y.; Guo, M.; Wang, Z.; Shao, N.; Zhang, P.-b.; Chen, X..Huang, Y. Degradable 3D printed PLA scaffold with long-term antibacterial activity. *ACS Sustainable Chemistry & Engineering* (2017), *6*.

47. Wu, J.C.-C.; Ray, S.; Gizdavic-Nikolaidis, M.; Uy, B.; Swift, S.; Jin, J..Cooney, R.P. Nanostructured bioactive material based on polycaprolactone and polyaniline fiber-scaffolds. *Synthetic Metals* (2014), *198*, 41-50.

48. Hollister, S.J. Porous scaffold design for tissue engineering. *Nature Materials* (2005), *4*, 518-524.

49. Velasco, M.A.; Narv; ez-Tovar, C.A.; Garz.n-Alvarado, D.A. Design, Materials, and Mechanobiology of Biodegradable Scaffolds for Bone Tissue Engineering. *BioMed Research International* (2015), *2015*, 21.

50. Jeong, D.; Yun, A..Kim, J. Mathematical model and numerical simulation of the cell growth in scaffolds. *Biomechanics and Modeling in Mechanobiology* (2012), *11*, 677-688.

51. Freed, L.E.; Vunjak-Novakovic, G.; Biron, R.J.; Eagles, D.B.; Lesnoy, D.C.; Barlow, S.K..Langer, R. Biodegradable Polymer Scaffolds for Tissue Engineering. *Bio/Technology* (1994), *12*, 689-693.

52. Liu, X.; Holzwarth, J.M..Ma, P.X. Functionalized Synthetic Biodegradable Polymer Scaffolds for Tissue Engineering. *Macromolecular Bioscience* (2012), *12*, 911-919.

53. Rezwan, K.; Chen, Q.Z.; Blaker, J.J..Boccaccini, A.R. Biodegradable and bioactive porous polymer/inorganic composite scaffolds for bone tissue engineering. *Biomaterials* (2006), *27*, 3413-3431.

54. McMurry, L.M.; Oethinger, M..Levy, S.B. Triclosan targets lipid synthesis. *Nature* (1998), *394*, 531-532.

55. Mikos, A.G.; Bao, Y.; Cima, L.G.; Ingber, D.E.; Vacanti, J.P..Langer, R. Preparation of poly(glycolic acid) bonded fiber structures for cell attachment and transplantation. *Journal of Biomedical Materials Research* (1993), *27*, 183-189.

56. Díaz, A.; del Valle, L.J.; Tugushi, D.; Katsarava, R..Puiggalí, J. New poly(ester urea) derived from l-leucine: Electrospun scaffolds loaded with antibacterial drugs and enzymes. *Materials Science and Engineering: C* (2015), *46*, 450-462.

57. Sin, D.; Miao, X.; Liu, G.; Wei, F.; Chadwick, G.; Yan, C..Friis, T. Polyurethane (PU) scaffolds prepared by solvent casting/particulate leaching (SCPL) combined with centrifugation. *Materials Science and Engineering: C* (2010), *30*, 78-85.

58. Oh, S.H.; Kang, S.G..Lee, J.H. Degradation behavior of hydrophilized PLGA scaffolds prepared by melt-molding particulate-leaching method: Comparison with control hydrophobic one. *Journal of Materials Science: Materials in Medicine* (2006), *17*, 131-137.

59. Widmer, M.S.; Gupta, P.K.; Lu, L.; Meszlenyi, R.K.; Evans, G.R.D.; Brandt, K.; Savel, T.; Gurlek, A.; Patrick, C.W..Mikos, A.G. Manufacture of porous biodegradable polymer conduits by an extrusion process for guided tissue regeneration. *Biomaterials* (1998), *19*, 1945-1955.

60. Utela, B.; Storti, D.; Anderson, R..Ganter, M. A review of process development steps for new material systems in three dimensional printing (3DP). *Journal of Manufacturing Processes* (2008), *10*, 96-104.

61. Bergmann, C.; Lindner, M.; Zhang, W.; Koczur, K.; Kirsten, A.; Telle, R..Fischer, H. 3D printing of bone substitute implants using calcium phosphate and bioactive glasses. *Journal of the European Ceramic Society* (2010), *30*, 2563-2567.

62. Yao, D.; Chen, S.-C..H.Kim, B. *Rapid thermal cycling of injection molds: An overview on technical approaches and applications*. *Advances in Polymer Technology* (2008), *27*, 233-255.

63. Yao, D.; Chen, S.-C..H.Kim, B. *High-frequency proximity heating for injection molding applications*. *Polymer Enginnering & Science* (2006), *46*, 938-945.

64. Michaeli, W..Starke, C. *Ultrasonic investigations of the thermoplastics injection moulding process*. *Polymer Testing* (2005), *24*, 205-209.

65. Díaz, A.; Franco, L.; Casas, M.T.; del Valle, L.J.; Aymamí, J.; Olmo, C..Puiggalí, J. Preparation of micro-molded exfoliated clay nanocomposites by means of ultrasonic technology. *Journal of Polymer Research* (2014), *21*, 584.

66. Olmo, C.; Amestoy, H.; Casas, M.T.; Martínez, J.C.; Franco, L.; Sarasua, J.-R..Puiggalí, J. Preparation of Nanocomposites of Poly(ε-caprolactone) and Multi-Walled Carbon Nanotubes by Ultrasound Micro-Molding. Influence of Nanotubes on Melting and Crystallization. *Polymers* (2017), *9*, 322.

67. Brahatheeswaran Dhandayuthapani, Y.Y., Toru Maekawa, and D. Sakthi Kumar Polymeric Scaffolds in Tissue Engineering Application: A Review. *International Journal of Polymer Science* (2011), *2011*.

68. Heller, J. Biodegradable polymers in controlled drug delivery. *Crit Rev Ther Drug Carrier Syst* (1984), *1*, 39-90.

69. Olmo, C.; Franco, L.; del Valle, L.J..Puiggalí, J. Preparation of Medicated Polylactide Micropieces by Means of Ultrasonic Technology. *Applied Sciences* (2019), *9*, 2360.

70. Li, S.H.; De Wijn, J.R.; Layrolle, P..De Groot, K. Synthesis of macroporous hydroxyapatite scaffolds for bone tissue engineering. *Journal of Biomedical Materials Research* (2002), *61*, 109-120.

71. Kim, S.-S.; Sun Park, M.; Jeon, O.; Yong Choi, C..Kim, B.-S. Poly(lactide-co-glycolide)/ hydroxyapatite composite scaffolds for bone tissue engineering. *Biomaterials* (2006), *27*, 1399-1409.

72. Kramschuster, A..Turng, L.-S. An injection molding process for manufacturing highly porous and interconnected biodegradable polymer matrices for use as tissue engineering scaffolds. *Journal of Biomedical Materials Research Part B: Applied Biomaterials* (2010), *92B*, 366-376.

73. Huang, R.; Zhu, X.; Zhao, T..Wan, A. Preparation of tissue engineering porous scaffold with poly(lactic acid) and polyethylene glycol solution blend by solvent-casting/particulate-leaching. (2014).

74. Wu, D.; Lin, D.; Zhang, J.; Zhou, W.; Zhang, M.; Zhang, Y.; Wang, D..Lin, B. Selective Localization of Nanofillers: Effect on Morphology and Crystallization of PLA/PCL Blends. *Macromolecular Chemistry and Physics* (2011), *212*, 613-626.

75. Yang, M..Lin, Y. Measurement and Simulation of Thermal Stability of Poly(Lactic Acid) by Thermogravimetric Analysis. *Journal of Testing and Evaluation* (2009), *37*, 364-370.

76. Han, S.; Kim, C..Kwon, D. Thermal/oxidative degradation and stabilization of polyethylene glycol. *Polymer* (1997), *38*, 317-323.

77. Hassan, M.; Chong, L..Sultana Phd Ceng Csci, N. Wettability and water uptake properties of PLA and PCL/Gelatin-based electrospun. (2016), *11*.

78. Szewczyk, P.K.; Ura, D.P.; Metwally, S.; Knapczyk-Korczak, J.; Gajek, M.; Marzec, M.M.; Bernasik, A..Stachewicz, U. Roughness and Fiber Fraction Dominated Wetting of Electrospun Fiber-Based Porous Meshes. *Polymers* (2019), *11*, 34.

79. Puliafito, A.; Hufnagel, L.; Neveu, P.; Streichan, S.; Sigal, A.; Fygenson, D.K..Shraiman, B.I. Collective and single cell behavior in epithelial contact inhibition. *Proceedings of the National Academy of Sciences* (2012), *109*, 739-744.

80. Xi, W.; Sonam, S.; Beng Saw, T.; Ladoux, B..Teck Lim, C. Emergent patterns of collective cell migration under tubular confinement. *Nature Communications* (2017), *8*, 1517.

81. Tlili, S.; Gauquelin, E.; Li, B.; Cardoso, O.; Ladoux, B.; Delanoë-Ayari, H..Graner, F. Collective cell migration without proliferation: density determines cell velocity and wave velocity. *Royal Society Open Science* (2018), *5*, 172421.

82. Damm, C.; Münstedt, H..Rösch, A. Long-term antimicrobial polyamide 6/silver-nanocomposites. *Journal of Materials Science* (2007), *42*, 6067-6073.

83. Ramakrishna, S.; Mayer, J.; Wintermantel, E..Leong, K.W. Biomedical applications of polymer-composite materials: a review. *Composites Science and Technology* (2001), *61*, 1189-1224.

84. Shikinami, Y..Okuno, M. Bioresorbable devices made of forged composites of hydroxyapatite (HA) particles and poly l-lactide (PLLA). Part II: practical properties of miniscrews and miniplates. *Biomaterials* (2001), *22*, 3197-3211.

85. Martin, I.; Wendt, D..Heberer, M. The role of bioreactors in tissue engineering. *Trends in Biotechnology* (2004), *22*, 80-86.

86. Choi, D.; Marra, K.G..Kumta, P.N. Chemical synthesis of hydroxyapatite/poly(ε-caprolactone) composites. *Materials Research Bulletin* (2004), *39*, 417-432.

87. Ioku, K.; Yamauchi, S.; Fujimori, H.; Goto, S..Yoshimura, M. Hydrothermal preparation of fibrous apatite and apatite sheet. *Solid State Ionics* (2002), *151*, 147-150.

88. Li, X.; Feng, Q.; Liu, X.; Dong, W..Cui, F. Collagen-based implants reinforced by chitin fibres in a goat shank bone defect model. *Biomaterials* (2006), *27*, 1917-1923.

89. Wei, J..Li, Y. Tissue engineering scaffold material of nano-apatite crystals and polyamide composite. *European Polymer Journal* (2004), *40*, 509-515.

90. Yun, Y.-P.; Kim, S.-J.; Lim, Y.-M.; Park, K.; Kim, H.-J.; Jeong, S.-I.; Kim, S.E..Song, H.-R. The Effect of Alendronate-Loaded Polycarprolactone Nanofibrous Scaffolds on Osteogenic Differentiation of Adipose-Derived Stem Cells in Bone Tissue Regeneration. *Journal of Biomedical Nanotechnology* (2014), *10*, 1080-1090.

91. Zhou, H.; Lawrence, J.G..Bhaduri, S.B. Fabrication aspects of PLA-CaP/PLGA-CaP composites for orthopedic applications: A review. *Acta Biomaterialia* (2012), *8*, 1999-2016.

92. Elgendy, H.M.; Norman, M.E.; Keaton, A.R..Laurencin, C.T. Osteoblast-like cell (MC3T3-E1) proliferation on bioerodible polymers: an approach towards the development of a bone-bioerodible polymer composite material. *Biomaterials* (1993), *14*, 263-269.

93. Hench, L.L. Bioceramics. *Journal of the American Ceramic Society* (1998), *81*, 1705-1728.

94. Wei, G..Ma, P.X. Structure and properties of nano-hydroxyapatite/polymer composite scaffolds for bone tissue engineering. *Biomaterials* (2004), *25*, 4749-4757.

95. Zhang, R..Ma, P.X. Poly(α-hydroxyl acids)/hydroxyapatite porous composites for bone-tissue engineering. I. Preparation and morphology. *Journal of Biomedical Materials Research* (1999), *44*, 446-455.

96. Cool, S.M.; Kenny, B.; Wu, A.; Nurcombe, V.; Trau, M.; Cassady, A.I..Grøndahl, L. Poly(3-hydroxybutyrate-co-3-hydroxyvalerate) composite biomaterials for bone tissue regeneration: In vitro performance assessed by osteoblast proliferation, osteoclast adhesion and resorption, and macrophage proinflammatory response. *Journal of Biomedical Materials Research Part A* (2007), *82A*, 599-610.

97. Ren, J.; Zhao, P.; Ren, T.; Gu, S..Pan, K. Poly (d,l-lactide)/nano-hydroxyapatite composite scaffolds for bone tissue engineering and biocompatibility evaluation. *Journal of Materials Science: Materials in Medicine* (2008), *19*, 1075-1082.

98. Diao, H.; Si, Y.; Zhu, A.; Ji, L..Shi, H. Surface modified nano-hydroxyapatite/poly(lactide acid) composite and its osteocyte compatibility. *Materials Science and Engineering: C* (2012), *32*, 1796-1801.

99. Zhang, C.Y.; Zhang, C.L.; Wang, J.F.; Lu, C.H.; Zhuang, Z.; Wang, X.P..Fang, Q.F. Fabrication and in vitro investigation of nanohydroxyapatite, chitosan, poly(L-lactic acid) ternary biocomposite. *Journal of Applied Polymer Science* (2013), *127*, 2152-2159.

100. Han, W.; Zhao, J.; Tu, M.; Zeng, R.; Zha, Z..Zhou, C. Preparation and characterization of nanohydroxyapatite strengthening nanofibrous poly(L-lactide) scaffold for bone tissue engineering. *Journal of Applied Polymer Science* (2013), *128*, 1332-1338.

101. Cheng, C.C.; Banakar, H.; Ooi, B.T..Jen, C.K. *Melting Quality of Polymers in Internal Mixer Diagnosed by Ultrasound*. *International Polymer Processing* (2009), *24*, 375-383.

102. SATO, A.; ITO, H..KOYAMA, K. *Study of Application of Ultrasonic Wave to Injection Molding*. *Polymer Engineering & Science* (2009), *49*, 768-773.

103. Li, J.; Xu, K.; Lin, X.; Wu, X..Gao, G. *Research on the Flow Characteristics of Polymer Injection Molding Under Ultrasonic Vibration and Plastics' Mechanical Strength*. *Applied Mechanics and Materials* (2010), *37-38*, 1092-1100.

104. Giboz, J.; Copponnex, T..Melé, P. *Microinjection molding of thermoplastics polymer: a review*. *J. of Micromechanics and Microengineering* (2007), *17*, R96-R109.

105. Herdocia-Lluberes, C.S.; Laboy-López, S.; Morales, S.; Gonzalez-Robles, T.J.; González-Feliciano, J.A..Nicolau, E. Evaluation of Synthesized Nanohydroxyapatite-Nanocellulose Composites as Biocompatible Scaffolds for Applications in Bone Tissue Engineering. *Journal of Nanomaterials* (2015), *2015*, 310935.

106. Rehman, I..Bonfield, W. Characterization of hydroxyapatite and carbonated apatite by photo acoustic FTIR spectroscopy. *Journal of Materials Science: Materials in Medicine* (1997), *8*, 1-4.

107. Landi, E.; Celotti, G.; Logroscino, G..Tampieri, A. Carbonated hydroxyapatite as bone substitute. *Journal of the European Ceramic Society* (2003), *23*, 2931-2937.

108. De Santis, P..Kovacs, A.J. Molecular conformation of poly(S-lactic acid). *Biopolymers* (1968), *6*, 299-306.

109. Hoogsteen, W.; Postema, A.R.; Pennings, A.J.; Ten Brinke, G..Zugenmaier, P. Crystal structure, conformation and morphology of solution-spun poly(L-lactide) fibers. *Macromolecules* (1990), *23*, 634-642.

110. Olmo, C.; Franco, L.; del Valle, L.J..Puiggalí, J. Biodegradable Polylactide Scaffolds with Pharmacological Activity by Means of Ultrasound Micromolding Technology. *Applied Sciences* (2020), *10*, 3106.

4. Ultrasound micromolding: Preparation of nanocomposites

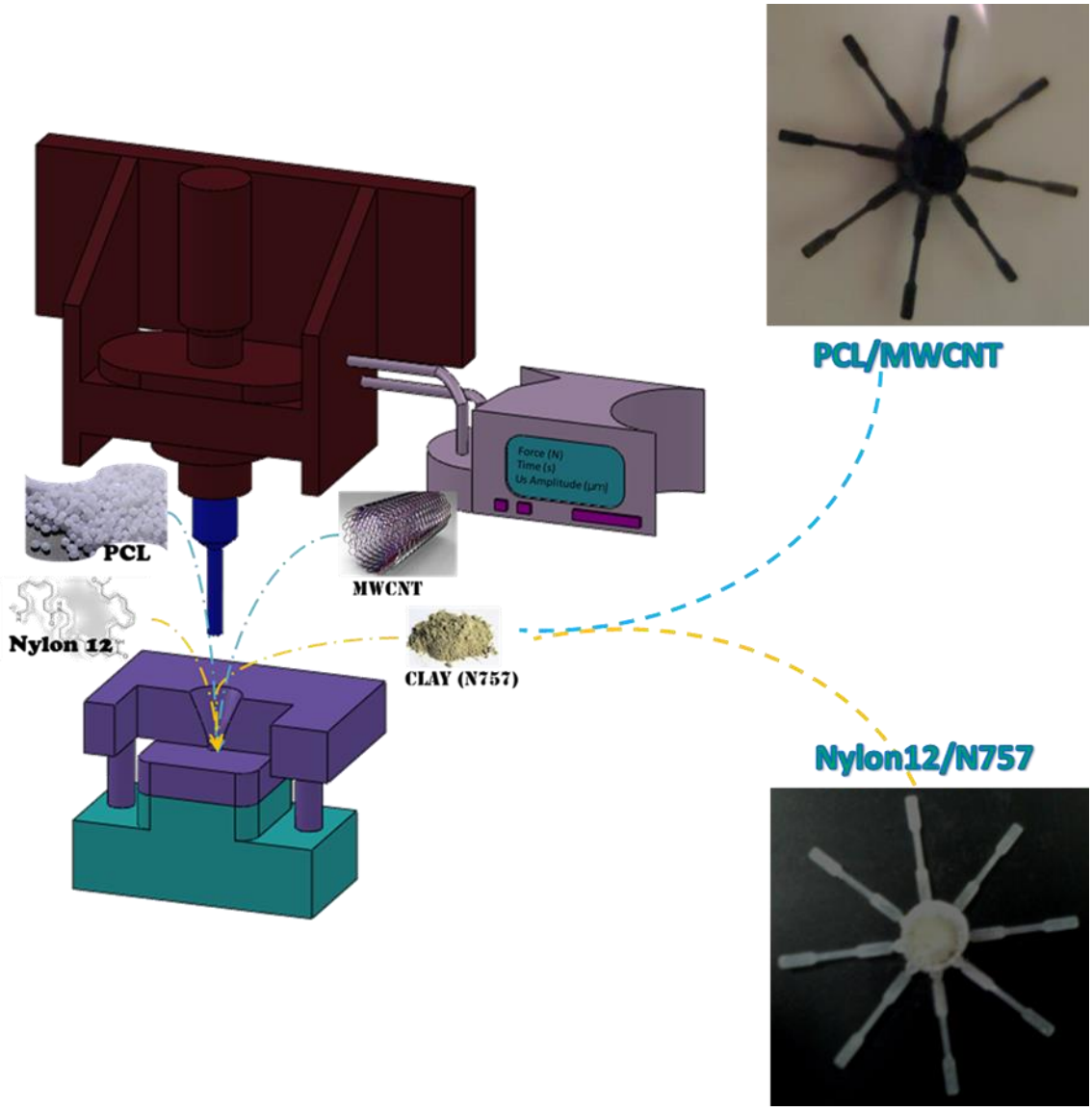
PCL/MWCNT
Force (N)
Time (s)
Us Amplitude (µm)
PCL
MWCNT
Nylon 12
CLAY (N757)
Nylon12/N757

Ultrasound micromolding technology was successfully applied to prepare nanocomposites using multi-walled carbon nanotubes (MWCNT) or clays. Two types of polymers were assayed, poly(ε-caprolactone) and polyamide 12. US micromolding was also revealed to be efficient in getting fully exfoliated nanocomposites according to X-ray diffraction data and TEM images, even when the non-organo modified clay (Nanofil 757) was selected.

Appropriate processing conditions (i.e. amplitude, force and time) were crucial to process, with a minimum molecular weight loss, both neat polymers and their nanocomposites. Good dispersion of nanotubes was archived after processing previously formed solvent casting; this dispersion was even partially detected in pieces obtained from direct powdered mixture of both components.

Incorporation of MWCNTs had a remarkable influence on melting and crystallization processes, which were systematically studied by time resolved synchrotron experiments. Results indicated higher melting and crystallization temperatures for the nanocomposite, with temperature differences higher than 5 ºC. Carbon nanotubes were effective nucleating agents and had an influence on crystallinity, crystallization rate and even on lamellar morphology, which was evaluated by analysis of the correlation function of small angle diffraction profiles. Crystallinity within lamellar stacks was lower for the solvent casting nanocomposite, but in this case lamellae underwent a thickening process during heating that accounted for the increase in the melting temperature. Crystallization from the melt rendered similar lamellar morphologies at the end of the process due to a lamellar insertion mechanism.

The incorporation of the clay prepared by US micromolding had a remarkable influence on the final crystalline form of the processed specimen compared with those obtained from conventional technologies (e.g., melt mixing and solution intercalation). This influence was analyzed in the crystallization study undertaken with nylon 12. Thus, the α' form was stabilized with respect to other processing technologies, probably as consequence of a crystallization in presence of nanoclay sheets and under a high shear stress. Typical Avrami analyses confirmed the influence of clays in the non-isothermal crystallization, which involved a higher nucleation and a lower crystal growth rate than those found with the neat polymer. Melting characteristics and degree of crystallinity were also influenced by the incorporation of the nanoclay.

Additionally, crystalline polymorphic transitions of nylons 12 (i.e., the named α, α', γ and γ' forms) were evaluated through analyses of real time synchrotron diffraction patterns of samples prepared under different conditions and submitted to different heating/cooling runs. Temperature induced polymorphic transitions were also rationalized.

4.1. Materials and Methods

4.1.1. Materials

All reagents and solvents were purchased from Sigma-Aldrich (Sant Louis, MO, USA) and used without purification. Poly(ε-caprolactone) was purchased from Solvay (Warrington, United Kingdom). The number average molecular weight was 128,900 g/mol and the polydispersity index 2.2 as determined by GPC. The nylon 12 used in this study is a commercial sample (Rilsan® AMNO) from Arkena characterized by a molecular weight of 73,400 g/mol.

Graphistrength® C10 carbon nanotubes were purchased from Arkema, being their main characteristics: 10-15 nm diameter, 1-10 μm length, 90% purity and 5-15 walls. Clay-nanocomposites were prepared using pristine sodium montmorillonite (NANOFIL 757).

4.1.2. Micromolding equipment

This first-generation prototype Ultrasound Molding Machine (Sonorus®, Ultrasion S.L., Barcelona, Spain) is composed by a digital ultrasound generator (1000 W–30 kHz) and a controller (3010 DG digital system, Mecasonic, Barcelona, Spain). A focused piezoelectric transducer (designed by Mecasonic) converts the high frequency electrical signal produced in the generator in a mechanical oscillation. The acoustic unit (constituted by a booster and a sonotrode) operates in longitudinal vibration and was able to amplify/reduce (i.e., amplitude variable from 43 to 137.5 μm) and transfer the mechanical oscillation to the polymer sample placed in a plasticizing chamber. The equipment is also composed of an electric servomotor control (Berneker and Rainer, Barcelona, Spain) fitted with software from Ultrasion S.L. (Barcelona, Spain), and a mold capable of preparing 8 test specimens of dimensions 1.5 cm × 0.1 cm × 0.1 cm upgraded with an automatic ejection system.

4.1.3. Preparation of nanocomposites

The micromolding equipment was employed to prepare nanocomposites by feeding previously prepared physical mixtures of the appropriate amounts of polymer and reinforcement (Nanofil or MWCNT). For comparison purposes clay nanocomposites were also prepared by solution-intercalation film-casting technique and melt mixing[1]. In the first case, 100 mg of nylon 12 were dissolved in 10 mL of formic acid. In a separated beaker a Nanofil 757 dispersion in formic acid (0.1 wt-%) was prepared and stirred for 30 min. Appropriate volumes of the two preparations (i.e., to get a preparation with 3 wt-% of Nanofil) were mixed and then sonicated for 120 min with a Sonorex Super 10P sonicator. The mixture was finally cast on a glass surface and the solvent was removed in a vacuum oven at 40 ºC. In the second case, nanocomposites containing 3% of Nanofil 757 were prepared by a

two-step melt mixing process using a co-rotating tightly intermeshed twin-screw extruder (DSM Xplore 5 ml microcompounder). The processing temperature, screw rotation and cycle time were 200 ºC, 100 rpm and 3min, respectively.

In the case of PCL/MWCNT nanocomposites prepared by solvent casting, 5 mg of PCL were dissolved in 50 mL of chloroform while 0.25 mg of MWCNTs were dispersed in 2.5 mL of chloroform by sonification for 20 min at 40% of the maximum sonicator energy. Subsequently, solution and dispersion were mixed while ultrasounds were applied for other 10 min at 60% of the energy. The solvent was then evaporated in a Petri dish and the final film dried under vacuum in an oven at 120 ºC.

4.1.4. Measurements

Molecular weight was determined by size exclusion chromatography (GPC) using a liquid chromatograph (Shimadzu, model LC-8A) equipped with an Empower computer program (Waters). The polymer was dissolved and eluted in 1,1,1,3,3,3-hexafluoroisopropanol (HFIP) containing CF_3COONa (0.05 M). The flow rate was 1 mL/min, the injected volume 20 μL, and the sample concentration 2 mg/mL. A PL HFIP gel column (Polymer Lab Agilent Technologies Deutschland GmbH, Böblingen, Germany) and a refractive index detector (Shimadzu RID-10A, model LC-8A, Tokyo, Japan) were employed. The number and weight average molecular weights were determined using polymethyl methacrylate standards.

Calorimetric data were recorded by differential scanning calorimetry using a TA instrument Q100 series (TA instruments, New Castle, DE, USA) equipped with a refrigerated cooling system operating from −50 ºC to 300 ºC. Experiments were performed at heating rates of 10 ºC/min and cooling rates from 2.5 to 10 ºC/min with a sample weight of 5 mg and under a flow of dry nitrogen. The instrument was calibrated for temperature and heat of fusion using an indium standard. Tzero technology required two calibrations, with empty pans and sapphires discs.

A Philips TECNAI 10 electron microscope (Philips Electron Optics, Eindhoven, The Netherlands) was used and operated at 80 kV and 100kV for the bright field mode. Specimens were cut in small sections at room temperature using a Sorvall Porter-Blum microtome equipped with a diamond knife. These sections were collected in a trough filled with water and lifted onto carbon coated copper grids. Bright field micrographs were taken with a SIS MegaView digital camera.

Focused Ion Beam Zeiss Neon40 microscope (Zeiss, Oberkochen, Germany) operating at 5 kV was used to obtain SEM micrographs of micromolded specimens. Samples were mounted on a double-side adhesive carbon disc and sputter-coated with a thin layer of carbon by using a Mitec K950 Sputter Coater (Quorum Technologies Ltd., Ashford, UK).

Tensile deformation tests were performed using the Universal Testing Machine Zwick Z 2.5 equipped with a cell charge of 100 N and testXpert 8.1 software. Gauge length was 5 mm and test

crosshead speed was 1 mm/min, fifteen tensile probes (1.5 x 0.1 x 0.1 cm^3) were tested for each processing condition. The width of each one of them was accurately measured with width measurement equipment Uno-Check Fe.

Combined SAXS (small angle X-ray scattering) and WAXD (wide angle X-ray diffraction) experiments were carried out in the Non Crystalline Diffraction beamline, BL-11, at ALBA synchrotron light source (www.albasynchrotron.es). Polymer samples were confined between Kapton films and then placed on a Linkam hot stage with temperature control within ± 0.1 ◦C. Diffraction profiles were acquired during heating and cooling runs in time frames of 10 s and rates of 10 and 5 ºC/min.

The energy of the incident photons was 12.4 keV or equivalently a wavelength, λ, of 0.1 nm. The SAXS diffraction patterns were collected by means of a photon counting detector ImXPAD S1400 (ImXPAD, La Ciotat, France) with an active area of 152 × 149.6 mm^2, an effective pixel size of 130 × 130 μm^2 and a dynamic range of 32 bits. The sample-to-detector distance was set to 6163 mm, resulting in a q range with a maximum value of $q = 2\ nm^{-1}$.

WAXS diffraction patterns were collected by means of a 3 CCD detector Rayonix LX255-HS (Rayonix LLC, Evanston, IL, USA) with an active area of 85 × 255 mm^2, an effective pixel size of 44 × 44 μm^2 and a dynamic range of 16 bits. In this case, the sample-to-detector distance was set to 225 mm, corresponding to a maximum q value of 62 nm^{-1}. This detector was tilted with a pitch of 29.8º.

The data reduction was treated by pyFAI python code (ESRF), modified by ALBA beamline staff,that is able to do on-line azimuthal integrations from a previously calibrated file. The calibration files were created from well-known standards, i.e., silver behenate (AgBh) and Cr_2O_3 for SAXS and WAXS respectively.

WAXD peaks were deconvoluted with the PeakFit v4 program by Jandel Scientific Software (V 4.0). The correlation function and corresponding parameters were calculated with the CORFUNC program for Fiber Diffraction/Non-Crystalline Diffraction provided by Collaborative ComputationalProject 13 (CCP13) (Chester, UK).

Characteristic lamellar parameters (i.e., long period, L_γ, amorphous layer thickness, la, and crystalline lamellar thickness, l_c) and crystallinity (i.e., crystallinity within lamellar stacks,$X_c^{SAXS} = l_c / L_\gamma$) were determined by the normalized one-dimensional correlation function[2], γ(r):

$$\gamma(\mathrm{r}) = \int_0^\infty q^2 I(q) \cos(q \cdot r)\, dq \Big/ \int_0^\infty q^2 I(q)\, dq \qquad (1)$$

where I (q) is the intensity at each value of the scattering vector (q = 2π/d, where d is the Bragg spacing). SAXS data were collected within a limited angular range, with application of the Vonk's model[3] and Porod's law to perform extrapolations to low and high q values.

4.2. Preparation of Nanocomposites of Poly(ε-caprolactone) and Multi-Walled Carbon Nanotubes by Ultrasound Micro-Molding. Influenceof Nanotubes on Melting and Crystallization

4.2.1. Introduction

The use of an ultrasonic source has been proposed as an alternative and effective processing method to prepare micro-molded pieces. The process may offer advantages over conventional micro-injection techniques and even may be highly interesting to obtain nanocomposites with good dispersion of nanoparticles [4-6]. The technology allows plasticization of the material and direct injection of the molten material [7-9]. Micro-molding equipment is simple and requires only a plasticizing chamber, a controller, an ultrasonic generator to produce high frequency (30 kHz) from line voltage, a resonance stack or acoustic unit connected to the generator and a mold. The main element is the acoustic unit, which consists of: (a) a converter (piezoelectric transducer), where high frequency signals from the generator are transmitted through piezoelectric crystals that expand and contract at the same rate as electrical oscillation; (b) a booster, which amplifies or reduces mechanical oscillation (from 0 to 137.5 μm); and (c) a sonotrode, which transfers this oscillation to the polymer sample placed in the plasticizing chamber by applying a force (from 0 to 3500 N).

Ultrasonic waves have physical effects on the melt rheology of the polymer, facilitating the injection process, but also have chemical effects that could lead to polymer chain degradation. This is the result of cavitation and the possible high temperature inside the plasticizing chamber [10-13]. Therefore, processing parameters must be optimized in order to obtain minimally degraded samples. It was demonstrated that polylactide can be easily micro-molded [14], and so can other polyesters such as poly(butylene succinate)[4] and poly(nonamethylene azelate)[6], although in these cases the processing window was narrower.

Ultrasound technology was recently proven to be particularly interesting due to its ability to render exfoliated clay nanocomposites even when inorganic polar clays were mixed with apolar polymers (e.g., polylactide)[4]. This feature is significant since more expensive organo-modified clays must usually be employed to improve compatibilization with the organic polymer matrix when conventional processing techniques are applied (e.g., solvent casting, melt mixing or in situ polymerization). Furthermore, it should be considered that the use of an organo-modifier compound can have a negative effect on the thermal stability of the final nanocomposite because it may enhance thermal decomposition. Being that said, typical nanocomposites should have better properties (e.g.,

barrier, physical, chemical, and mechanical properties) than those attained with conventionally filled composites [15-17].

Nanocomposites incorporating multi-walled carbon nanotubes (MWCNTs) are being widely studied because good conductive properties can be achieved, in addition to the typical advantages derived from the high surface to volume ratio of the reinforcing phase. It is, however, well-known that this kind of nanocomposites has serious problems concerning the high agglomeration trend of carbon nanotubes.

Poly(ε-caprolactone) (PCL) is a degradable and biocompatible polymer that is being widely employed as an implantable biomaterial. The main limitations of PCL are a consequence of its relatively poor mechanical and thermal properties, which justifies the recent intensive work on the preparation of composites with different nanofillers[18, 19].

The present study has two main goals: (a) The evaluation of the suitability of ultrasound technology to produce micro-molded nanocomposites of MWCNTs and poly(ϵ-caprolactone) as a polymer matrix, insisting on their ability to keep adequate dispersion of nanotubes and an unaltered polymer molecular weight after processing, and (b) The evaluation of the influence of MWCNTs on the melting and crystallization processes as well as on the derived morphology.

4.2.2. Results and Discussion

4.2.2.1. Ultrasound Micro-Molding of PCL and PCL/MWCNT Nanocomposites

Processing parameters (i.e., amplitude, force and time) were optimized to obtain appropriate melt rheology and minimum degradation of polymer chains. The first point was evaluated by optical inspection of the morphology of the specimens (i.e., sprue and eight test specimens obtained after processing, as shown in **Fig. 4-1b** for some representative micro-molded pieces) and considering the ability of the polymer to completely fill the mold cavities. The second point was quantitatively determined through GPC measurements, as shown in **Fig. 4-2** and **Table 4-1** for some selected cases.

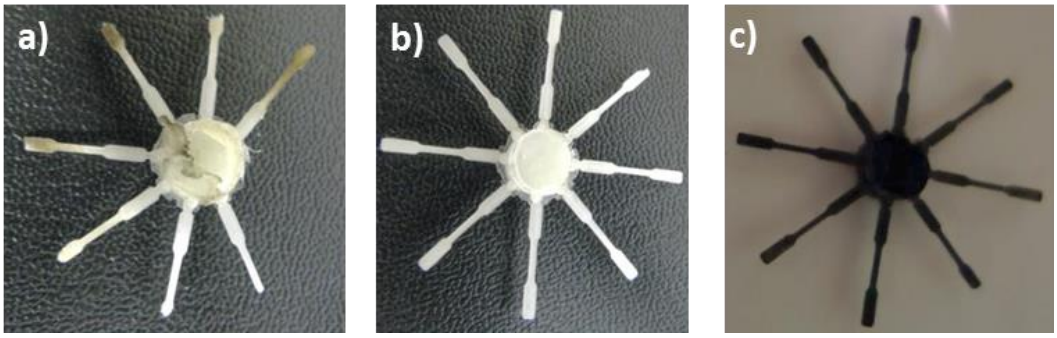

Fig. 4-1. *Micro-molded pieces of PCL (**a** and **b**) and PCL/MWCNT-5 (**c**) specimens processed under optimized (**b** and **c**) and non-optimized (**a**) processing conditions.*

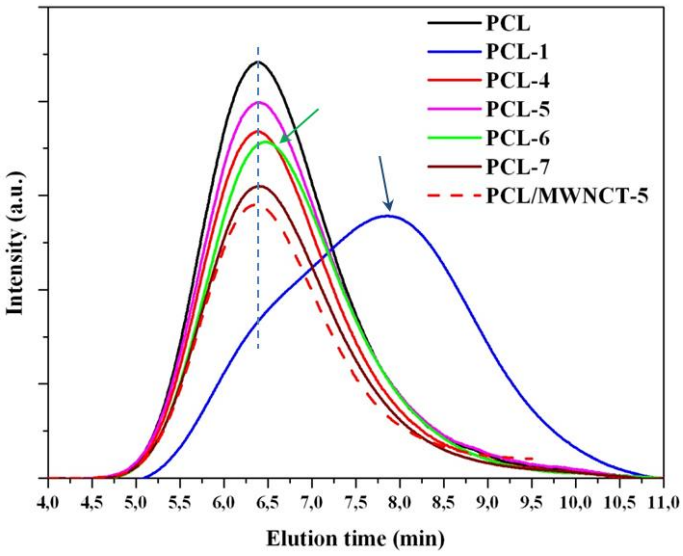

Fig. 4-2. *GPC molecular weight distribution curves determined for selected micro-molded PCL and PCL/MWCNT-6 specimens.*

The optimization process started considering a relatively high force of 2000–2500 N despite the fact that previous works indicated that degradation of polyesters such as polylactide could be significant when a high force/pressure was applied even if the energy/amplitude was kept at a low level[14]. It was specifically suggested that chain scissions were enhanced by high mechanical shear stresses generated under a high force which, however, facilitated melt flow and complete filling of the mold cavities. A low force was also demonstrated ineffective[14] since it was not enough to reduce the melt viscosity of the polymer. On the other hand, the applied ultrasonic oscillations led to slight or significant polymer degradation. This effect could be observed upon comparison of the molecular weight of samples PCL-2 and PCL-3 or PCL-5 and PCL-7 (**Table 4-1**). Data demonstrate a significant molecular weight decrease (i.e., from 56,700 g/mol to 47,000 g/mol and from 57,500 g/mol to 47,400 g/mol), although the force was minimally varied from 2500 N to 2000 N.

Table 4-1. *Influence of micro-molding processing parameters on sample molecular weight.*

Sample	Molding[b]	Efficiency[c] (%)	M_n (g/mol)	M_w (g/mol)	PDI
PCL	Raw	-----	58,100	128,900	2.2
PCL-1	43-2000-6	60	5,900	49,200	8.4
PCL-2	37-2000-6	70	47,00	120,100	2.6
PCL-3	37-2500-6	80	56,700	127,300	2.2
PCL-4	**37-2500-8**	100	58,100	128,900	2.2
PCL-5	37-2500-7	100	57,500	128,100	2.2
PCL-6	37-2500-9	80	37,100	116,400	3.1
PCL-7	37-2000-7	100	47,400	127,100	2.7
PCL/MWCNT-5	37-2500-8	100	58,000	128,000	2.2

(a) Optimized conditions use in this work is highlighted.
(b) Micro-molding conditions: Amplitude (μm), Force (N) and Time (s)
(c) Mold filling, qualitative evaluation (i.e. 8 half pieces or 4 full corresponded to 50%. –Ovl- Sonotrode overload

Amplitude/energy played a relevant role in the degradation process of PCL. It was thus determined that amplitude could not exceed a value of 43 μm. Note that the GPC curve of samples processed at this amplitude (sample PCL-1 in **Fig. 4-2)** shows a shift of the peak to clearly higher retention times than those observed for the neat PCL sample. Nevertheless, a shoulder corresponding to the initial population of PCL chains could still be observed. Obviously, the generation of small polymer fragments led to a high decrease of the number average molecular weight (i.e., from 58,100 g/mol to 5900 g/mol) and an increase of the polydispersity index (from 2.2. to 8.4), as summarized in **Table 4-1**.

Optimization of processing time was also fundamental despite the short time required to perform ultrasound micro-molding. Note that this, together with the high material saving associated with this process (i.e., the efficient dosage precision allows the large amount of material usually rejected in conventional processing techniques to be reduced[7]), is probably the greatest advantage of the micro-molding technique over conventional micro-injection. In this way, assays performed for 9 s and keeping optimal amplitude and force (sample PCL-6 in **Table 4-1**) gave rise to processed specimens with a yellow/brown coloration (**Fig. 4-1a**) indicative of degradation, a slight shift of the GPC curve (**Fig. 4-2**) and a significant decrease of the molecular weight (Mn = 37,100 g/mol, **Table 4-1**). By contrast, short test times led to deficient filling of the mold (e.g., 6 s was insufficient, as indicated in **Table 4-1** for samples PCL-2 and PCL-3). Times of 7 s and 8 s appeared ideal; specifically, complete filling of the mold and a molecular weight identical to that determined for the neat polyester were obtained with amplitude and force values of 37 μm and 2500 N, respectively (sample 4 in **Table 4-1** and **Fig. 4-2).** These optimized conditions were also satisfactory for processing the nanocomposite (**Table 4-1** and **Fig. 4-1c** and **Fig. 4-2**). In summary, the new ultrasound technology was suitable to produce micro-pieces with minimum degradation and high processing speed of both PCL and its nanocomposite with a large ratio of MWCNTs (i.e., up to 5 wt %). Furthermore, it was demonstrated[14] that micro-pieces with high precision details (e.g., around 50–100 μm) can be well molded. By contrast, conventional micro-injection techniques require the application of very high pressures[20].

The morphology of PCL and PCL/MWCNT samples processed under optimized conditions was observed by scanning electron microscopy (SEM). **Fig. 4-3a** is a micrograph of a transverse section of a PCL specimen showing the high homogeneity of the material and lack of pores and cracks. **Fig. 4-3b** shows the outer surface of the PCL/MWCNT-5 sample (see external marks used for numbering the pieces). A smooth and relatively homogeneous surface can be observed, although a few small pores may be detected. Note that loaded MWCNTs can be clearly observed in the enlarged image of a specific pore.

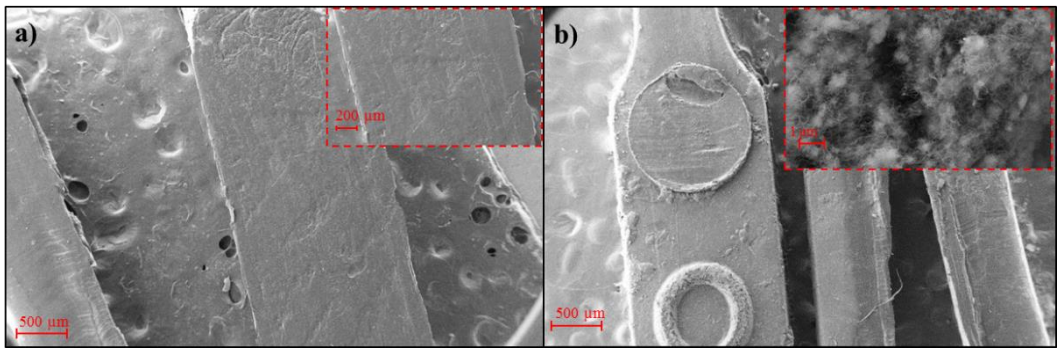

Fig. 4-3. *SEM micrographs showing details of micro-molded PCL (**a**) and PCL/MWCNT-5 (**b**) specimens. Magnifications are given in the insets.*

In order to evaluate the ability of ultrasounds to disaggregate MWCNTs into powder and render homogeneous dispersion in the final micro-molded specimen, direct molding of PCL and MWCNT powder mixtures without using solvent casting nanocomposite films was assayed. Results were promising although more effort is required to optimize conditions. That being said, well-formed micro-pieces without evidence of degradation were obtained using the above processing parameters. TEM images reveal the existence of zones where MWCNTs were well dispersed inside the PCL matrix (**Fig. 4-4**), but unfortunately some aggregates (not shown) were also detected, as expected from the inherent difficulty of dispersing nanotubes at loads as high as 5 wt %.

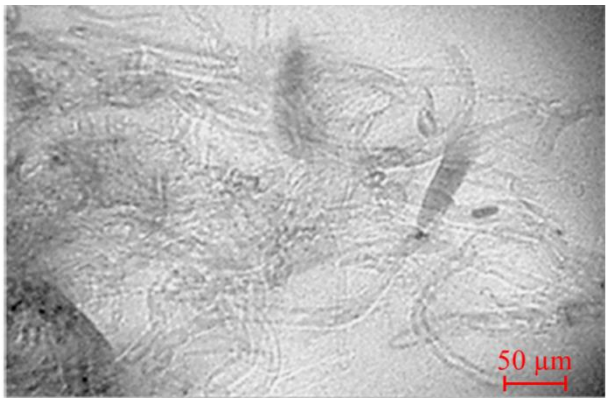

Fig. 4-4. *TEM micrograph showing dispersion of MWCNTs in the PCL nanocomposite incorporating5 wt % of nanotubes.*

4.2.2.2. Thermal Properties of PCL/MWCNT Nanocomposites

Incorporation of carbon nanotubes had a significant influence on both melting and crystallization processes, as shown in **Fig. 4-5**, where the sequence of heating-cooling-reheating scans performed with PCL (solid lines) and PCL/MWCNT-5 (dashed lines) samples is displayed. Incorporation of nanotubes increased the melting and corresponding crystallization temperatures of solvent casting films. By contrast, the influence on the melting temperature of melt crystallized samples was low (1–2 °C), which may be indicative of different molecular arrangements of the nanocomposite that depend on the way it is prepared (i.e., by solvent casting or from the melt).

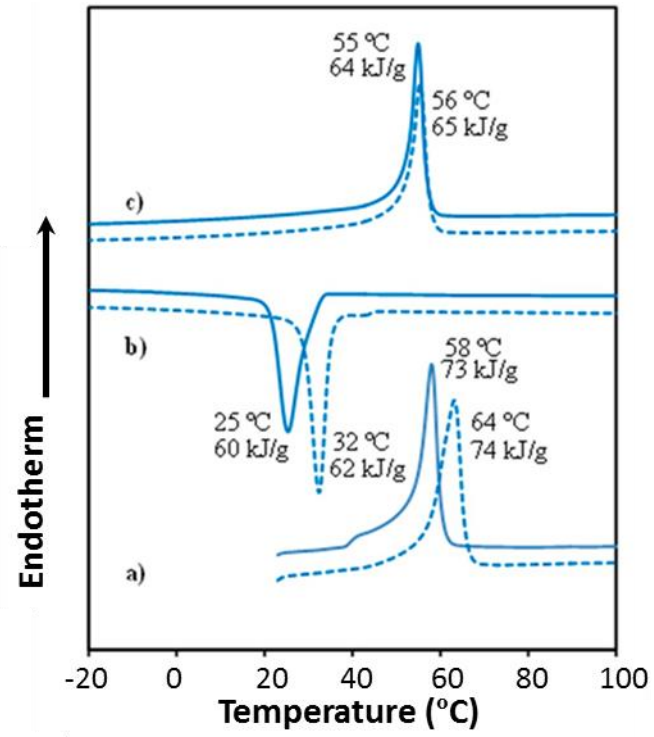

Fig. 4-5. *DSC scans performed with PCL (solid lines) and PCL/MWCNT-5 specimens (dashed lines): (**a**) Heating of solvent casting films; (**b**) Cooling from the melt state and (**c**) Heating of melt crystallized samples.*

It should also be pointed out that the crystallization peak is clearly narrower for the nanocomposite, indicating a faster crystallization process and suggesting an enhanced nucleation effect when nanotubes were incorporated. Finally, melting and crystallization enthalpies were rather similar for the two samples, with slightly higher values for the nanocomposite. Note that enthalpies of nanocomposites for the first heating, cooling and second heating runs were 79, 65 and 68 kJ/g if the 5 wt % content of MWCNT is considered.

4.2.2.3. Melting and Crystallization of PCL and PCL/MWCNT-5 Nanocomposites from Time-ResolvedWAXD Experiments

In order to study in detail the influence of these nanoparticles in the melting and crystallization processes, time-resolved WAXD profiles of the nanocomposite having 5 wt % of MWCNTs were taken during a heating-cooling-reheating sequence (**Fig. 4-6**). Diffraction profiles of the neat polyester werealso taken for comparative purposes.

The first heating run was performed with solvent casting samples to start with materials crystallized at the same temperature (i.e., room temperature) and avoid any effect attributable to differences in the initial morphology (e.g., variation in lamellar thickness) that could be expected if samples were non-isothermally processed from the melt state (e.g., by injection or micro-molding).

X-ray diffraction profiles showed an amorphous halo centered at 0.418 nm and four diffraction peaks at 0.417, 0.404, 0.375 and 0.367 nm. These are indexed as (110), (111), (200) and (201)

reflections of the rectangular unit cell, with a = 0.748 nm, b = 0.498 nm and c = 1.726 nm, as postulated for poly(ε-caprolactone)[21-23]. The X-ray diffraction profile of the initial PCL sample was peculiar since the intensities of (110) and (200) reflections were very similar, in contrast with the clear predominance of the (110) reflection in the profile of the nanocomposite (see also the 2D-diffraction patterns in the insets of **Fig. 4-6**) as well as in the profiles of the PCL and nanocomposite obtained at 25 ◦C of samples cooled from the melt state (see cooling runs in **Fig. 4-6**). Differences in the packing mode of PCL chains and even the molecular conformation (all trans and non-planar conformations have been proposed in the literature for PCL[22]) are thus observed depending on the preparation method and the incorporation of MWCNTs. In any event, a high intensity of the (200) reflection indicates that the average plane defined by the methylene carbon atoms of a molecular chain tends to be parallel to the ac crystallographic plane.

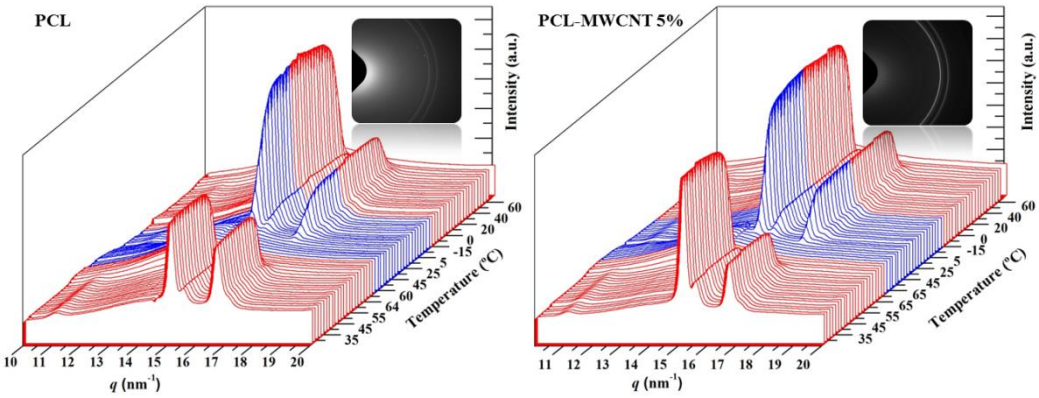

Fig. 4-6. *Three dimensional representations of WAXD profiles of PCL (**a**) and the PCL/MWCNT-5 nanocomposite; (**b**) during a sequence involving heating (red), cooling (blue) and subsequent heating(red) runs performed at a rate of 5 °C/min. Insets show the corresponding 2D diffraction patterns taken at room temperature.*

Significant differences were detected in the evolution of the WAXD profiles of the nanocomposite and the pristine polymer because the decrease in the intensity of the four Bragg peaks (i.e., the beginning of fusion) started at a higher temperature for the nanocomposite (i.e., 63 °C versus 52 °C). This suggests differences in the lamellar morphology and the associated recrystallization process, which are discussed in the next section.

The subsequent cooling runs of the two samples were also very different because the crystallization of the nanocomposite started at a higher temperature (60 ºC as opposed to 51 ºC) and ended at a higher temperature too (15 ºC as opposed to −3 ºC). The plot of the intensity of the strongest peak versus temperature (**Fig. 4-7,** blue lines) clearly shows the lower supercooling needed for the nanocomposite (see dashed double arrow) and the faster crystallization process, which could also be deduced from the higher slope of the linear representation.

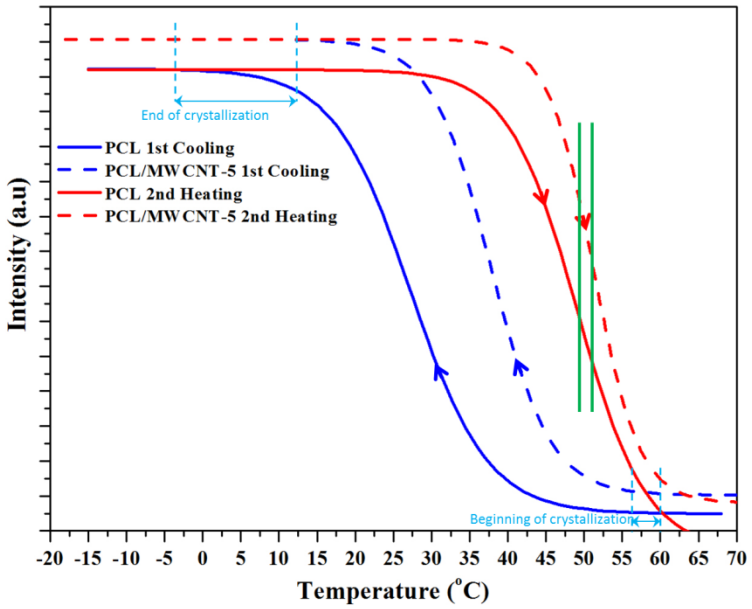

Fig. 4-7. *Variation in intensity of the main WAXD reflection during cooling (**blue**) and the subsequent heating (**red**) runs performed at a rate of 5 °C/ min for PCL (**solid lines**) and the PCL/MWNCT-5 nanocomposite (**dashed lines**).*

This faster crystallization rate is a consequence of the nucleation induced by the nanoparticles, as also revealed by optical microscopy micrographs taken during isothermal crystallization at a given temperature. Specifically, **Fig. 4-8** shows that PCL crystallizes at 48 ◦C, giving rise to large negatively birefringent spherulites with a mean diameter of 50 μm and a low nucleation density (i.e., 800 nuclei/mm2). By contrast, MWCNTs prevented the growth of PCL in large size spherulites (**Fig. 4-8b**) due to their strong nucleating effect. On the other hand, the nanocomposite sample was highly crystalline, as evidenced by its strong overall birefringence. The morphology of nanocomposites loaded with different MWCNT percentages was always similar even for a minimum load of 0.5 wt % (not shown). It has been reported that the high nucleation effect of MWCNTs can lead to peculiar morphologies; specifically, nanohybrid shish-kebab structures with CNTs as shish and polymer crystals as kebab have been reported for polyethylene and nylon 66 based nanocomposites[24].

The crystalline structures of PCL and the nanocomposite were similar when samples were crystallized from the melt. Therefore, minimum differences in the melting temperature should be expected, as shown in the DSC profiles recorded during the second heating run (**Fig. 4-5**). Nevertheless, it is also highly interesting to point out that melting started at a significantly higher temperature for the nanocomposite (i.e., 37 ºC versus 32 ºC, see **Fig. 4-7**). Finally, the plot of the evolution of the intensity of the main reflection during heating (**Fig. 4-7**) also shows a higher slope for the nanocomposite, indicating a more homogeneous lamellar population that undergoes the melting process. In any event, the temperature corresponding to the maximum slope (see green lines in **Fig. 4-7**) was similar (difference lower than 2 ºC) for both samples, in agreement with the identical melting peak temperature observed in the DSC scan.

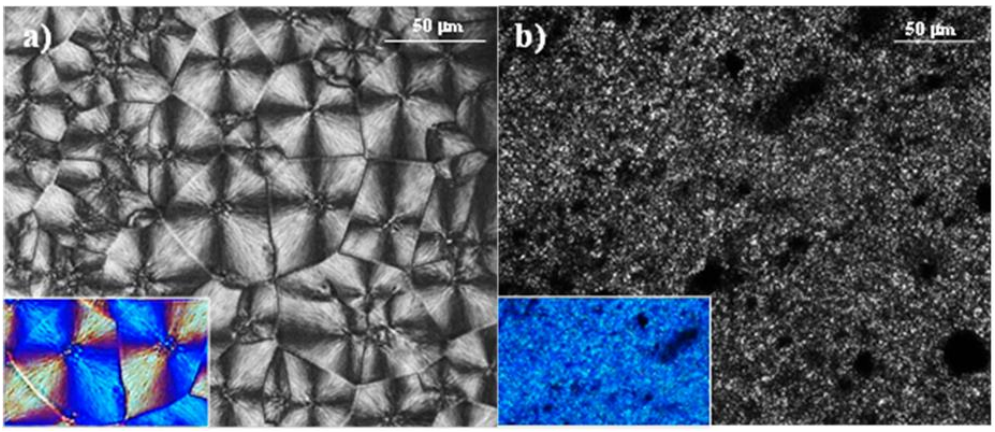

Fig. 4-8. *Polarized optical micrographs of PCL (**a**) and PCL/MWCNT (**b**) samples crystallized fromthe melt state at 48 ºC.*

Deconvolution of X-ray diffraction profiles (**Fig. 4-9**) allowed sample crystallinity, χ_c^{WAXD}, to be accurately estimated by measuring the intensity of Bragg reflections and the amorphous halo. Results indicate a higher degree of crystallinity for the nanocomposite probably as a consequence of enhanced nucleation, which even favors the development of solvent casting crystals. Thus, χ_c^{WAXD} values of 40% and 50% were determined for the initial PCL and PCL/MWCNT-5 samples, respectively. A slight increase was found when samples crystallized from the melt but the higher value was still observed for the nanocomposite. Thus, crystallinities of 42% and 51% were determined at room temperature (before end of the crystallization process) for PCL and PCL/MWCNT-5 samples, respectively. These crystallinities increased to 47% and 53% at the end of the crystallization process. **Fig. 4-9** also shows the profiles obtained with melt-quenched samples, with the expected significant decrease of χ_c^{WAXD}. Again, a higher value was determined for the nanocomposite (i.e., 38% versus 23%).

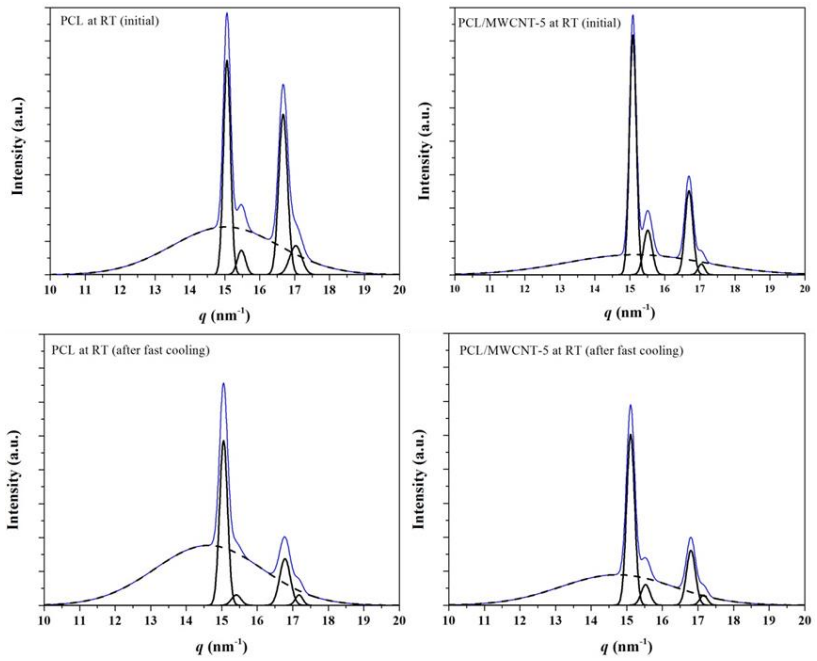

Fig. 4-9. *Deconvoluted X-ray diffraction profiles of PCL (**a**,**c**) and PCL/MWNCT-5 (**b**,**d**) samples takenat room temperature at the beginning of the heating process (**a**,**b**) and after being cooled from the meltstate at the maximum rate allowed by the equipment (50 ºC/min) (**c**,**d**).*

Some contradictions are found between DSC melting enthalpies and the calculated χ_c^{WAXD} values. They can be explained by the fact that the high melting enthalpies observed for the solvent casting films and specifically for the PCL sample are due to an enhanced hot crystallization process during heating and to an energetically more favorable molecular arrangement in the peculiar PCL structure. Otherwise, neither the above crystallinities of 40% and 50% nor the higher crystallinities determinedfor the melt crystallized samples can be justified.

4.2.2.4. SAXS Analysis of the Melting Crystallization of PCL and PCL/MWCNT Nanocomposites

Time-resolved SAXS profiles of the neat PCL sample taken during the heating-cooling-reheatingsequence (**Fig. 4-10)** are clearly different from those acquired for the nanocomposite sample. Analyses could be easily performed using the plots in **Fig. 4-11**, which show the evolution of intensity (Iq2) and the corresponding value of the q scattering vector of the SAXS peak during the heating and cooling processes for both samples.

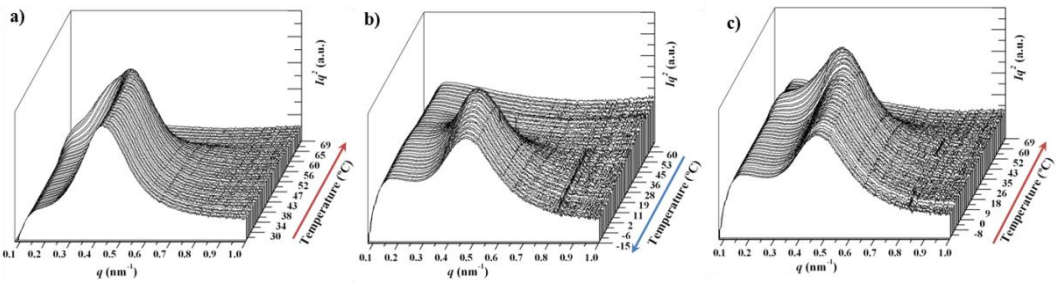

Fig. 4-10. *Three dimensional representations of PCL SAXS profiles taken during first heating (**a**),cooling; (**b**) and second heating and (**c**) runs performed at a rate of 5 °C/min.*

Fig. 4-11a reveals differences between profiles taken during the first heating. PCL showed a practically of intensity at temperatures higher than 32 °C and a slight decrease of *q* from 52 °C until the beginning of fusion (63 °C) was characteristic of the nanocomposite (see blue arrows in **Fig. 4-11a**). The increase observed for the peak intensity can be associated with the higher contrast between the electron density of the crystalline and amorphous phases. It seems that a lamellar reorganization took place, leading to an increase in the lamellar thickness, as demonstrated by the decrease of the scattering vector, and in the chain mobility of the amorphous phase, resulting in a lower density and higher contrast. These morphological changes were very important above 52 °C (see red line in **Fig. 4-11a** which corresponds to the beginning of fusion for the neat PCL). Thus, the nanocomposite underwent recrystallization and expansion at the temperature at which the neat polymer melted. constant value of intensity and *q* until the beginning of fusion at 52 °C, while a significantincrease

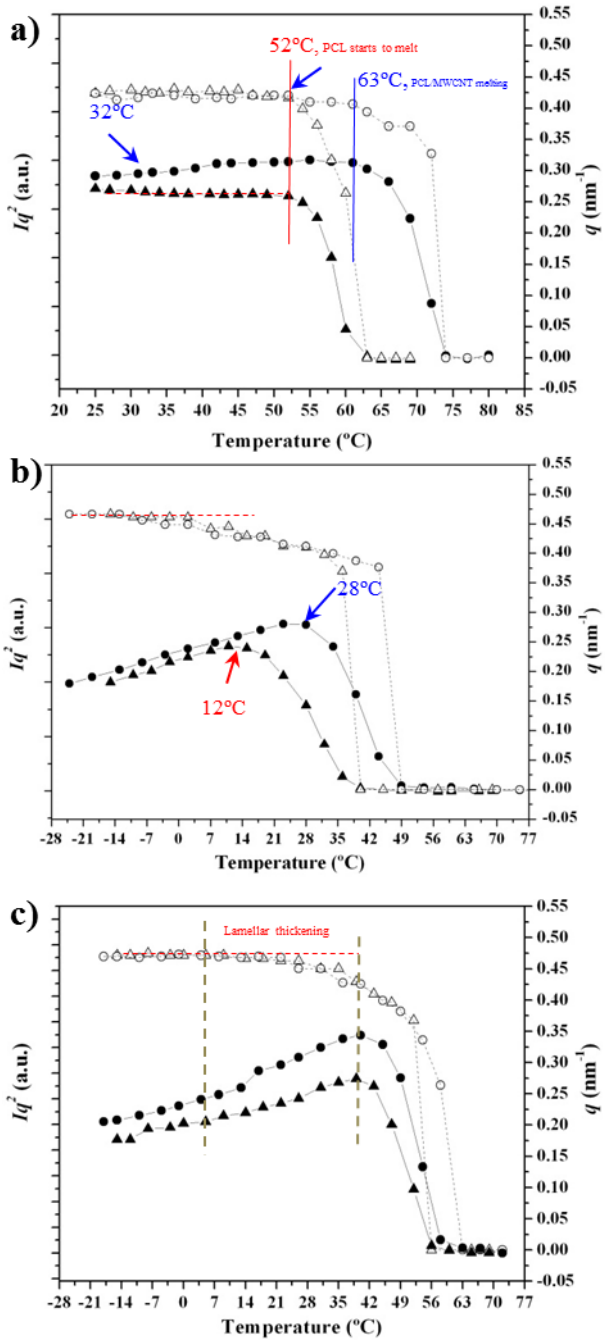

Fig. 4-11. *Variation in intensity (Iq^2) (full symbols) and scattering vector (q) (empty symbols) of the SAXS peak observed in the diffraction profiles taken during the first heating run (5 ºC/min) (**a**), the subsequent cooling run from the melt state (5 ºC/min); (**b**) and the second heating run and (**c**) of PCL(⊿, triangles) and PCL-MWCNT-5 nanocomposite (O, circles).*

The evolution of intensity and *q* during cooling for both samples can be seen **Fig. 4-11b**. The intensity data clearly show that the nanocomposite started to crystallize at a higher temperature (52 °C as opposed to 42 °C), leading to densification of the amorphous phase (as deduced from the decrease in peak intensity) at a higher temperature (28 °C as opposed to 12 °C, see blue and red arrow in **Fig. 4-11b**). This compaction process was more evident for the nanocomposite. Both samples showed an increase of q at lower temperatures, which could be attributed to the decrease of the crystallization temperature. This results in thinner lamellae and a typical lamellar insertion

mechanism once crystallization has proceeded extensively (e.g., temperatures lower than 28 and 12 °C associated with the maximum intensity). In this case, lamellae crystallized in the confined space between the previously formed lamellae. *q* values were logically practically constant at temperatures lower than 10 °C, coinciding with the endof the crystallization process.

Fig. 4-11c shows the evolution during the subsequent heating process. As can be seen, the most interesting characteristics were the intensity increase, which reached a maximum value at a similar temperature for both samples (i.e., 39 ºC), a clear recrystallization process (lamellar thickening) that also occurred at a similar temperature for both samples (note the evolution of q between 7 and 39 ºC) and a melting process that was also similar for both samples (i.e., melting temperature of 63 versus 61 ºC). In this way, the influence of carbon nanotubes was different depending on the way the nanocomposites were obtained (i.e., solvent casting or melt crystallization).

Morphological lamellar parameters were analyzed by the correlation function that corresponds to the Fourier transform of the SAXS profile. Representative profiles and the corresponding correlation functions are shown in **Fig. 4-12**. It can be observed that profiles taken at room temperature of the initial sample (i.e., that obtained by solvent casting) and after melt crystallization are similar with respect to the value of the scattering vector associated with the peak but clearly different with respect to peak width (**Fig. 4-12a**), which is indicative of a broader lamellar distribution.

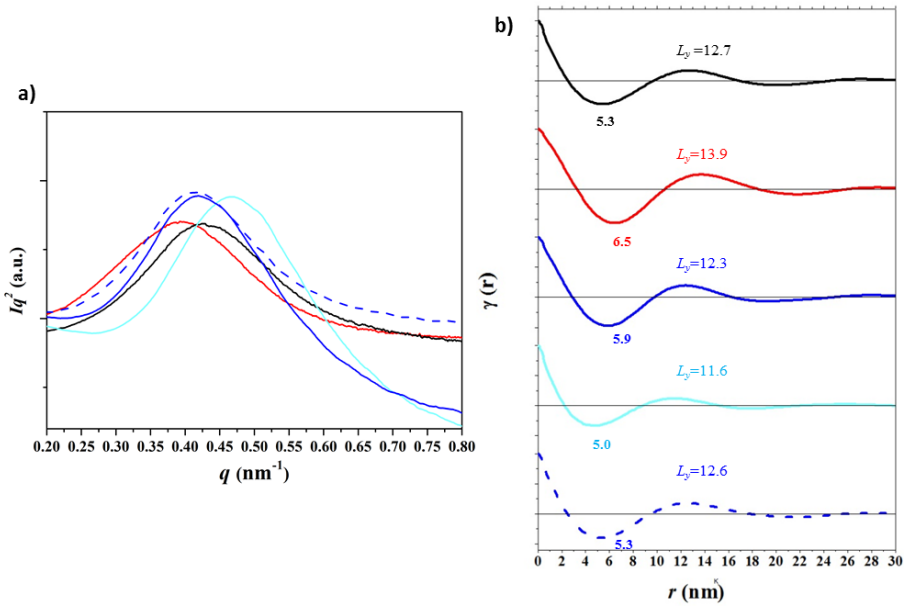

Fig. 4-12. *SAXS profiles (**a**) and corresponding correlation functions (**b**) for initial PCL (**black**), PCL heated to 55 ºC (**red**), non-isothermally crystalized PCL at 25 ºC (**blue**) and −10 ºC (**light blue**). For the sake of completeness, the correlation function of the non-isothermally melt crystallized nanocompositeat 25 ºC (**blue dashed line**) is shown.*

In fact, discrepancies between the L_γ value (derived from the first maximum of the correlation function) and the long period, L_γ^m (determined by doubling the value of the first minimum of the correlation function) are informative about the distribution of the layer widths of the major component. This was assigned to crystalline layer thickness in a typical two-phase lamellar model

although the correlation function cannot distinguish the thickness associated with each phase (i.e., amorphous and crystalline). This feature is explained below and has been well reported for other polymers [25-27].

Broader lamellar distributions are associated with L_γ values clearly larger than L_γ^m long period[28]. The latter are representative of the most probable distance between the centers of gravity of a crystal and its adjacent amorphous layer whereas the former are associated with the most probable distance between the centers of gravity of two adjacent lamellar crystals. Obviously, the two parameters should be practically identical for a regular distribution, as observed at room temperature for the partially melt crystallized sample (i.e., 12.3 nm and 11.9 nm). By contrast, L_γ and L_γ^m spacings of 12.7 nm and 10.6 nm, respectively, were determined for the more irregular solvent casting sample prepared. Interestingly, lamellar distribution broadened at the end of melt crystallization (i.e., at −15 ºC) since different and lower spacings were found (i.e., 11.6 nm and 10 nm). This is a clear indication of an irregular distribution caused by the lamellar insertion process. Finally, the function determined at 55 ºC supports again a relatively broad distribution caused, in this case, by the lamellar thickening process (i.e., L_γ and L_γ^m spacings increased to 13.9 nm and 13 nm, respectively).

Similar features were observed for the nanocomposite sample, although the analysis was more difficult because the scattering of MWCNTs had to be separated from the scattering contribution due to PCL crystallization (**Fig. 4-13**)[29]. In general, lamellar distributions were more irregular. For example, L_γ and L_γ^m spacings of 12.6 nm and 10.3 nm were respectively determined for a PCL/MWCNT-5 melt crystallized sample by the correlation function at 25 ºC (dashed line in **Fig. 4-12**).

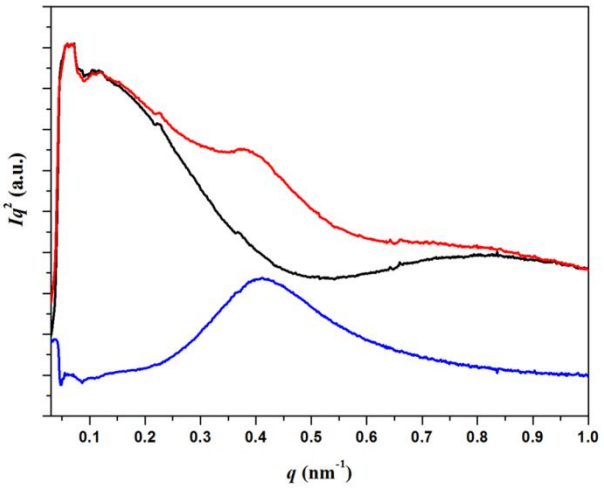

Fig. 4-13. *SAXS diffraction profiles of PCL/MWCNT-5 specimens taken at room temperature (**red**)and after fusion (**black**). The diffraction profile obtained after subtraction is indicated by the blue line.*

Analysis of the evolution of L_γ, l_c and l_a morphological parameters during heating and cooling scans for the neat PCL and the nanocomposite samples by the correlation function revealed significant differences between the two samples, as displayed in **Fig. 4-14a**. Crystallinity within lamellar stacks, X_c^{SAXS}, was easily calculated as l_c/L_γ and allowed the thickness associated with each phase to be

assigned. The derived crystallinities should always be greater than the crystallinity deduced from WAXD data (X_c^{WAXD}) because samples should always contain amorphous-rich domains that are not considered in the simple lamellar biphasic model associated with the correlation function analysis.

Specifically, X_c^{SAXS} values of 64% and 72% were determined for the solvent casting samples of thenanocomposite and the neat PCL, respectively.

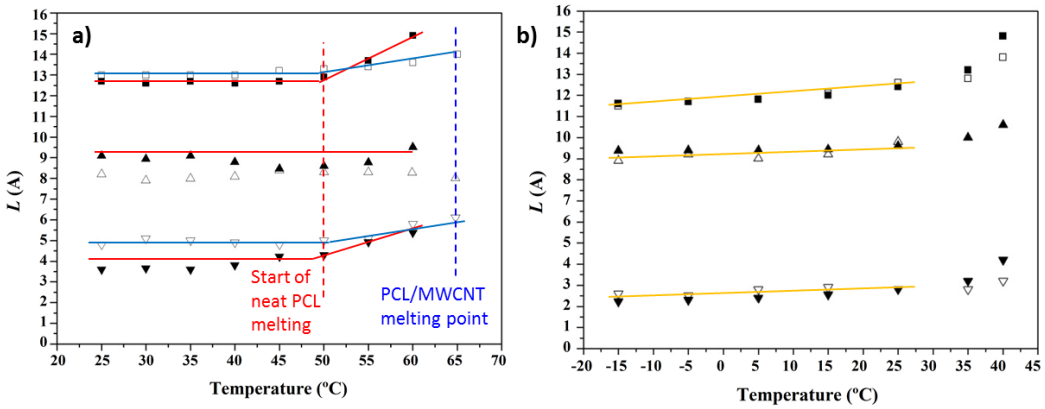

Fig. 4-14. *Plots showing the variation of the long spacing (■) and the crystalline (▲) and amorphous (▼) layer thicknesses of PCL (full symbols) and PCL/MWCNT-5 (empty symbols) during the first heating run (5 ºC / min) (**a**) and the subsequent cooling run (5 ºC / min) (**b**).*

Basically, the three morphological parameters remained practically constant up to the temperature at which the neat PCL started to melt (i.e., 52 ºC, dashed red line). At higher temperatures, the amorphous lamellar thickness of the neat PCL increased drastically as a consequence of the fusion, whereas a moderate change was observed for the nanocomposite because only a reordering process occurred in the temperature interval between 52 and 63 ºC (between dashed lines). Samples crystallized from solution according to slightly different morphologies. Specifically, the presence of MWCNTs led to crystals with greater and lower amorphous and crystalline layer thicknesses, respectively. Nanoparticles seem to have a nucleating effect, as previously indicated, but also influence the degree of perfection of lamellae. Probably, lamellae with the greatest amorphous contribution are more susceptible to undergoing reordering, leading to a higher melting point. Note also that the lower X_c^{SAXS} crystallinity determined for the nanocomposite is not in contradiction with its higher X_c^{WAXD} crystallinity because nucleation resultsin more but more imperfect crystals.

The evolution during cooling (**Fig. 4-14b**) shows the initial formation of thicker lamellae for the nanocomposite because of the nucleation effect and the higher temperature at which crystallization started. Nevertheless, the subsequent evolution was similar for both samples, with similar values of L_γ, l_c and la at low temperatures. This explains the similar behavior during the subsequent heating run. A similar X_c^{SAXS} crystallinity around 78% was determined for both samples, which was logically higher than that observed for solvent casting samples.

4.2.3. Conclusions

It was demonstrated that ultrasound micro-molding is a suitable technology to process poly(ε-caprolactone) as well as its nanocomposite with MWCNTs, even for high loads (e.g., 5 wt %).

Amplitude, force and processing time need to be optimized in order to guarantee appropriate melt rheology to fill mold cavities completely and avoid molecular degradation. Thus, amplitude should be lower than 43 μm, time between 7–8 s and force close to 2500 N. Good dispersion of nanotubes was attained when solvent casting nanocomposite films prepared were processed. Even partial dispersionwas obtained when a simple powder mixture of the two components was molded.

Incorporation of nanotubes had an influence on the melting and crystallization processes,as determined by DSC and X-ray diffraction data taken during real time heating and cooling experiments. Both melting and crystallization temperatures increased for the nanocomposite. In the latter case, a clear nucleating effect of nanotubes was derived. Crystallinity values of the solvent casting nanocomposite sample determined by WAXD were higher than those found by SAXS. The nanofiller enhanced crystallization due to its nucleating effect but also resulted in more imperfect crystals.

Morphological changes during heating were different for the neat polyester and the nanocomposite as a consequence of the different degree of perfection of lamellae. Specifically, amorphous layer thickness was greater for the nanocomposite, facilitating a reordering process that led to an increased melting point. The evolution of the morphological parameters was similar on cooling although the nanocomposite rendered thicker lamellae at the beginning of the crystallization process due to the nucleation effect and the higher crystallization temperature.

4.3. Ultrasound processing on Nylon 12: Influence of Nanoclays on Structure and Crystallization.

4.3.1. Introduction

Aliphatic polyamides (nylons) are highly versatile engineering plastics that show excellent mechanical properties and high chemical, temperature and electrical resistance[30] . Nylons are widely employed in the automotive, electrical and electronic markets and are manufactured as different consumer goods. The presence of amide groups makes feasible the establishment of strong intermolecular hydrogen bonds that are responsible of the above indicated high performance.

Indeed, these interactions lead to a structural polymorphism that in some cases is not well-understood and that varies according to the chemical constitution of the nylon (e.g., nylons *n* derived from amino acids or nylons *m*,*n* derived from diamine and diacids; nylons with repeat units having long or short aliphatic segments). The first structures of nylons were reported by Bunn and Garner[31] (e.g. nylons 6,6 and 6,10) and consisted on a progressive (α-form) or an alternate (β-form) packing of sheets constituted by hydrogen bonded chains with a practically extended conformation.

Torsional angles of the CH_2-CO and NH-CH_2 bonds can be easily deviated from the energetically preferred value of 180º towards 120º if the energy loss can be compensated by an improved geometry of the intermolecular hydrogen bonds. In this way, pseudohexagonal arrangements where the strong interactions are established between different sheets can be produced. This modification is named the γ-form and is typical of odd-odd nylons[32] and also of nylons with long polymethylene (i.e., number of methylene groups in the repeat unit ≥ 5) segments[33]. Pseudohexagonal arrangements are also characteristic of melt quenched samples, being postulated that in this case hydrogen bonds were arranged in a disorderly way according to three coplanar directions at 120º [34] instead to be established along a single direction as the preceding cases.

Pseudohexagonal arrangements were also usually observed at temperatures just before fusion according to a not well explained Brill named transition[35] Basically, one explanation suggests again a disordering caused by a random distribution of hydrogen bonds[34], while a second interpretation suggests the maintenance of hydrogen bonds along a single direction, a vibrational movement of methylene groups and a preferent dilatation of the unit cell along the direction where the strong intermolecular interactions were not established [36, 37].

The situation becomes more complicated when nylons constituted by peculiar units like glycine[38], malonic acid[39] or methylene diamine[40] are considered since new structures with three, two and one hydrogen bond directions were respectively derived. Two hydrogen bonds were also postulated for odd polyoxalamides[41] and nylons *m*,*n* where the diamine or the diacid unit had an odd number of carbon atoms[42, 43].

Nylon 12 has the lowest amide density of all commercial nylons and had remarkable specific characteristics like low moisture absorption, high dimensional stability in variable humidity conditions, high toughness and processability, resistance to abrasion, to stress cracking, to fatigue and to chemicals[44]. Nowadays, nylon 12 has been receiving great attention since it is one of the most tested materials for 3D printing technologies due to its excellent price-performance balance[45, 46].

The structure of nylon 12 has extensively been studied and specifically four crystalline forms (α, α', γ and γ' forms) have been described. The γ form is the most stable structure and it is usually obtained from melt processing at atmospheric pressure[33]. This form is characterized by a pseudohexagonal packing with hydrogen bonded chains established between parallel chains (e.g., chains 1 and 3 in **Fig. 4-15a**) and amide groups that pointed outside of the typical sheet defined by the methylene carbon atoms. The strongest X-ray reflexion is observed around 0.420 nm. Some authors have described a deviation of the symmetry towards a monoclinic unit cell defined by an angle that slightly deviated from 120º. The α form can be obtained by crystallization from strong acid solutions, from the melt at high pressure or by drawing [47-49]. The structure corresponds to the typical arrangement of sheets (those defined also by the methylene carbons of the repeat unit) of hydrogen bonded antiparallel chains (chains 1 and 2 in **Fig. 4-15c**). The unit cell becomes monoclinic and the main observed spacings correspond to 0.44 nm and 0.37 nm[50]. Heating of the α form causes that the two main reflections progressively merge into a single reflection at the so named Brill transition temperature. This reflection is indicative of a new pseudohexagonal packing that is named γ' form (***Fig. 4-15d***)[35, 51]. In this case, hydrogen bonds seem to be stablished between antiparallel chains since probably the disruption of the initial interactions does not take place during heating. A pseudohexagonal arrangement (mesomorphic phase) is also found in melt quenched samples, being ordered to the γ form during a subsequent heating process. When nylon 12 is crystallized at high temperature a new and not fully understood structure, named α' form, can be developed [52]. In addition, this form can be obtained by heating γ-form samples to high temperatures. The diffraction pattern of the α' form shows two main reflections at 0.440 nm and 0.426 nm (i.e., higher distances than observed ot the α form) and may be consequence of a thermal dilatation that lead to an orthorhombic packing that preserves the hydrogen bond interactions between parallel chains (**Fig. 4-15b**). Basically, distance between hydrogen bonded chains is always close to 0.479 nm being a high dilatation detected between non-hydrogen bonded chains when temperature is raised. Therefore, distance between chains 1 and 3 of the α-form increases (as well the angle between 1-2-3 decrease) and chains 1 and 2 of the γ form increases (and the angle between 1-2-3 chains increases) with temperature, leading to the γ' and α' structure, respectively.

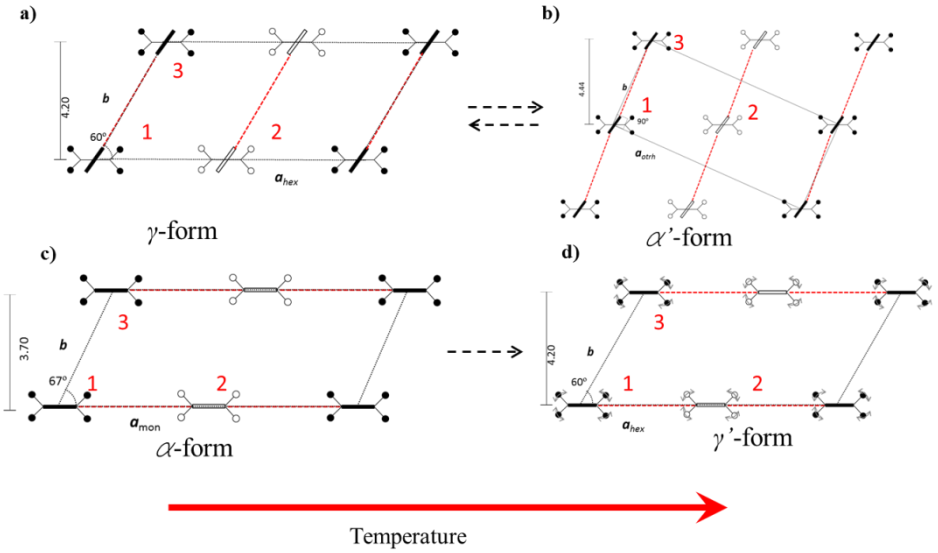

Fig. 4-15. *Schemes showing the chain axis projection of nylon 12 molecular chains in the γ pseudohexagonal (**a**) and the α monoclinic (**c**) arrangements at room temperature. Temperature induced transitions led to the α' orthorhombic (**b**) and the γ' pseudohexagonal (**d**) structures. Parallel and antiparallel molecular chains are differentiated by solid and hollow representations, representative molecular chains are labelled with numbers, hydrogen bonds between chains are indicated by dashed red lines, and the movement of methylene groups is pointed out by the double arrows.*

Mechanical properties of polymers as well as other properties such as optical, transport barrier or ionic conductivity can be improved by incorporation of a low concentration of nanoclay particles[53]. These nanocomposites became interest in 1980s when precisely nylon composites containing 5% of clay showed an increase of tensile strength and modulus of 40% and 68%, respectively[15, 54]. Montmorillonite has been considered the most promising clay due to its natural abundance and high aspect ratio. Nevertheless, clays are usually modified by incorporating different organic cations (e.g., alkylammonium cations) to favour a dispersion in the polymer matrix of constitutive silicate layers by improving intermolecular interactions[55].

Few studies have been focused on the study of nylon 12/clay nanocomposites[56-58]. However, it is clear that an improvement of properties and proper clay exfoliation can be achieved by melt compounding using organo modified nanoclays[59, 60].

Ultrasound micromolding is a new processing technology that has been demonstrated effective to get micro pieces with small degradation, low material loss, good reproducibility, high resolution and processing times so low as 1-3 s[5, 14, 61, 62]. Ultrasonic waves are an energy source able to melt polymer samples and increase their flow index in such way that an efficient filling of mould cavities under the application of an appropriate force/pressure can be achieved. The technique was also revealed to be effective in rendering exfoliated nanocomposites even when non-organo modified clays were employed [4].

The present work is focused on the evaluation of the capability of ultrasounds to process nylon 12 micropieces and also on the preparation of nanocomposites using non-modified clays. Attention will also be paid to follow the structural transitions of nylon 12 by the continuous acquisition of diffraction patterns (i.e., consecutive frames were taken each 20 s) by synchrotron radiation during

heating and cooling runs. In addition, the influence of the nanoclay on the crystallization process and on the molecular arrangement of nylon 12 is also considered.

4.3.2. Results and Discussion

4.3.2.1. Synchrotron studies on the crystalline structures of nylon 12

Continuous acquisition of X-ray diffraction patterns during thermal processes (i.e., fusion and crystallization) allows to detect with precision the structural changes and temperatures at which polymorphic transitions take place. The sequence of consecutive heating, cooling and heating runs (e.g.; **Fig. 4-16**) performed with commercial nylon 12 samples allows detecting the distinct polymorphic forms and the corresponding transition temperatures.

Fig. 4-16 shows that the diffraction pattern of the commercial nylon 12 sample displays two strong reflections at 0.422 nm and 0.400 nm, which do not correspond with the pseudohexagonal arrangement of the γ-form and neither with the characteristic spacings of the monoclinic α-form structure. Nevertheless, we think that this structure can be associated to a slight distortion of the α-form structure. On heating the two reflections approach and merge at a temperature of 140 ºC as shown in **Fig. 4-17a** (being more significant the movement of the low spacing reflection as also usually observed during heating runs of nylons displaying their α form structure). This transition (α to γ) can also be detected in **Fig. 4-17b** where the intensity on the main representative reflection is plotted against temperature. Note the sudden increase of the intensity at 140 ºC, and its decrease after 170 ºC when the melting process starts. The end of fusion was observed at 200 ºC.

The crystallization process was characterized by the apparition of two reflections at 0.424 nm (higher intensity) and 0.440 nm, which are associated to the α' form, when temperature decreased to 140 ºC. On cooling both reflections seem to merge in a single reflection at 0.423 nm when temperature decreased to 129 ºC, being the shift again more significative for the less intense reflection (i.e., that detected at 0.440 nm). At room temperature a single reflection associated to the γ form (i.e., spacing of 0.415 nm) is observed. The intensity plot of **Fig. 4-17b** allowed detecting better the end of the transition since it should correspond to the maximum of intensity detected around 92 ºC. Note that between 129 ºC and 92 ºC the single peak has a practically undetectable shoulder (**Fig. 4-16b**), which is indicative of a non-complete transition.

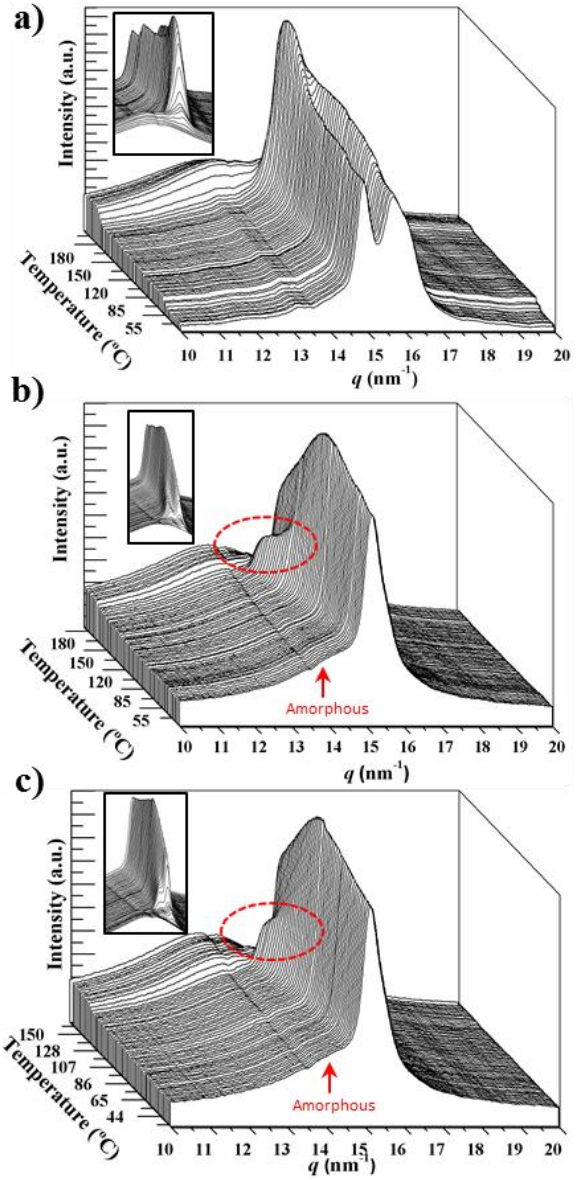

Fig. 4-16. *Three-dimensional representation of WAXD profiles of a commercial nylon 12 sample during heating from room temperature to fusion (**a**), the subsequent cooling run up to room temperature (**b**), and finally a new heating run performed with the melt crystallized sample to fusion (**c**). Labelling indicates the main features associated to polymorphic transitions. Insets show reverse views of the 3D profiles. All heating and cooling runs were performed at a rate of 10 ºC/min.*

In the reheating process, the transition from an initial γ-form to the α'-form is detected at 95 ºC from intensity values plotted in **Fig. 4-17b** or 129 ºC from the splitting of reflections shown in **Fig. 4-17a**. In this way a fully reversible α' to γ transition was verified in the corresponding cooling and heating runs. The α' form melted at 177 ºC without any evidence of a Brill transition. This melting temperature was obviously higher than the beginning of crystallization, being the supercooling for the α' form around 28 ºC (i.e., 177 ºC - 149 ºC).

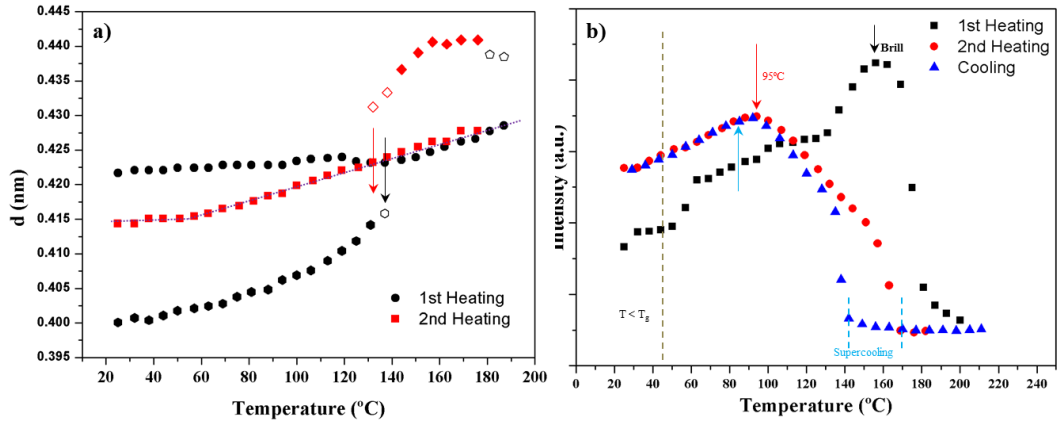

Fig. 4-17. ***a)*** *Evolution of the spacings of the main observed crystalline reflections observed during the heating runs (10 °C/ min) of the commercial and the melt crystallized nylon 12 samples. The purple dotted lined points out the continuous temperature evolution of the single spacing associated to the γ (red) and γ' (black) forms.* ***b)*** *Plot showing the variation of the relative intensity of the main diffraction peak with temperature for the sequence of heating, cooling and heating runs performed at a rate of 10 °C/ min with nylon 12 samples. Arrows indicate the temperatures at which polymorphic transitions seem to occur (black for the first heating, red for the second one and blue for cooling run).*

It is interesting to remark the continuous temperature evolution associated to the single pseudohexagonal spacing (from both γ- and γ'-forms) when data from the two heating runs are combined (see dotted line in **Fig. 4-17a**), a feature that agrees with a simple effect linked to the dilatation of the unit cell.

DSC scans plotted in **Fig. 4-18** points out the significant differences on the melting of γ' and α' forms, the different crystallinity of γ' and α' samples and the good agreement with synchrotron crystallization results. Note that α to γ' and α' to γ transitions cannot be observed in the DSC scans despite they should correspond to first order transitions. Only a broad exothermic process a temperatures lower than 140 °C could be detected and as will be discussed later may correspond to the indicated α' to γ transition together with overlapped secondary crystallization.

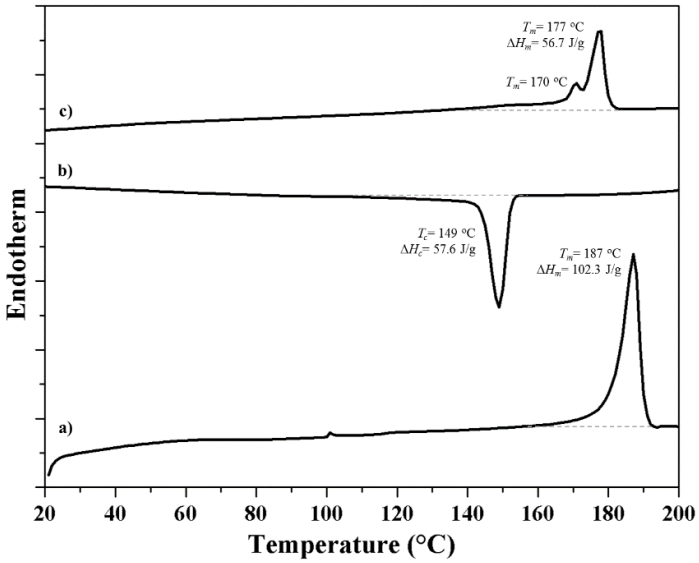

Fig. 4-18. *DSC sequence of heating (**a**), cooling (**b**) and reheating (**c**) runs (10 °C/ min) performed with commercial nylon 12. Note the high difference on the melting temperatures that correspond to the γ' and α' forms.*

Fig. 4-19 shows a plot of the free energy versus temperature for the different polymorphic structures and the melt state. This qualitative representation appears useful to justify the different transitions observed during the different heating and cooling processes and specifically the particular evolution observed in the first heating scan and the reversible behaviour detected in the subsequent cooling and heating scans.

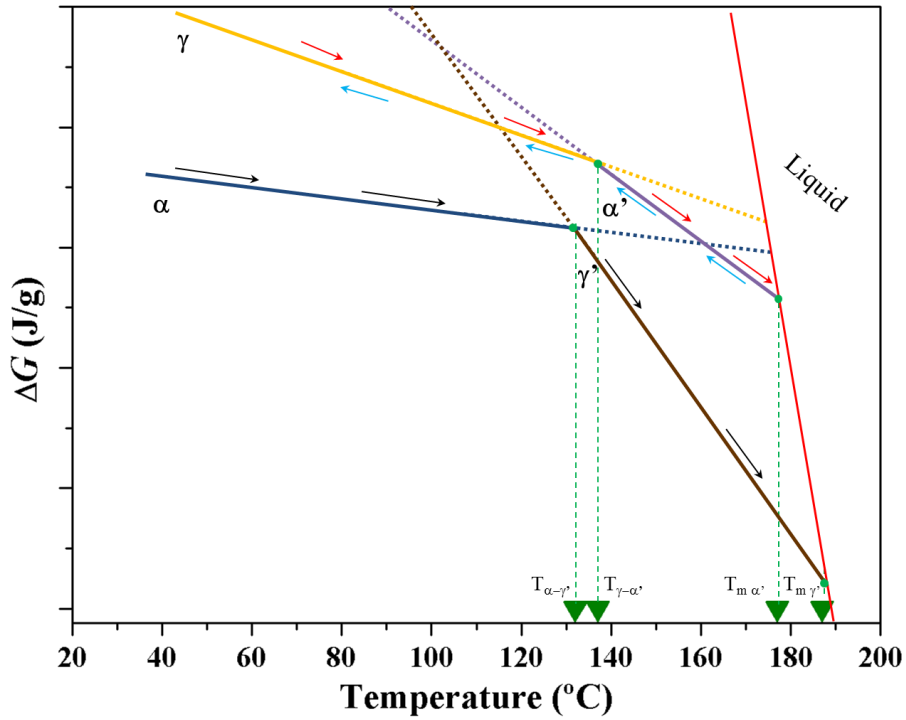

Fig. 4-19. *Plot of the free energy versus temperature for the melt and the different crystalline forms of nylon 12. Main temperatures associated to the observed transitions are indicated (green lines). black arrows point out the evolution of a commercial nylon 12 sample (i.e., from its α form), while blue and red arrows point out, according to its sense, the evolution during crystallization from the melt, the subsequent cooling run and reheating, respectively.*

As previously reported the structure of nylon 12 samples prepared by solvent casting is variable and depends on the chosen solvent as shown in **Fig. 4-20** for two well differentiated samples (i.e., diluted formic acid and 1,1,1,6,6,6-hexafluoroisopropanol, HFIP). Therefore, diffraction patterns having two main reflections (i.e., 0.422 nm and 0.400 nm) or one single reflection at 0.420 nm could be obtained depending on the solvent. The most interesting fact is that the temperature evolution of the X-ray profile was identical to those previously described. Namely, a Brill transition at 148 ºC (see blue circle) from distorted α-form to the γ' form and the transition from the γ form to the α' form at temperatures very close to fusion. It is also remarkable that the X-ray diffraction spacings detected from the formic acid solvent casting film were identical to those detected for the initial commercial sample.

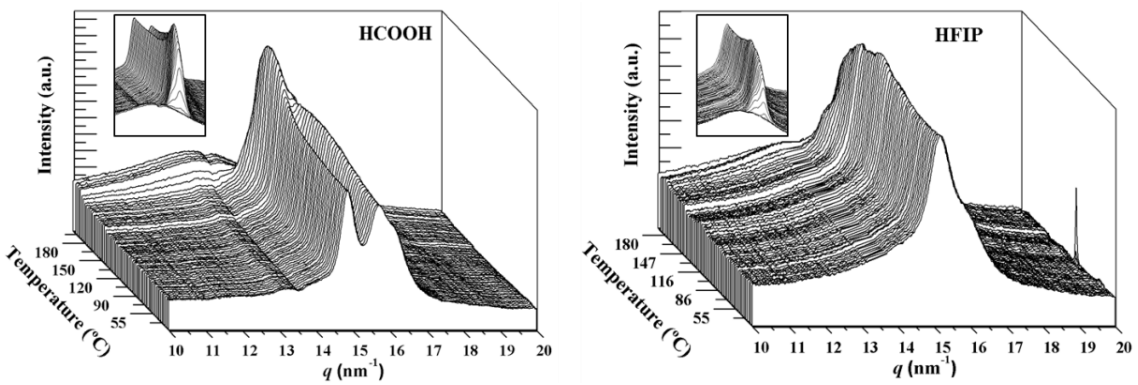

Fig. 4-20. *Three-dimensional representation of WAXD profiles taken during heating (10 ºC/ min) from room temperature to fusion of nylon 12 solvent casting samples from diluted formic acid (**left**) and HFIP (**right**) solutions. Insets show reverse views of the 3D profiles.*

4.3.2.2. Ultrasound micromolding of nylon 12

Basically, amplitude, force and processing time are the ultrasound micromolding parameters that should be optimized in order to get minimum degradation and a convenient melt rheology to fill completely the mold cavities. Many conditions could be discarded by simple optical inspection of the specimen morphology and the capacity to fill the mold. The range of parameters could also be easily delimited through our previous studies on different polyesters [5, 61, 62]. In this way, a time of 1.2 s was considered optimal to satisfy the requirements of low processing cost, maximum production and low degradation due to the minimum exposure to the energy source. Amplitude/energy has also an important effect on the degradation of the sample and therefore the minimum available amplitude of 43 μm was directly chosen. Low applied forces were inefficient to reduce the viscosity of the melt and get a correct flow of the polymer. By contrast, high forces were problematic since chain scissions were enhanced due to the generated high shear stresses. Furthermore, a high force could become inefficient considering the decrease on mold filling capacity. Experiments were successful in the 3000- 4000 N range, being possible to get homogeneous, entire and regular specimens from the eight cavities of the mould. **Fig. 4-21a** shows that GPC curves of commercial and ultrasound processed (under optimal conditions) specimens were practically identical. Specific molecular weight data are summarized in **Table 4-2** together with the main mechanical properties deduced from stress-strain assays performed with the micromolded specimens. Data revealed a semicrystalline character with a modulus lower than that typically reported (i.e., 1650 MPa) and maximum strength and elongation at break similar to those found in conventional samples (i.e., 48 MPa and 18%, respectively[63]). Optical and SEM micrographs are also shown in **Fig. 4-21c** to point out the degree of perfection of micromolded specimens and the absence of internal pores and cavities that could be indicative of cavitation phenomena.

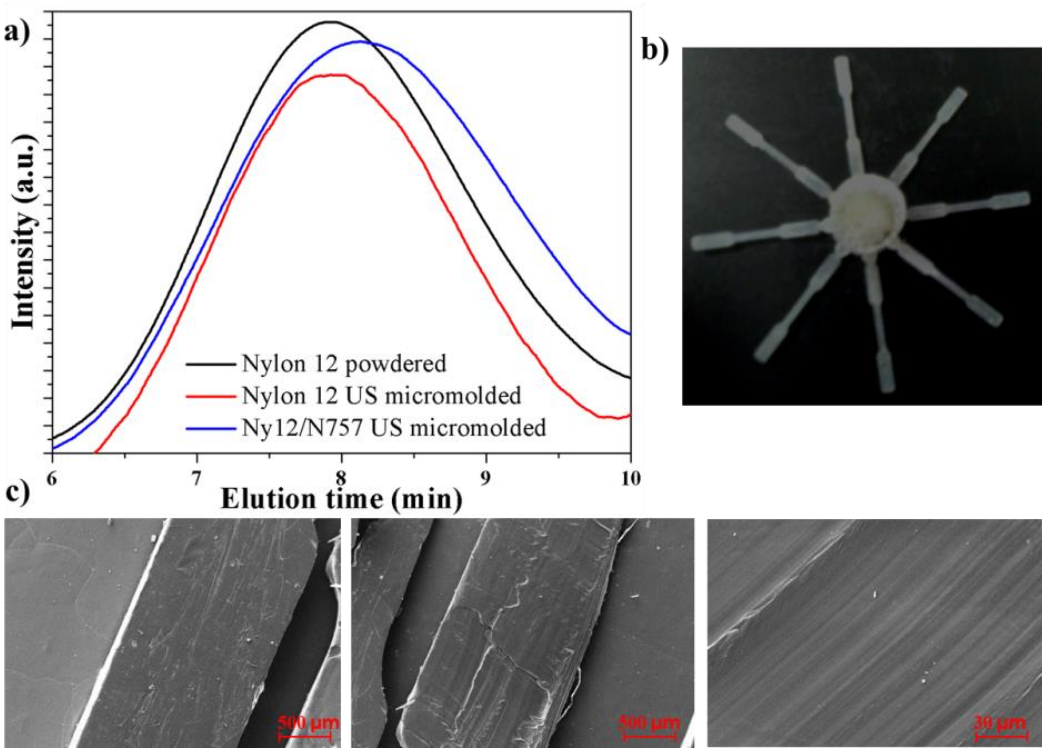

Fig. 4-21. ***a)*** *GPC curves comparing commercial nylon 12 and US micromolded specimen (processed at the optimal conditions: 43 µm / 3000 N / 1.2 s, with and without Nanofil 757).* ***b)*** *Optical micrograph showing the specimen and sprue morphology.* ***c)*** *SEM micrographs showing the internal section of US a micromolded specimen.*

Table 4-2. *GPC and stress-strain data of commercial nylon 12 and US micromolded specimens.*

Sample	Molecular Weight			Molecular Weight		
	Mn (g/mol)	Mw (g/mol)	PI	E (MPa)	ε (%)	σ_r (MPa)
Nylon 12[a]	32,200	73,400	2.28	1650	18	48
Nylon 12[b]	31,950	72,400	2.26	368	15	45
Nylon 12/N757[b]	30,600	70,300	2.30	408	11	33

(a) Commercial powdered sample.
(b) Ultrasound micromolded specimens.

DSC curves (**Fig. 4-22**) indicated that after US processing the nylon 12 amorphous content increased with respect to the commercial sample (i.e., melting enthalpies of 102.2 J/g and 56.4 J/g), a feature that agrees with the significant decrease of the Young modulus after ultrasound processing. In addition, very small exothermic exothermic process (1 J/g) corresponding to molecular reordering was detected some degrees before fusion (i.e., at 158 ºC). The melting point decreased to 178 ºC as typical of melt processed samples. Note also that heating runs of both samples after being crystallized from the melt were practically identical as presumable from a reduced degree of degradation.

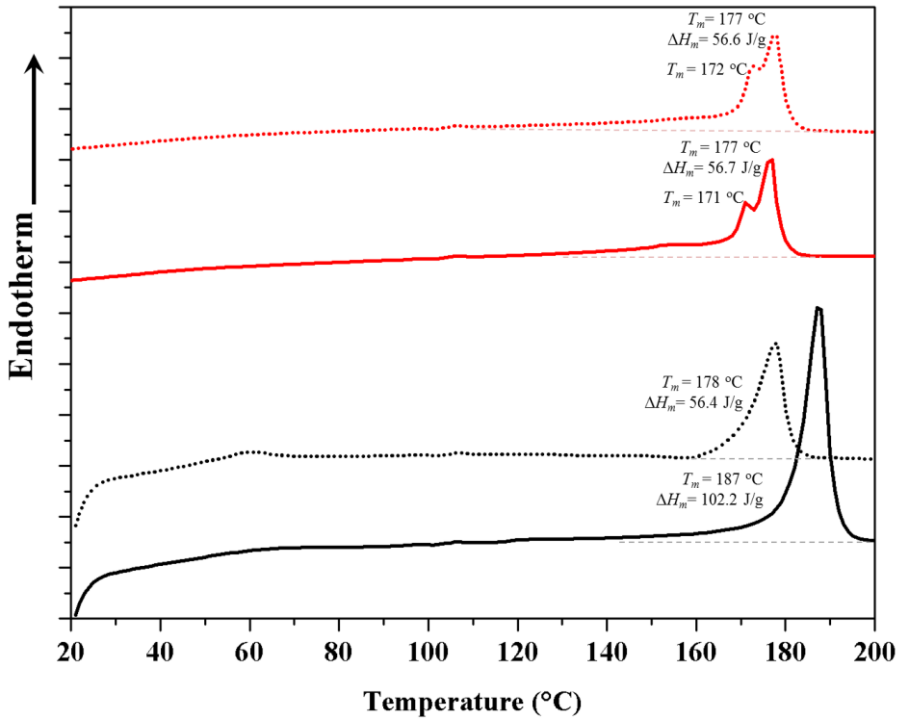

Fig. 4-22. *DSC heating traces (10 °C/min) comparing the thermal behaviour of the commercial sample (black solid line) and the US processed sample (black dotted line) as well as the second heating run (solid and dashed red lines for commercial and US processed samples, respectively) performed with samples melt crystallized samples at a cooling rate of 7.5 °C/min.*

Differences between the first heating runs can be justified considering that commercial nylon 12 and micromolded specimens have different structures (i.e., α and γ forms). It is interesting to point out the broad exothermic event that is observed in both samples at temperatures higher than 120 °C (this event is partially masked in the case of the micromolded specimen by the previously indicated hot crystallization). First heating runs revealed also a glass transition around 50 °C that is logically more significant in the trace of the more amorphous micromolded specimen.

X-ray diffraction profile of the US micromolded specimen is characterized by a great amorphous halo at 0.415 nm and a single crystalline reflection at 0.410 nm, which allowed determining a crystallinity degree of 22% and a γ-form structure. The evolution during the heating process (**Fig. 4-23a**) shows a continuous decrease of the main peak intensity from a temperature close to 120 °C that could be associated to the γ-α' transition. Profile evidenced also a last crystallization process (note the new increase of the peak intensity) that took place just before fusion. The behaviour of the melt crystallized sample (**Fig. 4-23b**) is different and appears to be in good agreement with that displayed in **Fig. 4-16c**. Namely, the melt crystallized sample is less amorphous (crystallinity degree becomes 33%) and no crystallization phenomena during heating could be detected. Again the γ to α' form transition could be envisaged (i.e., at temperatures higher than 120 C as detected from the decrease of the intensity of the main reflection).

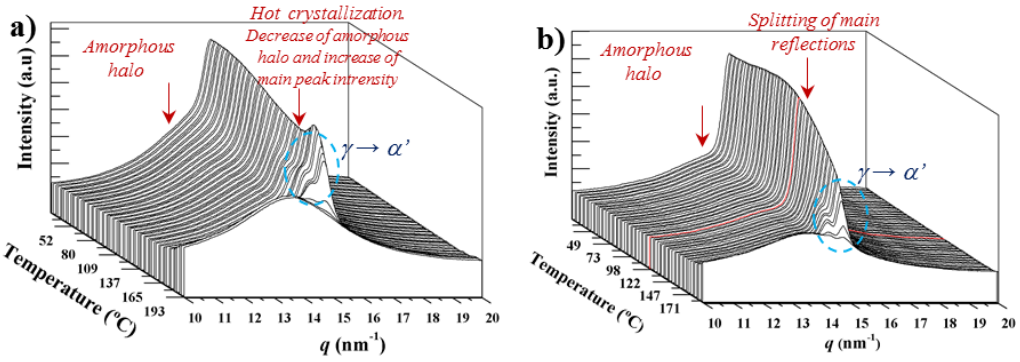

Fig. 4-23. *Three-dimensional representation of WAXD profiles taken during heating (10 ºC/ min) from room temperature to fusion of an US micromolded nylon 12 sample (**a**) and the subsequent heating run (10 ºC/ min) of the melt crystallized (cooling rate of 10 ºC/ min) sample (**b**).*

4.3.2.2.1 Ultrasound micromolding of nanocomposites of nylon 12/ Nanofil 757 (Nylon 12/N757)

US processing of nanocomposites with Nanofil 757 could be performed using the same parameters employed for the neat nylon 12 due to the scarce selected clay content (i.e., 3 wt-%). GPC measurements indicated a practically null influence (i.e., a decrease of the weight average molecular weight lower than 5% was detected) of the clay on degradation (**Table 4-2** and **Fig. 4-21),** which is also a logical result due to the fact that the clay was free of the most aggressive amine salts used as organomodifiers.

X-ray diffraction profiles of neat nylon 12, the US processed nanocomposite and the neat clay are compared in **Fig. 4-24**.

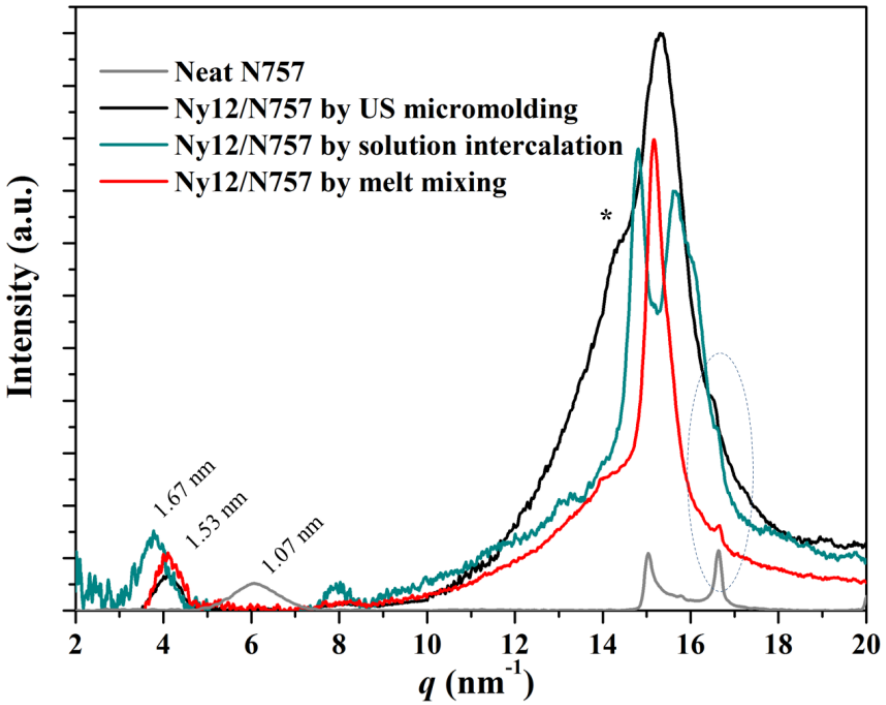

Fig. 4-24. *Room temperature X-ray diffraction profiles of US processed nylon 12 and its nanocomposite with Nanofil 757. For the sake of completeness profiles corresponding to nanocomposites prepared by solution intercalation and melt blending methods are also given. Note that the sample prepared by solution intercalation is crystallized in the α form as deduced for the higher spacing associated to the chain repeat unit and the two strong reflections at 0.422 and 0.400 nm. It is also remarkable the shoulder detected at 0.440 nm in the pattern of the ultrasound processed nanocomposite that is labelled with the asterisk.*

The characteristic and intense (001) interlayer clay spacing at 1.07 nm fully disappeared in the pattern of the nanocomposite as expected for the achievement of an exfoliated structure. Note that only the (002) reflection associated to the nylon 12 chain repeat unit (1.67 nm for the α form coming from solution intercalation and 1.53 nm for the γ form coming from melt mixing) was detected in the low angle region. The profile of the ultrasound processed nanocomposite was also characterized by a significant amorphous halo and two reflections at 0.440 nm and 0.411 nm (highest intensity), being the first one relevant as will be later discussed. Melt and solution nanocomposites were prepared for comparative purposes adding the same percentage of nanoclay. X-ray profiles were practically identical demonstrating the capacity of the non-modified clay to be dispersed into the nylon 12 matrix giving rise to exfoliated structures. Note, however the absence of a 0.440 reflection in the patterns.

Clay dispersion in the US processed nanocomposite was also evaluated by TEM observations of ultrathin sections. **Fig. 4-25** clearly shows that a good dispersion of silicate layers with a slight orientation along the flow direction was observed for the US processed nanocomposites. Note that the dispersion was attained from a simple physical mixture of nylon 12 and Nanofil 757 powders.

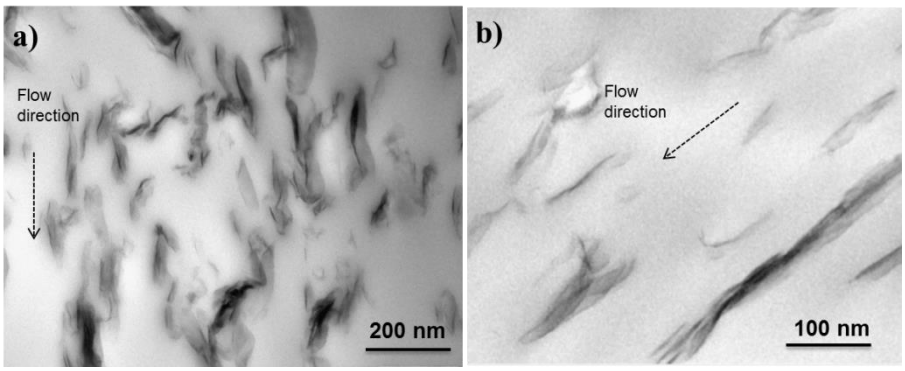

Fig. 4-25. *TEM micrographs of ultrathin sections of ultrasound processed nylon 12/Nanofil 757 nanocomposite.*

4.3.2.3. Influence of Nanofil 757 in the crystallization and structure of nylon 12

The incorporation of Nanofil 757 had a remarkable influence on the crystalline structure obtained after ultrasound processing as deduced from the comparison of X-ray profiles depicted in **Fig. 4-26** for the nanocomposite and in **Fig. 4-23** for the neat polymer. Thus, the room temperature profile of the nanocomposite is the characteristic one for the α' form, namely a shoulder and a peak at 0.440 nm and 0.422 nm. Temperature evolution of the diffraction profile showed a decrease of the amorphous halo, a hot crystallization process (see the slight increase of the main reflection around 120 ºC) and the starting of the melting process at a temperature close around 147 ºC (note the progressive decrease of the intensity of both indicated reflections while the shoulder-peak shape is kept). Reflections related to the clay basal planes remained constant in position and intensity and demonstrated the effective incorporation of the clay. Note also that a small clay reflection was overlapped with the intense shoulder and that it was only visible at last stage of fusion where practically

only the amorphous was detected. It seems highly important to remark that this processing based on the use of ultrasounds and the presence of the Nanofil 757 clay has been the only case where the α' form has been obtained at room temperature as a metastable form (i.e., the above explained α'-γ transition was avoided during the solidification step in the mould).

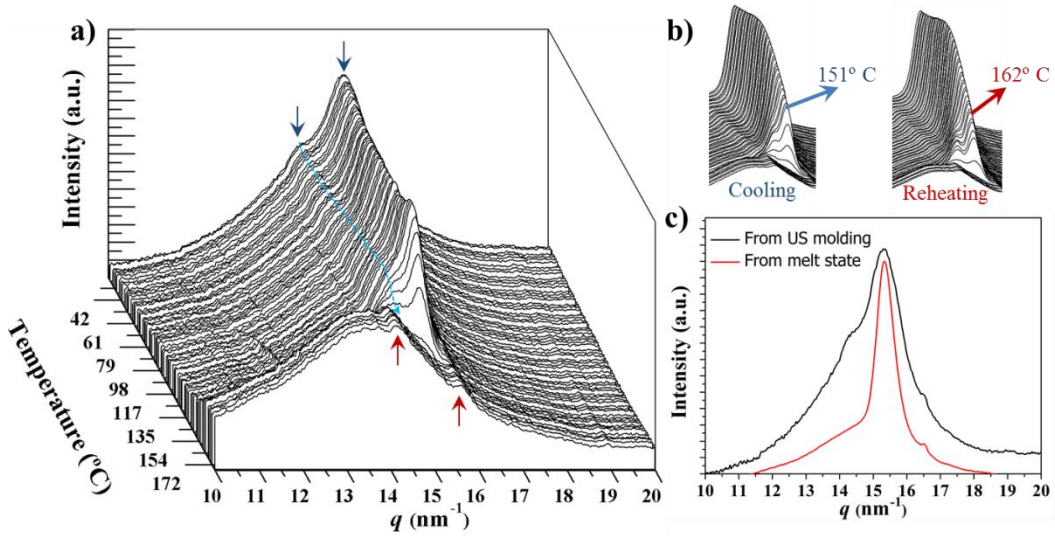

Fig. 4-26. ***a)*** *Three-dimensional representation of WAXD profiles of an ultrasound processed nylon 12/Nanofil 757 nanocomposite during the heating run (10 ºC/min) from room temperature to the melt (red and blue arrows, point out to Nanofil and α' reflections, respectively).* ***b)*** *A complete reversible behaviour involving α' and γ phases was detected in the subsequent cooling (**left**) and heating runs (**right**) performed at a rate of 10 ºC/min.* ***c)*** *Room temperature X-ray profiles of nylon12/nanofil 757 nanocomposites obtained from the ultrasound processed sample and after being slowly crystallized from the melt sate.*

Note that the ultrasound processing of nylon 12 without clay led to the γ-form and that the nanocomposites processed without ultrasounds led to α (solution intercalation) or γ (melt mixing) forms as indicated in the first subsection. It is also interesting to note, as shown in the insets of **Fig. 4-26b**, that the ultrasound processed nanocomposite displayed a fully reversible α'-γ transition which was observed on the subsequent cooling and heating runs. Specifically, **Fig. 4-26c** evidences the α' and γ structures obtained at room temperature after ultrasound processing and after the subsequent crystallization from the melt. It seems that α' form was stabilized under the influence of the exfoliated clay that allowed to establish high interactions between the polyamide and the silicate layers and under a shear stress caused by the fast flow of the melted sample through the mould cavities as evidenced by the high orientation of silicate layers shown in **Fig. 4-25**. This situation is not the case of the crystallization from the melt state as evidenced in **Fig. 4-26b** or even when nanocomposites were prepared by solution intercalation or by a conventional melt mixing. It has been indicated that strong flow fields can led to strong density fluctuations and gave rise to domains with high local molecular alignment and preferred nucleation[64]. This nucleation effect is probably enhanced by the presence of nanoclays and can favour the prevalence of the α' phase after the fast cooling in the mold.

In addition to the relevant effect of the clay on the crystalline structure, it is interesting to evaluate its influence on the crystallization kinetics in function of the way as the nanocomposite was

prepared. **Fig. 4-27a** shows that crystallization clearly started at higher temperature for the ultrasound processed nanocomposite (i.e., the crystallization peak temperature was observed at 153.7 ºC more than 4 ºC higher than that detected for the neat commercial sample). An intermediate behaviour was observed for nanocomposites prepared by melt mixing and solution intercalation (i.e. peak temperature close to 152 ºC). In this, way nucleation process seems to be enhanced in the ultrasound prepared nanocomposite, although the overall crystallization rate became slower as deduced from the broader crystallization peak and the following Avrami kinetic analysis that suggests an hindered crystallization process. Probably, the presence of exfoliated silicate layers decreased the crystal growth rate as reported in the literature, for other nylons, as for example nylon 4 7[65].

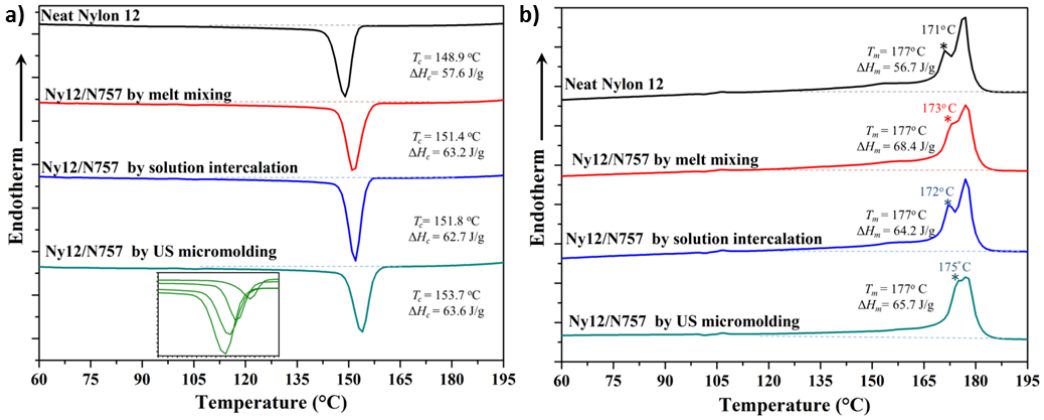

Fig. 4-27. ***a)*** *DSC cooling runs showing the crystallization peak of the indicated melted samples. The inset shows the crystallization peak of the ultrasound processed nanocomposite obtained at cooling rates of 10, 7.5, 5and 2.5ºC/ min (from left to right).* ***b)*** *DSC heating runs performed at 10 ºC/ min for the indicated melt crystallized samples.*

Differences on the crystallization process were also evidenced in a subsequent heating run (10 ºC/min) where the first peak moved to the right as presumable for a crystallization that occurred at a higher temperature (**Fig. 4-27b**). Therefore, thicker crystals were obtained when clay particles where added and thus the corresponding melting peak increased from 170.8 ºC to 174.6 ºC (ultrasound processed sample). Intermediate temperatures (i.e., 172.6-173.2 ºC) were determined for nanocomposites prepared by melt mixing and solution intercalation.

The overall crystallization rate was evaluated from the temperature dependence of the degree of crystallization deduced from integration of the crystallization peak (equation 2) and subsequent conversion to a time dependence (equation 3):

$$\chi(\mathrm{T}) = \frac{\int_{T_0}^{T}(dH_c/dT)\cdot dT}{\int_{T_0}^{T_\infty}(dH_c/dT)\cdot dT} \qquad (2)$$

$$(t - t_0) = \frac{(T - T_0)}{\phi} \qquad (1)$$

where dH_c is the enthalpy of crystallization released within an infinitesimal temperature range dT, T_0 denotes the initial crystallization temperature and T_∞ is the temperature required to complete the crystallization process, t_0 is the time at which crystallization begins and ϕ is the cooling rate.

Application of typical Avrami analysis (equation 4) allowed evaluating the Avrami exponent, n, indicative of the type of nucleation and a kinetic constant, $k = Z^{1/n}$, by plotting log {-ln {1 – $\chi(t-t_0)$}} versus log ($t-t_0$) and using the linear region for degree of crystallinities lower than 0.80:

$$1 - \chi(t - t_o) = e^{-Z \cdot (t-t_0)^n} \qquad (4)$$

Despite, the Avrami exponent loose its physical sense when non-isothermal analyses are performed and values of the exponent can be higher than 4, which is the expected value for a spherulitic growth and a time-dependent thermal nucleation, results are interesting for comparative purposes and also for allowing to determine the overall crystallization rate. Integration of the exothermal crystallization peak is problematic due to the overlapping with the exothermic process associated to the α' to γ polymorphic transition that takes place in the wide temperature interval centred at 120 ºC. **Fig. 4-28** shows a non-realistic evolution of the relative degree of crystallinity that attains values lower than 80% at 140 ºC. In order to carry out an accurate kinetic analysis the exotherm was deconvoluted. The main crystallization peak (see dashed black line) could therefore be considered free of influence of other calorimetric events. A realistic evolution of the relative degree of crystallinity was in this case derived.

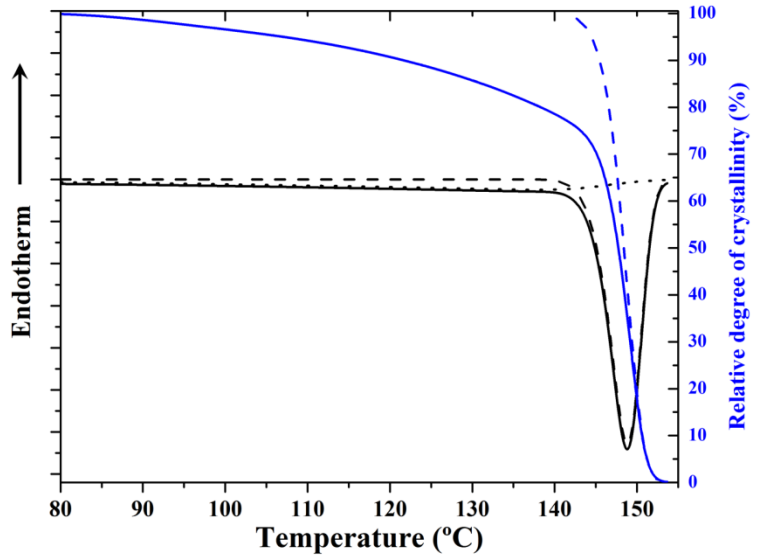

Fig. 4-28. *DSC cooling (10 ºC/min) run of nylon 12 and temperature evolution of relative crystallinity (**black** and **blue** solid lines respectively). Dashed lines represent the deconvoluted exothermic crystallization peak (**black**) and the evolution of relative crystallinity (**blue**) from the deconvoluted main peak (i.e., without considering posterior secondary crystallization and structural exothermic transition).*

Fig. 4-29 compares the time evolution of relative crystallinity (a) and the Avrami plots (b) for both ultrasound processed nylon 12 and nanocomposite specimens at the indicated cooling rates.

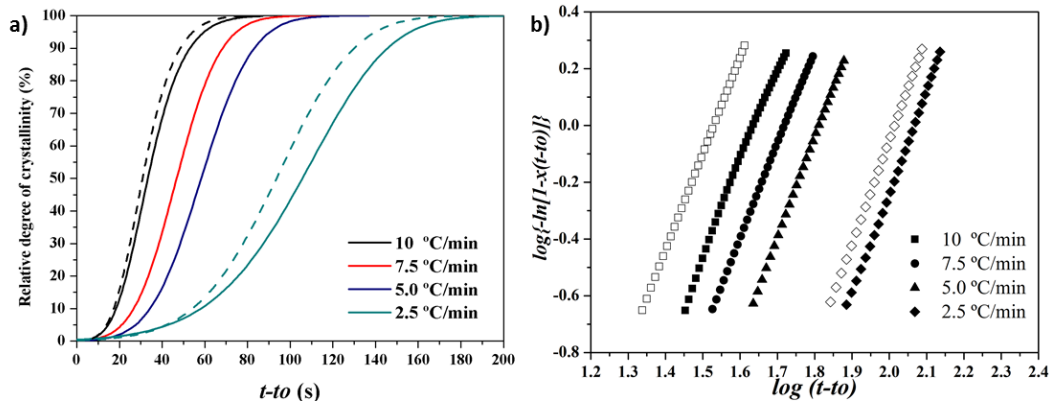

Fig. 4-29. *Time evolution of relative crystallinity (**a**) and Avrami plots (**b**) of nylon 12 (dashed lines and empty symbols) and its nanocomposite with N757 (solid lines and full symbols) ultrasound processes samples at the indicated cooling rates.*

The corresponding kinetic data are summarized in **Table 4-3**. This shows also a good agreement between the reciprocal crystallization half-times ($1 / \tau_{1/2}$) that were directly determined from the experimental data and those that were deduced from the Avrami parameters (i.e., $1/\tau_{1/2} = (Z / \ln 2)^{1/n}$). In conclusion, the deduced Avrami parameters are at least appropriate to simulate the non-isothermal crystallization process of the studied samples. Kinetic data obviously indicated that the overall crystallization rate ($k = Z^{1/n}$) increased with the cooling rate, but much more interesting the crystalline rate decreased with the incorporation of nanoclays as expected for the hindered molecular movement of molecular chains to the crystal front edge. Avrami exponents were in the 3.3-3.8 range without showing a distinctive trend when cooling rate was varied or when the clay was added. Therefore, type of nucleation and crystal growth geometry were not significantly influenced by the incorporation of the exfoliated clay.

Table 4-3. *Non-isothermal crystallization kinetic parameters deduced from DSC experiments for US micromolded specimens of neat nylon 12 and its nanocomposite with N757 (3 wt-%).*

Cooling rate (°C/min)	Nylon 12				Nylon12/N757			
	n	*k* 10^3 (s-1)	$\tau_{1/2}{}^a$ (s-1)	$\tau_{1/2}{}^b$ (s-1)	*n*	*k* 10^3 (s-1)	$\tau_{1/2}{}^a$ (s-1)	$\tau_{1/2}{}^b$ (s-1)
2.5	3.6	9.7	93.6	93.4	3.6	8.6	105.6	105.2
5	3.8	16.4	56.6	55.2	3.5	15.4	58.2	58.4
7.5	3.7	21.7	42.7	41.8	3.3	19.1	46.7	46.9
10	3.4	29.4	30.9	30.6	3.5	26.3	33.5	34.2

(a) Deduced from the experimental degree of crystallinity curve.
(b) Deduced from Avrami analyses.

4.3.3. Conclusions

Nylon 12 and its nanocomposite with Nanofil 757 could be processed without significant degradation by an ultrasound micromolding technology. Regular and homogeneous micropieces could therefore be obtained with a processing time than can be as low as 1.2 s and a minimum loss of material. A fully reversible transition between γ and α' form of nylon 12 was detected by analysis of

real time synchrotron diffraction patterns obtained during the corresponding heating and cooling runs. The qualitative temperature dependence of the Gibbs energy associated to each crystalline structure of nylon 12 may justify the observed reversibility.

Nanocomposites with an exfoliated microstructure were achieved without necessity of using typical organomodifiers in order to improve compatibilization between the clay and the polymer matrix. Nylon 12 crystallized according to its α' form structure when processed by ultrasounds in presence of clay particles. This result was unusual since nanocomposite samples obtained by solvent casting and melt crystallization rendered α or γ form structures. Clay nanolayers have a remarkable influence on crystallization of nylon 12 under the effect of the high shear stress during ultrasound processing. Silicate clays reduced the overall crystallization rate but caused a remarkable shift of the peak crystallization temperature to higher values due to a nucleation effect. Exfoliated layers hindered the crystal growth and caused a decrease on the degree of crystallinity.

4.4. References

1. Sinha Ray, S..Okamoto, M. Polymer/layered silicate nanocomposites: a review from preparation to processing. *Progress in Polymer Science* (2003), *28*, 1539-1641.

2. Vonk, C.G..Kortleve, G. X-ray small-angle scattering of bulk polyethylene. *Kolloid-Zeitschrift und Zeitschrift für Polymere* (1967), *220*, 19-24.

3. Vonk, C.G. A general computer program for the processing of small-angle X-ray scattering data. *J. App. Cryst.* (1975), 340-341.

4. Planellas, M.; Sacristán, M.; Rey, L.; Olmo, C.; Aymamí, J.; Casas, M.T.; Valle, L.J.d.; Franco, L..Puiggalí, J. Micro-molding with ultrasonic vibration energy: New method to disperse nanoclays in polymer matrices. *Ultrasonics Sonochemistry* (2014), *21*, 1557-1569.

5. Díaz, A.; Franco, L.; Casas, M.T.; del Valle, L.J.; Aymamí, J.; Olmo, C..Puiggalí, J. Preparation of micro-molded exfoliated clay nanocomposites by means of ultrasonic technology. *Journal of Polymer Research* (2014), *21*, 584.

6. Díaz, A.; Casas, M.T..Puiggalí, J. Dispersion of Functionalized Silica Micro- and Nanoparticles into Poly(nonamethylene Azelate) by Ultrasonic Micro-Molding. *Applied Sciences* (2015), *5*, 1252-1271.

7. Michaeli, W.; Spennemann, A..Gärtner, R. *New plastification concepts for micro injection moulding*. *Microsystem Technologies* (2002), *8*, 55-57.

8. Michaeli, W..Starke, C. *Ultrasonic investigations of the thermoplastics injection moulding process*. *Polymer Testing* (2005), *24*, 205-209.

9. Michaeli, W.; Kamps, T..Hopmann, C. *Manufacturing of polymer micro parts by ultrasonic plasticization and direct injection*. *Microsystem Technologies* (2011), *17*, 243-249.

10. Chen, J.; Chen, Y.; Li, H.; Lai, S.-Y..Jow, J. Physical and chemical effects of ultrasound vibration on polymer melt in extrusion. *Ultrasonics Sonochemistry* (2010), *17*, 66-71.

11. Chen, G.; Guo, S..Li, H. Ultrasonic improvement of rheological behavior of polystyrene. *Journal of Applied Polymer Science* (2002), *84*, 2451-2460.

12. Kang, J.; Chen, J.; Cao, Y..Li, H. Effects of ultrasound on the conformation and crystallization behavior of isotactic polypropylene and β-isotactic polypropylene. *Polymer* (2010), *51*, 249-256.

13. Cao, Y..Li, H. Influence of ultrasound on the processing and structure of polypropylene during extrusion. *Polymer Engineering & Science* (2002), *42*, 1534-1540.

14. Sacristán, M.; Puiggalli, J.; Planta, X..Morell, M. *Effects of ultrasonic vibration on the micro-molding processing of polylactide*. *Ultrasonics Sonochemistry* (2014), *21*, 376-386.

15. Kojima, Y.; Usuki, A.; Kawasumi, M.; Okada, A.; Kurauchi, T..Kamigaito, O. Synthesis of nylon 6–clay hybrid by montmorillonite intercalated with ϵ-caprolactam. *Journal of Polymer Science Part A: Polymer Chemistry* (1993), *31*, 983-986.

16. Usuki, A.; Kojima, Y.; Kawasumi, M.; Okada, A.; Fukushima, Y.; Kurauchi, T..Kamigaito, O. Synthesis of nylon 6-clay hybrid. *Journal of Materials Research* (1993), *8*, 1179-1184.

17. Kojima, Y.; Usuki, A.; Kawasumi, M.; Okada, A.; Kurauchi, T..Kamigaito, O. One-pot synthesis of nylon 6–clay hybrid. *Journal of Polymer Science Part A: Polymer Chemistry* (1993), *31*, 1755-1758.

18. Rhim, J.-W.; Park, H.-M..Ha, C.-S. Bio-nanocomposites for food packaging applications. *Progress in Polymer Science* (2013), *38*, 1629-1652.

19. Bikiaris, D.N. Nanocomposites of aliphatic polyesters: An overview of the effect of different nanofillers on enzymatic hydrolysis and biodegradation of polyesters. *Polymer Degradation and Stability* (2013), *98*, 1908-1928.

20. Tolunay, M.N.; Dawson, P.R..Wang, K.K. Heating and bonding mechanisms in ultrasonic welding of thermoplastics. *Polymer Engineering & Science* (1983), *23*, 726-733.
21. Chatani, Y.; Okita, Y.; Tadokoro, H..Yamashita, Y. Structural Studies of Polyesters. III. Crystal Structure of Poly-ε-caprolactone. *Polymer Journal* (1970), *1*, 555-562.
22. Hu, H..Dorset, D.L. Crystal structure of poly(iε-caprolactone). *Macromolecules* (1990), *23*, 4604-4607.
23. Iwata, T..Doi, Y. Morphology and enzymatic degradation of poly(ϵ-caprolactone) single crystals: does a polymer single crystal consist of micro-crystals? *Polymer International* (2002), *51*, 852-858.
24. Li, L.; Li, B.; Hood, M.A..Li, C.Y. Carbon nanotube induced polymer crystallization: The formation of nanohybrid shish–kebabs. *Polymer* (2009), *50*, 953-965.
25. Hsiao, B.S.; Gardner, K.H.; Wu, D.Q..Chu, B. Time-resolved X-ray study of poly(aryl ether ether ketone) crystallization and melting behaviour: 1. Crystallization. *Polymer* (1993), *34*, 3986-3995.
26. Ikada, Y.; Jamshidi, K.; Tsuji, H..Hyon, S.H. Stereocomplex formation between enantiomeric poly(lactides). *Macromolecules* (1987), *20*, 904-906.
27. Krueger, K.N..Zachmann, H.G. Investigation of the melting behavior of poly(aryl ether ketones) by simultaneous measurements of SAXS and WAXS employing synchrotron radiation. *Macromolecules* (1993), *26*, 5202-5208.
28. Hsiao, B.; Wang, Z.-g.; Yeh, F.; Gao, Y..Sheth, K. Time-resolved X-ray studies of structure development in poly(butylene terephthalate) during isothermal crystallization. *Polymer* (1999), *40*, 3515-3523.
29. Wurm, A.; Lellinger, D.; Minakov, A.A.; Skipa, T.; Pötschke, P.; Nicula, R.; Alig, I..Schick, C. Crystallization of poly(ε-caprolactone)/MWCNT composites: A combined SAXS/WAXS, electrical and thermal conductivity study. *Polymer* (2014), *55*, 2220-2232.
30. Kohan, M.I. *Nylon plastics handbook*, Hanser Publishers ; Distributed in the USA and in Canada by Hanser/Gardner Publications:Munich; New York; Cincinnati, (1995).
31. Bunn, C.W.; Garner, E.V..Bragg, W.L. The crystal structures of two polyamides ('nylons'). *Proceedings of the Royal Society of London. Series A. Mathematical and Physical Sciences* (1947), *189*, 39-68.
32. Kinoshita, Y. An investigation of the structures of polyamide series. *Die Makromolekulare Chemie* (1959), *33*, 1-20.
33. Arimoto, H.; Ishibashi, M.; Hirai, M..Chatani, Y. Crystal structure of the γ-form of nylon 6. *Journal of Polymer Science Part A: General Papers* (1965), *3*, 317-326.
34. Franco, L.; Cooper, S.J.; Atkins, E.D.T.; Hill, M.J..Jones, N.A. Nylon 6 9 can crystallize with hydrogen bonding in two and in three interchain directions. *Journal of Polymer Science Part B: Polymer Physics* (1998), *36*, 1153-1165.
35. R. Brill, V. Beziehungen zwischen wasserstoffbindung und einigen eigenschaften von polyamiden. (1956), *18*, 294-309.
36. Feldman, A.Y.; Wachtel, E.; Vaughan, G.B.M.; Weinberg, A..Marom, G. The Brill Transition in Transcrystalline Nylon-66. *Macromolecules* (2006), *39*, 4455-4459.
37. Wendoloski, J.J.; Gardner, K.H.; Hirschinger, J.; Miura, H..English, A.D. Molecular Dynamics in Ordered Structures: Computer Simulation and Experimental Results for Nylon 66 Crystals. *Science* (1990), *247*, 431-436.
38. Bella, J.; Puiggalí, J..Subirana, J.A. Glycine residues induce a helical structure in polyamides. *Polymer* (1994), *35*, 1291-1297.
39. Puiggalí, J.; Aceituno, J.E.; Navarro, E.; Campos, J.L..Subirana, J.A. Structure of n,3 Polyamides, a Group of Nylons with Two Spatial Hydrogen-Bond Orientations. *Macromolecules* (1996), *29*, 8170-8179.

40. Franco, L.; Navarro, E.; Subirana, J.A..Puiggali, J. Synthesis and Structure of Nylons 1,n. *Macromolecules* (1994), *27*, 4284-4297.

41. Franco, L.; Subirana, J.A..Puiggalí, J. Structure and Morphology of Odd Polyoxamides Nylon 9,2. A New Example of Hydrogen-Bonding Interactions in Two Different Directions. *Macromolecules* (1998), *31*, 3912-3924.

42. Morales-Gámez, L.; Soto, D.; Franco, L..Puiggalí, J. Brill transition and melt crystallization of nylon 56: An odd–even polyamide with two hydrogen-bonding directions. (2010), *51*, 5788-5798.

43. Morales-Gámez, L.; Ricart, A.; Franco, L..Puiggalí, J. Study on the brill transition and melt crystallization of nylon 65: A polymer able to adopt a structure with two hydrogen-bonding directions. *European Polymer Journal* (2010), *46*, 2063-2077.

44. McKeen, L.W., 8 - Polyamides (Nylons), in: L.W. McKeen (Ed.), Film Properties of Plastics and Elastomers (Fourth Edition), William Andrew Publishing (2017), pp. 187-227.

45. Rahim, T.N.A.T.; Abdullah, A.M.; Akil, H.M.; Mohamad, D..Rajion, Z.A. The improvement of mechanical and thermal properties of polyamide 12 3D printed parts by fused deposition modelling. *Express Polym. Lett.* (2017), *11*, 963-982.

46. Espera Jr, A.H.; Valino, A.D.; Palaganas, J.O.; Souza, L.; Chen, Q..Advincula, R.C. 3D Printing of a Robust Polyamide-12-Carbon Black Composite via Selective Laser Sintering: Thermal and Electrical Conductivity. *Macromolecular Materials and Engineering* (2019), *304*, 1800718.

47. Hiramatsu, N.; Haraguchi, K..Hirakawa, S. Study of Transformations among α, γ and γ' Forms in Nylon 12 by X-Ray and DSC. *Japanese Journal of Applied Physics* (1983), *22*, 335.

48. Monobe, K..Fujiwara, Y. A Study on single Crystals of Nylon 12. *Memoirs of the School of Engineering, Okayama University* (1967), *2*, 88-92.

49. Ishikawa, T.; Nagai, S..Kasai, N. The γ → α partial transformation in nylon 12 by drawing. *Die Makromolekulare Chemie* (1981), *182*, 977-988.

50. Li; Koch, M.H.J..de Jeu, W.H. Crystalline Structure and Morphology in Nylon-12: A Small- and Wide-Angle X-ray Scattering Study. *Macromolecules* (2003), *36*, 1626-1632.

51. Brill, R. Über das Verhalten von Polyamiden beim Erhitzen. *Journal für Praktische Chemie* (1942), *161*, 49-64.

52. Ramesh, C. Crystalline Transitions in Nylon 12. *Macromolecules* (1999), *32*, 5704-5706.

53. Yao, H.; Zhu, J.; Wilkie, C.A..Morgan, A.B. Crown ether-modified clays and their polystyrene nanocomposites. *Polymer Engineering & Science* (2002), *42*, 1808-1814.

54. Okada, A..Usuki, A. Twenty Years of Polymer-Clay Nanocomposites. *Macromolecular Materials and Engineering* (2006), *291*, 1449-1476.

55. Fornes, T.D.; Hunter, D.L..Paul, D.R. Nylon-6 Nanocomposites from Alkylammonium-Modified Clay: The Role of Alkyl Tails on Exfoliation. *Macromolecules* (2004), *37*, 1793-1798.

56. Reichert, P.; Kressler, J.; Thomann, R.; Müllhaupt, R..Stöppelmann, G. Nanocomposites based on a synthetic layer silicate and polyamide-12. *Acta Polymerica* (1998), *49*, 116-123.

57. Kim, G.M.; Lee, D.H.; Hoffmann, B.; Kressler, J..Stöppelmann, G. Influence of nanofillers on the deformation process in layered silicate/polyamide-12 nanocomposites. *Polymer* (2001), *42*, 1095-1100.

58. McNally, T.; Raymond Murphy, W.; Lew, C.Y.; Turner, R.J..Brennan, G.P. Polyamide-12 layered silicate nanocomposites by melt blending. *Polymer* (2003), *44*, 2761-2772.

59. Phang, I.Y.; Liu, T.; Mohamed, A.; Pramoda, K.P.; Chen, L.; Shen, L.; Chow, S.Y.; He, C.; Lu, X..Hu, X. Morphology, thermal and mechanical properties of nylon 12/organoclay nanocomposites prepared by melt compounding. *Polymer International* (2005), *54*, 456-464.

60. Gill, Y.Q.; Abid, U..Song, M. High performance Nylon12/clay nanocomposites for potential packaging applications. *Journal of Applied Polymer Science* (2020), *137*, 49247.

61. Olmo, C.; Amestoy, H.; Casas, M.T.; Martínez, J.C.; Franco, L.; Sarasua, J.-R..Puiggalí, J. Preparation of Nanocomposites of Poly(ε-caprolactone) and Multi-Walled Carbon Nanotubes by Ultrasound Micro-Molding. Influence of Nanotubes on Melting and Crystallization. *Polymers* (2017), *9*, 322.

62. Olmo, C.; Franco, L.; del Valle, L.J..Puiggalí, J. Preparation of Medicated Polylactide Micropieces by Means of Ultrasonic Technology. *Applied Sciences* (2019), *9*, 2360.

63. EOS, Polyamide 12 for 3D Printing, (2021). https://www.eos.info/en/additive-manufacturing/3d-printing-plastic/sls-polymer-materials/polyamide-pa-12-alumide.

64. Nicholson, D.A..Rutledge, G.C. Flow-induced inhomogeneity and enhanced nucleation in a long alkane melt. *Polymer* (2020), *200*, 122605.

65. Morales-Gámez, L.; Casas, M.T.; Franco, L..Puiggalí, J. Structural transitions of nylon 47 and clay influence on its crystallization behavior. *European Polymer Journal* (2013), *49*, 1354-1364.

5. Even-Odd polyamides: Crystalline structures and Polymorphic transitions

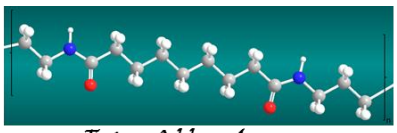

Even-Odd nylon

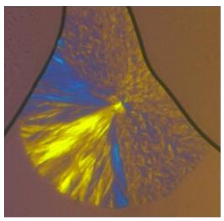

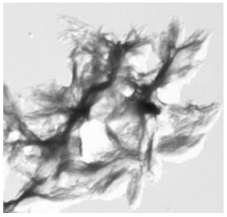

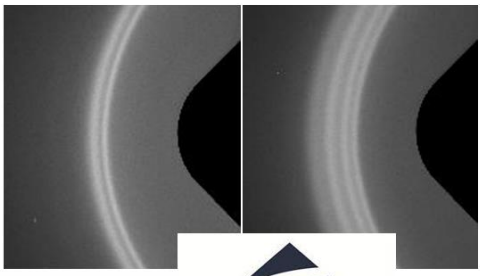

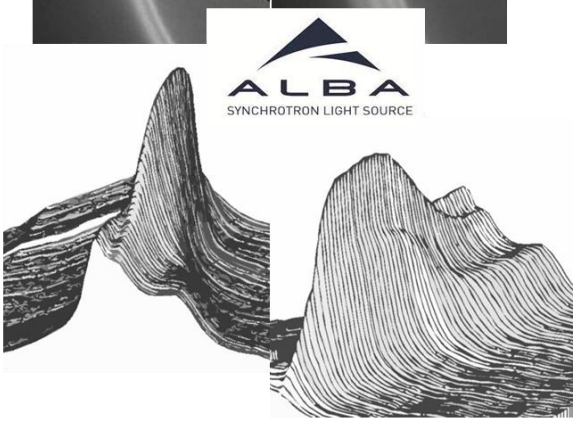

Polyamides based on even diamines (i.e. 1,4-diaminobutane, 1,8-diaminododecane and 1,12-diaminooctane and) and azelaic acid (nylons 4 9, 8 9 and 12 9 respectively) and copolyamides derived from 1,4-butanediamine and different mixtures of odd dicarboxylic acids (i.e., glutaric and azelaic acids with 3 and 7 groups, respectively), have been synthesized, characterized and structurally studied. These last copolyamides were named as nylons 4, 5+9_X where X refers to the molar feed percentage of azelate units.

Structural transitions of nylons 12 9, 8 9, 4 9, 4 5 and copolymers derived from 1,4-diaminobutane and different ratios of glutaric and azelaic acids (nylon 4, 5+9) were investigated on heating and cooling processes using real time calorimetric, spectroscopic and X-ray diffraction data. These even-odd nylons had three polymorphic forms related to structures where hydrogen bonds were established in two planar directions. Heating processes showed a first structural transition at low temperature where the two strong reflections related to the packing mode of the low temperature structure (form I) disappeared instead of moving together and merging into a single reflection, as observed for conventional even-even nylons. The high temperature structure corresponded to a typical pseudohexagonal packing (form III) attained after the named Brill transition temperature. Moreover, an intermediate crystalline structure (form II) is developed on heating before merging to form III. Structural transitions were not completely reversible for nylon 8 9 and 12 9 since form II became clearly predominant at room temperature in subsequent cooling processes, especially for nylon 12 9 where form I and II coexist at room temperature in the as-synthesized sample. As seen for nylon 4 9 polymorphic transitions are highly dependent on the initial crystalline structure, being enhanced the structural transition from the low temperature structure to the intermediate one when traces of the latter were initially present. For example, transition to form II was not presence in the as-synthesized sample of nylon 4 9 while it is in the melt crystallized sample. Same behavior was seen in the polymorphic transitions of nylon 4, 5+9 copolymers, transition to the intermediate structure (form II) were not detected during heating for samples exclusively crystallized in the form I (these enriched on the azelate component).

A single spherulite morphology with negative birefringence and a flat-on edge-on lamellar disposition was obtained for nylons 12 9 and 8 9 crystallized from the melt state. Polyamide 4 9 crystallized from the melt state gave rise to negative birefringent spherulites with a morphology (axialitic, speckled or ringed) that was dependent on the crystallization temperature.

Copolyamides were able to crystallize even for samples with comonomer percentages close to 50%. Negative and ringed spherulites from the melt state and small lath-like lamellar crystals

from dilute solution crystallizations were attained. Furthermore, calorimetric data pointed out the exclusion of the less abundant monomer from the lattice of the predominant structure.

Crystalline morphology of nylon 4 9 have been studied by means of optical and transmission electron microscopies. Rhombic crystals were characteristic of crystallization from glycerin dilute solutions, although the final morphology was dependent on the crystallization temperature. In any case, a single electron diffraction pattern was always obtained, being characteristic a 2 *mm* symmetry and reflections at spacings that were indicative of a projected rectangular unit cell with hydrogen bonds established along two planar directions (i.e., the diagonals of the unit cell), as it was determined from related polyamides.

Representative morphologies attained with the copolymer nylon 4 5+9_50 shows the formation of aggregates derived from a common nucleus and having radial arms with extremities consistent on small lath-like single crystals. The pattern showed again the characteristic 2*mm* symmetry with four prominent reflections at 0.385 nm. However, the crystal morphology changes to rectangular instead of rhombic geometry.

Kinetic analyses indicated that nylons 12 9 and 8 9 crystallized according to a single regime and a thermal nucleation. Results also pointed out a secondary nucleation constant for nylon 12 9 higher than that for nylon 8 9, suggesting greater difficulty in crystallizing when the amide content decreased. In contrast nylon 4 9 crystallize according to two growth mechanisms (Regimes II and III), which reflect distinct secondary nucleation rates.

Calorimetric analyses of copolymers revealed a complex behavior with multiple melting peaks associated to lamellar reordering and the presence of defective crystals. Equilibrium melting temperatures were evaluated and showed a eutectic behavior with composition.

5.1. Materials and Methods

5.1.1. Materials

5.1.1.1. Synthesis of Nylon 8 9 and 12 9

All reagents and solvents were purchased from Sigma-Aldrich and used without purification. Nylons 8 9 and 12 9 were synthesized by interfacial polycondensation of azeloyl dichloride with1,8-diaminooctane and1,12-diaminododecane, respectively. Nylon 8 9 was initially synthesized by dropwise addition of approximately 15 mmol of the dichloride dissolved in 75 mL of dry carbon tetrachloride to 75 mL of a stirred aqueous solution containing 15 mmol of 1,8-diaminooctane and 2.4 g of sodium hydroxide. After addition was complete a film was formed at the interface but the final molecular weight was moderate (M_n = 13,000 g/mol). This synthesis was improved according to the method reported for nylon 6, 10,[1] where an excess of diamine was employed (i.e. ×2.5), the sodium hydroxide was substituted by sodium carbonate and the organic solution was vigorously stirred before addition of the aqueous layer.

This method was slightly modified again for the synthesis of nylon 12 9 due to the water insolubility of the 1,12-diaminododecane. In this case, the diamine was dissolved in a mixture of water/acetone (2:1). A powdered polymer was formed instead of a continuous film and consequently reaction was carried out under stirring for a minimum period of 30 min.

Nylons 8 9 and 12 9 were in both cases recovered by filtration, washed successively with water, ethanol and ethyl ether before drying in a vacuum desiccator at 60 ºC. After that they were purified by precipitation with water of dilute formic acid solutions.

5.1.1.2. Synthesis of Nylon 49

All reagents and solvents were purchased from Sigma-Aldrich (Sant Louis, MO, USA) and used without purification. Nylons 4 9 was synthesized by interfacial polycondensation of azeloyl dichloride with 1,4-diaminobutane. To this end, 15 mmol of the dichloride were dissolved in 75 mL of dry carbon tetrachloride and vigorously stirred while 75 mL of an aqueous solution containing 35 mmol of 1,4-diaminobutane and 6.4 g of sodium carbonate was dropwise added. After addition was complete, stirring was kept for 30 min and then the powdered polymer was recovered by filtration, washed successively with water, ethanol and ethyl ether before drying in a vacuum desiccator at 60 °C. After that, it was purified by precipitation, by adding water to a dilute formic acid solution.

5.1.1.3. Synthesis of copolymers

All reagents and solvents were purchased from Sigma-Aldrich and used without purification. Copolymers were synthesized by interfacial polycondensation with sodium carbonate as proton acceptor and carbon tetrachloride as organic solvent (**Fig. 5-1).** To this end, 15 mmol of the appropriate dichloride mixture were dissolved in 75 mL of dry carbon tetrachloride and vigorously stirred while 75 mL of an aqueous solution containing 34.5 mmol of 1,4-diaminobutane and 6.4 g of sodium carbonate was dropwise added. After addition was complete, stirring was kept for 30 min and then the powdered polymer was recovered by filtration, washed successively with water, ethanol and ethyl ether before drying in a vacuum desiccator at 60 °C. After that, polymers were purified by precipitation of their solutions in formic acid (10 mg/ml) by dropwise addition of methanol. Polymers were finally filtered, rinsed again with water, ethanol and acetone and kept in a vacuum desiccator for one week.

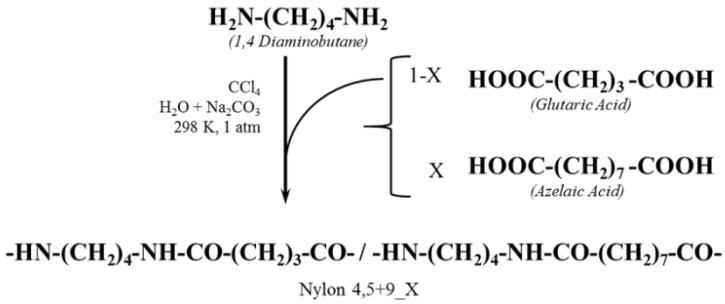

Fig. 5-1. *Scheme showing the synthesis of nylons 4,5+9_X.*

5.1.2. Measurements

Molecular weights of synthesized samples were determined by gel permeation chromatography (GPC). A Shimadzu LC-8A cromatograph (Shimadzu, Tokyo, Japan) equipped with an Empower computer program (Waters) was employed together with a PL HFIP gel column (Polymer Lab, Agilent Technologies Deutschland GmbH, Böbligen, Germany)) and a refractive index detector RID-10A (Shimadzu, Tokyo, Japan). Molecular weights were calibrated using polymethyl methacrylate standards.

Infrared absorption spectroscopic data were acquired with a FTIR 4100 Jasco spectrometer (Jasco International Co. Ltd., Tokyo, Japan) dotted with attenuated total reflection (ATR) (Specac model MKII Golden Gate. A heated Diamond Top-Plate was employed to study thermal induced transition.

^{1}H nuclear magnetic resonance (NMR) spectra were recorded on A Bruker AMX-300 spectrometer (Bruker Co., Bremen, Germany) at 25.0 °C operating at 300.1 MHz and 25 °C was used

to record ^{1}H NMM spectra. A mixture of deuterated chloroform and trifluoroacetic acid (9:1) was employed as solvent. Tetramethylsilan was added as internal reference.

Differential scanning calorimetric data were recorded with a TA instrument Q100 series (New Casttle, DE, USA) equipped with a refrigerated cooling system. Measurements were carried out with samples weighting approximately 5 mg and under a flow of dry nitrogen. Thermal characterization involved a four-run protocol consisting in: a first heating run (20 °C/min) of the as-synthesized sample, a cooling run (10 °C/min) after keeping the sample in the melt state for 3 min to erase thermal history and a subsequent heating run (20 °C/min) to determine the behavior of a non-isothermally crystallized sample.

Thermogravimetric (TGA) and differential thermogravimetric (DTGA) data were acquired with a Q50 thermogravimetric analyzer of TA Instruments (New Casttle, DE, USA) under a flow of dry nitrogen with approximately 5 mg samples and at a heating rate of 20 °C/min.

Samples for optical microscopy observations were prepared from small sections of melt-crystallized films, which were subsequently pressed between cover slides, inserted in a hot stage, heated a 10 °C higher than its melting point for 3 min and quickly cooled to the selected isothermal crystallization temperature. A Zeiss Axioscop 40 Pol light polarizing microscope (Carl Zeiss, Göttingen, Germany) was employed to measure the spherulite growth rate, while temperature was controlled with a Linkam system having a THMS 600 heating and freezing stage connected to an LNP 94 liquid nitrogen cooling system (Linkam Scientific, Tadworth, UK). A Zeiss AxiosCam MRC5 digital camera (Carl Zeiss, Göttingen, Germany) was employed to get micrographs at appropriate time intervals. Sign of spherulite birefringence was determined inserting a first-order red tint plate between crossed polarizers.

Lamellar crystals of nylon 4 9 and nylon 4,5+9_50 were obtained by isothermal crystallization in dilute (ca. 0.1 mg/mL) glycerin solutions at temperatures between 90 and 130 °C and between 30 °C and 50 °C, respectively. In all cases, the crystals were recovered from the mother liquor by centrifugation, repeatedly washed with *n*-butanol and deposited on carbon-coated grids, which were shadowed with Pt–Carbon at an angle of 15° for bright field observations.

A Philips TECNAI 10 electron microscope (Philips Electron Optics, Eindhoven, The Netherlands) was used and operated at 80 and 100 kV for bright field and electron diffraction modes, respectively. Selected area electron diffraction patterns and bright field micrographs were taken with a SIS MegaView digital camera (Olympus Soft Imaging Systems Inc., LLC, Lakewood, WA, USA). Diffraction patterns were internally calibrated with gold (d_{111} = 0.235 nm).

The real-time variable temperature synchrotron study was carried out on beamline BL11-NCD at ALBA (Cerdanyola del Vallès, Barcelona, Spain) by using a wavelength of 0.100 nm and a WAXD LX255-HS detector from Rayonix. Polymer samples were confined between Kapton films and then held on a Linkam hot stage with temperature control within ± 0.1 °C. WAXD profiles were acquired during heating and cooling runs in time frames of 20 s and rates of 10 °C/min. WAXD

diffraction patterns were calibrated by means of a geometrical calibration process of a well-known sample (standard Cr_2O_3). Diffraction profiles were normalized to the beam intensity and corrected considering the empty sample background.

5.2. Temperature-induced structural changes in even-odd nylons with long polymethylene: Nylons 8 9 and 12 9.

5.2.1. Introduction

Nylons, or aliphatic polyamides, are important industrial materials due to their excellent physical properties which include high strength, abrasion resistance, ductility and good stability at high temperatures [2, 3]. Recent studies have also demonstrated that several nylons derived from odd units might be interesting for electroactive applications[4]. The geometry and density of hydrogen bonds play a key role in the crystallization process, the crystalline structure and the final properties of nylons[5]. In general, nylons are semicrystalline polymers capable of adopting different crystalline structures depending on the number and parity of methylene groups of their repeat unit. The most conventional structures of nylons are found in even derivatives (i.e. those synthesized from ω-amino acids and those obtained from diamines and dicarboxylic acids). These structures are based on the stack of sheets composed of hydrogen bonded molecular chains [6-12]. The chain folded sheets are held together by weak van der Waals forces and may have different packing modes (e.g. the progressive and alternating shear characteristic of α and β forms, respectively)[5]. The corresponding X-ray fiber diffraction patterns of such structures are characterized by the presence of two strong equatorial reflections associated with intrasheet and intersheet spacings and appearing close to 0.440 and 0.380 nm, respectively.

On heating, even and even-even nylons can undergo a transition still not well understood where the two strong reflections in the diffraction patterns are seen to move together and meet, typically at a spacing close to 0.415 nm which defines a pseudohexagonal phase. The temperature at which this phenomenon occurs is the so called Brill transition temperature[13]. For even-even nylons with one or more relatively short alkane segments, this temperature is below the melting point, while for most others the two temperatures are practically coincident [14]. Note that the melting point increases with the density of hydrogen bonds along the chain, and consequently the structural transition can be observed for nylons with short aliphatic segments.

Brill transition has been widely discussed for nylons having the indicated sheet structure but interpretation is still controversial, especially when other polymorphic forms can be observed. For example, a new pseudohexagonal structure was described for some nylons (e.g. nylon 6[15]) depending on the temperature at which they crystallized from the melt. This phase, which was obtained at high supercoolings, rendered the Brill structure on heating and the typical sheet structure on cooling. In addition, other nylons adopt another pseudohexagonal structure known as *γ-phase*, which is

characterized by the establishment of intersheet hydrogen bonds between parallel chains[16]. In the case of nylon 6, the γ structure cannot undergo polymorphic transitions on both heating and cooling runs, and could therefore be distinguished from the above pseudohexagonal form. The hydrogen bonding pattern of this structure is probably different from that found in the γ-phase (i.e. intrasheet hydrogen bonds between antiparallel chains are established) despite the similarity of the packing spacings.

Attention was consequently paid to the hydrogen bonding arrangement during heating and cooling processes. First interpretations assumed a reorganization of hydrogen bonds during heating that gave rise to a network where hydrogen bonds were established along three planar directions, in contrast with the initial one-dimensional hydrogen bonding arrangement [17, 18].This model therefore implies the breakage of some intrasheet hydrogen bonds and the formation of intersheet bonds. The latter can counteract a weakening of the van der Waals interactions between layers as the intersheet spacing increases because of thermal dilatation. Note that the population of hydrogen bonds can be different in the three trigonal directions, and that is why properties (e.g. birefringence) along them may vary. Alternatively, some authors argued from NMR and FTIR results that hydrogen bonds do not break during heating, and consequently the sheet-like structure remains at high temperatures[19-23]. Basically, the methylene segments started to disorder and the torsional angles of amide–CH_2 bonds changed. In parallel with these structural changes, the hydrogen bonds became gradually weaker.

Different structures with hydrogen bonds established along more than one direction have also been postulated for nylons. Logically, in this case, breakage of intermolecular interactions is not necessary to justify temperature-induced structural changes, which are mainly a consequence of the increasing degrees of freedom of the alkane segments. Formation of a network of intermolecular hydrogen bonds can be justified by: a) Conformational preferences of peculiar residues such as glycine and malonic acid, and b) Optimization of the hydrogen bonding geometry. Specifically, alternate copolymers[24] and oligomers[25] constituted by ω-amino acid and glycine units adopt a similar structure (i.e. with three planar hydrogen bonding directions) to that described for polyglycine II[26], whereas structures with two hydrogen bonding directions have been postulated for polyamides[27] derived from a diamine and malonic acid. This kind of structure was also deduced from crystallographic analysis of small model compounds[28].

Nylons having odd diamine or dicarboxylic units (i.e. odd-even or even-odd nylons) cannot form the typical sheet structure when molecular chains have an extended planar zigzag conformation as shown in **Fig. 5-2.** Nevertheless, X-ray diffraction patterns of solution crystallized samples usually showed the typical strong reflections of conventional nylons (e.g. those appearing at spacings close to 0.440 and 0.380 nm). This feature has been described for both odd-even nylons, such as 5 6[29, 30], 5 10[31], 9 2[32, 33], 11 10[34], 11 12[34], and 13 6[35], and even-odd nylons like 6 5[36, 37],12 5[38], 6 13[39], 4 7[40] and 6 9[41, 42].Therefore, a new structure based on a molecular chain conformation that causes a slight rotation of consecutive amide groups of the odd diamide unit was proposed. This structure allows the

establishment of strong hydrogen bonding interactions with four neighboring chains when they were conveniently shifted along the chain axis direction

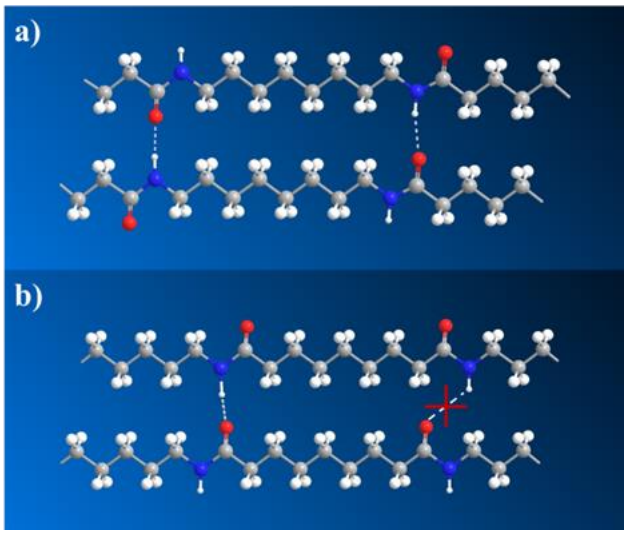

Fig. 5-2. *Scheme comparing the hydrogen bonding geometry that could be stablished between nylon 8 8 (a) and nylon 8 9 (b) chains having an all trans conformation.*

Accurate analyses of diffraction patterns performed during heating and cooling runs of some representative even-odd nylons having the indicated two-hydrogen bonding structure (named as form I) demonstrated that a pseudohexagonal phase (named as form III) was attained at high temperature. However, a new intermediate structure close to a pseudohexagonal form (named as form II) could also be observed in some cases. Thus, nylons 4 7[40] and 6 9[42] gave predominantly rise to form II when crystallized from the melt state, but a partial transition towards form I could be detected at low temperature (e.g. 80-100 ºC). On the contrary, solution crystallized samples showed a well differentiated behavior on heating. Specifically, nylon 4 7 underwent a complete transition towards form II at a temperature that was again close to 100 ºC (while nylon 6 9 showed only a direct transition from form I to form III). The structural changes from form I to form II seem only to involve a change in the rotation angle between consecutive amide groups of the odd unit and a slight modification in the packing geometry. That is, a breakage of hydrogen bonds is not expected at such low temperatures. In addition, this transition influences on properties and specifically a reversible change on the birefringence spherulite sign has been reported[40, 42].

The different structural behavior of nylons 4 7 and 6 9 on heating is difficult to explain considering their similar crystalline structure at low temperature (i.e. form I). Therefore, a possible influence of the length of the polymethylene segment should be taken into account. Note that both diamine and dicarboxylic units are longer for nylon 6 9. The present work is focused on the study of nylons 8 9 and 12 9, whose diamine unit is slightly or considerably longer than that of nylon 6 9. A second goal of the paper is the melt crystallization study (i.e. morphology and kinetics) of these polyamides characterized by a peculiar structure different from that of conventional nylons. Although

the spherulitic morphology of several even-odd polyamides has previously been studied[30, 37, 40, 42, 43], no data concerning crystallization kinetics have been reported.

5.2.2. Results and Discussion

5.2.2.1. Chemical characterization

The chemical constitution of both polymers was checked by infrared and ^{1}H NMR spectroscopy and molecular weight and polydispersity index were estimated by GPC. A 60% yield, a polydispersity index of 2.5 and a number average molecular weight of 21,000 were obtained for nylon 8 9. The corresponding values for nylon 12 9 were 70%, 2.1 and 15,000, respectively.

Infrared spectra of the two studied nylons showed all the characteristic absorption bands of amide and methylene groups at≈ 3302 cm^{-1} (Amide A, N-H stretching), ≈3079 cm^{-1}(Amide B, overtone of amide II), 2922-2917 and 2850 cm^{-1} (asymmetric and symmetric CH-stretching bands), ≈ 1633 cm^{-1}(Amide I, C=O stretching), ≈ 1545 cm^{-1}(Amide II, C-N stretching and CO-N-H bending), ≈ 940cm^{-1}(Amide IV, C-CO stretch), ≈ 721 cm^{-1} (CH_2 waging), ≈ 690 cm^{-1} (Amide V, N-H out of plane bending) and ≈ 580cm^{-1} (Amide VI, C=O out of plane bending).

^{1}H NMR spectra were characterized by peaks at 3.56 ppm (NHCH_2, broad, 4H), 2.65 ppm (COCH_2, triplet, 4H), 1.76 ppm (NHCH_2CH_2, broad, 4H), 1.71 (COCH$_2$CH_2, broad, 4H) and 1.41 ppm (-(CH$_2$)$_4$- + -(CH$_2$)$_3$-, broad, 14H) for nylon 8 9 and 3.51 ppm (NHCH_2, broad, 4H), 2.65 ppm (COCH_2, triplet, 4H), 1.73 ppm (NHCH_2CH_2, broad, 4H), 1.71 (COCH$_2$CH_2, broad, 4H) and 1.35 ppm (-(CH$_2$)$_8$- + -(CH$_2$)$_3$-, broad, 22H) for nylon 12 9.

5.2.2.2. Thermal properties

Fig. 5-3 shows a sequence of three scans of the as-synthesized nylons 8 9 and 12 9samples. As expected, the melting point of nylon 8 9 (T_m= 203 ºC) is higher than that of nylon 12 9 (T_m= 184 ºC) because the diamine segment of the former is shorter. Also, these temperatures are similar to those determined for other even-odd nylons with the same methylene content as nylons 6 11[44](T_m= 212 ºC) and 10 11[44] (T_m= 190 ºC). In both cases, the glass transition is clearly visible in the first heating run and appears at very close temperatures (52 ºC for nylon 8 9 and 51 ºC for nylon 12 9). In any case, the solution crystallized samples have a significant amorphous character.

The first heating run of nylon 8 9 showed a defined endothermic peak at 203 ºC and a wide exothermic interval from 90 ºC to 175 ºC, which is indicative of the occurrence of a significant recrystallization process. Note the low melting enthalpy compared with that detected for the melt crystallized sample (i.e. 57 as opposed to 79 J/g). The cooling run revealed a narrow exothermic crystallization peak at 178 ºC and a broad exothermal process at lower temperatures which could be associated with a secondary crystallization or even a structural transition (see the arrow pointing to a

small peak close to 125 ºC). The subsequent heating run showed a complex fusion where the main peak at 203 ºC is preceded by two smaller peaks (180ºC and 191ºC). The intermediate temperature endothermic peak can be a consequence of the melting of thin lamellar crystals having the high temperature structure (i.e. form III), the lowest temperature peak can be related to defective lamellar crystals having a crystalline structure different from form III (e.g. form II), and finally the highest temperature peak is attributed to the melting of recrystallized crystals during the heating process.

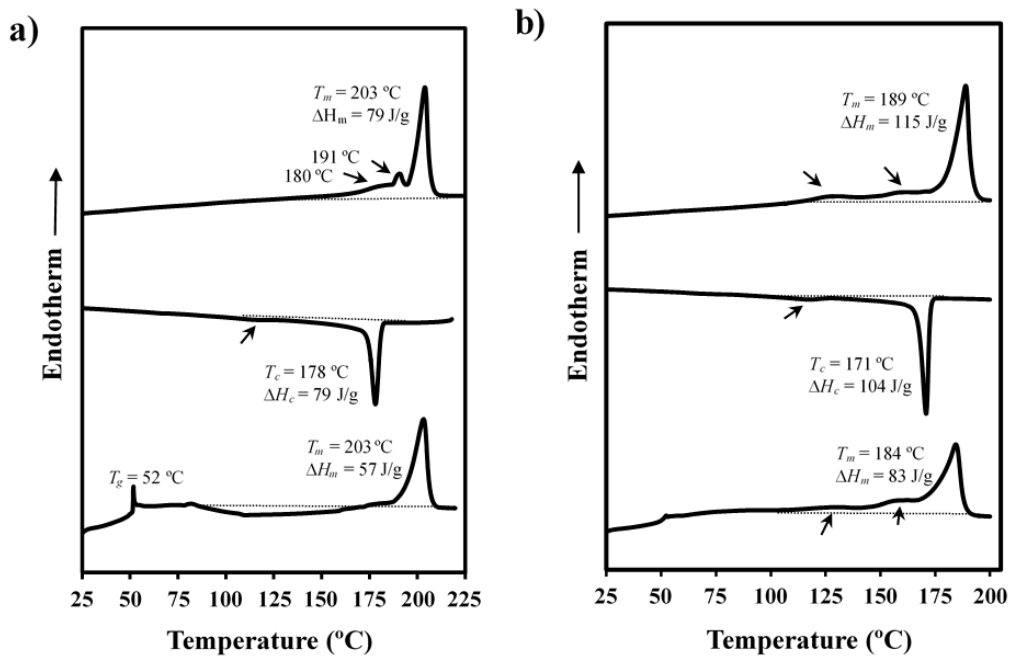

Fig. 5-3. *From down to up, calorimetric scans of the heating run of the as-synthesized sample, the cooling run from the melt state and the subsequent heating run of nylon 8 9 (**a**) and nylon 12 9 (**b**). Arrows indicate small endothermic and exothermic peaks.*

Melting behavior was slightly different for nylon 12 9. In this case, the first run showed a main and broad melting peak at 184 ºC and two small and broad peaks at 130 ºC and 160 ºC. This last temperature is very low for a melting process and both endotherms should be related to structural transitions (e.g. from form I to form II and from form II to form III). Note that the endotherm at 180 ºC was also observed for nylon 8 9 whereas the previous one could not be detected due to the significant exothermic process that took place at the low temperature range. It must be pointed out that an exothermic process during the first heating run of nylon 12 9 cannot be completely discarded in view of the initial high amorphous content (revealed by the clear glass transition) and a compensation effect caused by the indicated endothermic processes. The trace of the cooling run is similar to that observed for nylon 8 9, with a narrow peak at 171ºC and a broad exothermic peak indicative of a secondary crystallization. A small exothermic peak (see arrow) that can be related to a polymorphic transition is also worth noting. The third run is similar to the first one although the main endothermic peak appears at a higher temperature (i.e. 189ºC). The melting enthalpy is clearly higher than that determined in the first heating run and is in agreement with the crystallization enthalpy of the second

run. For this reason, the second heating run does not reveal any exothermic process in the 100-175 ºC temperature intervals. By contrast, small endotherms are clearly visible although they may involve transitions of very minor phases, as will be discussed below.

The difference between the melting temperature (T_m) and the crystallization temperature (T_c) (i.e. ΔT) points to an easier crystallization process for nylon 12 9 as a consequence of its lower molecular weight (i.e. values of 25 ºC and 13 ºC were determined for nylons 8 9 and 12 9, respectively).

5.2.2.3. Equilibrium melting temperatures of nylons 8 9 and 12 9

Fig. 5-4a illustrates the melting behavior of nylon 12 9 samples isothermally crystallized at different temperatures in the 175 ºC - 185 ºC range. Logically, the low temperature endotherms (i.e. those appearing at 130 and 160 ºC) could not be detected and the high temperature peak appeared clearly split when the sample crystallized at the lowest temperature. The low temperature peak seemed to be associated with thinner crystals and gradually shifted to higher temperatures and increased in intensity when the crystallization temperature was raised. The high temperature peak, which appeared around 190 ºC, is related to the thicker crystals formed during the heating scan because of a lamellar reorganization, and was therefore always observed at the same temperature. Logically, the reorganization process was more significant when the sample crystallized at the lowest temperature. In this case, the high temperature peak was more intense and the difference in temperature between the two endotherms was greater. A similar behavior was observed for nylon 8 9, with the above peaks at 191 and 204 ºC being related to the reorganization process.

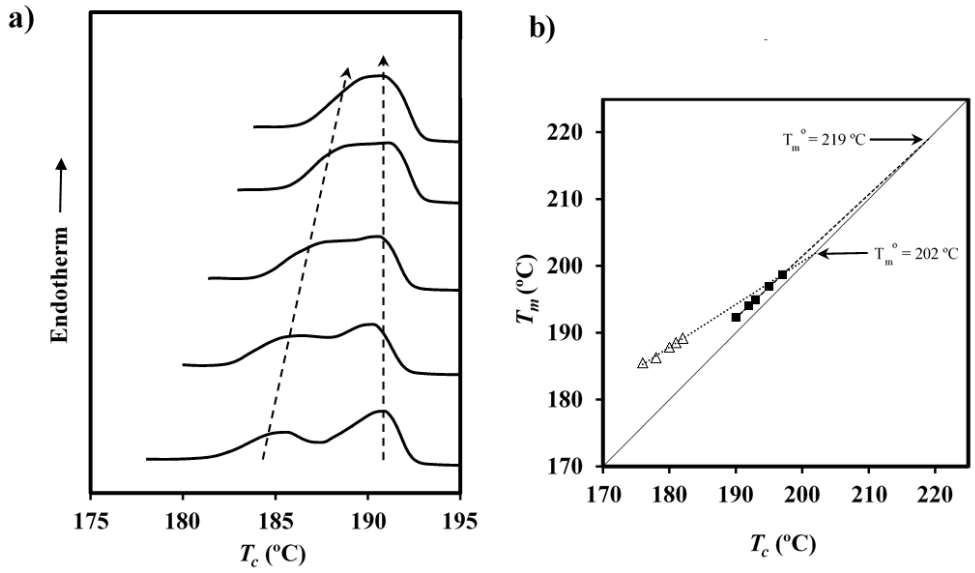

Fig. 5-4.*a)* *DSC heating runs of nylon 12 9 samples after being crystallized from the melt at (from down to up) 176 ºC, 178 ºC, 180 ºC, 181 ºC and 182 ºC. Evolution of main peaks is indicated by the dashed arrows.* ***b)*** *Hoffman-Weeks plot of temperatures corresponding to the melting peak versus crystallization temperature for nylon 8 9 (squares) and nylon 12 9 (triangles). Equilibrium melting temperatures are indicated for both nylons at the intersection point with the T_m=T_c line.*

A linear Hoffman-Weeks relationship[45] has been widely accepted to estimate the equilibrium melting point (T_m^o), which is defined as the melting temperature of infinitely thick crystals and determined by extrapolation of T_m versus T_c to $T_m = T_c$. Equilibrium melting temperatures of 202 ºC and 219 ºC were graphically deduced for nylons 12 9 and 8 9, respectively (**Fig. 5-4b**).

5.2.2.4. Wide angle X-ray diffraction analyses of nylon 8 9 polymorphic transitions during heating and cooling processes

Fig. 5-5a is a three-dimensional representation of the evolution of the WAXD profile of the as-synthesized nylon 8 9 during a heating process performed at 10 ºC/min from room temperature to fusion, and one-dimension profiles taken at some representative temperatures are given in **Fig. 5-5b**.

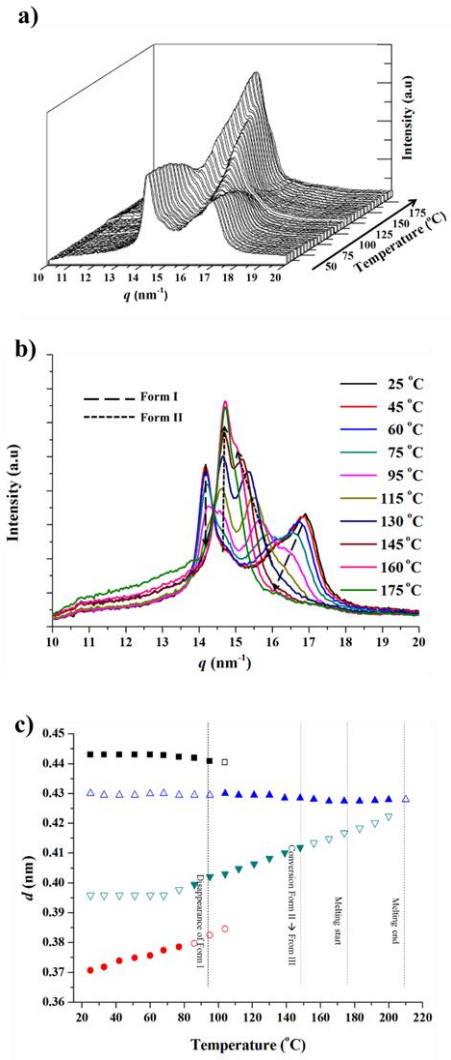

Fig. 5-5. ***a)*** *Three dimensional representation of WAXD profiles of nylon 8 9, during heating (10 ºC/ min) from room temperature to fusion.* ***b)*** *One-dimensional WAXD profiles of nylon 8 9 during heating at selected temperatures. Dashed and dotted lines represent the evolution of the main reflections of form I and form II, respectively.* ***c)*** *Evolution of the main reflections found in the diffraction pattern of nylon 8 9 during the heating process. Full and empty symbols indicate well-defined and intuited reflections, respectively. The temperatures at which structural transitions occur are indicated with vertical lines.*

Two very intense reflections of nylon 8 9 corresponding to spacings of 0.442 and 0.370 nm, which are characteristic of the structure with two hydrogen-bonding directions (form I), appeared at the beginning of the experiment. Two low intensity reflections were also observed at 0.430 and 0.395 nm (form II) at room temperature. Note that these spacings are clearly different from those found close to 0.415 nm in nylons having a pseudohexagonal γ structure with a single hydrogen-bonding direction. Initially, the intensity of the signals decreased slightly with increasing the temperature (i.e. to 95 ºC) and then (i.e. between 95 and 120 ºC) they practically disappeared. The spacing of the 0.370 reflection increased gradually during heating (i.e. to 0.384 nm) while that of the 0.442 reflection decreased only to 0.440 nm. At the same time, the 0.430 and 0.395 nm diffraction signals increased in intensity and moved together with increasing the temperature, meeting at a single spacing of 0.428 nm just before the melting point. The presence of a single peak suggests a typical Brill transition, where a pseudohexagonal packing (form III) is favored at a temperature slightly lower than the melting point.

The intensity of signals at 0.430 and 0.395 nm increased when the temperature was raised from 95 ºC to 150 ºC, where the conversion from form II to form III began. Above 150ºC, the behavior of signals was different, i.e. the intensity of the signal at 0.430 nm remained practically constant whereas that of the signal at 0.405 nm (initially at 0.395 nm) became weaker and the signal moved gradually to a higher spacing until reaching the 0.428 nm value.

In the last stages of the heating process, the intensity of the Bragg reflections began to decrease until becoming an amorphous asymmetric halo characteristic of the melt state. The evolution of all spacings with the temperature is graphically represented in **Fig. 5-5c**, where the occurrence of transitions is also highlighted.

The observed polymorphic transitions were not completely reversible when the sample was subsequently cooled (10 ºC/min) to room temperature. The 3D WAXD profiles in **Fig. 5-6a** show that nylon 8 9 first crystallized in the high temperature form III (i.e. only a single spacing at 0.428 nm was observed). Around 160 ºC, a weak signal started to appear at 0.420 nm, as is characteristic of form II, whereas the intensity of the high spacing reflection clearly decreased. When the temperature was around 120 °C, the transition from form III to form II finished, with two strong signals being clearly visible at 0.428 and 0.415nm. The spacing and intensity of the first reflection remained practically constant whereas they decreased for the second one, suggesting an anisotropy for thermal contraction. In fact, a spacing of 0.405 nm was determined at room temperature. Around 65 ºC, the diffraction pattern showed two very low intensity signals at 0.443 nm and 0.376 nm related to form I. The evolution of all spacings and the occurrence of structural transitions are given in **Fig. 5-6b**. It can be concluded that at room temperature both structures coexist, with form II being the predominant one, in disagreement with the room temperature pattern of the as-synthesized sample.

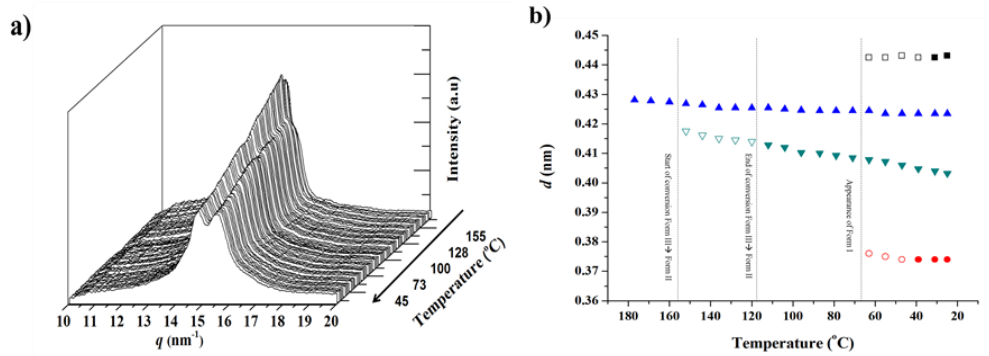

Fig. 5-6. ***a)*** *Three-dimensional representation of WAXD profiles of nylon 8 9 during cooling (10 ºC/min) from the melt state to room temperature.* ***b)*** *Changes on the spacing of the main reflections of nylon 8 9 during the cooling process. Full and empty symbols indicate well-defined and intuited reflections, respectively.*

For the sake of completeness, **Fig. 5-7** shows representative X-ray diffraction profiles and patterns taken at selected temperatures during heating and cooling runs. The difference in the diffraction patterns of the sample taken at 25 °C before heating and after crystallizing from the melt state is highlighted. In both cases, four rings associated with forms I and II could be detected, but the ratio between them changed drastically (i.e. forms I and II were predominant in the initial sample and the melt crystallized one, respectively). Note also that the reflections of both structures had similar intensity in the diffraction pattern taken at 95 ºC during the heating process.

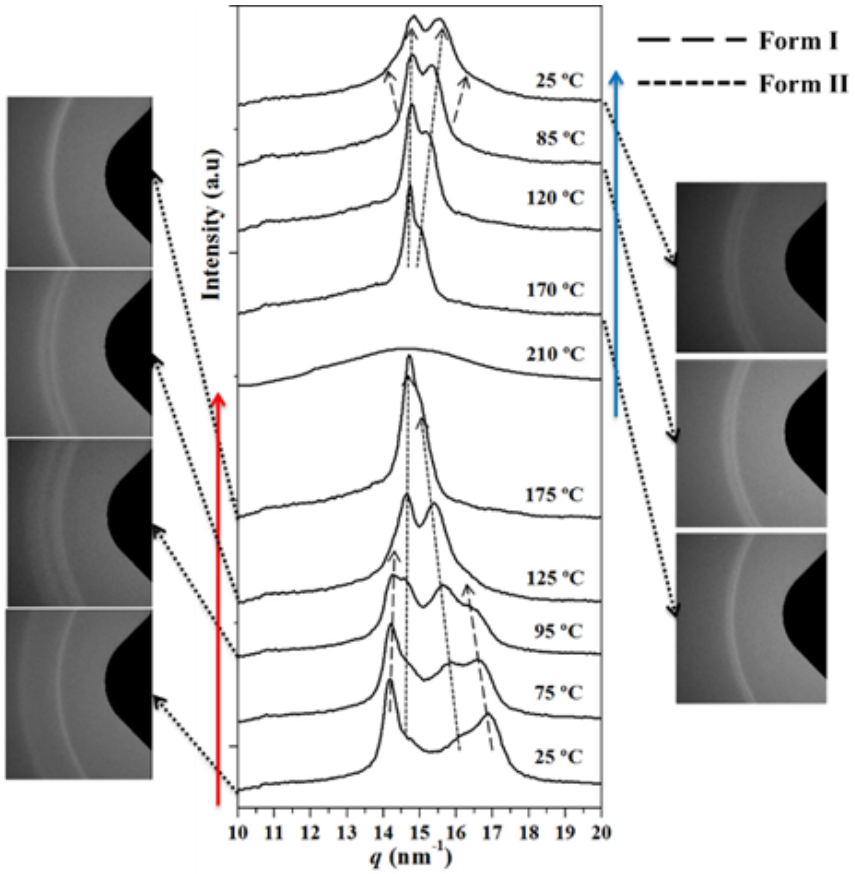

Fig. 5-7. *One-dimensional WAXD profiles of nylon 8 9 taken at selected temperatures during the heating scan (bottom of the graph) and the cooling scan (top of the graph). Dashed and dotted lines represent the evolution of the main reflections of form I and form II, respectively. Diffraction patterns corresponding to some characteristic temperatures are also included.*

In summary, nylon 8 9 has two different crystalline structures at room temperature depending on the thermal treatment of the sample. These structures are probably related to molecular arrangements where hydrogen bonds are established along two directions since transitions involving the breakage of intermolecular hydrogen bonds seem difficult to be favored at temperatures as low as 75 ºC-95 ºC. In any case, transitions from form I to form II and from form II to form III took place in wide temperature intervals that could be related to the low and broad peaks observed in the DSC scans.

5.2.2.5. Wide angle X-ray diffraction analyses of nylon 12 9 polymorphic transitions during heating and cooling processes

The evolution of X-ray diffraction profiles of the as-synthesized sample during heating at 10 ºC/min (**Fig. 5-8a**) is highly similar to the above evolution of nylon 8 9. Four reflections can be clearly observed in the initial pattern, two more intense at 0.446 and 0.382 nm, which are related to form I, and two less intense at 0.430 and 0.400 nm, which are related to form II. However, the initial proportion of form II is clearly higher for nylon 12 9 than for nylon 8 9. Around 120 ºC, the intensity of the former pair of signals decreased significantly whereas that of the latter pair of signals started to increase, suggesting the occurrence of a form I to form II structural transition. This is in clear agreement with the endothermic peak observed in the DSC heating scan. The peak at 0.400 nm shifted progressively to a larger spacing until reaching the peak at 0.430 nm at a temperature of 175 ºC. A typical pseudohexagonal arrangement (form III) was completely obtained before the melting process began.

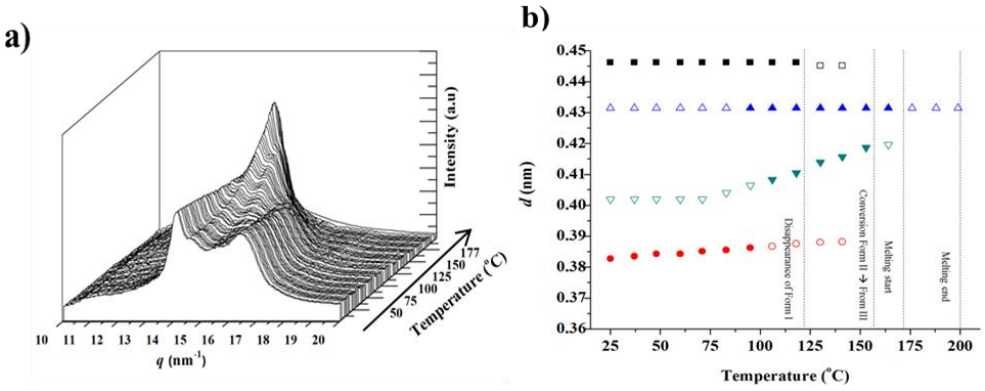

Fig. 5-8. ***a)*** *Three dimensional representation of WAXD profiles of nylon 12 9 during heating (10 ºC/min) from room temperature to fusion.* ***b)*** *Evolution of the main reflections found in the diffraction pattern of nylon 12 9 during the heating process. Full and empty symbols indicate well-defined and intuited reflections, respectively. The temperatures at which structural transitions occur are indicated with vertical lines.*

Fig. 5-8b illustrates the evolution of the spacing of the different signals during the heating process whereas **Fig. 5-9** shows one dimensional WAXD profiles and diffraction patterns taken at selected temperatures to better show the structural transitions. As can be seen, forms I and II have a similar importance in the profile taken at 125 ºC. A single peak, related to form III, is observed at 175

ºC, just before the melting temperature, where an amorphous halo was detected. The similar evolution of reflections of nylons 8 9 and 12 9 is worth noting. It agrees with that previously reported for nylon 4 7[39] and is different from that observed for nylon 6 9,[42] where only a form I to form III transition was detected on heating. Therefore, the observed polymorphism does not seem to be related to the length of the polymethylene segment, but rather it seems to be dependent on the presence of reminiscent crystals having the form II structure in the initial sample, as it is the case of nylons 4 7,[39] 8 9 and 12 9 but not of nylon 6 9.[41].

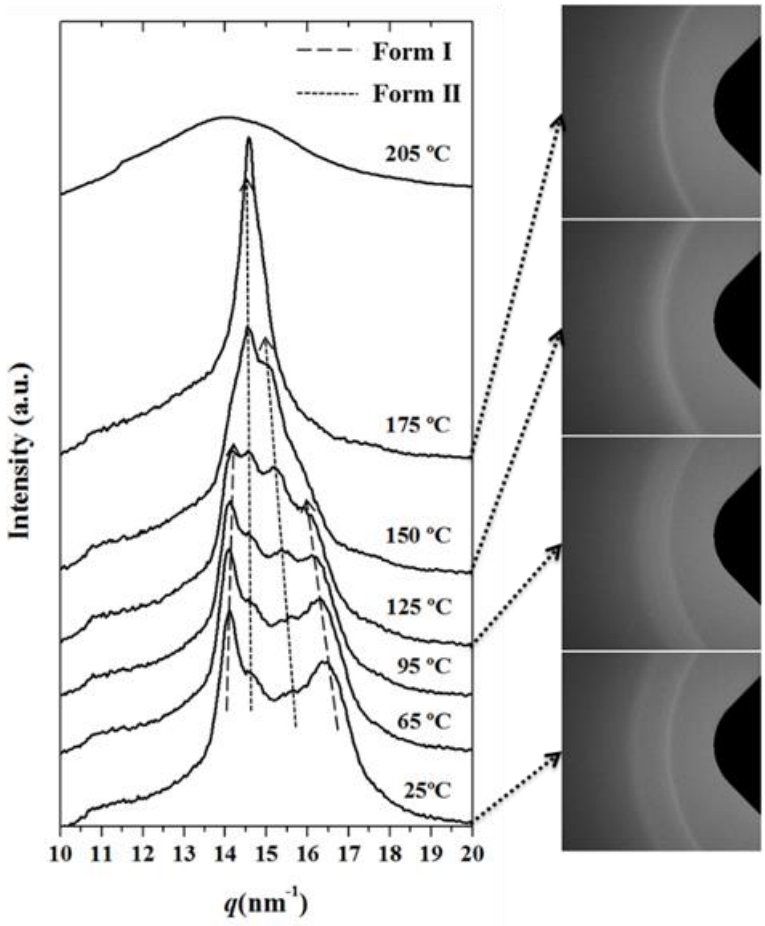

Fig. 5-9. *One-dimensional WAXD profiles of nylon 12 9 taken at selected temperatures during the heating scan. Dashed and dotted lines represent the evolution of the main reflections of form I and form II, respectively. Diffraction patterns corresponding to some characteristic temperatures are also included.*

When the polymer was cooled from the melt (**Fig. 5-10**), it crystallized into form III, as deduced from the single reflection at 0.430 nm. However, this reflection immediately became split into the two characteristic reflections of form II (i.e. 0.428 nm and 0.420-0.405 nm). Note that the intensity of the high spacing reflection clearly decreased in the 150 ºC-125 ºC temperature interval while the reflection at 0.420 nm increased in intensity and moved towards a spacing of 0.405 nm. The transition from form III to form II took place mainly in this temperature range, in agreement with the broad exothermic peak detected in the corresponding DSC scan. At the end of the cooling process, the

diffraction pattern consisted in two rings at 0.405 and 0.421 nm, but very weak signals associated with form I could also be made out.

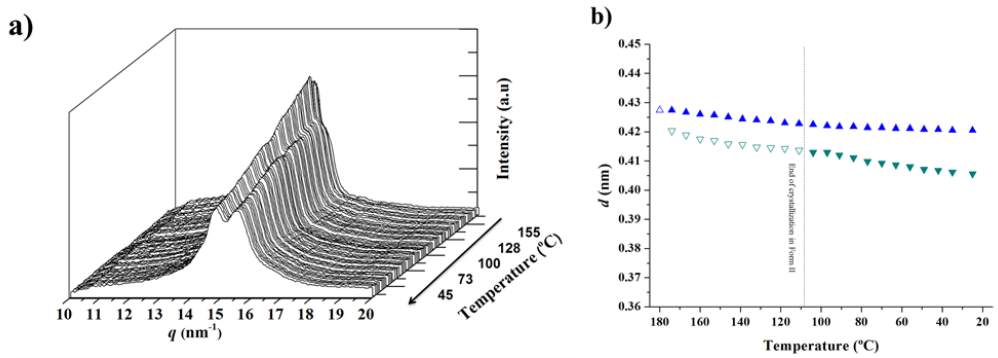

Fig. 5-10. ***a)*** *Three-dimensional representation of WAXD profiles of nylon 12 9 during cooling (10 ºC/min) from the melt state to room temperature.* ***b)*** *Changes on the spacing of the main reflections of nylon 12 9 during the cooling process. Full and empty symbols indicate well-defined and intuited reflections, respectively.*

Results also indicate that different ratios between form I and form II were achieved at room temperature depending on the crystallization process (i.e. from solution or from the melt). Furthermore, thermal treatment also had an effect on this ratio, as shown in the patterns of **Fig. 5-11.** Thus, a high ratio of form I was still observed when the as-synthesized sample was cooled after heating at a temperature of 150 ºC, namely, at a temperature where the transition to form II was practically completed. On the other hand, form II became predominant when the sample was heated to 175 ºC (i.e. before fusion). Nevertheless, a small proportion of form I could still be observed at room temperature, and specifically the corresponding signals were stronger than those made out for melt crystallized samples. It should be pointed out that some reminiscence of form I crystals should still occur at 175 ºC in such a way that they could act as nuclei for the development of such structure in the subsequent cooling process.

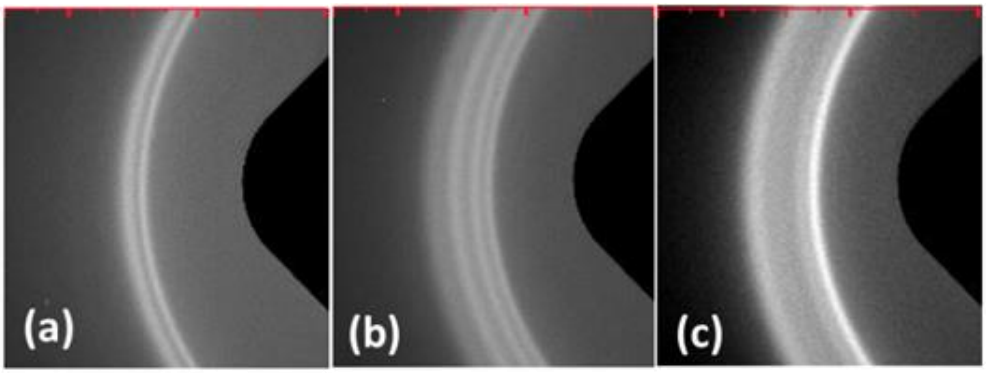

Fig. 5-11. *X-Ray diffraction patterns of nylon 12 9 at room temperature:* ***a)*** *Sample cooled from the melt state,* ***b)*** *Sample cooled from a partially melted state (i.e. from 175 ºC) and* ***c)*** *Sample cooled after being heated to 150 ºC (i.e. previous to fusion and before disappearance of form I).*

5.2.2.6. Temperature dependence of infrared amide A band

Crystalline transitions were also evaluated by FTIR spectra taken during the heating and cooling processes. In particular, temperature dependence of the amide A band was studied for nylon 8 9 because this polymer had the greatest ratio of form I during cooling (i.e. highest reversibility). The amide A band (NH stretching mode) is highly sensitive to the hydrogen bond geometry, and may therefore provide additional information concerning structural transitions induced by temperature changes.

Fig. 5-12 shows the evolution of the amide A band from room temperature to the melting temperature for the as-synthesized sample. Three different regions can be distinguished in the plot: first, a region where the wavenumber remained practically constant (3295 cm-1) up to a temperature close to 75 ºC, which is related to the beginning of a significant recrystallization process (DSC data) and the structural transformation from form I to form II (synchrotron data); second, a region where the wavenumber increased gradually (i.e. from 3295 to 3308 cm-1) because of the decrease in the strength of hydrogen bondings caused by the development of form II and their higher sensitivity to thermal expansion, and finally a last region at temperatures higher than 175 ºC where the wavenumber remained constant again (3308 cm-1), which corresponded to the development of form III (synchrotron data).

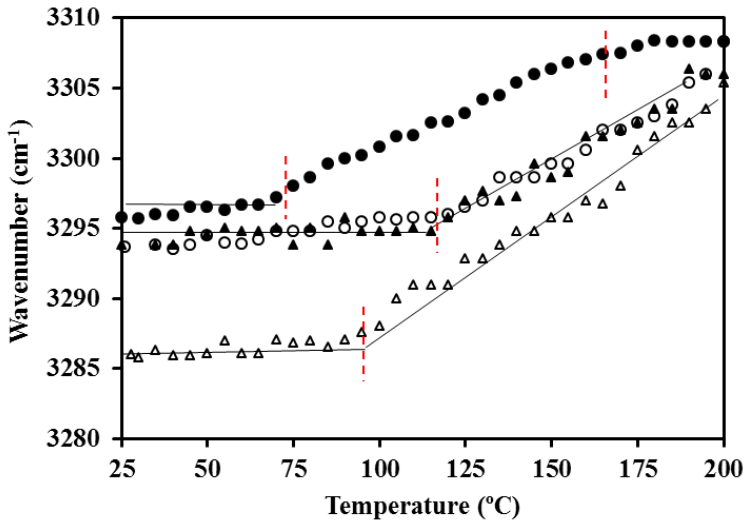

Fig. 5-12. *Variation of the wavenumber corresponding to the amide A absorption band of nylon 8 9 during a first heating run (full circles), the subsequent cooling (empty circles) and heating (full triangles) runs and finally a cooling run from an externally melted sample (empty triangles).*

When the sample was cooled from 200 ºC to room temperature, a decrease in the amide A band frequency was observed in the temperature range between 190 ºC and 110 ºC while a constant value was again detected at higher and lower temperatures (**Fig. 5-12**). These temperature limits are in agreement with the transition from form III to form II (190 ºC) and from form II to form I (110 ºC, although this temperature was slightly higher than that determined in DSC and synchrotron experiments). Logically, the contraction of the unit cell during the cooling process resulted in strong

hydrogen bonds because of the continuous decrease in intermolecular distance. The behavior observed in the cooling run was reproduced in a subsequent heating run, indicating the reversibility of all transitions. Note also that great differences were found between the first and the second heating run since the predominant initial structure was different in each case (form I and form II).

A crucial factor to consider is that it was not possible to completely melt the sample in these experiments because the temperature controller of the ATR could only reach a maximum temperature of 200 ºC (i.e. slightly lower than the melting temperature of nylon 8 9). Therefore, it was also interesting to evaluate the cooling run of a sample previously melted externally on a hotplate. **Fig. 5-12** shows a different behavior because the transition to form I took place at a lower temperature (i.e. 90 ºC), which, in this case, was in full agreement with DSC and X-ray diffraction observations. The difference in behavior between the two cooling runs could be due to a higher difficulty for the transition to occur when residual form I crystals were completely melted, namely when a potential nucleation effect was prevented. In this case, the wavenumber of the Amide A band decreased to 3286 cm-1, a value significantly lower than that observed for the as-synthesized sample (3295 cm-1). This difference is due to the predominant crystalline structure that is achieved at room temperature and indicates a better hydrogen bonding geometry for form II compared to form I.

5.2.2.7. Spherulitic morphologies

The only studies on the morphology of melt crystallized spherulites of even-odd polyamides derived from azelaic acid published so far are those concerning nylons 4 9[43] and 6 9[42]. Spherulites of both nylons showed a great diversity of morphologies depending on the crystallization temperature. Nevertheless, some peculiar and common trends could be detected.

Nylon 4 9 showed the formation of mixed spherulites comprised of a low positively birefringent zone and a higher negatively birefringent zone in a narrow temperature range. In fact, morphologies were rather complex and ranged from aggregates to not well understood flecked or mottled crystals. Furthermore, the birefringence signs of some of these spherulites changed during heating/cooling treatments. These preliminary observations were not interpreted from a structural point of view but suggested the occurrence of a reversible polymorphic transition that affected the birefringence sign. Logically, typical justifications given for conventional nylons with a single hydrogen-bonding direction cannot be applied[46, 47]. Note that a reversible change from a structure with hydrogen bonds aligned with the radial direction (positive birefringence) to a structure with tangential alignment (negative birefringence) implies a sheet reorganization that is not possible without causing melting of the initial spherulite.

Crystallization of nylon 6 9 could also give rise to positive and negative spherulites depending on the crystallization temperature[42]. A reversible change in the sign of birefringence was again observed for spherulites developed in a very narrow temperature interval ranging between 232ºC and 225ºC. These spherulites were characterized by a very low birefringence and a flat-on lamellar

disposition that allowed the detection of small changes derived from a modification in the packing mode. Interestingly, the change in optical properties took place in the low temperature range, where a transition from form I to form II was confirmed by synchrotron radiation experiments.

Crystallization experiments with nylons 8 9 and 12 9 were limited due to the high nucleation and fast crystal growth of these polymers. Therefore, isothermal measurements could only be performed in a very narrow temperature range. Polarizing optical microscopy observation of the crystallization process confirmed a thermal nucleation process because new nuclei emerged over time before impinging upon each other (**Fig. 5-13a-c**).

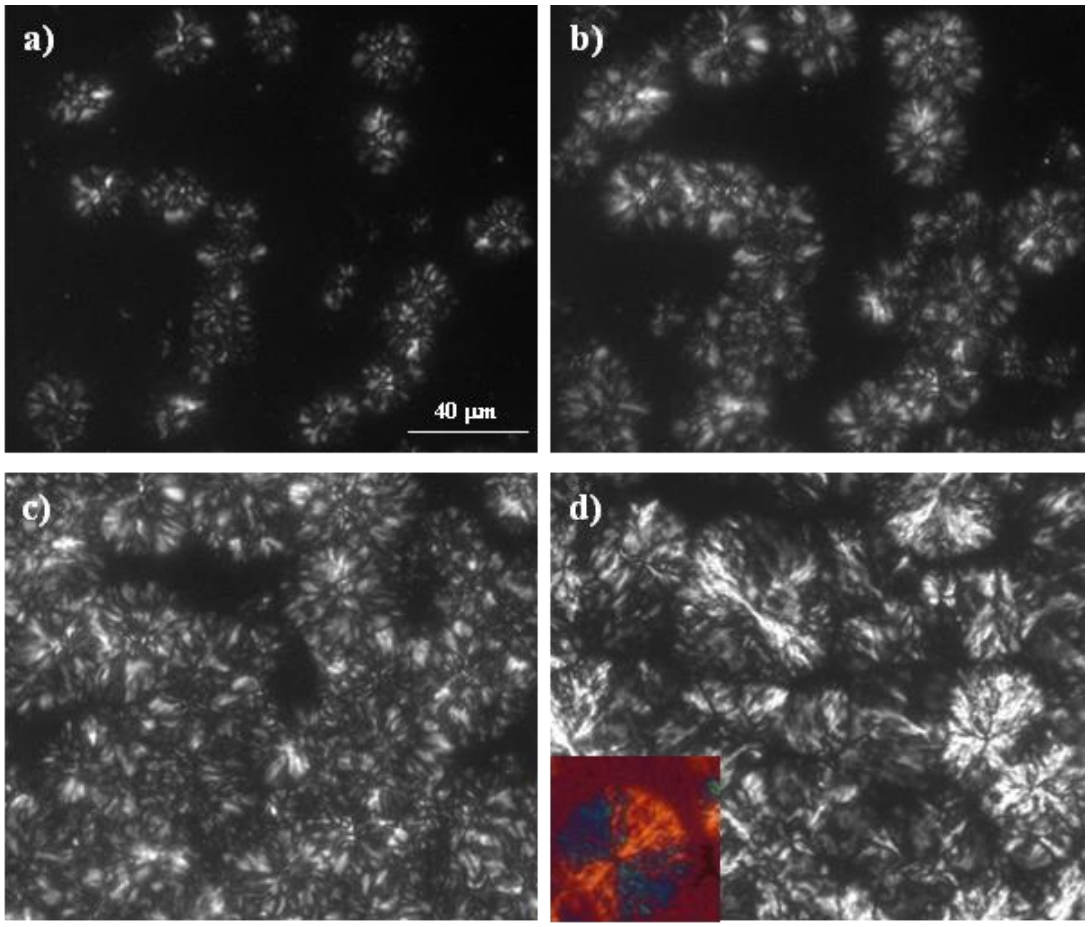

Fig. 5-13. *Polarized optical micrographs of samples isothermally crystallized at the indicated temperatures and crystallization times:* ***(a)*** *Nylon 8 9 at 200 ºC, 540 seconds;* ***(b)*** *Nylon 8 9 at 200 ºC, 1260 seconds* ***(c)*** *Nylon 8 9 at 200 ºC, 2625 seconds and* ***(d)*** *Nylon 12 9 at 180 ºC, 1850 seconds. A colour micrograph taken with a red tint plate is given in the inset of d) in order to observe the sign of birefringence. All micrographs were taken at the same magnification.*

Isothermal crystallization of nylon 89 from the melt rendered small spherulites with some axialite reminiscences over the studied narrow temperature range. Nylon 12 9 also crystallized from the melt, resulting in spherulites (**Fig. 5-13d**) with a fairly defined Maltese cross and a trend to a ringed texture. The birefringence sign remained negative for both nylons at all test temperatures. A flat-edge lamellar disposition was always observed and it was unfeasible to detect a birefringence change when small variations in the two hydrogen-bonding schemes occurred (i.e. from form II to form I).

The growth of individual spherulites as a function of time was measured by optical microscopy at different crystallization temperatures. After nucleating, they grew with a radius increasing linearly with time (**Fig. 5-14a**) up to impingement. Spherulite growth was studied in the temperature range where spherulites with adequate dimensions formed, i.e. from 195 to 203 ºC and from 175 to 185 ºC for nylons 8 9 and 12 9, respectively. The high nucleation density hindered the observation of growth at lower temperatures.

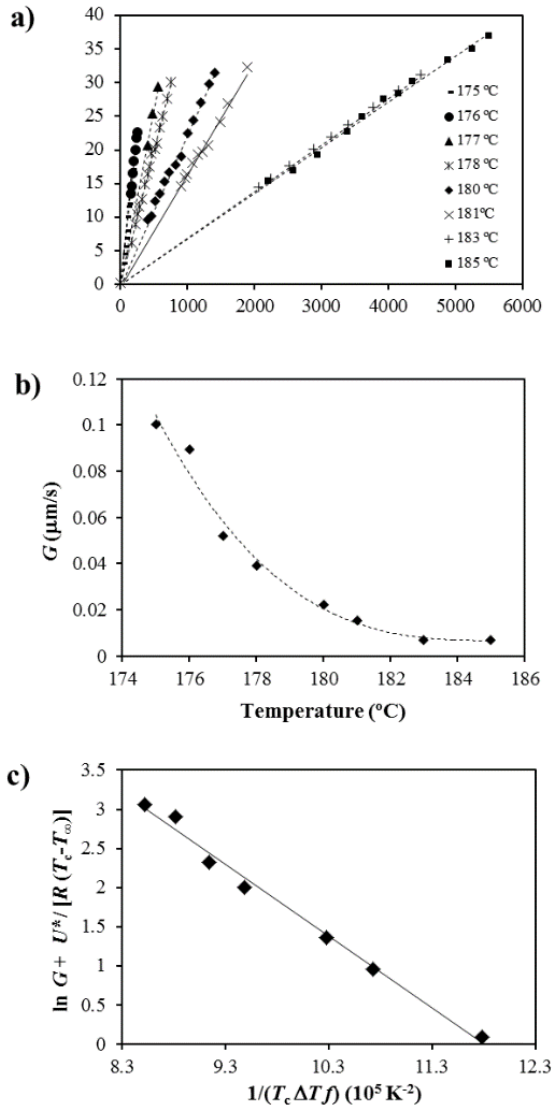

Fig. 5-14. ***a)*** *Plots of the radius of nylon 12 9 spherulites versus crystallization time for isothermal crystallizations performed at temperatures ranging between 175 ºC and 185 ºC.* ***b)*** *Temperature dependence of the crystal growth rate of spherulites of nylon 12 9.* ***c)*** *Plot of ln G + U* / {R (Tc-T∞)} versus 1 / (Tc ΔTf) to determine the Kg nucleation parameter of nylon 12 9.*

The growth rate of both nylons showed an exponential dependence with decreasing the temperature, but the exact temperature at which the maximum rate was attained could not be determined. Measured radial growth rates, *G*, varied from 0.002 μm/s at 203 ºC to 0.02 μm/s at 195 ºC for nylon 8 9 and from 0.007 μm/s at 185 ºC to 0.10 μm/s at 175 ºC for nylon 12 9. Higher values were always determined for nylon 12 9 (**Fig. 5-14b**), as expected from its lower molecular weight.

The radial growth rate, G, of polymer crystals can be described by the Lauritzen and Hoffman equation,[48] which is formulated as

$$G = G_0 \exp\{-U^*/(R(T_c-T_\infty))\} \exp\{-K_g/(T_c(\Delta T)f)\}, \quad (1)$$

where G_0 is a constant pre-exponential factor, U^* represents the activation energy characteristic of the transport of crystallizing segments across the liquid-crystal surface, T_∞ is the temperature below which such motion ceases, T_c is the crystallization temperature, R is the gas constant, K_g is the secondary nucleation constant, ΔT is the degree of supercooling measured as $T_m^0-T_c$, and f is a correction factor accounting for the variation in the bulk melting enthalpy per unit volume with temperature ($f= 2T_c/(T_m^0 + T_c)$).

The values of U^* and T_∞ hardly affect the temperature dependence of the radial growth rate at isothermal test temperatures far above the glass transition temperature. Thus, standard values reported by Suzuki and Kovacs[49] (U^*= 1500 cal/mol and $T_\infty = T_g$-30 K) were used in the calculation.

The rearrangement of equation 1 into a logarithmic form made it possible to obtain K_g from the slope of the linear plot of $\ln G + U^*/R(T_c-T_\infty)$ versus $1/(T_c(\Delta T)f)$ (shown for nylon 12 9 in **Fig. 5-14c**).

Secondary nucleation constants of 0.53 x 10^5 K^2 and 0.92 x 10^5 K^2 were determined for nylon 8 9 and 12 9, respectively. These values indicate greater difficulty in crystallization because of the increase in methylene chain length.

5.2.3. Conclusions

The room temperature structure of as-synthesized samples of nylons 8 9 and 12 9 is characterized by a peculiar arrangement (form I) where hydrogen bonds are established along two planar directions. This structure is characterized by strong X-ray diffraction reflections at spacings close to 0.446-0.442 and 0.382-0.370 nm. The typical behavior of conventional even-even nylons was not observed on heating because an intermediate structure with X-ray diffraction spacings close to 0.430 and 0.400-0.395 nm was developed before the spacings merged into a single reflection above the Brill transition temperature. Previous works indicated that similar transitions could be found for nylon 4 7 but not for nylon 6 9. Therefore, polymethylene segment length does not seem to play a key role in the thermally induced polymorphism of even-odd nylons. The presence of reminiscent crystals having the intermediate form II structure in the as-synthesized sample could probably favor the occurrence of the low temperature transition.

On cooling, form II structures, and form I structures in a much lower proportion, could be detected. Nevertheless, the form I ratio increased when the sample was not completely melted in the previous heating run because of the presence of reminiscent nuclei having this structure.

Both polymers crystallized from the melt as negative birefringent spherulites following a single crystallization regime and a thermal nucleation process. The increase in length of the polymethylene segment hindered the crystallization process, as reflected by the higher secondary nucleation constant of nylon 12 9.

5.3. Thermally Induced Structural Transitions of Nylon 4 9 as a New Example of Even–Odd Polyamides

5.3.1. Introduction

Aliphatic polyamides (nylons) are the first synthetic and semicrystalline polymers that displayed outstanding mechanical and thermal properties to be used as fibers and engineering thermoplastics[2, 50]. Nylons are nowadays employed in a wide range of applications that mainly cover the textile, and automotive industries. The high performance of polyamides is a consequence of the strong intermolecular interactions that can be established between their constitutive NH and CO groups. Nylons are often classified according to the type of monomers implied in the polymerization, being distinguished between those obtained from a single monomer (i.e., AB polymers prepared by ring opening polymerization of lactams or alternatively by condensation of α-amino acids or their derivatives) and those obtained from two monomers (AABB polymers prepared by the polycondensation of a diamine and a dicarboxylic acid or their derivatives). Such polymers are usually named as nylons *n* and nylons *n m*, being *n* and *m* indicative of the number of carbon atoms of the respective monomers. Final properties of nylons are logically dependent on the density of amide groups (i.e., the specific values of *n* and *m*), but also on the crystalline structure. This structure should correspond to a minimum of the packing energy and consequently is governed by the formation of hydrogen bonds, keeping a practically linear geometry, between all constitutive amide groups. In this sense, the parity of the number of carbon atoms of the different monomers (i.e., odd or even *n* and *m* values) plays a remarkable influence on structure and properties. Nylon 6, nylon 11, nylon 12, nylon 6 6, nylon 6 10 and nylon 6 12 are specifically the aliphatic polyamides with higher commercial applications[50].

In general, the structure of such commercial nylons is based on the stack of sheets composed of hydrogen bonded molecular chains that could be in a parallel, antiparallel (e.g., even nylons) or both (e.g., odd nylons) dispositions, and had a practically all trans molecular conformation[6, 12]. The antiparallel arrangement was postulated to be preferred for the odd nylons[51], while for centrosymmetric even–even nylons both dispositions are equivalent. Weak van der Waals forces are established between the consecutive hydrogen bonded sheets, being the packing energy optimized by a shift along both the single hydrogen bonding direction and the chain axis direction. This displacement may be progressive or recuperative giving rise to the well-known α and β structures, respectively. The corresponding X-ray fiber diffraction patterns of such crystalline forms are characterized by the presence of two strong equatorial reflections associated with intrasheet and intersheet spacings (at 0.440 and 0.380 nm, respectively) and a meridional or off-meridional

orientation of reflections associated to the chain repeat for recuperative and progressive shears, respectively. Experimental limitations of fiber X-ray diffraction analyses (broad and scarce number of reflections) induced to use other approximations to confirm the structural models. Force field calculations[52] and resolution of small model compounds by direct methods[53] can be mentioned.

Even nylons with many carbon atoms (e.g., nylon 12) crystallize according to a pseudohexagonal packing (defined by one or two close equatorial reflections in the 0.420–0.400 nm range), a deviation towards skew conformations for torsional angles of methylene-amide bonds, and a tilting of amide groups from the plane defined by the methylene carbon atoms[54]. In this way, hydrogen bonds become established between parallel chains and along a single direction that becomes outside the sheet plane defined by the methylene groups. This arrangement (γ form) is also found as a polymorphic form of even nylons with a medium length of its polymethylene segment (e.g., nylon 6[55]), and was also postulated for odd–odd nylons due to impossibility to form a good hydrogen bonding geometry between chains having an all trans conformation[16]. The high applied interest of the indicated conventional polyamides have involved a considerable structural research, which is complex due to the indicated variety of molecular arrangements and molecular conformations that deals to polymorphic structures as it is the case of nylon 11[56].

Thermal induced structural transitions are also a common characteristic observed for conventional nylons displaying the indicated α/β forms. In this way, equatorial reflections gradually merge into a single peak indicative of a pseudohexagonal arrangement at the named Brill temperature. This transition seems reversible but shows a hysteresis effect since it took place at a lower temperature on cooling. Understanding of Brill transition is problematic and different interpretations have been postulated [13, 21, 57-61]. In this way, it has been proposed an increased mobility of methylene groups that lead to a pseudohexagonal packing or alternatively the disruption of the initial hydrogen bonds (note that they are established along a single direction for α, β and γ forms) to form new interactions randomly distributed along three planar directions at 120°.

In these cases, a single methylene group is placed between two amide groups causing distinctive conformational preferences that lead to structures with a single (nylons 1 *n* [62]), double (nylons *n* 3 [27]) and three (nylons 2/*n* [24]) coplanar hydrogen-bond orientations. Such structures were peculiar and consequently were also corroborated by the study of small model compounds [25, 28, 63].

Structures having two hydrogen bond orientations have also been postulated for several odd–even (e.g., nylons 5 6[30], 5 10[31], 9 2[32, 33], 11 10[34], 11 12[34], and 13 6[35]) and even–odd (e.g., nylons 6 5[36, 37],12 5[38], 6 13[39], 4 7[40] and 6 9[41, 42] and 8 9[64]) nylons having longer polymethylene sequences (i.e., without a single methylene). In this case, new structures were a consequence of the impossibility to establish correct hydrogen bond interactions when odd diamides having extended conformations were involved as will then be explained in more detail. The interest on the study of odd derivatives is nowadays increasing due to two main points: (a) the necessity to produce polymers from renewable

resources that could substitute fossil-based materials [65-68]. In this sense, nylons 5 6[69-71], 6 9[72] and 13 6[35] are gaining attention. (b) The odd numbered polyamides may display ferroelectric properties[4, 73] and in particular the peculiar structure of nylon 6 9 has been considered to get polymers with piezoelectric activity[72].

The structural versatility of polyamides gave rise to a wide variety of spherulitic morphologies for a given polymer, being still unclear the drastic change with crystallization temperature of physical properties such as the birefringence sign. Therefore, it has been postulated that lamellar crystal growth inside spherulites varied and specifically conventional nylons gave rise to positive or negative spherulites depending if hydrogen bonds had a radial or tangential orientation, respectively[46, 47]. Obviously, complexity increased for structures having two hydrogen bond orientations as it is the case of odd derivatives[43]. Lately, efforts have been focused to relate morphological evidence with structural changes induced by temperature for different even–odd polyamides (i.e., nylons 4 7[40] and 6 9[42]). Interestingly, properties were dependent on the edge-on and flat-on disposition of constitutive lamellae, displaying in the last case reversible changes on birefringence with temperature as a consequence of polymorphic transitions.

Nylon 4 9 corresponds to a scarcely studied even–odd polyamide that has an intermediate composition of those recently considered (i.e., the total number of carbon atoms is 13 instead of 11 (nylon 4 7) or 15 (nylon 6 9)). The present work is focused on the comprehension of four aspects: (a) characterization of the low temperature predominant form from the study of structure and morphology of single crystals; (b) study of thermally induced phase transformations on heating and cooling processes by means of real time synchrotron experiments and having special consideration on the occurrence of intermediate crystalline structures; (c) evaluation of the influence of the sample preparation process on the crystalline structure and the derived thermal induced structural transitions; and (d) study of spherulites developed at different crystallization temperatures, considering morphology, properties and crystallization kinetics.

5.3.2. Results and Discussion

5.3.2.1. Chemical Characterization

Nylon 4 9 was obtained with a yield of 60%, polydispersity index of 2.5 and number average molecular weight of 21,000, as determined by GPC (**Fig. 5-15a**). Index was slightly higher than theoretically expected from Flory's theory (i.e., 2.5 with respect to 2.0), suggesting the presence of a small ratio of oligomers. FTIR and ^{1}H NMR spectra of the synthesized nylon are given in **Fig. 5-15b,c**, respectively.

Spectra were fully consistent with the anticipated chemical constitution. Specifically, infrared spectra showed the characteristic absorption bands of amide and methylene groups at: ≈3291 cm^{-1}

(Amide A, N-H stretching), ≈3066 cm^{-1} (Amide B, overtone of Amide II), 2927 and 2851 cm^{-1} (asymmetric and symmetric CH-stretching bands), ≈1633 cm^{-1} (Amide I, C=O stretching), ≈1539 cm^{-1} (Amide II, C-N stretching and CO-N-H bending), ≈940 cm^{-1} (Amide IV, C-CO stretch) ≈721 cm^{-1} (CH_2 waging), and ≈684 cm^{-1} (Amide V, N-H out of plane bending). ^1H NMR spectra were characterized by peaks at: 8.56 ppm (NH, broad, 2H), 3.50 ppm (NHCH_2, broad, 4H), 2.60 ppm (COCH_2, triplet, 4H), 1.69 ppm (NHCH$_2$CH_2, broad, 4H + COCH$_2$CH_2, broad, 4H) and 1.34 ppm (-$(CH_2)_3$-, broad, 6H). Nylon 4 9 had a high thermal stability as demonstrated by the thermogravimetric curves displayed in **Fig. 5-15d**. The onset degradation temperature was close to 290 °C, being the decomposition process defined by a single step with a maximum DTGA peak at 448 °C. This stability appears highly important to discard any evidence of thermal degradation during the heating scans at which samples were submitted for the study of structural transitions.

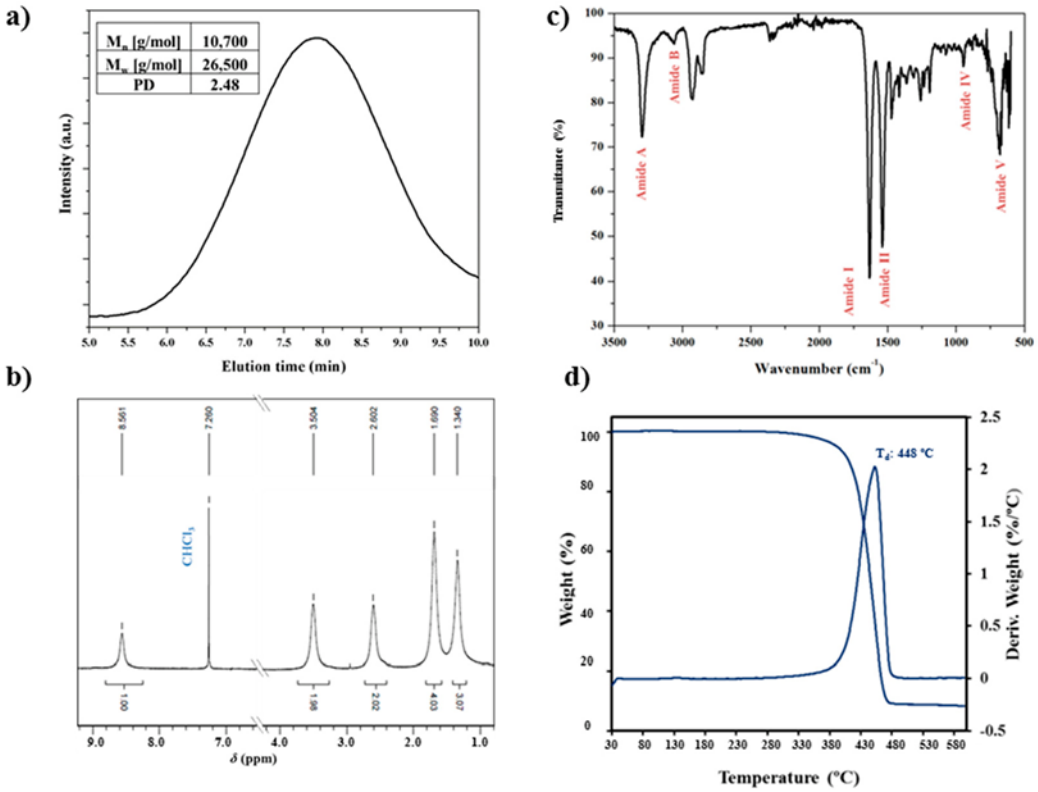

Fig. 5-15. GPC chromatograph (**a**); FTIR spectrum (**b**); 1H NMR spectrum (**c**); and TGA/DTGA thermogravimetric curves (**d**) of synthesized nylon 4 9.

5.3.2.2. Morphology of Nylon 4 9 Single Crystals

Crystals suitable for electron microscopy studies were obtained by isothermal crystallization from dilute solutions in glycerin. Their morphology varied depending on the conditions used for the preparation of samples and specifically on the selected temperature. Thus, crystallizations performed at temperatures higher than 90 °C rendered aggregates derived from a common nucleus having radial arms with well-defined extremities (**Fig. 5-16a**). Crystals with different orientations could be detected (i.e.,

parallel, tilted and perpendicular to the film surface). By contrast planar aggregate structures were observed at temperatures close to 110 °C.

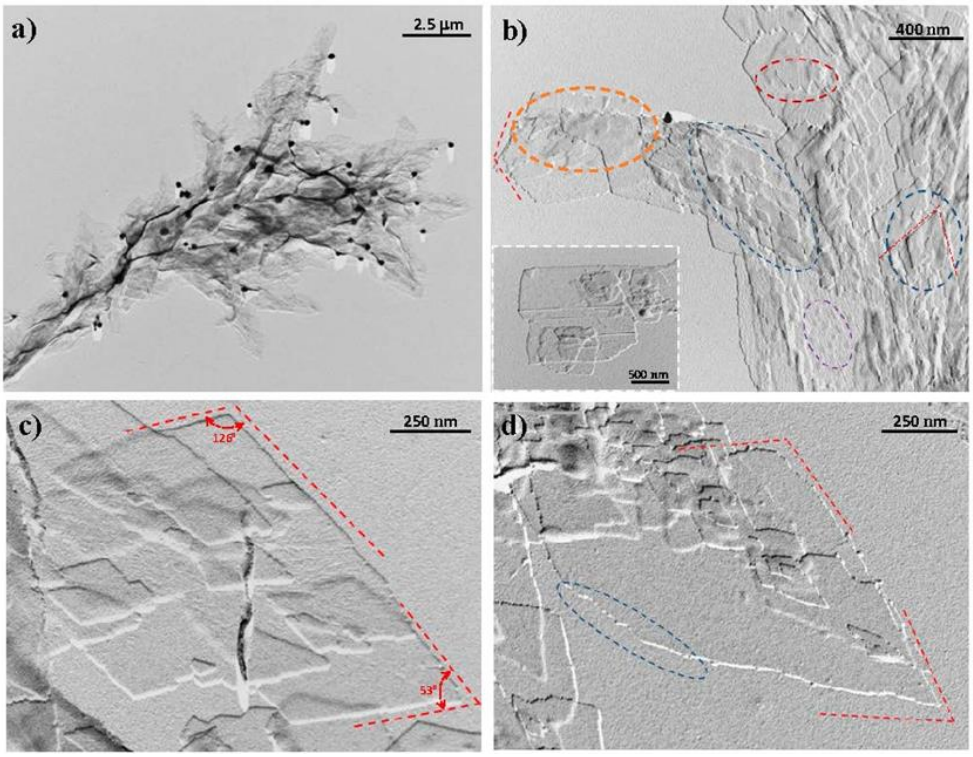

Fig. 5-16. *Transmission electron micrographs of nylon 4 9 crystals obtained from dilute glycerin solutions, illustrating the influence of crystallization conditions on morphology: (**a**) Arm of an spherulitic aggregate obtained at 90 ºC. (**b**) Aggregates constituted by planar crystals obtained at 110 ºC. Blue ellipsoid shows the presence of rhombic crystals whereas the orange ellipsoid and the inset point out the presence of lath shaped crystals. Serrated faces and globules are marked with garnet and violet ellipsoids, respectively. (**c**) Rhombic lamellar crystals obtained from crystallizations performed at 120 ºC. Red dashed lines define the theoretical angles between growth faces. (**d**) Elongated lamellar morphologies obtained at 130 ºC. Dashed lines indicate the theoretical growth faces according to the expected rhombic morphology. Obtuse angles could be recognized although curved morphologies could also be detected (blue ellipsoid).*

The morphology of constitutive lamellae was highly variable although rhombic crystals were predominant over lath shaped crystals (**Fig. 5-16b**). Different irregularities were common and easily detected, such as the presence of highly serrated edges and even of striations and globules on the surface of crystals. The best lamellar crystals were attained at 120 °C (**Fig. 5-16c**). An obtuse angle of 12° was measured accurately while the acute angle was less well defined (ca. 50°–53°), and specifically the rhombic appearance was lost at higher temperatures (e.g., **Fig. 5-16d** for crystallization performed at 130 °C). Obtuse angles could be well recognized, whereas the elongated morphology gave rise to a significant deviation of the acute angle. In all cases, individual lamellae were about 9 nm thick, as estimated from their shadows in the micrographs. This low thickness value and the high molecular weight of the polymer clearly indicate that molecular chains were folded, as is well established for polymer lamellar crystals.

Electron diffraction patterns of the different nylon 4 9 crystals have the same features, indicating that a single structure was always obtained. However, crystals prepared from glycerin at 120 °C gave the best pattern (**Fig. 5-17**) because single crystals of adequate dimensions could be selected for diffraction. This pattern was characterized by 2 mm symmetry with four and two prominent

reflections at 0.385 and 0.430 nm, respectively. The above symmetry was always observed, but no additional reflections with a variable intensity that could be associated with a twinned structure were detected, as is common in conventional nylons. Pattern resolution was up to 0.160 nm (i.e., 150 reflection) and allowed a rectangular unit cell with *a* and *b* dimensions of 0.430 nm and 0.860 nm, respectively, to be determined. The angles between the indexed 110 and −110 reflections and between 110 and 1–10 reflections were 126° and 54°, respectively, in full agreement with the obtuse and acute angles observed in the bright field micrographs. Therefore, the lateral faces of rhombic crystals corresponded to 110 planes.

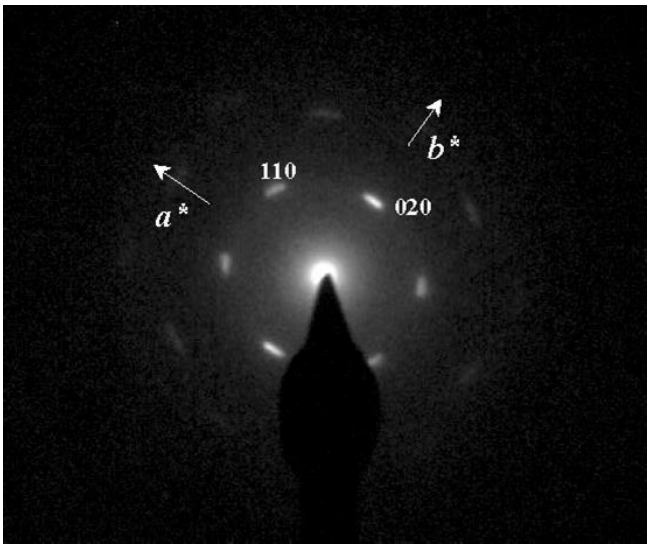

Fig. 5-17. *Selected-area electron diffraction pattern of nylon 4 9 single crystals prepared from glycerin at 120 °C. Only the most intense hk0 reflections are labeled. The pattern shows a clear 2 mm symmetry and reciprocal axes are labeled.*

Diffraction data of solution crystallized nylon 4 9 samples agree with previous observations performed with different odd–even[30-35] and even–odd[37-42] nylons. In all these cases, hydrogen bonds were not well established between molecular chains having an extended conformation and along a single direction, as is typical of the sheet structure described for conventional nylons. Therefore, a different molecular arrangement involving the establishment of intermolecular hydrogen bonding interactions along two directions was postulated because it could justify the observed symmetry of the electron diffraction pattern. This structure implied minimum distortion of the zig-zag molecular conformation and was compatible with spacings similar to those reported for conventional α/β forms of conventional nylons.

Basically, the model is based on a slight deviation towards 150° (or −150°) of the two torsional angles vicinal to the odd diamide units, which allows all NH and CO groups of neighboring chains to be faced. The two amide groups of the odd unit rotated in opposite senses from the plane defined by the methylene carbon atoms, allowing the establishment of a good hydrogen-bonding geometry when neighboring chains became conveniently shifted along the chain axis direction (**Fig. 5-18**). A monoclinic unit cell containing two molecular segments was derived and the chain axis

projection corresponded to a rectangular unit cell, with the dimensions of the diagonals being in full agreement with the expected distances between hydrogen bonded chains. Nylon 9 2 is probably the clearest example of such structure due to its highly rich diffraction pattern and the existence of a highly rigid oxalamide unit in the molecular chain[32]. X-ray diffraction pattern of the as synthesized sample is shown in **Fig. 5-19**).

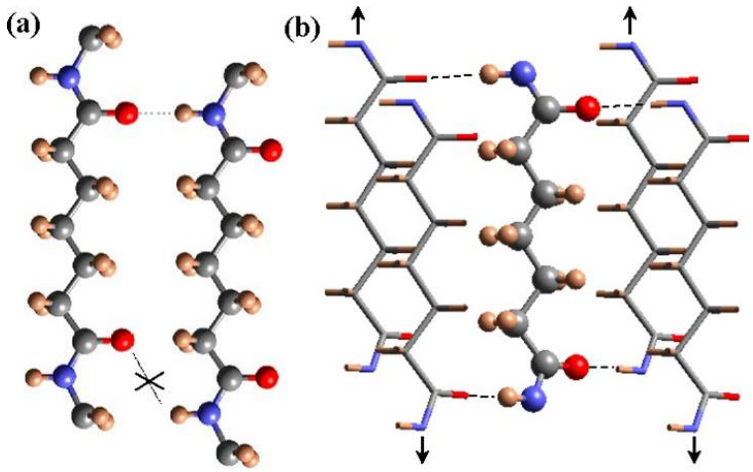

Fig. 5-18. *Scheme of the unfavorable hydrogen bonding geometry between odd carboxamide (i.e., pimelamide) units having an all-trans conformation (**a**); and the favorable interaction established according to the proposed structure where hydrogen bonds are established along two directions (**b**). For shake of clarity different representations are employed for the external and inner chains of the unit cell and a shorter dicarboxylic unit (i.e., pimelamide) has been considered. Arrows indicate the shift of neighboring chains with respect the central one. Color code: nitrogen, blue; oxygen, red; carbon, gray; hydrogen, brown.* [42]

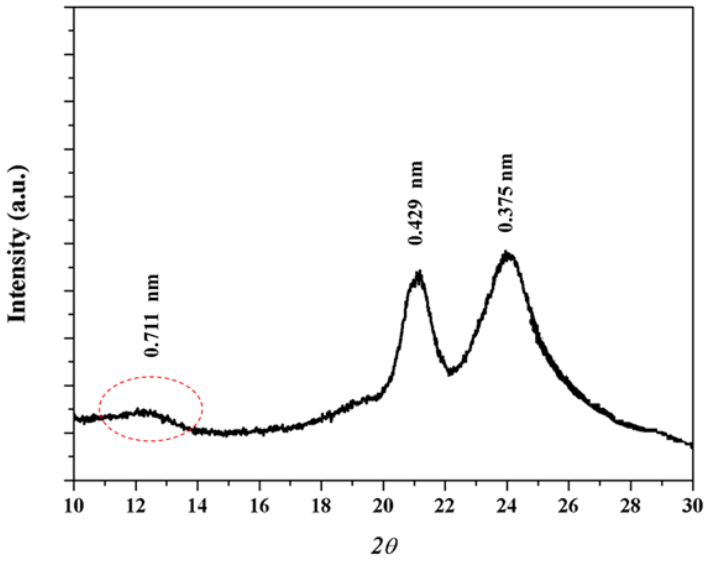

Fig. 5-19. *X-ray diffraction profile of as synthesized nylon 4 9 sample.*

As shown in **Fig. 5-19** the as synthesized sample showed two strong reflections at 0.429 and 0.375 nm that are associated to the molecular packing and correspond with those observed in the electron diffraction patterns. A 002 reflection at 0.711 nm (red ellipsoid) can also be detected and allows postulating a non-orthorhombic structure since this value is clearly lower than the calculated value for

the chain repeat length from either an all trans conformation or a typical γ form conformation (0.890 and 0.850 nm, respectively).

5.3.2.3. Structural Transitions of Nylon 49 during Heating and Cooling Processes from Real Time WAXD Data

The evolution of the X-ray diffraction pattern with increasing temperature is illustrated in **Fig. 5-20a** for the two main peaks associated with the molecular packing. The sample recovered from synthesis displayed clear and well-distinguished peaks at 0.430 nm and 0.375 nm, which correspond to the same crystalline form (named Form I), determined for the solution crystallized lamellar crystals. Minor differences are found for the spacing of the 110 reflection, which could be due to the different temperatures at which the crystalline structure was formed (i.e., 25 °C and 120 °C for precipitated and solution crystallized samples, respectively). Temperature evolution of diffraction profiles showed several remarkable features:

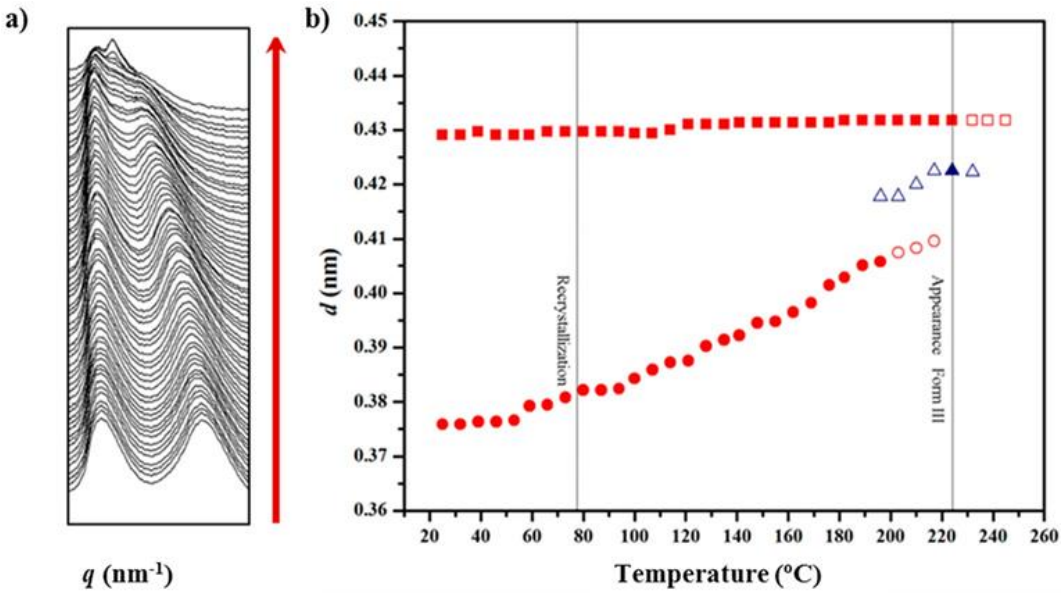

Fig. 5-20. *(**a**) Three-dimensional representation of WAXD profiles of a solution crystallized nylon 4 9 sample during heating (10 °C / min) from room temperature to fusion; and (**b**) evolution of the spacings of the two main reflections during the first heating. Full and empty symbols indicate well-defined and intuited reflections, respectively. The temperatures at which structural transitions occur are indicated with vertical lines. Reflections corresponding to Forms I and III are indicated in red and blue, respectively.*

a) The peak at 0.375 nm progressively shifted to higher spacings up to a maximum value of 0.410 nm (**Fig. 5-20b**), whereas the spacing of the 020 reflection remained practically constant (i.e., 0.430 nm). Basically, the *a* parameter of the unit cell increased (i.e., from 4.30 to 4.67 nm) while the *b* parameter was constant. The projected unit cell therefore became distorted with increasing temperature, with a dilatation being observed in the (100) direction where neighboring chains were closer (i.e., 4.30 nm as opposed to 0.480 nm in the (110) direction). This change can be

produced by a small change in the rotation angle between consecutive amide planes (i.e., from 53° to 57°, as determined from basic geometry considerations). It should also be pointed out that the 110 spacing becomes 0.385 at temperatures close to 120 ºC, a feature that is in full agreement with the electron diffraction data from lamellae crystallized at such temperature.

b) Around 120 ºC, a recrystallization phenomenon involving Form I can be detected (**Fig. 5-20a**). This feature is clearer in **Fig. 5-21a**, where the intensity of mean peak is displayed (see ellipsoid).

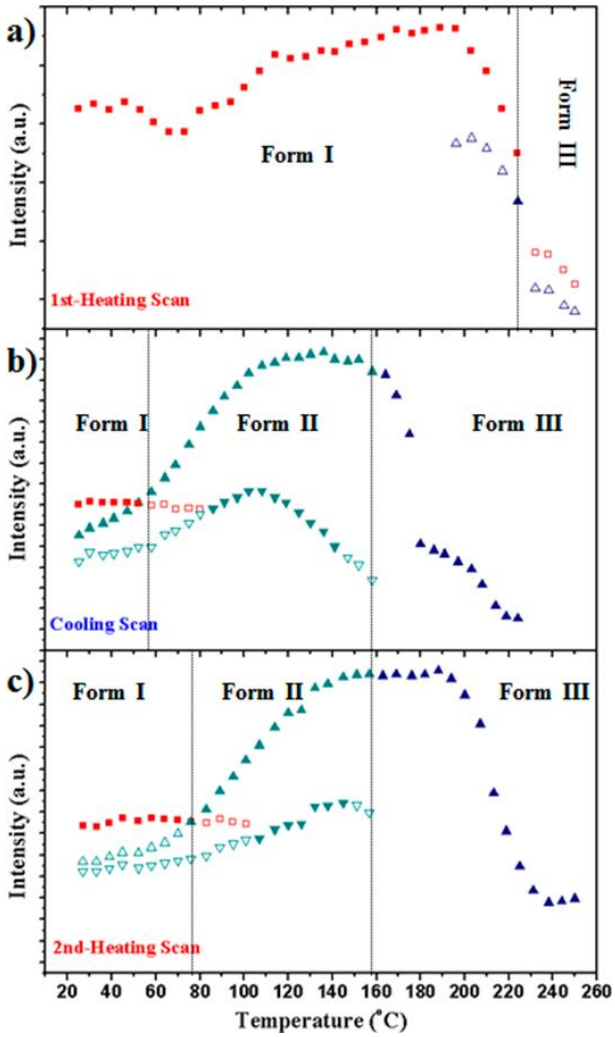

Fig. 5-21. *Temperature evolution of the intensity of the main peaks (for the clarity of representation the Form I peak at 0.375–0.410 nm is not plotted) during: the first heating (**a**); cooling (**b**); and second heating (**c**) processes. Full and empty symbols indicate well-defined and intuited reflections, respectively. The temperatures at which structural transitions occur are indicated with vertical lines. Reflections corresponding to Forms I, II and III are indicated in red, green and blue, respectively.*

c) At temperatures close to 195 ºC a new peak started to appear and reached its maximum intensity just before polymer melting. The spacing of the new reflection increased slightly from 0.418 to 0.423 nm and suggested the formation of the typical high temperature pseudohexagonal packing (named here Form III) that is achieved after the Brill transition. It is interesting that Form I reflections did not meet at high temperature, as is usually observed for conventional nylons. Profiles clearly suggest that Form I progressively disappeared and became

the new Form III (see the intensities displayed in **Fig. 5-21a**). Nevertheless, the transition is not completely clear due to the start of the melting process (225 ºC), just when the Form III peak appears better defined.

The evolution of X-ray diffraction profiles during cooling from the melt state is considerably more complicated because a new crystalline form (named Form II) appeared, as shown in the 3D profiles. The plot of spacings associated with the main observed reflections and the plot of intensity of representative reflections of each crystalline form, as shown in **Fig. 5-22a,b** and **Fig. 5-21b**, respectively.

The main features observed in the cooling process can be summarized as follows:

a) The sample crystallized from the melt in the high temperature Form III, giving rise to a single peak at around 238 ºC, which spacing slightly decreased from 0.426 to 0.422 nm when temperature diminished from 230 to 162 ºC. This change corresponds to a simple cell contraction and is a reversible process with respect to the observed one during heating. The peak reached its maximum intensity around 162 ºC, suggesting that the primary crystallization process completely finished, which is in agreement with calorimetric (at the same cooling rate of 10 ºC/min) and optical microscopy observations as then will be shown. Furthermore, diffraction profiles supported, as also will be indicated, that the different kinds of spherulites formed in the 238–229 ºC temperature range had the same Form III structure at the temperature where the micrographs were taken (i.e., when further structural transitions that took place on cooling were avoided).

b) A peak shoulder around 0.410 nm could be envisaged when temperature decreased from 160 ºC, being clearly defined at 140 ºC. The splitting of the single reflection suggests a minor structural change since a pseudohexagonal packing is still detected (i.e., reflections appeared at 0.420–0.417 nm and 0.410 nm while a single reflection at 0.415 nm is expected for a hexagonal packing defined by a typical hydrogen bonding distance of 0.479 nm between neighboring chains).

c) A dramatic decrease of the intensity of the two reflections associated to Form II is observed in the 130–60 ºC temperature range while new reflections associated to Form I appeared. Profiles clearly demonstrated that a structural transition took place rather than a continuous divergence of reflections as commonly described for a Brill transition. Finally, and with respect to Form I reflections, it can be pointed out that the 110 reflection was again the most sensitive to the temperature change since its spacing decreased from 0.393 to 0.385 nm (a value that is in full agreement with electron diffraction patterns). Logically, structural transition was stopped when the glass transition temperature was reached (i.e., 60 ºC) and consequently no further changes on the diffraction profiles were detected.

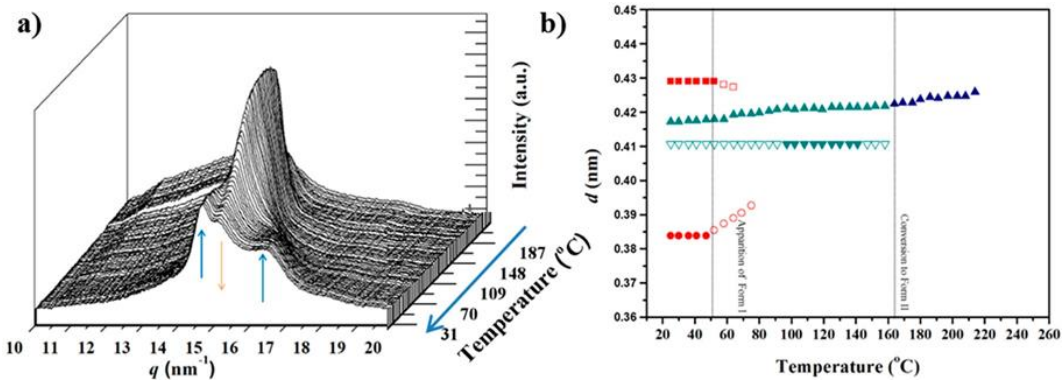

Fig. 5-22. ***(a)*** *Three-dimensional representation of WAXD profiles of nylon 4 9 during cooling (10 °C / min) from the melt to room temperature; and* ***(b)*** *evolution of the spacings of the two main reflections during the cooling run. Full and empty symbols indicate well-defined and intuited reflections, respectively. The temperatures at which structural transitions occur are indicated with vertical lines. Reflections corresponding to Forms I, II and III are indicated in red, green and blue, respectively.*

Fig. 5-23 compares the diffraction profiles of nylon 4 9 taken at room temperature for the solution and melt crystallized samples.

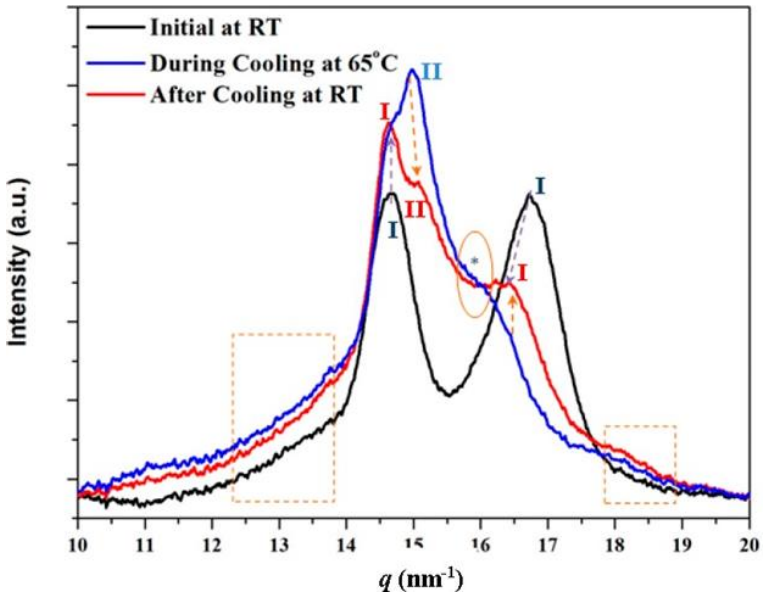

Fig. 5-23. *Diffraction profiles taken at room temperature for the solution (black) and melt (red) crystallized samples. Purple arrows compare the peaks associated with Form I. For the sake of completeness, a profile taken during cooling at 65 °C (blue) is also given. Evolution during cooling of some Form I and Form II representative peaks is indicated by the orange arrows and the shoulder associated with Form II with the asterisk and the ellipsoid. Dashed rectangles indicate the regions where tails of the amorphous halo could be detected.*

In the first case, only the two characteristic peaks at 0.430 nm and 0.375 nm were detected with similar intensity (**Fig. 5-23**). On the other hand, the second peak shifted to 0.385 nm while an additional highly intense peak at 0.417 nm appeared for the melt crystallized sample. The relative intensity between the two peaks associated with Form I also appeared clearly different in the profile of the melt crystallized sample because of the presence of the predominant peak of Form II. A profile taken during the cooling process is also given to emphasize the increase of Form I and the decrease of Form II during cooling, as well as the problematic presence of the shoulder associated with Form II (see ellipsoid and asterisk). Profiles also indicate the presence of an amorphous halo, which appears less

intense in the solution crystallized sample and reflects the higher crystallinity of this sample (i.e., see dashed rectangles).

Fig. 5-24a,b shows the evolution of profiles and main spacing of a melt crystallized sample during heating. In this case, it is clear that Form I experiences a structural transition towards Form II in the interval temperature between 75 and 120 ºC. This behavior clearly differs to the observed one during the first heating run, where Form I is kept up to fusion. It seems that the initial presence of Form II facilitates the polymorphic transition. That is to say, the initial Form II domains displayed a nucleating effect that facilitated the development of new Form II crystals. The plot showing the evolution of spacings (**Fig. 5-24b**) is similar to that obtained during the cooling run (**Fig. 5-22b**) although the transition between Forms II and I took place at slightly higher temperatures. It should also be pointed out that the maximum peak intensity during heating processes is observed at a temperature of 185–190 ºC, but it corresponds to different crystalline structures: Form I in the first heating run and Form III in the second one. This feature is again a clear indication of the dependence of the structural transition with the distribution of crystalline phases in the initial sample as then will be more extensively discussed.

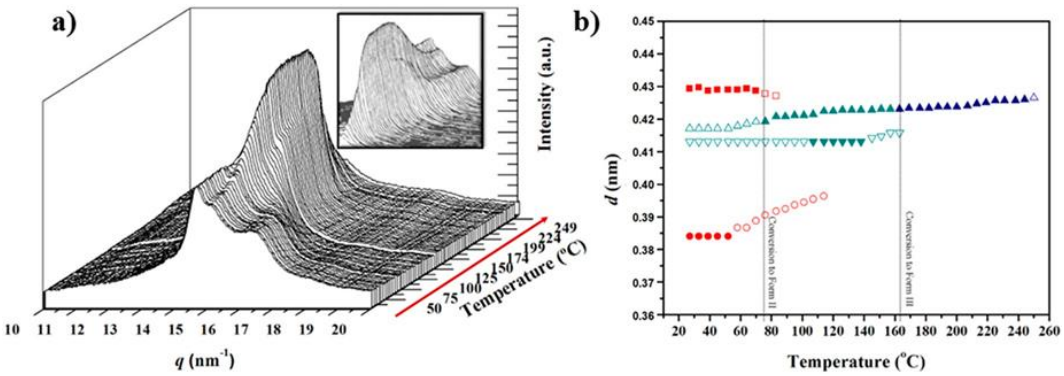

Fig. 5-24. ***(a)*** *Three-dimensional representation of WAXD profiles of a melt crystallized nylon 4 9 sample during the second heating (10 ºC/min) from room temperature to fusion. Insets show a different orientation to clarify the temperature evolution of the main reflections.* ***(b)*** *Evolution of the spacings of the main reflections during the cooling run. Full and empty symbols indicate well-defined and intuited reflections, respectively. The temperatures at which structural transitions occur are indicated with vertical lines. Reflections corresponding to Forms I, II and III are indicated in red, green and blue, respectively.*

5.3.2.4. FTIR Changes during Heating Processes

FTIR spectra are sensitive to structural changes. Specifically, the region between 1560 and 1500 cm^{-1} was found to be very useful to follow the polymorphism of nylon 4 9. The spectrum of the solution crystallized sample showed two minor bands at 1576 cm^{-1} and 1505 cm^{-1}, together with a very broad band centered at 1535 cm^{-1}, which is typically associated with the Amide II band (coupling of the C-N stretching mode with N-H in plane bending mode) (**Fig. 5-25a**). The intensity of all these bands increased on heating around a temperature of 95 ºC as a consequence of the previously described cold crystallization process. The increase of the intensity of the Amide II band, together with

temperature induced broadening, allowed several shoulders to be detected. Nevertheless, no remarkable change was observed until a temperature of 200 °C was reached, which was the maximum value that could be attained with the heater controller adapted to the ATR cell. Therefore, it can be concluded that no structural transition took place, in agreement with synchrotron data.

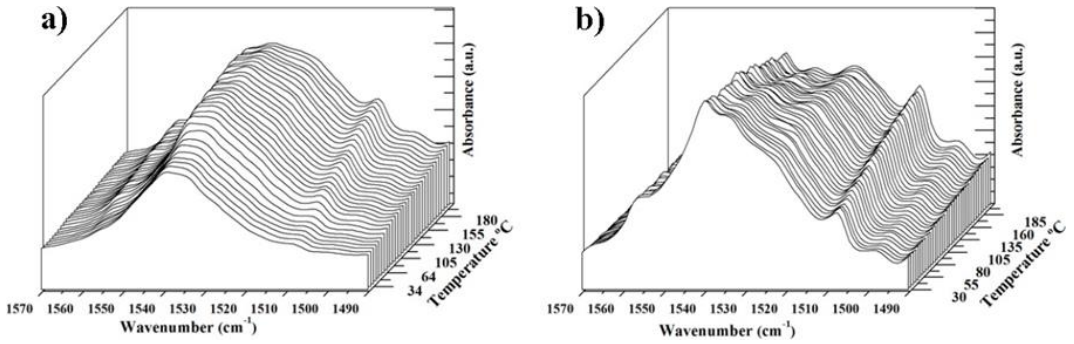

Fig. 5-25. *Temperature evolution of the 1570–1485 cm−1 region of the FTIR spectra of: solution crystallized* ***(a);*** *and melt crystallized* ***(b)*** *nylon 4 9 samples*

The sample was subsequently melted outside the ATR cell and then cooled at a rate of 10 °C/min. The room temperature spectrum was well differentiated from those previously described since the Amide II band was clearly split, with two additional peaks appearing at 1540 cm^{-1} and 1524 cm^{-1} (**Fig. 5-25b**). These peaks could be associated with Form II and had an increased intensity at high temperature while the intensity of the intermediate peak at 1534 cm^{-1} clearly increased during cooling, as expected for Form I. The temperature evolution of FTIR spectra indicates, again, a structural transition from Form II to Form I that took place in a wide temperature range during cooling. The spectra also showed a continuous increase of the intensity of the peak at 1505 cm^{-1}, which could therefore not be associated with a defined structure since the observed evolution was always detected, independent of the predominant structure (Form I or II).

5.3.2.5. Temperature Evolution on Heating of X-Ray Diffraction Profiles of Nylon 4 9 Samples Having Different Initial Structures

The ratio between the different crystalline forms of nylon 4 9 that can be found at room temperature logically depend on the preparation method as it was observed when the X-ray diffraction patterns of as synthesized and melt crystallized samples were compared. **Fig. 5-26** shows additional patterns of samples obtained by solvent casting from a 1,1,1,6,6,6-hexafluoroisopropanol (HFIP) solution, from formic acid solutions at different polymer concentrations and from a melt quenched sample. All samples coming from solution showed a clear peak at 0.375 nm and a second one in the 0.440–0.428 nm range, but differences on their relative ratio (measured as h_1/h_2, being the numerator and the denominator the height of the peaks corresponding to the higher and lower spacings, respectively) were found. Thus, the relative intensity of the lower spacing reflection decreased at the same time that appeared a shoulder (see red arrows in **Fig. 5-26**) close to 0.42 nm and related to Form

II. Profiles clearly indicated that formation of Form II was favored when HFIP was changed by formic acid and when the polymer concentration in the solution increased. The spectra of the melt quenched sample were clearly different since reflections at 0.42 and 0.375 were overlapped giving rise to a broad signal with a low intensity peak (i.e., Form II was obtained in a greater ratio than in the preceding cases).

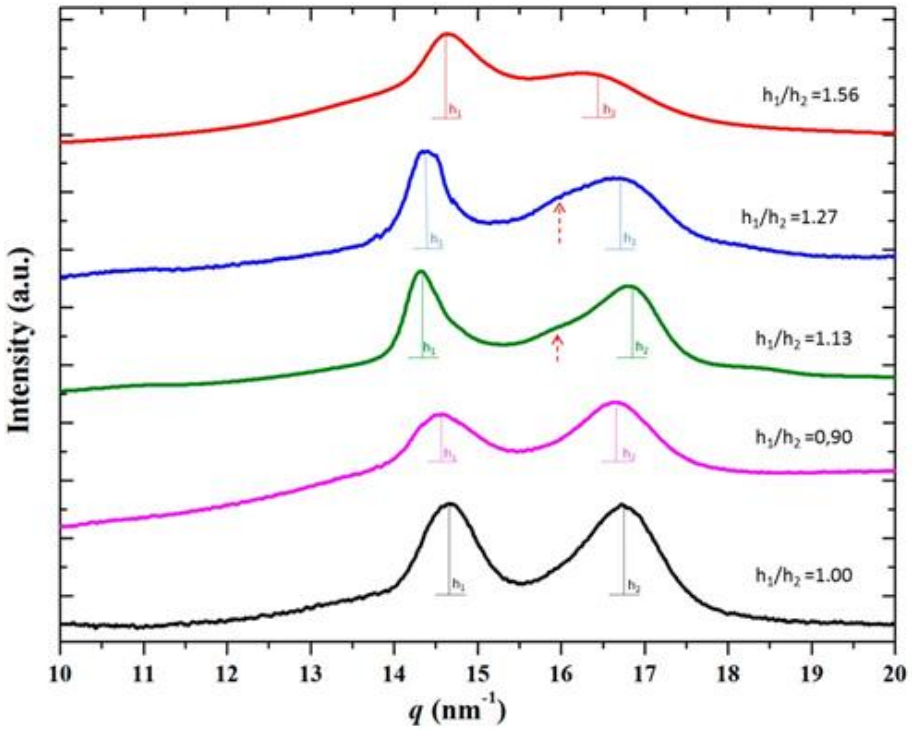

Fig. 5-26. *Diffraction profiles of nylon 4 9 samples taken at room temperature from down to up: as synthesized sample, solvent casting film from HFIP at a polymer concentration of 2 mg/mL, solvent casting film from formic acid at a polymer concentration of 2 mg/mL, solvent casting film from formic acid at a polymer concentration of 10 mg/mL and a melt quenched sample.*

Fig. 5-27 compares the evolution of diffraction profiles of the different solvent casting films and the melt quenched sample during a heating rate up to fusion. The most relevant feature is that all samples initially having some percentage of Form II displayed a clear transition from Form I to Form II, which appeared clearer for higher Form II contents (e.g., red arrows in the profiles of solvent casting films from formic acid at low and high polymer concentrations). This is obvious for the melt quenched sample, which is characterized by a significant content of Form II. By contrast, the solvent casting film from HIFP showed a similar behavior to that observed for the as synthesized sample. Results point out that samples having only Form I could not structurally transition to Form II, with the presence of Form III being detected only at temperatures close to fusion. More interesting is the finding that the presence of small amounts of Form II enhanced the structural transition. These became potential nuclei that favored the change in the packing arrangement.

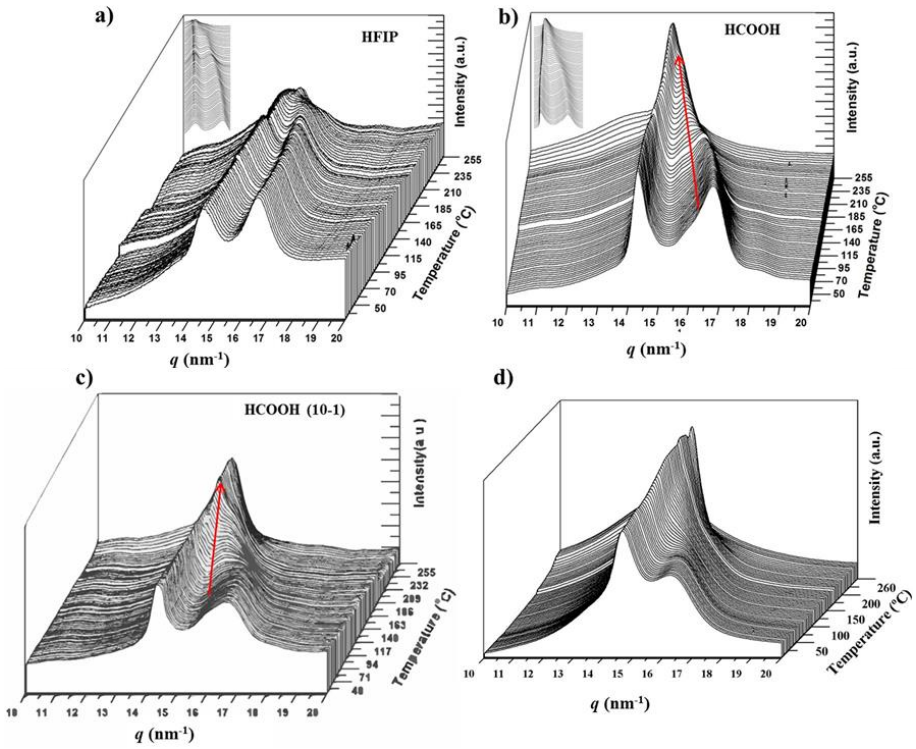

Fig. 5-27. *Three dimensional representation of WAXD profiles of nylon 4 9 during heating (10 ºC/min) from room temperature to fusion for:* ***(a)*** *solvent casting film from HFIP at a polymer concentration of 2 mg/mL;* ***(b)*** *solvent casting film from formic acid at a polymer concentration of 2 mg/mL;* ***(c)*** *solvent casting film from formic acid at a polymer concentration of 10 mg/mL; and* ***(d)*** *melt quenched sample.*

5.3.2.6. Thermal Properties of Nylon 49

DSC heating and cooling runs (**Fig. 5-28**) revealed a complex thermal behavior of nylon 4 9, which is logically linked to the above structural features during non-isothermal treatments.

The following points should be emphasized:

a) The first heating scan shows two clear endothermic peaks at 233 ºC and 244 ºC, which are related to a typical reorganization process where thin lamellae melt and recrystallize, giving rise to thicker crystals. An exothermic peak at an intermediate temperature (236 ºC) is also clearly detected and confirms the existence of the indicated reorganization process. According to the synchrotron data, only the high temperature Form III should be involved in the melting and recrystallization processes.

b) A very broad exothermic peak (red arrow) can also be detected in the first run after the glass transition temperature (50 ºC according to the change of the base line) and up to 150 ºC. This process fits with the cold crystallization associated with Form I that was detected in the diffraction profiles (**Fig. 5-20a** and **Fig. 5-21a**) during heating.

c) The first melting peak (233 ºC) observed in the first run shows two small shoulders in the low temperature region (blue arrows), which may be related to structural transitions that could involve thin and thick lamellae having the Form I structure, according to the X-ray diffraction data. Therefore, shoulders may correspond to the transition from Form I to Form III for the different lamellar populations. A similar complex process has recently been reported for nylon

6 9[42]. However, it cannot be ruled out that these endothermic transitions were associated with fusion of Form I lamellae.

d) The cooling scan is defined by a well-defined exothermic peak at 218 ºC followed by a small and broad exotherm that extends up to a temperature close to T_g. In this way, the first exotherm corresponds to crystallization into Form III, whereas the subsequent broad exotherm should be linked to the continuous structural transitions (involving Forms I and II) that were detected in the diffraction profiles.

e) The heating scan of the melt crystallized sample showed the indicated two melting peaks at 233 °C and 244 °C. The lamellar reordering process seems to be emphasized over that observed in the first heating scan because the relative area of the second melting peak clearly increased. This is expected when thin lamellae are less stable due to a worse crystallization process, suggesting that solution crystallized samples have a higher degree of perfection than melt crystallized ones. This conclusion is also in agreement with the differences observed in the global melting enthalpy of both samples (i.e., 85.8 + 28.3 − 13.3 = 100.8 J/g and 61.6 + 34.6 − 9.4 = 86.8 J/g for solution and melt crystallized samples, respectively). The DSC scan is also characterized by a constant deviation of the base line from T_g up to 200 °C, which may be due to the continuous structural transitions detected in the X-ray diffraction profiles during heating. Note also that shoulders before the first melting peak are less relevant for the melt crystallized samples, suggesting that structural transitions took mainly place during the heating process. It is highly relevant that the resultant endothermic enthalpy (86.8 J/g) associated with the processes occurring at temperatures higher than 200 °C was clearly higher than the enthalpy associated with the crystallization process performed in the previous scan (i.e., 60 J/g for the acute peak and 69.2 J/g if the broad exotherm is also considered). This suggests that shoulders of the first melting peak correspond to structural transitions and that the corresponding enthalpies are not associated with melting processes.

f) The heating scan of the melt quenched sample revealed, again, the above features with differences in the logical decrease of global melting enthalpy (39.9 + 39.2 − 3.2 = 75.2 J/g) and the increase of relative intensity of the high temperature melting peak over the low temperature one. In summary, the sample is less crystalline and the reorganization processes become enhanced.

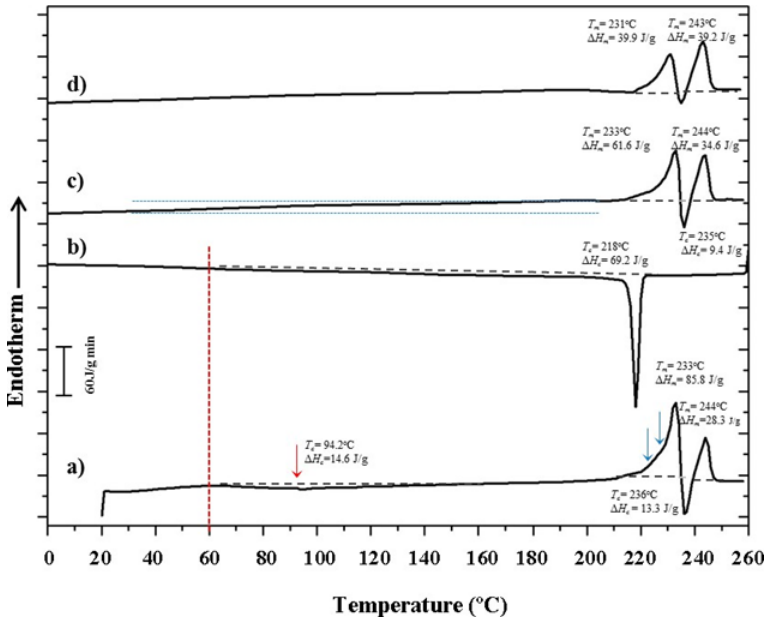

Fig. 5-28. *(**a**) Heating run of the as-synthesized nylon 4 9; (**b**) cooling run of nylon 4 9 from the melt state; (**c**) subsequent heating run of the melt crystallized sample; and (**d**) heating run from a nylon 4 9 melt quenched sample. Arrows indicate small endothermic and exothermic peaks.*

Equilibrium melting temperature (T_m^o) is a crucial parameter in determining crystal growth rate and specifically degree of supercooling ($T_m^o - T_c$). The Hoffman–Weeks extrapolation[45] is a commonly accepted method of estimating the equilibrium temperature due to its simplicity and straightforward implementation, although it is subject to criticism[74] and improvements have been proposed[75]. The method is based on Equation (2), which was deduced from a combination of the well-known Gibbs–Thomson equation and secondary nucleation theory[76]. This equation relates the melting temperature, T_m, of a crystal formed at a temperature T_c, the equilibrium melting temperature, T_m^o, and the thickening coefficient, γ, defined as the ratio between the thickness of the grown crystal and the initial thickness of a "virgin lamella":

$$T_m = T_m^0 (1 - 1/\gamma) + T_c/\gamma \qquad (2)$$

A straight line is obtained by plotting T_m as a function of T_c, with the equilibrium temperature corresponding to the intersection of this line with the $T_m = T_c$ line. The validity of Equation 2 implies that lamellar crystals thicken at a specific crystallization temperature, which also influences the thickening parameter.

Fig. 5-29 shows the complex melting behavior of nylon 4 9 crystallized at different temperatures. At the lowest temperature (226 °C) only the two crystallization peaks associated with fusion of thin and thick lamellae of nylon 4 9 in its Form III structure were detected. The predominant melting peak (labeled as peak II) shifted to higher temperatures with the crystallization temperature, allowing the unambiguous estimation of an equilibrium melting temperature of 243 °C from the Hoffman–Weeks plot (**Fig. 5-30).** The temperature of the melting peak associated with the thickest lamellae (labeled as peak III) remained practically constant and was practically identical to the estimated

equilibrium melting temperature. DSC heating runs also showed a low temperature endothermic peak whose area clearly increased as the crystallization temperature did. A careful interpretation of this behavior is out of the scope of the present work because different processes are involved: isothermal crystallization at the selected temperature and non-isothermal crystallization during the subsequent heating, which could imply structural transitions between the different crystalline forms. It seems that crystallizations performed at the highest temperatures were incomplete and a greater ratio of structures corresponding to Forms II or I was found during the cooling process. Therefore, the area of the lower temperature peak (labeled as peak I) increased.

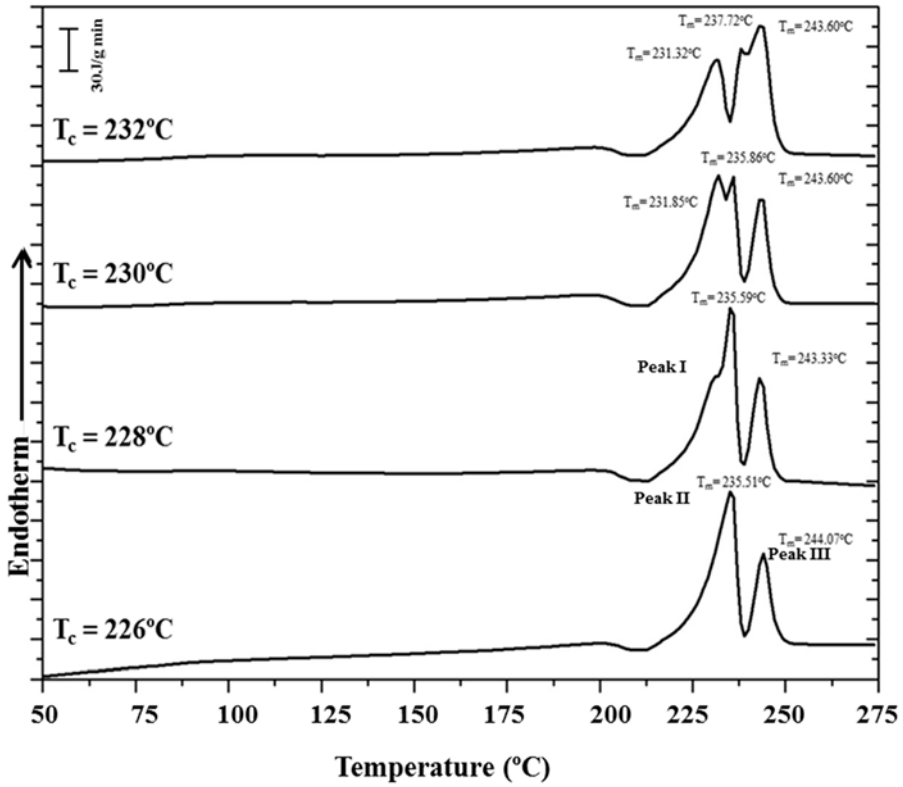

Fig. 5-29. *DSC traces corresponding to the heating run of samples isothermally crystallized at the indicated temperatures.*

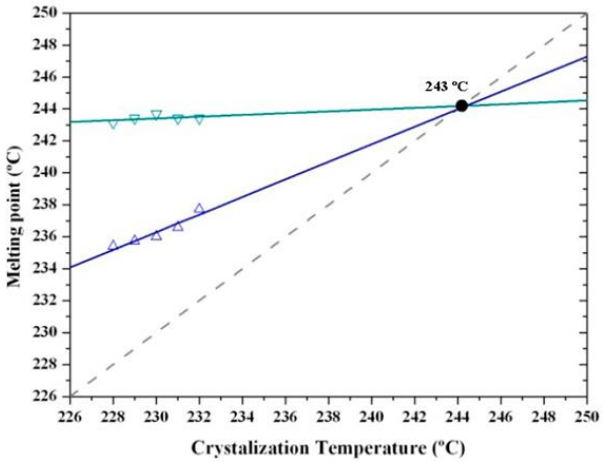

Fig. 5-30. *Hoffman–Weeks plot of temperatures corresponding to the observed endothermic Peaks II and III associated with the high temperature Form III versus hot crystallization temperature. An equilibrium melting temperature of 243 °C could be deduced*

5.3.2.7. Spherulitic Morphologies of Nylon 4 9 Crystallized from the Melt

Morphology of spherulites obtained by isothermal crystallization from the melt state depended on the crystallization temperature, as shown in **Fig. 5-31** for different representative temperatures. The number of active nuclei increased with decreasing crystallization temperatures, and logically the size of spherulites decreased. Thus, diameters close to 200 μm and 25 μm were characteristic of spherulites obtained at 238 and 229 ºC. Significant changes were detected despite the narrow crystallization temperature range (i.e., 9 ºC). At the highest temperature, axialitic entities with complex birefringence and including domains with well-formed planar crystals (see dashed ellipsoids) were characteristic. At the lowest temperature, only ringed spherulites with a clearly negative birefringence were usually detected. At intermediate temperatures (e.g., 235 ºC and 233 ºC), spherulites showed a speckled texture, being detected incipient rings and a confusing birefringence at 233 ºC. The predominant negative birefringence observed for nylon 4 9 spherulites contrasts with the positive sign characteristic of conventional nylons that is attained at low crystallization temperature and has been associated to a radial disposition of the single hydrogen bonding direction.

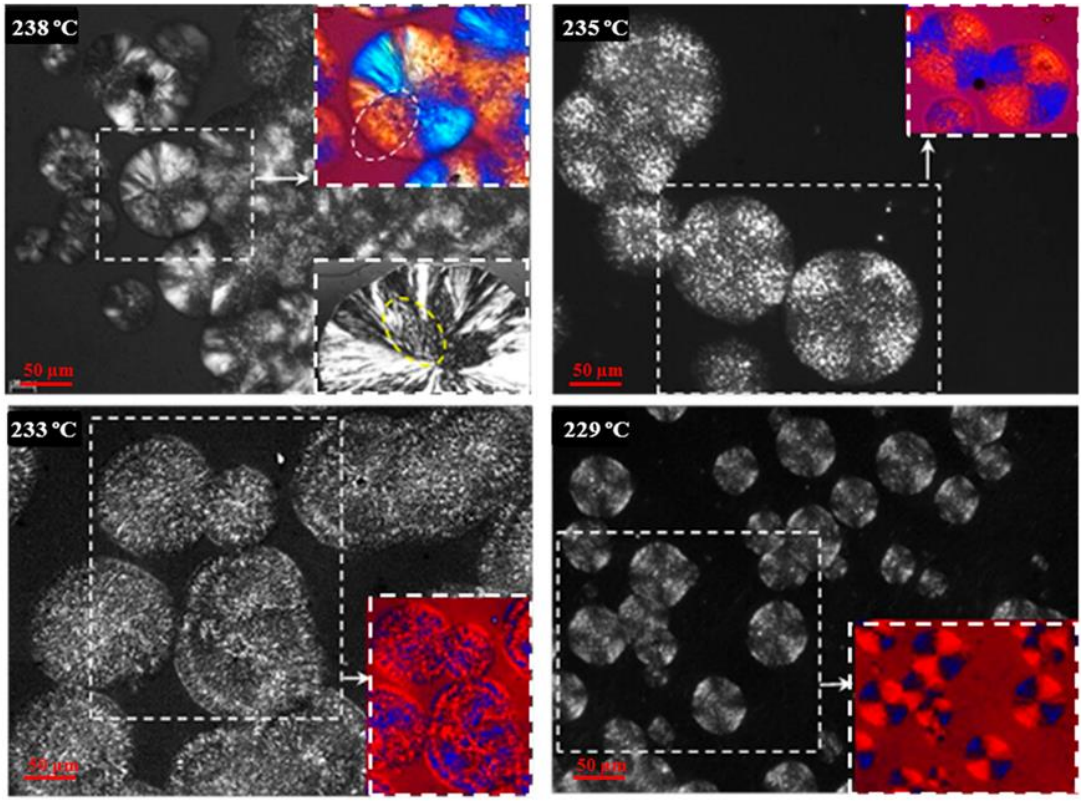

Fig. 5-31. *Typical spherulitic morphologies of nylon 4 9 isothermally crystallized at the indicated temperatures. Black and white inset of the micrograph taken at 238 ºC reveals the complex internal structure of the obtained spherulites. Color micrographs taken with a red tin plate to determine the sign of birefringence are shown as insets for all crystallizations.*

X-ray diffraction profiles taken in the narrow temperature interval between 238 and 229 ˚C corresponded to the single high temperature pseudohexagonal molecular arrangement (Form III). Thus, the differences observed in morphology and texture are not related to a change on the crystalline

structure. Nevertheless, it should be considered that micrographs were taken at room temperature and consequently optical properties should be related to the predominant Form I that was achieved during cooling as deduced from synchrotron data. Electron diffraction patterns taken at room temperature of thin spherulites crystallized in the above temperature interval reflect slight variations considering the symmetry of the pattern (**Fig. 5-32**). Note that lamellar twisting varied, being more difficult to obtain symmetric *hk*0 diffraction patterns at the lower temperature. **Fig. 5-32** shows the predominant electron diffraction pattern obtained from spherulites crystallized at 229 ºC and 238 ºC.

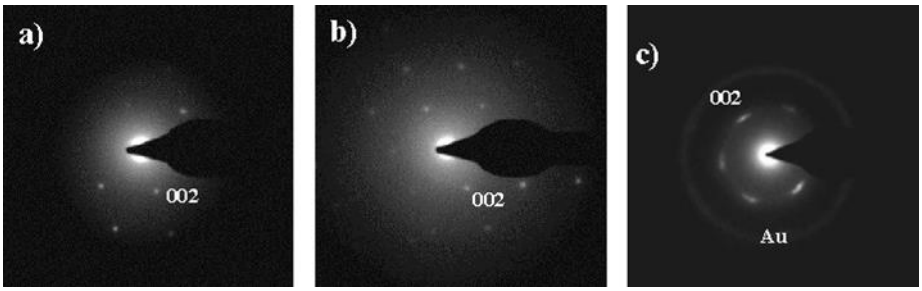

Fig. 5-32. *Selected-area electron diffraction pattern of nylon 4 9 spherulites crystallized at: 229 ºC (**a,b**); and 238 ºC **(c).** Patterns corresponded to the low temperature structure observed from solution crystallized samples. Symmetry is usually lost in the patterns coming from spherulites crystallized at 229 ºC (**a**) as consequence of lamellar twisting, although a 2 mm symmetry can also hardly detected (**b**). This symmetry is more easily observed from spherulites attained at the higher temperature as a consequence of a flat-on lamellar disposition (**c**).*

Kinetics of crystallization of nylon 4 9 from the melt was studied by optical microscopy. Spherulite radius grew linearly with time until impingement (not shown). Crystal growth rate (G) was determined in the studied temperature interval where measurable spherulites formed.

Primary nucleation density increased dramatically wit decreasing temperatures (i.e., 80 nuclei/mm^2 and 1600 nuclei/mm^2 were determined at 238 °C and 229 °C, respectively), and, consequently, the available temperature range for kinetic studies was highly limited. Micrographs taken during crystallization at the highest temperature showed that crystallization was mainly athermic since the number of nuclei was kept constant over time.

Secondary nucleation constants were determined by the Lauritzen–Hoffman equation[48]:

$$G = G_0 \times \exp\{-U^*/(R(T_c - T_\infty))\} \times \exp\{-K_g/(T_c(\Delta T) f)\} \quad (1)$$

where G_0 is the constant pre-exponential factor, U^* is the activation energy characteristic of the transport of crystallizing segments across the liquid-crystal interface, T_∞ is the temperature below which such motion ceases, R is the gas constant, K_g is the corresponding secondary nucleation constant, ΔT is the degree of supercooling measured as $T_m - T_c$ (where T_m is the equilibrium melting temperature and T_c is the crystallization temperature), and f is a correction factor accounting for the variation in the bulk melting enthalpy per unit volume with temperature ($f = 2T_c/T_m + T_c$).

The inset of **Fig. 5-33** shows the linear plots obtained using U^* and T_∞ parameters of 1600 cal/mol and $T_g - 35$ K, respectively. It is clear that two crystallization regimes defined by secondary nucleation constants of 0.33×10^5 K^2 and 0.15×10^5 K^2 fit the experimental data. Regimes III and II

could be assumed since the experimental ratio between slopes (2.2) was close to the theoretical K_g^{III}/K_g^{II} value of 2. **Fig. 5-33** also corroborates that the two bell-shaped curves calculated by the Lauritzen–Hoffman equations fit well with the experimental spherulitic growth data.

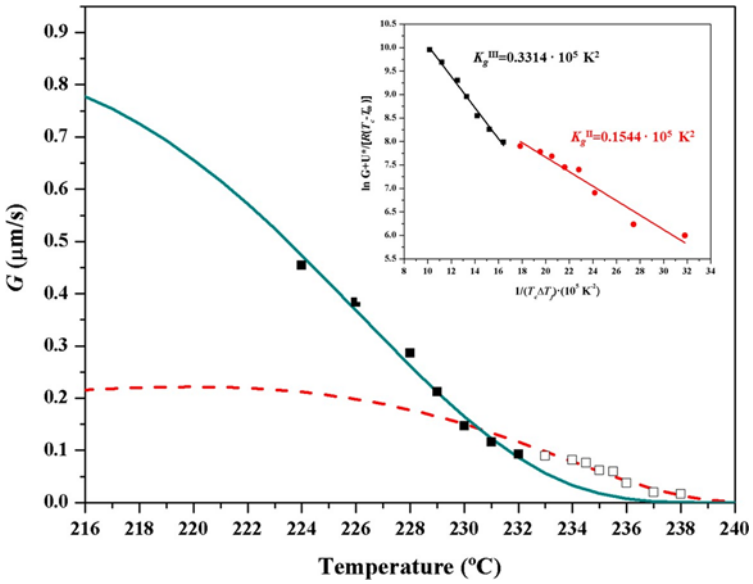

Fig. 5-33. *Temperature dependence of crystal growth rate (solid green line for Regime III and dashed red line for Regime II) determined by Lauritzen–Hoffman equation and using the best fit parameters deduced for the two crystallization regimes. Experimental crystal growth rates and indicated by the square symbols. The inset shows the plot of ln G + U*/R(Tc − T∞) versus 1/Tc (ΔT) f to determine the Kg secondary nucleation parameters.*

5.3.3. Conclusions

Nylon 4 9 crystallized from diluted glycerin solutions giving rise to lamellar single crystals which morphology varied according to the crystallization temperature. Specifically, regular rhombic crystals were attained at 120 °C, while aggregates or irregular and elongated crystals were characteristics of lower and higher temperatures, respectively. Electron diffraction patterns showed a 2 mm symmetry and pointed out a single structure (Form I) characterized by a disposition of hydrogen bonds along two planar orientations as reported for other even–odd nylons previously studied.

Nylon 4 9 isothermally crystallized from the melt giving rise to spherulites with a texture that clearly varied in a very narrow temperature interval (i.e., from 238 ºC to 229 ºC). Flat-on and edge-on lamellar dispositions were detected at the highest and the lowest crystallization temperatures, changing the morphology from axialites to ringed spherulites and the formation of speckled spherulites at intermediate temperatures. Electron diffraction patterns indicate that all these spherulites predominantly had the Form I structure when were observed at room temperature. At this temperature, the birefringence sign was negative in contrast with the positive sign detected for conventional even–even polyamides. Crystallization kinetic analysis indicated that two crystallization regimes were characteristic of nylon 4 9, being the involved temperatures in agreement with the observed morphologic changes.

Nylon 4 9 showed complex transitions during heating and cooling processes that depended on the way as the sample was prepared. Before melting, nylon 4 9 achieved a typical pseudohexagonal arrangement (Form III) that was consequence of the named Brill transition. A new polymorphic structure (II) appeared during crystallization from the melt as well as from crystallization from some specific solvents. Temperature evolution of diffraction patterns during heating processes was clearly dependent on the presence of Form II. Thus, profiles indicate a direct transition from Form I to Form III or from Form I to Form II when traces of the intermediate structure (Form II) were absent or present, respectively. The complex behavior was also supported by calorimetric and spectroscopic data, being of interest for the understanding/racionalization of the high structural variability described for nylons in general and even the differences detected between even–odd nylons in particular.

5.4. Crystalline Structures and Structural Transitions of Copolyamides Derived from 1,4-Diaminobutane and Different Ratios of Glutaric and Azelaic Acids

5.4.1. Introduction

Aliphatic polyamides (nylons) constitute a group of semi-crystalline polymers that could cover a wide range of properties (e.g. specific gravity, melting point and moisture content), depending in general on their amide/methylene ratio[2, 50, 77]. Nylons can be considered non-degradable and possess excellent mechanical properties because of their capability to establish strong hydrogen bonding intermolecular interactions. Nylons can crystallize according to a great variety of structures in function of temperature, crystallization procedure, thermal treatment and obviously of their chemical constitution. The derived crystalline structures are consequence of both the chain conformational preferences and the optimization of hydrogen bonding interactions/geometry [50]. Preferred molecular conformation corresponds to an all trans disposition. Thus, nylons derived from even and short ω-amino acids (i.e. even nylons like nylon 6) or even diamines and dicarboxylic acids (i.e. even-even nylons like nylon 6,6) have a typical α/β structure based on the stacking of H-bonded sheets constituted by molecules with the indicated all extended conformation [6, 12]. In this case, amide groups and methylene carbons of a molecular chain form part of a single sheet.

A deviation of the molecular conformation towards skew torsional angles for the single bonds vicinal to the amide groups has been postulated for nylons having units with an odd number of carbon atoms in order to improve intermolecular hydrogen bonding interactions. In this case, amide groups rotate with respect to the plane defined by the methylene carbon atoms giving rise to different hydrogen bonding geometries (i.e. according to one, two or three directions). In fact, final conformation is determined for the ability to form correct hydrogen-bonding geometries and specifically on the parity and length of the polymethylene sequences. Odd nylons (e.g. nylon 7) require a twist of their amide groups giving rise to the named γ structure where H-bonds could also be correctly established [16]. In this case, these bonds are formed along a single direction between adjacent chains belonging to different sheets (i.e. intersheet H-bonds are formed instead of the intrasheet interactions found in conventional α/β structures). Specifically, all amide groups rotate in the same direction from the sheet defined by the methylene carbons. Rotation of amide groups in two opposite directions from the above indicated sheet gave rise to another structure characterized by two H-bonding directions (**Fig. 5-34)** .This has been postulated for different odd-even[30-35] and even-odd nylons [38-42, 64, 78], being their diffractions patterns highly similar to those described for even-even nylons

and clearly different to those found for the γ-form. Pseudohexagonal arrangements with a random deviation of amide groups from the indicated plane constituted by methylene carbons were also postulated for the structure attained when nylons were heated at temperatures close to their melting point.

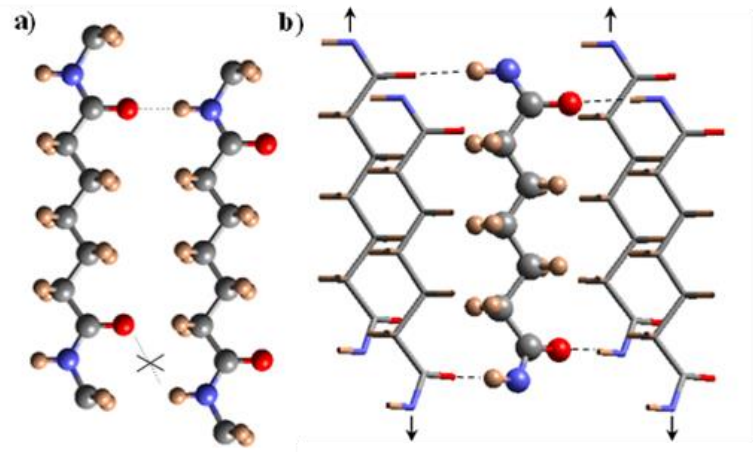

Fig. 5-34. *Schemes showing the unfavorable hydrogen bonding geometry between odd carboxamide units (e.g., pimelamide) having the all-trans conformation (a) and the favorable interaction established according to the proposed structure where hydrogen bonds are established along two directions. (b). Corner and central chains are indicated by stick, and ball and stick representations for the shake of clarity. In the same way, a shorter dicarboxylic unit (i.e., pimelate) has been considered. Arrows indicate the shift of corner chains with respect to the central one. Color code: nitrogen, blue; oxygen, red; carbon, gray; hydrogen, brown. Reproduced with permission from[42], copyright 2015.*

A thermal transition from the α/β low temperature structure to the pseudohexagonal high temperature structure is usually detected over the so named Brill transition temperature, according to a not well-understood process [13, 21, 57-61]. This high temperature structure is still controversial since models based on the establishment of a random distribution of H-bonds along three directions or alternatively on a librational motion of methylene groups keeping a single H-bonding direction have been formulated.

Nylons having peculiar units where only one methylene group is placed between two amide groups displayed also different molecular arrangements that varied from one- [62], two- [27, 28] and three H-bonding directions [24, 79].

Copolymers having different crystallizable units are able to crystallize, being in general distinguished between the exclusion of comonomers in the crystal lattice or their inclusion if a sufficient compatibility exists. In this case, one crystalline phase containing either crystalline units (isomorphic co-crystallization) or two crystalline phases (isodimorphic crystallization) can be observed. Similarity of chemical structure and molecular conformation are required for isomorphism, whereas not so restrictive conditions are needed in the second case, which logically becomes more frequent. Nevertheless, in the isodimorphic crystallization at least one of the two crystalline phases should incorporate the corresponding minor component in its crystalline lattice.

An extensive work has been performed on the study of the crystallization process of different random copolymers. Probably, copolyalkylene dicarboxylates are the most studied and specifically

systems having units with a similar parity and length have mainly been evaluated [80-84]. Nevertheless, and more recently, copolymers with highly dissimilar monomers (e.g. succinic and azelaic acids) have also been considered [85]. By contrast, scarce works have been focused on the structural study of random copolyamides. This point is interesting due to the additional difficulty to incorporate foreign units in a crystal lattice when the structure is governed by the formation of energetically favoured H-bonds. In the present work, even-odd copolyamides derived from 1,4-diaminobutane and two different dicarboxylate units (i.e. glutarate and azelate) have been selected. Specifically, phase transitions induced by temperature will be firstly studied due to the peculiar structure (i.e. two hydrogen bonding directions) of such even-odd nylons, and secondly the crystallization behavior of such copolymers having units with well-differentiated lengths will be evaluated.

5.4.2. Results and Discussion

5.4.2.1. Synthesis of Nylons 4,5+9_X

Copolymers were obtained with a relatively good yield that ranged between 63% and 50%, corresponding to the higher values to samples with the higher azelate content. Molecular weight (***Table 5-1***) ranged between acceptable values for polycondensation polymers and specifically, values were between 16,000 and 22,000 g/mol and 40,000 and 51,000 g/mol for the number and weight average molecular weights, respectively. A well-defined trend was not found, although the higher values were detected for copolyamides with an intermediate composition and the lower values for copolymers with higher glutaric acid content. Nevertheless, differences were not significant to deduce an effect caused for example by greater insolubility of samples having higher glutaric acid content (i.e., chains with a higher amide group density).

Table 5-1. Synthesis data of nylons 4,5+9_X.

Sample	Yield (%)	f_A	M_n (g/mol)	M_w (g/mol)	PDI
Nylon 4,5+9_0	50	0	16,000	40,000	2.5
Nylon 4,5+9_15	54	0.15	18,000	43,000	2.4
Nylon 4,5+9_40	53	0.45	17,000	41,000	2.4
Nylon 4,5+9_50	60	0.55	22,000	51,000	2.3
Nylon 4,5+9_60	58	0.73	20,000	44,000	2.2
Nylon 4,5+9_85	57	0.9	21,000	47,000	2.2
Nylon 4,5+9_100	63	1	20,000	46,000	2.3

Infrared spectra were consistent with the anticipated chemical constitution and showed in all cases typical amide A (NH stretching at 3296 cm^{-1}), amide B (overtone of amide II at ≈ 3030 cm^{-1}), amide I (C=O stretching at ≈ 1633 cm^{-1}) and amide II (C-N stretching and CO-N-H bending at ≈1540 cm^{-1}) bands together with those associated to methylene groups (asymmetric and symmetric CH stretchings at 2990 and 2980 cm^{-1}, respectively) (**Fig. 5-35**). The main differences corresponded

to the relative intensity between amide and methylene bands, which in any case was scarce along the series as could be deduced from the high similarity between the spectra of the two homopolymers. In any case, it is relevant that each type of amide band appears at practically the same wavenumber for all the series. This feature suggests that all homopolymers and copolymers have a similar predominant hydrogen bonding structure. Note for example that the amide A band is highly sensitive to the geometry of intermolecular hydrogen bonds, being expected clear differences between amorphous and crystalline phases. Furthermore, evolution of the amide A band during heating and cooling processes could be useful to detect polymorphic transitions. **Fig. 5-36** shows as the wavenumber increases when temperature increases as expected from weaker interactions associated to the dilatation of the unit cell. More interestingly, a non-linear dependence with temperature was observed and specifically an abrupt change around 120 °C was detected during heating, cooling and reheating processes as a clear evidence of a polymorphic transition that will be discussed below.

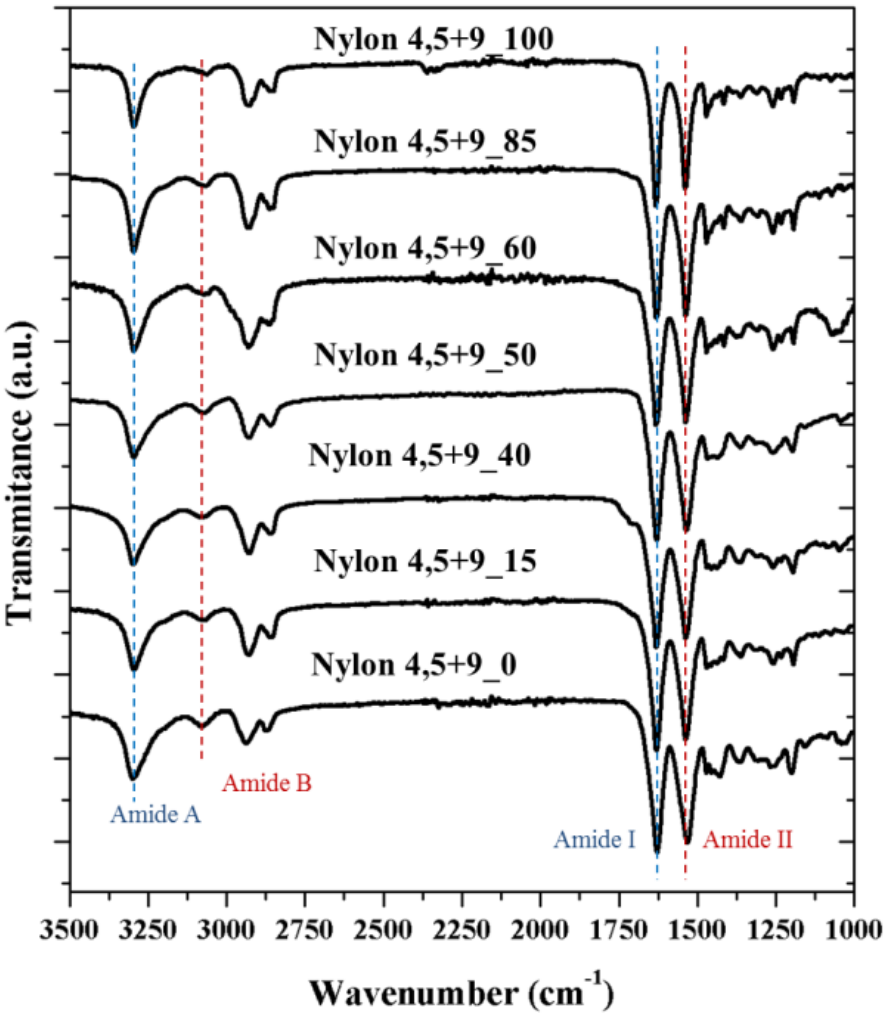

Fig. 5-35. *FTIR spectra of the series of nylons 4,5+9_X.*

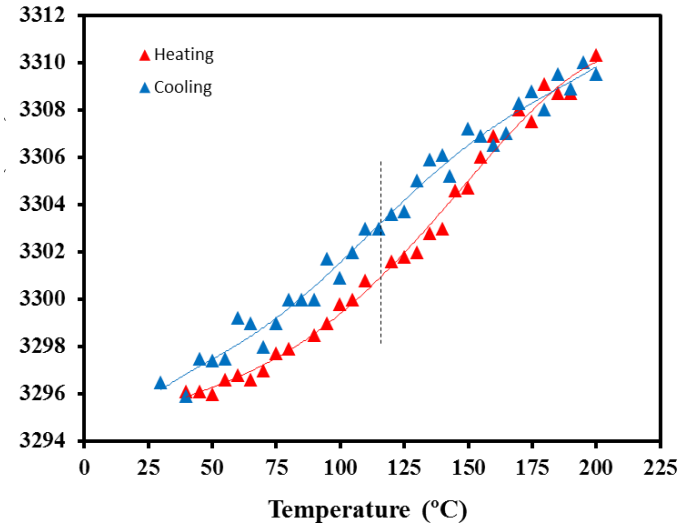

Fig. 5-36. *Variation of the Amide A wavenumber of nylon 4,5+9_50 during heating and cooling processes. In both cases the maximum variation (associated to a transition between forms I and II) took place around 120 ºC.*

^{1}H nuclear magnetic resonance (NMR) spectra showed the characteristic signals associated to the different units as can be seen in **Fig. 5-37** for the representative nylon 4,5+9_60 copolymer. Signals were broad, although a triplet associated to the $COCH_2$ protons of the azelate units could be distinguished as expected for polymers of moderate molecular weight (e.g., those coming from polycondensation). ^{1}H NMR spectra were characterized by peaks at: 7.62–7.38 ppm (NH, 2H),3.43 ppm (NHCH_2, 1,4-diaminobutane, 4H), 2.62 ppm ($COCH_2$, glutarate, 4 (1-(X/100)) H), 2.48 ppm ($COCH_2$, azelate, 4 (X/100) H), 2.04 ($COCH_2CH_2$, glutarate 2 (1-(X/100)) H), 1.66 ppm ($NHCH_2CH_2$+ $COCH_2CH_2$, (4 + 4 (X/100) H) and 1.38 ppm (–$(CH_2)_3$–, 6 (X/100) H). Areas of signals at 2.62 and 2.48 ppm were employed to determine the ratio between azelate and glutarate units incorporated into the polymer chain (i.e., $f_A = A_{2.48}/(A_{2.52} + A_{2.48})$). These values are summarized in Table 1 and show a lower incorporation of glutarate units with respect to the monomer feed ratio (i.e., $X/100 < f_A$) for copolymers prepared for a glutarate feed ratio higher than 0.15. This feature indicates a higher effective reaction of sebacoyl dichloride. Logically, composition could also be inferred from the areas of 2.04, 1.66 or 1.38 ppm signals considering the 3.43 ppm signal as reference (e.g., $f_A = (1 - (2 \times A_{2.04}/A_{3.43})) = (A_{1.66}/A_{3.43}) - 1 = 4/6 \times A_{1.38}/(A_{3.43})$.

The signal corresponding to NH protons was complex being probably a consequence of formation of hydrogen bonds in solution and also of the kind of carbonyl group (i.e., from glutarate or azelate groups) involved in such interactions. 13C spectra (not shown) was also non-useful to detect a splitting of signals that allowed information concerning sequence distribution to be obtained.

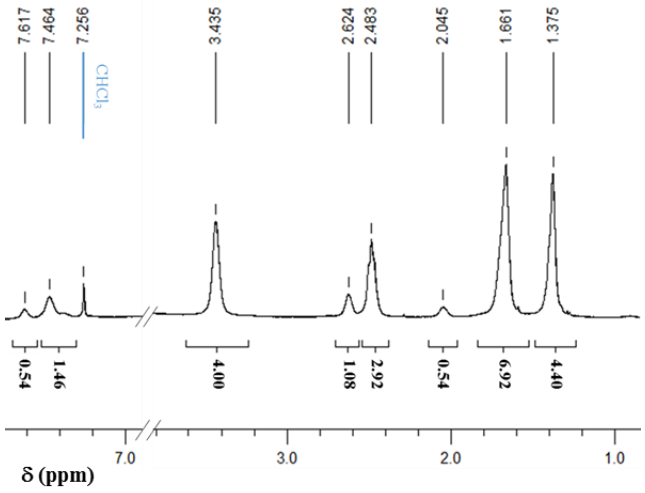

Fig. 5-37. *1H NMR of the representative 4,5+9_60 copolymer with peaks assignment.*

5.4.2.2. Thermal Properties of Nylons 4,5+9_X

The protocol of the performed thermal analysis is shown in **Fig. 5-38a** for the representative nylon 4,5+9_60 copolymer. Differential scanning calorimetry (DSC) data revealed that all samples were semicrystalline as shown in **Fig. 5-38b** where heating scans of samples slowly cooled from the melt state (i.e., submitted to a similar thermal history) are displayed. Fusion was always characterized by a highly complex signal, which was variable according to composition and also on the previous treatment at which the sample was submitted (e.g., precipitation from solution, slow crystallization from the melt or quenching). **Table 5-2** summarizes the main calorimetric properties of the studied samples, being possible to deduce some general trends despite the high complexity of the system.

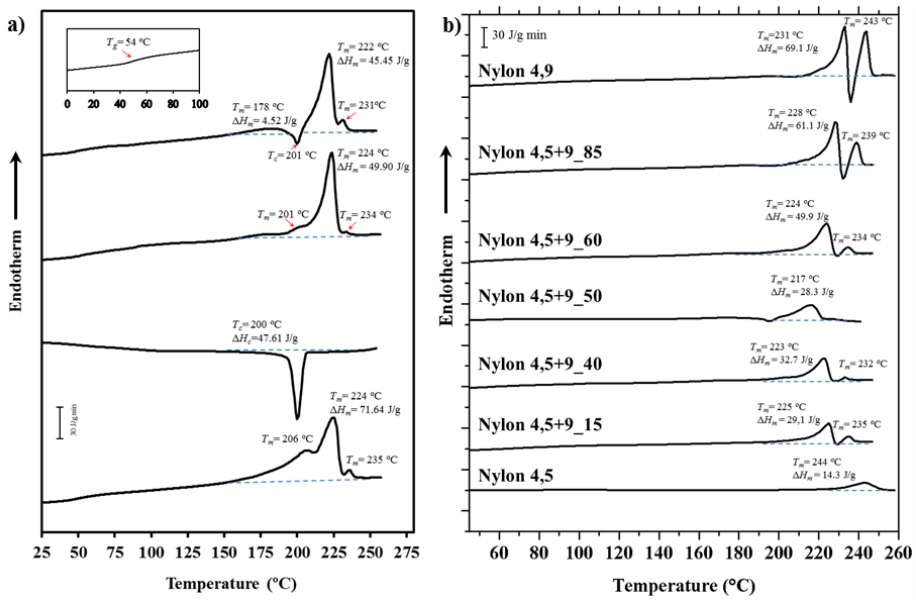

Fig. 5-38. *(**a**) Differential scanning calorimetry (DSC) traces of nylon 4,5+9_60 taken from (bottom to top): first heating run, first cooling run, second heating run and thirdd heating run from a melt quenched sample. (**b**) Comparison between the second heating run (i.e., from melt crystallized samples) of the studied nylons.*

a) Melting enthalpies were clearly dependent on the specific composition and specifically decreased as the comonomer content increased (i.e., nylons 4,5+9_40 and 4,5+9_50 with f_A values of 0.45 and 0.55 showed the lower melting enthalpies) for compositions with f_A higher than 0.15. Thus, the enthalpies observed in the second heating scan varied from a minimum of 43.5 J/g (for f_A = 0.55) and a maximum of 86.8 J/g (for f_A = 1). Nevertheless, the minimum enthalpy was detected for nylon 4,5+9_15 (i.e., 31.0 J/g) probably due to the occurrence of some degradation before fusion as discussed later.

b) Melting enthalpies of solution-precipitated samples were clearly higher than those determined from melt crystallized samples and obviously than exhibited after fast cooling. Nevertheless, it is significant that the capacity to crystallize even for samples with a high comonomer content and even after the quenching process (e.g., 37.7 J/g for nylon 4,5+9_50).

c) A predominant melting peak in the 220–244 °C interval (second heating run) was always observed. This peak is associated to the fusion of lamellar crystals formed during the previous crystallization process. Peak temperature decreased with the comonomer content (e.g., 233 °C, 220 °C and 244 °C for samples with X equal to 100, 50 and 0, respectively).

d) A peak of variable intensity in the 228–244 °C interval is also usually observed. This peak can be associated with the fusion of lamellae recrystallized during the heating process and appeared at a practically constant temperature when copolymer composition was varied. Thus, the predominant initial lamellae followed a typical reorganization process that led to an increase of the thickness and obviously of the melting temperature. A hot crystallization exotherm can be observed in some cases between the two main melting peaks (e.g., see nylon 4,5+9_100 in **Fig. 5-38b** and data corresponding to the third heating run in **Table 5-2**). Comparison between second and third heating traces points out that reordering was favoured when the sample was less crystalline (i.e., samples obtained by fast cooling) since probably more segments able to be incorporated into the crystalline lamellae are disposable on the lamellar surface.

e) Additional low-intensity endothermic processes can be envisaged at temperatures lower than the main melting peak temperature. These processes may correspond to the fusion of high defective crystals or the melting of crystals having a different crystalline structure.

f) Samples easily crystallized in the cooling run from the melt state, decreasing the crystallization peak temperature (i.e., from 212/218 °C to 196 °C) and enthalpy (i.e., from 69.2 to 39.3 J/g for f_A > 0.15) with the comonomer content. Logically, the presence of structural foreign units hindered the crystallization process.

g) A single glass transition temperature was always detected as evidence that phase separation did not occur in the amorphous fraction. In any case the T_g varied in a narrow interval (e.g., between 50 and 71 °C) being difficult to deduce a specific trend since both composition and molecular weight played a significant influence. Logically the homopolymer derived from glutaric acid was slightly more rigid than that constituted by azelaic acid (i.e., 71 °C with respect to 50 °C).

Table 5-2. *Thermal properties of nylons 4,5+9_X*[a].

Sample	1st Heating Scan		Cooling Scan	
	T_m (°C)	ΔH_m (J/g)	T_c (°C)	ΔH_c (J/g)
Nylon 4,5+9_0	**233**,249	56.8	212	30.1
Nylon 4,5+9_15	207,**225**,237	50.3	203	29.4
Nylon 4,5+9_40	205,**224**,239	57.2	199	39.3
Nylon 4,5+9_50	206,**224**,234	65.0	196	38.9
Nylon 4,5+9_60	207,**225**,236	72.0	200	48.6
Nylon 4,5+9_85	213,**229**,239	82.2	209	56.0
Nylon 4,5+9_100	215,**233**,244	104	218	69.2

Sample	2nd Heating Scan		
	T_m (°C)	ΔH_m (J/g)	T_g (°C)
Nylon 4,5+9_0	221,**244**	35.9	71.2
Nylon 4,5+9_15	205,**224**, 228	31.0	54.9
Nylon 4,5+9_40	175,201 ,**222**	43.5	50.2
Nylon 4,5+9_50	178,198, **220**	45.3	50.6
Nylon 4,5+9_60	177,201, **224**,234	59.9	52.6
Nylon 4,5+9_85	185,212, **289**,237	64.4	52.6
Nylon 4,5+9_100	195,**233**, 244	86.6	50.0

Sample	3rd Heating Scan			
	Tm (°C)	ΔH_m (J/g)	T_{hc} (°C)	ΔH_{hc}(J/g)
Nylon 4,5+9_0	**239**	36.6	-	-
Nylon 4,5+9_15	188,**209**	20.8	-	-
Nylon 4,5+9_40	178,**218**	5.5,32.2	197	2.7
Nylon 4,5+9_50	178,**220**, 228	5.6,32.1	199	0.6
Nylon 4,5+9_60	177,**222**, 232	5.6,45.7	200	3.1
Nylon 4,5+9_85	183,**227**, 237	1.9,54.4	207	3.5
Nylon 4,5+9_100	195,**231**, 243	39.9,39.2	236	0.4

[a]Data for the main peak is indicated by bold characters.

Thermogravimetric analyses demonstrated that thermal stability decreased as the content of glutarate units increases (see **Fig. 5-39** for comparison of the two homopolymers and the copolymer having an intermediate composition). Decomposition took place according to a highly predominant step, which DTGA peak increased from 422 °C to 455 °C. The onset degradation temperature was high for all copolymers (e.g., close to 350 °C for a sample with X = 50) and surely higher than the corresponding melting temperature. However, nylons 4,5+9_0 and 4,5+9_15 showed a continuous mass loss that represented a weight loss close to 4% when the above indicated onset decomposition temperature (i.e., 350 °C) was reached. This feature is significant since it indicates the occurrence of some degradation during heating that should influence on the anomalous decrease on thermal properties previously commented about for the studied series. A char yield variable of 7%–9% was detected without any special correlation with composition.

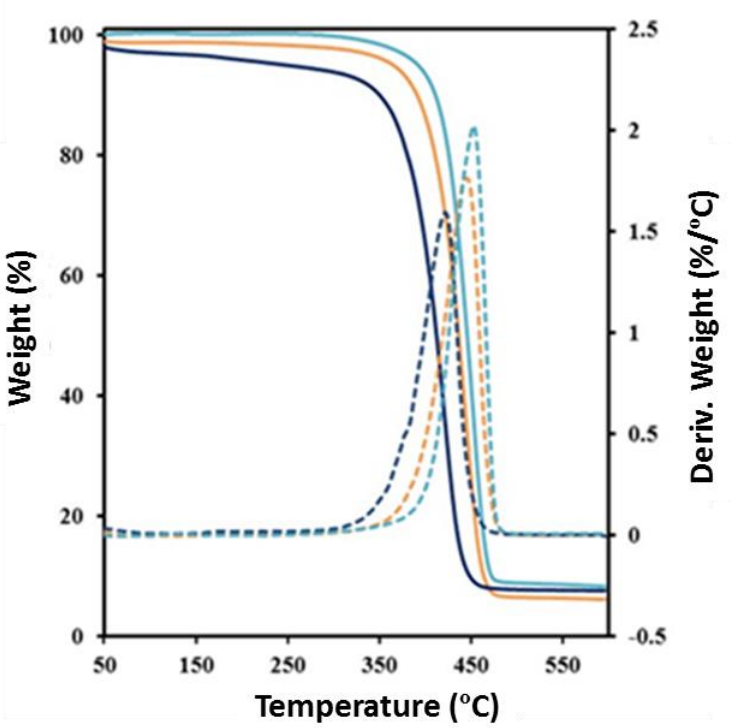

Fig. 5-39. *Thermogravimetric TGA and DTGA curves of the glutarate (black lines) and azelate (blues lines) homopolymers and the copolymer with the intermediate composition (brown lines).*

Thermogravimetric analyses demonstrated that thermal stability decreased as the content of glutarate units increases (see **Fig. 5-39** for comparison of the two homopolymers and the copolymer having an intermediate composition). Decomposition took place according to a highly predominant step, which DTGA peak increased from 422 ºC to 455 ºC. The onset degradation temperature was high for all copolymers (e.g. close to 350 ºC for sample with X = 50) and surely higher than the corresponding melting temperature. However, nylons 4,5+9_0 and 4,5+9_15 showed a continuous mass loss that represented a weight loss close to 4% when the above indicated onset decomposition temperature (i.e. 350 ºC) was reached. This feature is significant since indicates the occurrence of some degradation during heating that should influence on the anomalous decrease on thermal properties previously commented for the studied series. A char yield variable in the 7-9% was detected without any special correlation with composition.

5.4.2.3. Equilibrium melting point of nylon 4,5+9_X copolymers

Equilibrium melting temperature (T_m^0) is a crucial parameter to evaluate the nucleation capacity of growing crystals and also to determine the degree of supercooling ($T_m^0 - T_c$). The Hoffman–Weeks extrapolation [45] is a commonly accepted method to estimate the equilibrium melting temperature due to its simplicity and straightforward experimental implementation, although it is subject to criticism [74] and some improvements have been proposed [75]. The method is based on equation 2, which was deduced from a combination of the well-known Gibbs-Thomson equation and

secondary nucleation theory [76]. The derived equation relates the melting temperature, T_m, of a crystal formed at a temperature T_c, the equilibrium melting temperature and the thickening coefficient, γ, defined as the ratio between the thickness of the grown crystal, l_c, and the initial thickness of a "virgin lamella" l_g^*:

$$T_m = T_m^0 (1 - 1/\gamma) + T_c/\gamma \quad (2)$$

A straight line is obtained by plotting T_m as a function of T_c, with the equilibrium temperature corresponding to the intersection of this line with the $T_m = T_c$ line. The validity of equation 2 implies that lamellar crystals thicken at a specific crystallization temperature, which also influences the thickening parameter. **Fig. 5-40a** shows the evolution of the melting peak for the representative nylon 4,5+9_50 copolymer when it was crystallized at different temperatures. It is clear that the predominant peak, which is associated to the fusion of the initial crystallized lamellae, shifted to higher temperatures with increasing crystallization temperature.

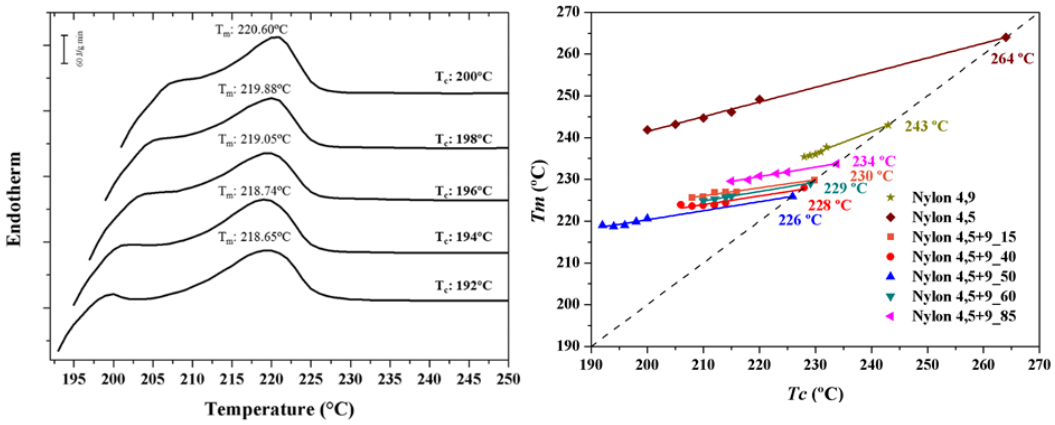

Fig. 5-40. *DSC heating scans (20 °C/min) of nylon 4,5+9_50 (**a**) samples isothermally crystallized at the indicated temperatures. (**b**) Hoffman–Weeks plot of temperatures corresponding to the predominant melting peak versus crystallization temperature for nylons 4,5+9_X samples. Equilibrium melting temperatures are explicitly indicated at the intersection point with the $T_m = T_c$ line.*

Fig. 5-40b shows the Hoffman–Weeks plots of all copolymers studied, considering the evolution of the predominant melting peak. Equilibrium melting temperature of copolymers clearly decreased with respect to that found for the related homopolymer (i.e., that derived from the predominant dicarboxylate unit). Thus, equilibrium temperatures followed the sequence nylon 4,5+9_40 < nylon 4,5+9_15 < nylon 4,5+9_0 and nylon 4,5+9_50 < nylon 4,5+9_60 < nylon 4,5+9_85 < nylon 4,5+9_100. It is also worth pointing out that the slope of the plots, $1/\gamma$, can be regarded as a measure of the stability of crystals undergoing the melting process and that significant differences could be found. Thus, the incorporation of comonomer units clearly decreased the slope, suggesting a greater difference between l_c and l_g^*. In the same way, the homopolymer derived from glutarate acid units seemed less stable than that constituted by azelate units.

5.4.2.4. Melting point depression

Crystallization of random copolymers constituted by two monomers (e.g. A and B) can take place by the exclusion of the less abundant monomer from the lattice of the predominant structure or alternatively this monomer can be included as defects in the lattice [86-89]. Melting point depression in the thermodynamic equilibrium is characteristic, being possible to estimate it by means of the Flory equation 3 [87]:

$$1/T_m^0 - 1/T_m = R/\Delta H_m^0 \ln(1 - X_B), \quad (3)$$

where X_B is the molar ratio of the minor comonomer (B) in the copolymer, ΔH_m^0 is the homopolymer equilibrium heat of fusion and R is the gas constant. 32 kJ/mol for nylon 4,5+9_0 and 48 kJ/mol for nylon 4,5+9_100 were estimated from the group contribution theory [90] that assigns 4 kJ/mol and 2 kJ/mol for each CH_2 and amide group of the chemical repeat unit.

Fig. 5-41 compares the experimental equilibrium melting temperatures of copolymers with those predicted by the Flory equation. It is clear that a clear disagreement exists, which could be consequence of serious limitations of the assumed model (e.g. the hypothesis of a homopolymer sequence of infinite length). To avoid this problem, other models such as that proposed by Baur were postulated. In this case, homopolymer sequences of a defined length, ξ, have been considered to build crystals of lamellar thickness corresponding to that length [89]. Thus, the melting point becomes now defined by equation 4:

$$1/T_m^0 - 1/T_m = R/\Delta H_m^0 \{\ln(1 - X_B) - \langle \xi \rangle^{-1}\}, \quad (4)$$

where $\langle \xi \rangle = \{2 X_B (1 - X_B)\}^{-1}$ is the average length of homopolymer sequences in the melt.

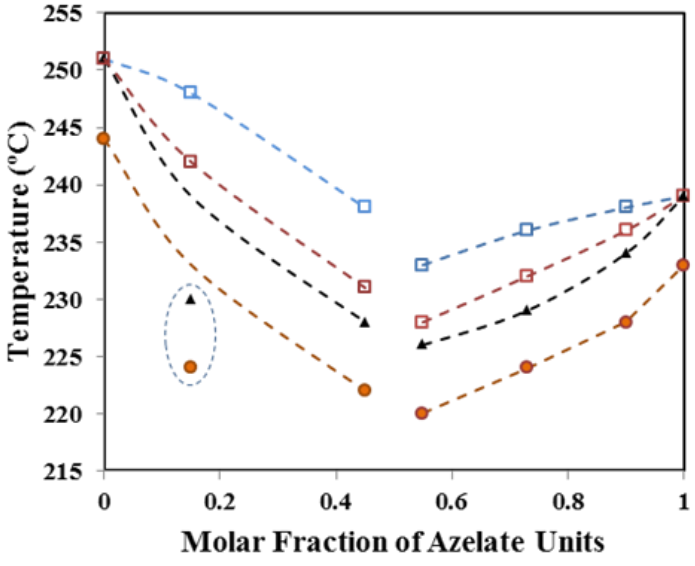

Fig. 5-41. *Composition dependence of the experimental (▲) and theoretical equilibrium melting temperature according to Flory (□) and Bauer (□) models. For the sake of completeness the main melting peak temperatures observed in the second heating run (●) are also plotted. Dashed circle points out experimental values that strongly deviate from theoretical values.*

A better agreement was found in this case between experimental and calculated data (**Fig. 5-41**), supporting the idea of an exclusion model. Only nylon 4,5+9_15 shows a clear deviation and specifically the experimental value becomes clearly lower than expected probably as a consequence of other factors like the occurrence of a minor degradation, as previously indicated, and the presence of some impurities. The exclusion model seems highly coherent when dicarboxylic acids with a clearly differentiated length should coexist in a crystalline lattice with the strong geometrical restriction imposed by the establishment of intermolecular hydrogen bonds.

5.4.2.5. Morphology of nylon 4,5+9 single crystals

Copolymers were able to crystallize from dilute glycerin solutions giving rise to lamellar crystals even for a high comonomer content (e.g. nylon 4,5+9_50). Crystallization of nylon 4,5+9_100 has been previously studied [78], being described a morphology dependence with crystallization temperature. **Fig. 5-42a** shows specifically the formation at a relatively high crystallization temperature (i.e. 130 ºC) of lenticular basal crystals that could attain 2 μm in its longer dimension. Small overgrowths with a rhombic morphology are also characteristic (see red circles). The electron diffraction pattern of this homopolymer was in agreement with a rectangular unit cell with a and b dimensions of 0.430 nm and 0.860 nm, respectively. Main relevant features of the diffraction patterns were the clear 2mm symmetry, which was postulated for the model with two hydrogen bonding directions [40-42, 64, 78], the presence of four and two prominent reflections at 0.385 and 0.430 nm, respectively, and a pattern resolution up to 0.160 nm (i.e. the 150 reflection could still be distinguished). The orientation of the diffraction pattern with respect to the crystal morphology indicates that the b* reciprocal axis was aligned with the long crystal dimension and that the lateral faces of rhombic crystals corresponded to 110 planes.

Obviously, crystallization into single crystals was more difficult when the comonomer content increased. Specifically, representative morphologies attained with the nylon 4, 5+9_50 sample are displayed in **Fig. 5-42b-d**. Thus, **Fig. 5-42b** shows the formation of aggregates derived from a common nucleus and having radial arms with extremities consistent on small lath-like single crystals (see higher magnification micrographs of samples crystallized at higher temperatures that are given in **Fig. 5-42c,d**). These lamellae had a thickness around 10 nm as determined from their shadows in the micrographs, a length less than 0.5 μm and wideness less than 0.1 μm. Such crystals were aligned in some regions, being possible to get a practically oriented electron diffraction pattern (**Fig. 5-42d**). The pattern showed again the characteristic 2*mm* symmetry with four prominent reflections at 0.385 nm. Nevertheless, some particular features should be highlighted: a) Morphology of crystals changed from rhombic to rectangular and consequently 100 and 020 become now the preferred growth faces. In any case the b^* reciprocal axis still remained aligned with the higher crystal growth direction; b) Diffraction patterns had a lower resolution as a consequence of the very small crystal dimensions, being only

detected the six more intense reflections; c) reflections associated to 020 planes become weak, highly diffuse and even appeared at a lower spacing than expected. This feature can be explained as a consequence of a very low stability of crystals during exposure that mainly affect the molecular arrangement along the {010} direction and even a tilting of the small lamellar crystals.

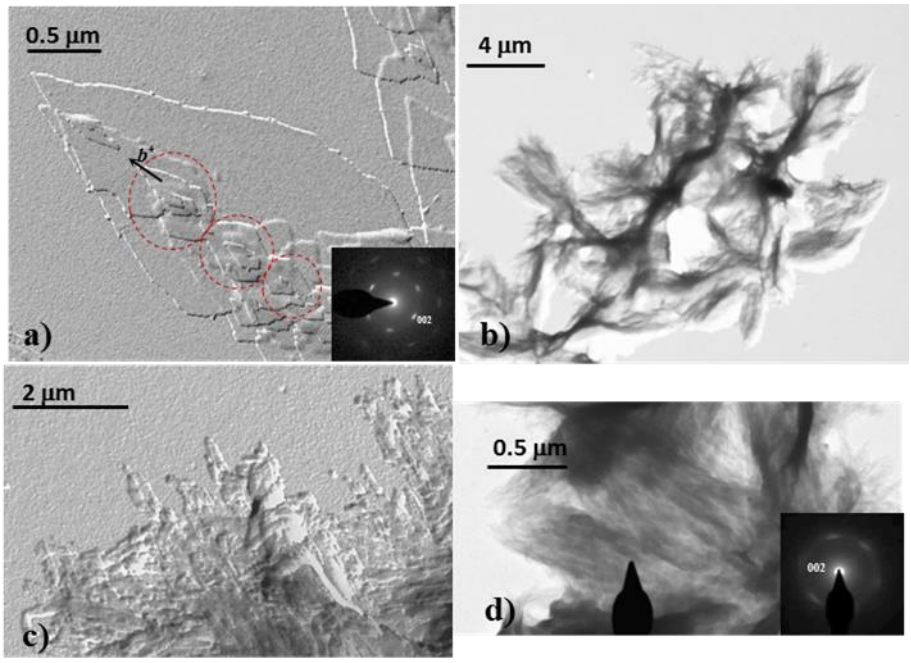

Fig. 5-42. *Transmission electron micrographs of nylon 4 9_100 (**a**) and nylon 4 5+9_50 (**b–d**) crystals obtained from dilute glycerin solutions, illustrating the influence of the presence of comonomer (**a**,**d**) and crystallization conditions (**b–d**) on the crystal morphology: (**a**) lenticular lamellar crystals obtained at 130 °C and corresponding electron diffraction pattern (inset); (**b**) spherulitic aggregate obtained at 90 °C. (**c**) Aggregates constituted by planar crystals obtained at 110 °C. (**d**) Oriented lath-shaped crystals obtained at 120 °C. The inset corresponds to the 2mm electron diffraction pattern of the bright field selected-area indicated by the beam stop. Pattern is oriented in agreement with the bright field image.*

5.4.2.6. Morphology of nylon 4,5+9_X spherulites obtained from melt crystallization

Crystallization from the melt state rendered small spherulites due to the high primary nucleation density. Thus, diameters reached a maximum size for the homopolymer derived from azelate units when crystallization was performed at 238 °C, which represented a supercooling degree of only 5 °C. This size decreased obviously when crystallization temperature did and specifically a diameter close to 60 µm was measured at a supercooling degree of 15 °C (i.e., T_c = 229 °C) as shown in the inset of **Fig. 5-43.**

Incorporation of glutarate comonomer units decreased the crystal growth rate due to the presence of foreign units that hindered the correct arrangement of crystallizable units. However, it is remarkable to point out that typical spherulites were developed even for the nylon 4,5+9_50 copolymer. **Fig. 5-43** displays typical spherulites of this nylon that were developed at a degree of supercooling close to 15 °C (i.e., T_c = 205 °C). These spherulites showed a negative birefringence and a ringed texture indicative of lamellar twisting, being the spacing between rings close to 2 µm. Micrographs showed the impingement of spherulites, the lack of amorphous regions between them and

a maximum size of 20 μm, which was clearly inferior to that observed for nylon 4 5+9_100 crystallized under the same degree of supercooling. Micrographs demonstrated the ability to get well formed spherulites even for the most adverse composition and allow the inference that foreign comonomer units should be located in the amorphous regions (i.e., the surface of constitutive lamellae and the interlamelar and interspherulitic regions).

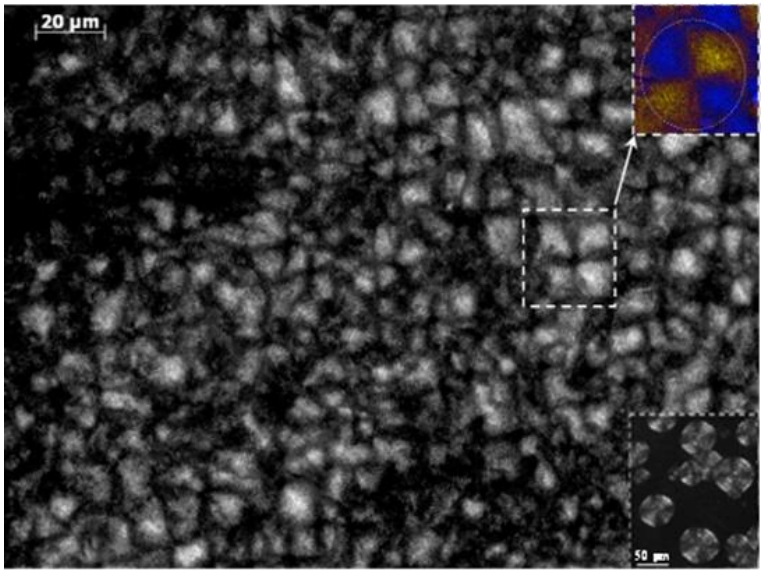

Fig. 5-43. *Spherulitic morphology of nylon 4 5+9_50 isothermally crystallized at 205 ºC. Insets show a colour micrograph taken with a red tin plate to determine the sign of birefringence and a black and white micrograph of nylon 4 5+9_100 spherulites crystallized at 229 ºC (i.e. a temperature corresponding to a similar degree of supercooling than that applied for the copolymer melt crystallization).*

5.4.2.7. X-ray diffraction patterns of solution crystallized samples

X-ray diffraction profiles of the as synthesized samples (**Fig. 5-44a**) are characterized by two strong reflections at 0.428-0.433 nm and 0.376-0.385 nm (**Fig. 5-44b**) that are characteristic of the typical α-form of conventional nylons or the named form I postulated for even-odd polyamides, which is characterized by a monoclinic structure with two hydrogen bonding directions and a rectangular chain axis projected unit cell. The recorded patterns mainly differ in the relative intensity of the two observed reflections (**Fig. 5-44b**), being the lower spacing reflection more intense when the content of glutaric acid units decreased. This feature may be justified considering the lower crystallinity of such copolymers and the presence of an amorphous halo, which is centered around 0.410-0.406 nm and has a tail that mainly overlapped with the Bragg reflection at 0.430 nm. Even a second crystalline phase (form II) with a main peak around 0.420 nm may be present. Logically X-ray profiles differ also in the 004 reflection associated to the chain repeat, which is detected at 0.711 nm and 0.591 nm for nylons 4,5+9_100 and nylon 4,5+9_0, respectively. Copolymer samples had 004 reflections at only one of the two indicated spacings (i.e. 0.711 nm was characteristic of samples with X varying from 50 to 100 while 0.591 was detected for samples with X equal 0 and 40). The lack of a distortion for the c axis parameter

when composition is modified suggests that comonomer units were not incorporated in the cell unit of the predominant structure.

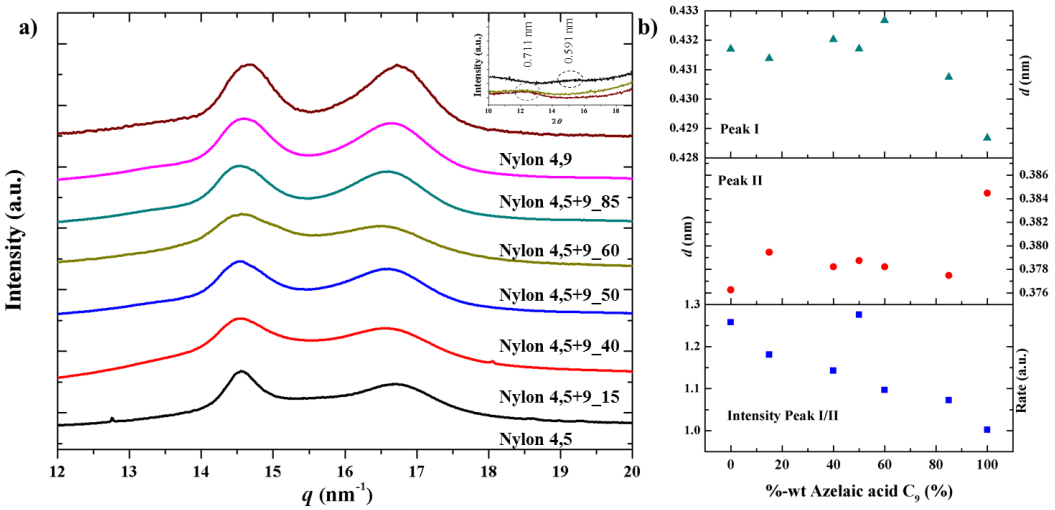

Fig. 5-44. ***(a)*** *X-ray diffraction profiles of as synthesized nylon 4,5+9_X samples. Inset shows the 004 reflection for the two homopolymers and the copolymer having the 50% intermediate composition. Arrows pointed out the presence of shoulders that could be associated to the amorphous halo and a second crystalline structure,* ***(b)*** *Variation of the spacing of the (110) reflection (up), the (020) reflection (middle) and the intensity ratio of the two indicated reflections with the azelate content.*

5.4.2.8. Structural transitions during the heating process of solution crystallized homopolymer samples

Structural transitions of nylon 4,5+9_100 have been previously studied by means of synchrotron radiation [78], being a complex behavior involving three crystalline phases determined. In brief, the sample recovered from synthesis and also that crystallized from dilute solutions correspond to the two dimensional hydrogen-bonded structure named form I and characterized by two strong reflections around 0.428-0.433 nm and 0.376-0.385 nm. Depending on the sample preparation method (e.g. precipitation, solvent casting, solution or melt crystallization) a second crystalline structure (form II) was developed during the heating process. This form was postulated as a consequence of a slight modification of the molecular conformation that allowed keeping the hydrogen bonded structure and gave rise to two reflections at 0.420–0.417 nm (strong) and 0.410 nm (weak). Finally, when samples reached temperatures close to fusion a pseudohexagonal arrangement (form III or Brill structure) with a single reflection close to 0.423 nm was observed. The different behavior on heating (i.e. direct transition from form I to form III or progressive transition from form I to form II and finally to form III) was found dependent on the initial crystalline structure, being enhanced the progressive transitions when the initial sample had traces of form II (e.g. melt crystallized and solvent casting samples).

Fig. 5-45a shows the heating behavior of the synthesized azelate homopolymer, which is characterized by a progressive shift of the peak at 0.376 nm to higher spacings up to a maximum value of 0.410 nm, while the spacing of the 020 reflection remained practically constant (i.e., 0.430 nm). During heating a lamellar reordering process is observed around 130 ºC as detected by the slight

increase of the intensity of reflections associated to form I. Form III appeared at a temperature close to 195 ºC, but was not a consequence of the overlapping of the indicated 110 and 020 reflections.

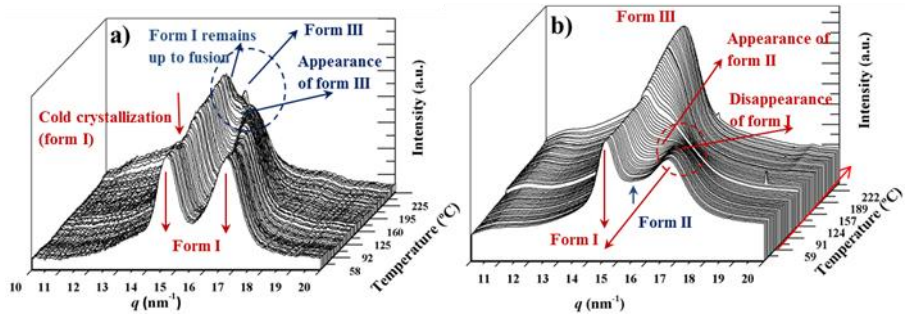

Fig. 5-45. *Three dimensional representation of WAXD profiles of nylons 4,5+9_100* ***(a)*** *and 4,5+9_0* ***(b)*** *during heating (10 °C/min) from room temperature to fusion. Labels indicate main polymorphic transitions and reflections associated to the different crystalline forms (see dashed circles and arrows).*

Fig. 5-45b shows the different behavior during heating that was observed for the homopolymer constituted by glutarate units. In this case, reflections associated to form 1 disappeared around 120 ºC (see the evolution of the 020 reflection), while reflections associated to form II gradually increased on intensity. Probably the clearer evidence corresponds to the weak shoulder observed around 0.410 nm. In any case, form I has completely disappeared some degrees before fusion, appearing a single peak around 0.423 nm, which can be associated to form III (i.e. the pseudohexagonal Brill structure). Differences between homopolymers constituted by azelate or glutarate units can be attributed as previously reported [78] to the existence of a minor ratio of form II in the initial sample of the glutarate homopolymer (see blue arrow in **Fig. 5-45b**).

5.4.2.9. Structural transitions during the heating process of solution crystallized copolymer samples

Behavior of the different copolymers is similar to that observed for the related homopolymers as displayed for the representative nylons 4,5+9_85, 4,5+9_60 and 4,5+9_15 in **Fig. 5-46**. It is clear that copolymers rich in azelate units do not show a form I to form II transition and that only just before melting appears the reflection associated to form III (see dashed blue circle in **Fig. 5-46a,b**). Note that again the main strong reflections of form I are converging but do not meet each other, giving rise to the single reflection associated to form III. This form appears at the end but not as a consequence of a typical Brill transition.

By contrast, samples rich in glutarate units showed the behavior described for the glutarate homopolymer that is characterized by a clear form I to form II transition at a relatively low temperature and the collapse of the two reflections of form II into the single one associated to form III (i.e., a Brill transition from form II took place) (**Fig. 5-46c**).

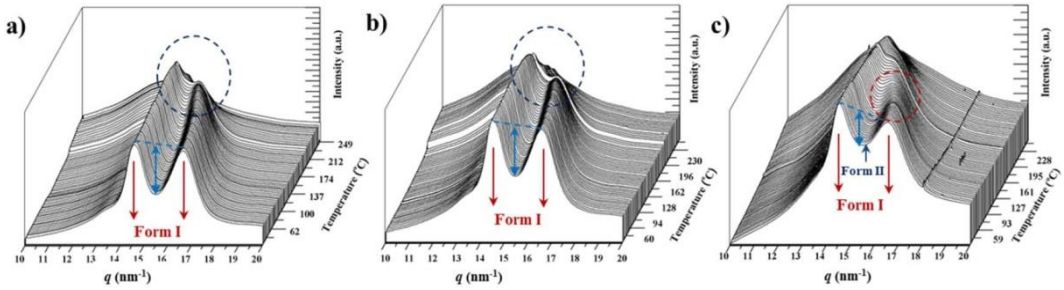

Fig. 5-46. *Three dimensional representation of WAXD profiles of nylons 4,5+9_85 (**a**), 4,5+9_60 (**b**) and 4,5+9_15 (**c**) during heating (10 °C/min) from room temperature to fusion. Red and blue dashed circles pointed out regions where a form I to form II transition and the appearance of form III can be detected, respectively.*

The main distinctive feature between the two series of copolymers (i.e., glutarate or azelate rich samples) seems to be the presence in the initial sample of a small peak associated to the weaker reflection of form II. As indicated before, the presence of this structure can be easily deduced trough the decrease on the ratio between the intensities of 110 and 020 reflections of form I. This feature is evidenced by the clear decrease of the valley between these two reflections (i.e., see the differences between light blue double arrows in **Fig. 5-46b,c**).

5.4.2.10. Structural Transitions During the Cooling and Reheating Process of Nylon 4,5+9 Samples

Fig. 5-47 shows the complete sequence of heating, cooling and reheating processes that was performed with the copolymer having an intermediate composition. The first heating run revealed the transition from form I to form II that took place around 120-125 ºC, which is logical considering the presence of form II in the initial sample as can be deduced from the small valley between the two strong form I reflections. It should also be pointed out that the great amorphous content (see the tail of the broad halo in **Fig. 5-47a**) contributes also to this low intensity ratio. More interestingly the copolymer, which structure is mainly associated to that of the azelate homopolymer, is able to undergo the indicated transition. Heating run is also interesting since the form II to form III transition could be detected through the increase of the intensity of the final peak (see blue dashed circle in **Fig. 5-47a**) after the merging of the two reflections associated to form II (i.e. after the Brill transition). Cooling run (**Fig. 5-47b**) shows that the samples initially crystallized in the pseudohexagonal form, being not clear the transition between forms III and II. However, when a temperature of 100 ºC was reached a clear transition that leads to form I can be detected (see red arrow and the dashed red circle that point out the intensity increase of the long spacing reflection and the appearance of the 0.380 nm reflection associated to form I, respectively).

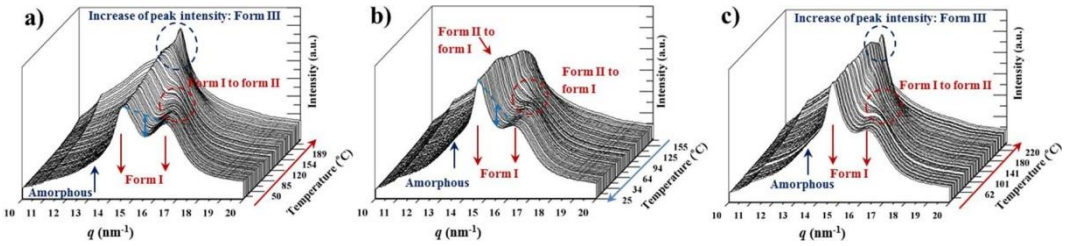

Fig. 5-47. *Three dimensional representation of WAXD profiles of nylons 4,5+9_50 during heating (10 °C/ min) from room temperature to fusion* ***(a)****, cooling from the melt state to room temperature* ***(b)*** *and subsequent heating of the melt crystallized sample* ***(c)****.*

Fig. 5-48 shows the profiles of all the studied samples after the cooling process. All of them are characterized by the strong reflections of the form I structure, although the low intense peak of form II can always be guessed. This feature is highly relevant since the behavior on a subsequent heating process drastically changed, being a complete form II to form I transition always observed. Profiles after cooling showed slight differences in some cases as for example, a greater content of form II and the amorphous phase in the nylon 4,5+9_15 copolymer.

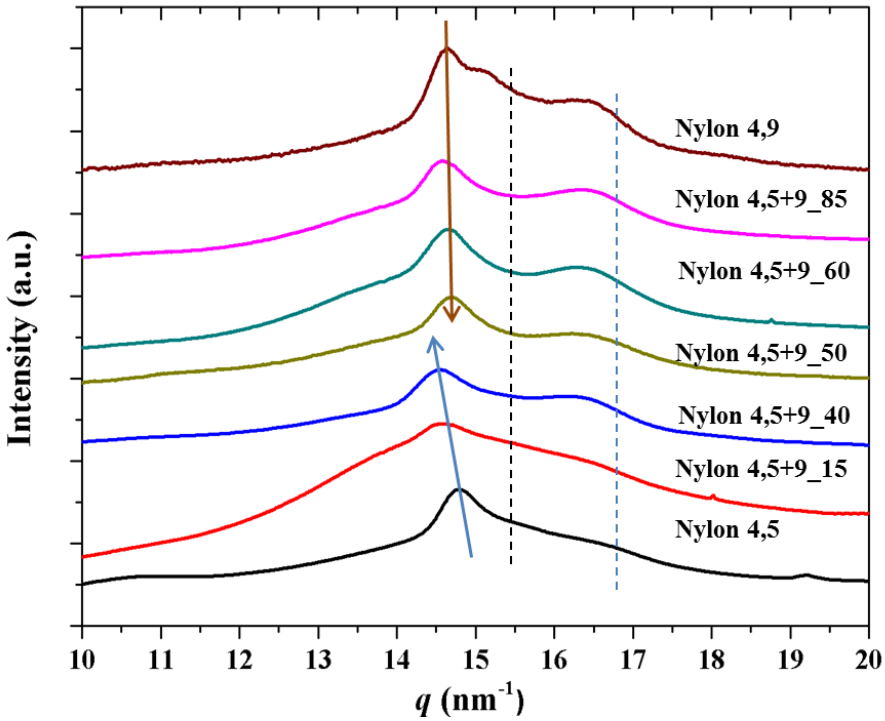

Fig. 5-48. *X-ray diffraction profiles of melt crystallized nylon 4,5+9 samples. Arrows show the evolution of the main peak while dashed lines points out the minor peaks.*

Fig. 5-49 summarizes the observed variations on the spacings of the observed reflections for representative copolymers during heating, cooling and reheating processes. Two evidences can be highlighted: a) The different behavior between melt (second heating run) and solution crystallized samples (first heating run) when form II was not initially present; b) Transitions between form I and II are always observed during cooling and reheating processes, suggesting a reversible behavior that took place in the narrow temperature interval between 100 and 130 ºC.

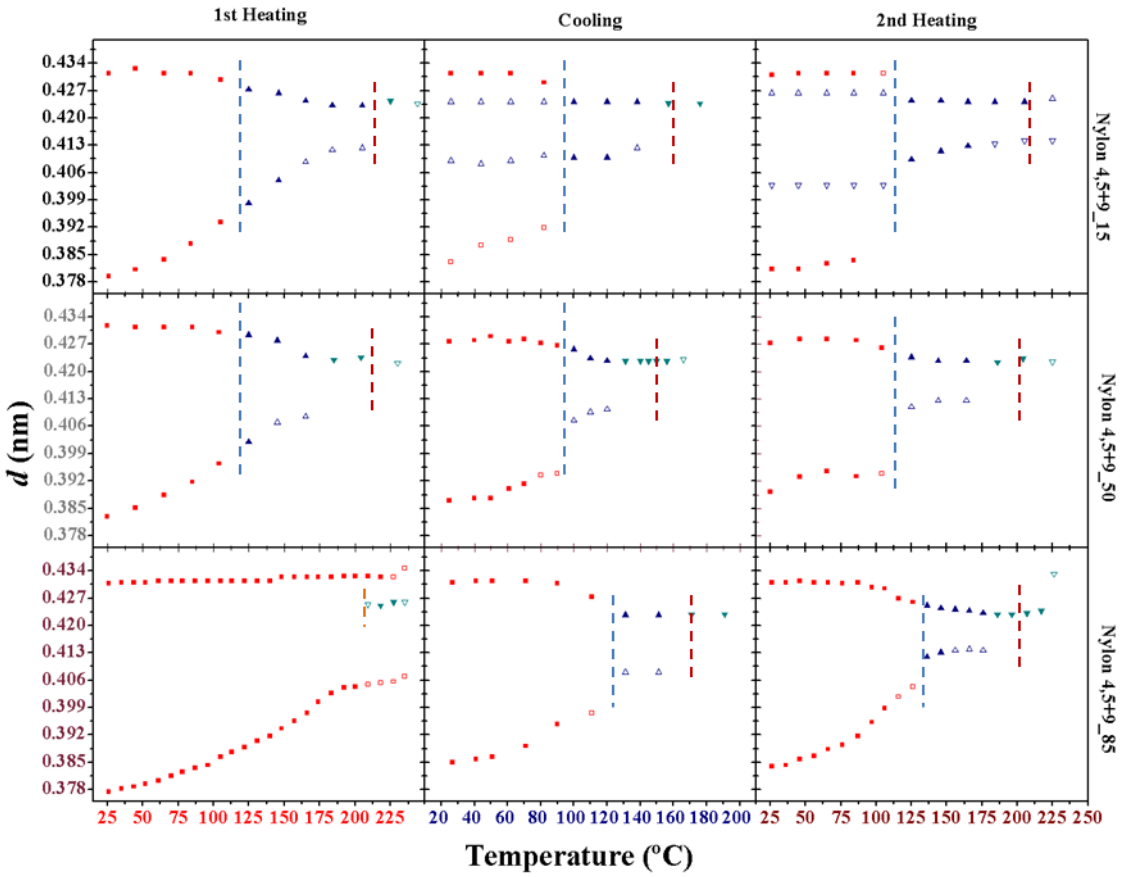

Fig. 5-49. *Temperature evolution of the intensity of the main peaks during the first heating (left), cooling (middle) and second heating (right) processes for nylons 4,5+9_15 (top), nylon 4,5+9_50 (middle) and nylon 4,5+9_85 (bottom). Full and empty symbols indicate well-defined and intuited reflections, respectively. The temperatures at which structural changes occurred are indicated with vertical lines (blue for I-II transition, red for II-III transition and orange when form III appeared without any associated transition). Reflections corresponding to forms I, II and III are indicated in red, green and blue, respectively.*

5.4.3. Conclusions

Homopolymers and copolymers derived from even 1,4-diaminobutane and odd glutarate or/and azelate units preferentially crystallized from solution and the melt according to a crystalline structure characterized by strong reflections at 0.430 and 0.380 nm. This structure can be associated to a two hydrogen-bonding molecular arrangement named form I. Structural transitions could be observed on subsequent heating processes but they mainly depended on the presence or absence of a second structure, named form II. Experiments demonstrated that this behavior was independent of the chemical constitution of the crystalline fraction. Samples that exhibited only form I showed on heating a progressive shift of characteristic spacings without being detected a polymorphic transition to form II. However, at temperatures close to fusion a new pseudohexagonal arrangement (form III) was developed but in never could be associated to a transition from the initial form I. Samples having initially a ratio of form II showed a well-differentiated behavior on heating and specifically a conversion from form I to form II was detected at relatively low temperatures (e.g. ca. 120 ºC) until the complete disappearance of form I. At high temperatures a second transition from form II to form III was observed. In all cases, samples crystallized from the melt according to form III and experimented

transitions during cooling to form II and form I (ca. 120 ºC) occurred. The last transition was not complete and consequently the melt crystallized samples was constituted by forms I and II, being the later the minority one.

All copolymers were able to render spherulites and single crystals when crystallized from the melt state or from diluted solutions, respectively, even when the comonomer content was high. Calorimetric data supported that comonomer units were excluded from the crystalline domains (i.e. were incorporated into the amorphous folding surfaces or into the amorphous interlamellar spherulitic regions).

5.5. References

1. Bieber, T.I. Improving the Nylon rope trick. *Journal of Chemical Education* (1979), *56*, 409.

2. Marchildon, K. Polyamides – Still Strong After Seventy Years. *Macromolecular Reaction Engineering* (2011), *5*, 22-54.

3. Bennett, C.; Kaya, E.; Sikes, A.M.; Jarrett, W.L..Mathias, L.J. Synthesis and characterization of nylon 18 18 and nylon 18 adamantane. *Journal of Polymer Science Part A: Polymer Chemistry* (2009), *47*, 4409-4419.

4. Liu, S.; Cui, Z.; Fu, P.; Liu, M.; Zhang, L.; Li, Z..Zhao, Q. Ferroelectric behavior and polarization mechanism in odd-odd polyamide 11,11. *Journal of Polymer Science Part B: Polymer Physics* (2014), *52*, 1094-1099.

5. Xenopoulos, A..Wunderlich, B. Conformational motion and disorder in aliphatic nylons The case of nylon 6.6. *Colloid and Polymer Science* (1991), *269*, 375-391.

6. Bunn, C.W.; Garner, E.V..Bragg, W.L. The crystal structures of two polyamides ('nylons'). *Proceedings of the Royal Society of London. Series A. Mathematical and Physical Sciences* (1947), *189*, 39-68.

7. Jones, N.A.; Atkins, E.D.T.; Hill, M.J.; Cooper, S.J..Franco, L. Chain-Folded Lamellar Crystals of Aliphatic Polyamides. Comparisons between Nylons 4 4, 6 4, 8 4, 10 4, and 12 4. *Macromolecules* (1996), *29*, 6011-6018.

8. Hill, M.J..Atkins, E.D.T. Morphology and Structure of Nylon 68 Single Crystals. *Macromolecules* (1995), *28*, 604-609.

9. Jones, N.A.; Atkins, E.D.T.; Hill, M.J.; Cooper, S.J..Franco, L. Chain-folded lamellar crystals of aliphatic polyamides. Investigation of nylons 4 8, 4 10, 4 12, 6 10, 6 12, 6 18 and 8 12. *Polymer* (1997), *38*, 2689-2699.

10. Franco, L..Puiggalí, J. Structural data and thermal studies on nylon-12,10. *Journal of Polymer Science Part B: Polymer Physics* (1995), *33*, 2065-2073.

11. Jones, N.A.; Atkins, E.D.T.; Hill, M.J.; Cooper, S.J..Franco, L. Polyamides with a Choice of Structure and Crystal Surface Chemistry. Studies of Chain-Folded Lamellae of Nylons 8 10 and 10 12 and Comparison with the Other 2N 2(N + 1) Nylons 4 6 and 6 8. *Macromolecules* (1997), *30*, 3569-3578.

12. Holmes, D.R.; Bunn, C.W..Smith, D.J. The crystal structure of polycaproamide: Nylon 6. *Journal of Polymer Science* (1955), *17*, 159-177.

13. R. Brill, V. Beziehungen zwischen wasserstoffbindung und einigen eigenschaften von polyamiden. (1956), *18*, 294-309.

14. Jones, N.A.; Atkins, E.D.T..Hill, M.J. Comparison of Structures and Behavior on Heating of Solution-Grown, Chain-Folded Lamellar Crystals of 31 Even−Even Nylons. *Macromolecules* (2000), *33*, 2642-2650.

15. Ramesh, C..Gowd, E.B. High-Temperature X-ray Diffraction Studies on the Crystalline Transitions in the α- and γ-Forms of Nylon-6. *Macromolecules* (2001), *34*, 3308-3313.

16. Kinoshita, Y. An investigation of the structures of polyamide series. *Die Makromolekulare Chemie* (1959), *33*, 1-20.

17. Brill, R. Über das Verhalten von Polyamiden beim Erhitzen. *Journal für Praktische Chemie* (1942), *161*, 49-64.

18. Cooper, S.J.; Atkins, E.D.T..Hill, M.J. Temperature-Induced Changes in Lamellar Crystals of Monodisperse Nylon 6 and Nylon 6 6 Oligoamides. *Macromolecules* (1998), *31*, 8947-8956.

19. Miura, H..English, A.D. Segmental dynamics in nylon 66. *Macromolecules* (1988), *21*, 1543-1544.

20. Hirschinger, J.; Miura, H.; Gardner, K.H..English, A.D. Segmental dynamics in the crystalline phase of nylon 66: solid state deuterium NMR. *Macromolecules* (1990), *23*, 2153-2169.

21. Wendoloski, J.J.; Gardner, K.H.; Hirschinger, J.; Miura, H..English, A.D. Molecular Dynamics in Ordered Structures: Computer Simulation and Experimental Results for Nylon 66 Crystals. *Science* (1990), *247*, 431-436.

22. Yoshioka, Y.; Tashiro, K..Ramesh, C. Structural change in the Brill transition of Nylon m/n (2) conformational disordering as viewed from the temperature-dependent infrared spectral measurements. *Polymer* (2003), *44*, 6407-6417.

23. Tashiro, K..Yoshioka, Y. Molecular dynamics simulation of the structural and mechanical property changes in the Brill transition of nylon 10/10 crystal. *Polymer* (2004), *45*, 4337-4348.

24. Bella, J.; Puiggalí, J..Subirana, J.A. Glycine residues induce a helical structure in polyamides. *Polymer* (1994), *35*, 1291-1297.

25. Tormo, J.; Puiggali, J.; Vives, J.; Fita, I.; Lloveras, J.; Bella, J.; Aymamí, J..Subirana, J.A. Crystal structure of a helical oligopeptide model of polyglycine II and of other polyamides: Acetyl-(glycyl-β-alanyl)2-NH propyl. *Biopolymers* (1992), *32*, 643-648.

26. Crick, F.H.C..Rich, A. Structure of Polyglycine II. *Nature* (1955), *176*, 780-781.

27. Puiggalí, J.; Aceituno, J.E.; Navarro, E.; Campos, J.L..Subirana, J.A. Structure of n,3 Polyamides, a Group of Nylons with Two Spatial Hydrogen-Bond Orientations. *Macromolecules* (1996), *29*, 8170-8179.

28. Tereshko, V.; Navarro, E.; Puiggali, J..Subirana, J.A. Structures of two malonamide derivatives as models of nylons n,3 and of peptidomimetic compounds. *Macromolecules* (1993), *26*, 7024-7028.

29. Puiggalí, J.; Franco, L.; Alemán, C..Subirana, J.A. Crystal Structures of Nylon 5,6. A Model with Two Hydrogen Bond Directions for Nylons Derived from Odd Diamines. *Macromolecules* (1998), *31*, 8540-8548.

30. Morales-Gámez, L.; Soto, D.; Franco, L..Puiggalí, J. Brill transition and melt crystallization of nylon 56: An odd–even polyamide with two hydrogen-bonding directions. (2010), *51*, 5788-5798.

31. Villaseñor, P.; Franco, L.; Subirana, J.A..Puiggalí, J. On the crystal structure of odd–even nylons: Polymorphism of nylon 5,10. *Journal of Polymer Science Part B: Polymer Physics* (1999), *37*, 2383-2395.

32. Franco, L.; Subirana, J.A..Puiggalí, J. Structure and Morphology of Odd Polyoxamides Nylon 9,2. A New Example of Hydrogen-Bonding Interactions in Two Different Directions. *Macromolecules* (1998), *31*, 3912-3924.

33. Nakagawa, T.; Nozaki, K.; Maeda, S..Yamamoto, T. Polymorphism of poly(nonamethyleneoxamide) crystal. (2015), *57*, 99-104.

34. Cui, X..Yan, D. Preparation, characterization and crystalline transitions of odd–even polyamides 11,12 and 11,10. (2005), *41*, 863-870.

35. Samanta, S.; He, J.; Selvakumar, S.; Lattimer, J.; Ulven, C.; Sibi, M.; Bahr, J..Chisholm, B.J. Polyamides based on the renewable monomer, 1,13-tridecane diamine II: Synthesis and characterization of nylon 13,6. *Polymer* (2013), *54*, 1141-1149.

36. Navarro, E.; Franco, L.; Subirana, J.A..Puiggali, J. Nylon 65 has a Unique Structure with Two Directions of Hydrogen Bonds. *Macromolecules* (1995), *28*, 8742-8750.

37. Morales-Gámez, L.; Ricart, A.; Franco, L..Puiggalí, J. Study on the brill transition and melt crystallization of nylon 65: A polymer able to adopt a structure with two hydrogen-bonding directions. *European Polymer Journal* (2010), *46*, 2063-2077.

38. Navarro, E.; Subirana, J.A..Puiggali, J. The structure of nylon 12,5 is characterized by two hydrogen bond directions as are other polyamides derived from glutaric acid. *Polymer* (1997), *38*, 3429-3432.

39. Cui, X.; Yan, D..Xiao, D. Synthesis and characterization of novel polyamides based on tridecanedioic acid: Nylons 3 13, 5 13, 6 13, 7 13, 9 13, 10 13, 11 13. (2004), *4*.

40. Morales-Gámez, L.; Casas, M.T.; Franco, L..Puiggalí, J. Structural transitions of nylon 47 and clay influence on its crystallization behavior. *European Polymer Journal* (2013), *49*, 1354-1364.

41. Franco, L.; Cooper, S.J.; Atkins, E.D.T.; Hill, M.J..Jones, N.A. Nylon 6 9 can crystallize with hydrogen bonding in two and in three interchain directions. *Journal of Polymer Science Part B: Polymer Physics* (1998), *36*, 1153-1165.

42. Murase, S.K.; Casas, M.T.; Martínez, J.C.; Estrany, F.; Franco, L..Puiggalí, J. Reversible changes induced by temperature in the spherulitic birefringence of nylon 6 9. *Polymer* (2015), *76*, 34-45.

43. Magill, J.H. Spherulitic crystallization studies of poly(tetramethyl-p-silphenylene)–siloxane (TMPS). Part III. *Journal of Polymer Science Part A-2: Polymer Physics* (1969), *7*, 1187-1195.

44. Cui, X.; Liu, Z..Yan, D. Synthesis and characterization of novel even–odd nylons based on undecanedioic acid. *European Polymer Journal* (2004), *40*, 1111-1118.

45. Weeks, J.D.H.a.J.J. Melting Process and Equilibrium Melting Temperature of Polychlorotrifluoroethylene. *Journal of Research of the National Bureau of Standards Section a-Physics and Chemistry* (1962), *66*, 13-28.

46. Lovinger, A.J. Crystallographic factors affecting the structure of polymeric spherulites. I. Morphology of directionally solidified polyamides. *Journal of Applied Physics* (1978), *49*, 5003-5013.

47. Lovinger, A.J. Crystallographic factors affecting the structure of polymeric spherulites. II. X- ray diffraction analysis of directionally solidified polyamides and general conclusions. *Journal of Applied Physics* (1978), *49*, 5014-5028.

48. Jr., J.I.L..Hoffman, J.D. Extension of theory of growth of chain-folded polymer crystals to large undercoolings. *Journal of Applied Physics* (1973), *44*, 4340-4352.

49. Suzuki, T..Kovacs, A.J. Temperature Dependence of Spherulitic Growth Rate of Isotactic Polystyrene. A Critical Comparison with the Kinetic theory of Surface Nucleation. *Polymer Journal* (1970), *1*, 82-100.

50. Kohan, M.I. *Nylon plastics handbook*, Hanser Publishers ; Distributed in the USA and in Canada by Hanser/Gardner Publications:Munich; New York; Cincinnati, (1995).

51. Prieto, A.; Montserrat, J.M..Munoz-Guerra, S. Structure of nylon 7 solution grown crystals. *Journal of Materials Science* (1990), *25*, 2091-2094.

52. Dasgupta, S.; Hammond, W.B..Goddard, W.A. Crystal Structures and Properties of Nylon Polymers from Theory. *Journal of the American Chemical Society* (1996), *118*, 12291-12301.

53. Urpí, L.; Villaseñor, P.; Rodríguez-Galán, A..Puiggalí, J. Crystal structure of N,N′-dipropylsuberamide and N,N′-dipropylsebacamide as a packing model of the α-form of even-even nylons. *Macromolecular Chemistry and Physics* (2000), *201*, 1726-1731.

54. Owen, A..Koliross, P. A note on the crystal structure of nylon-12. *Polymer communications* (1983), *24*, 303-306.

55. Arimoto, H.; Ishibashi, M.; Hirai, M..Chatani, Y. Crystal structure of the γ-form of nylon 6. *Journal of Polymer Science Part A: General Papers* (1965), *3*, 317-326.

56. Kawaguchi, A.; Ikawa, T.; Fujiwara, Y.; Tabuchi, M..Monobe, K. Polymorphism in lamellar single crystals of nylon 11. *Journal of Macromolecular Science, Part B* (1981), *20*, 1-20.

57. Feldman, A.Y.; Wachtel, E.; Vaughan, G.B.M.; Weinberg, A..Marom, G. The Brill Transition in Transcrystalline Nylon-66. *Macromolecules* (2006), *39*, 4455-4459.

58. Nair, S.S.; Ramesh, C..Tashiro, K. Crystalline Phases in Nylon-11: Studies Using HTWAXS and HTFTIR. *Macromolecules* (2006), *39*, 2841-2848.

59. Wolanov, Y.; Feldman, A.; Harel, H..Marom, G. Amorphous and crystalline phase interaction during the Brill transition in nylon 66. (2009), *3*, 452-457.

60. Chi Wang, S.-Y.T., Hsuan-Sheng Lin Brill transition of nylon-6 in electrospun nanofibers. *Colloid Polym Sci* (2012), *290*, 1799-1809.

61. Suzuki, H.; Ishii, S.; Sato, H.; Yamamoto, S.; Morisawa, Y.; Ozaki, Y.; Uchiyama, T.; Otani, C..Hoshina, H. Brill transition of nylon-6 characterized by low-frequency vibration through terahertz absorption spectroscopy. *Chemical Physics Letters* (2013), *575*, 36-39.

62. Franco, L.; Navarro, E.; Subirana, J.A..Puiggali, J. Synthesis and Structure of Nylons 1,n. *Macromolecules* (1994), *27*, 4284-4297.

63. Navarro, E.; Puiggalí, J..Subirana, J.A. Study of 1,4-bis(propylaminomalonylamino)butane as a model compound for nylons n,3. *Macromolecular Chemistry and Physics* (1995), *196*, 2361-2370.

64. Olmo, C.; Rota, R.; Carlos Martínez, J.; Puiggalí, J..Franco, L. Temperature-induced structural changes in even-odd nylons with long polymethylene segments. *Journal of Polymer Science Part B: Polymer Physics* (2016), *54*, 2494-2506.

65. van Velthoven, J.L.J.; Gootjes, L.; Noordover, B.A.J..Meuldijk, J. Bio-based, amorphous polyamides with tunable thermal properties. *European Polymer Journal* (2015), *66*, 57-66.

66. Jasinska, L.; Villani, M.; Wu, J.; van Es, D.; Klop, E.; Rastogi, S..Koning, C.E. Novel, Fully Biobased Semicrystalline Polyamides. *Macromolecules* (2011), *44*, 3458-3466.

67. Gandini, A.; Lacerda, T.M.; Carvalho, A.J.F..Trovatti, E. Progress of Polymers from Renewable Resources: Furans, Vegetable Oils, and Polysaccharides. *Chemical Reviews* (2016), *116*, 1637-1669.

68. Winnacker, M..Sag, J. Sustainable terpene-based polyamides via anionic polymerization of a pinene-derived lactam. *Chemical Communications* (2018), *54*, 841-844.

69. Eltahir, Y.A.; Saeed, H.A.M.; Yuejun, C.; Xia, Y..Yimin, W. Effect of hot drawing on the structure and properties of novel polyamide 5,6 fibers. *Textile Research Journal* (2014), *84*, 1700-1707.

70. Eltahir, Y.A.; Saeed, H.A.M.; Yuejun, C.; Xia, Y..Yimin, W. Parameters characterizing the kinetics of the non-isothermal crystallization of polyamide 5,6 determined by differential scanning calorimetry. *Journal of Polymer Engineering* (2014), *34*, 353-358.

71. Li, Y.L.; Hao, X.M.; Guo, Y.F.; Chen, X.; Yang, Y..Wang, J.M. Study on the Acid Resistant Properties of Bio-Based Nylon 56 Fiber Compared with the Fiber of Nylon 6 and Nylon 66. *Advanced Materials Research* (2014), *1048*, 57-61.

72. Capsal, J.-F.; Dantras, E.; Dandurand, J..Lacabanne, C. Dielectric relaxations and ferroelectric behaviour of even–odd polyamide PA 6,9. *Polymer* (2010), *51*, 4606-4610.

73. Scheinbeim, J.I.; Lee, J.W..Newman, B.A. Ferroelectric polarization mechanisms in nylon 11. *Macromolecules* (1992), *25*, 3729-3732.

74. Strobl, G. From the melt via mesomorphic and granular crystalline layers to lamellar crystallites: A major route followed in polymer crystallization? (2000), *3*, 165-183.

75. Marand, H.; Xu, J..Srinivas, S. Determination of the Equilibrium Melting Temperature of Polymer Crystals: Linear and Nonlinear Hoffman−Weeks Extrapolations. *Macromolecules* (1998), *31*, 8219-8229.

76. J.D. Hoffman, G.T.D., J.I. Lauritzen Jr. *Treatise on Solid State Chemistry*, Plentum:New York, (1976).

77. Winnacker, M. Polyamides and their functionalization: recent concepts for their applications as biomaterials. *Biomaterials Science* (2017), *5*, 1230-1235.

78. Olmo, C.; Casas, M.T.; Martínez, J.C.; Franco, L..Puiggalí, J. Thermally Induced Structural Transitions of Nylon 4 9 as a New Example of Even–Odd Polyamides. *Polymers* (2018), *10*, 198.

79. Puiggali, J.; Muñoz-Guerra, S..Subirana, J.A. Morphology and crystalline structure of nylon-2/6. *Polymer* (1987), *28*, 209-212.

80. Li, X.; Hong, Z.; Sun, J.; Geng, Y.; Huang, Y.; An, H.; Ma, Z.; Zhao, B.; Shao, C.; Fang, Y.; Yang, C..Li, L. Identifying the Phase Behavior of Biodegradable Poly(hexamethylene succinate-co-hexamethylene adipate) Copolymers with FTIR. *The Journal of Physical Chemistry B* (2009), *113*, 2695-2704.

81. Li, X.; Sun, J.; Huang, Y.; Geng, Y.; Wang, X.; Ma, Z.; Shao, C.; Zhang, X.; Yang, C..Li, L. Inducing New Crystal Structures through Random Copolymerization of Biodegradable Aliphatic Polyester. *Macromolecules* (2008), *41*, 3162-3168.

82. Liang, Z.; Pan, P.; Zhu, B.; Dong, T.; Hua, L..Inoue, Y. Crystalline Phase of Isomorphic Poly(hexamethylene sebacate-co-hexamethylene adipate) Copolyester: Effects of Comonomer Composition and Crystallization Temperature. *Macromolecules* (2010), *43*, 2925-2932.

83. Liang, Z.; Pan, P.; Zhu, B..Inoue, Y. Isomorphic Crystallization of Poly(hexamethylene adipate-co-butylene adipate): Regulating Crystal Modification of Polymorphic Polyester from Internal Crystalline Lattice. *Macromolecules* (2010), *43*, 6429-6437.

84. Liang, Z.; Pan, P.; Zhu, B..Inoue, Y. Isomorphic crystallization of aliphatic copolyesters derived from 1,6-hexanediol: Effect of the chemical structure of comonomer units on the extent of cocrystallization. (2011), *52*, 2667-2676.

85. Díaz, A.; Franco, L..Puiggalí, J. Study on the crystallization of poly(butylene azelate-co-butylene succinate) copolymers. (2014), *575*, 45–54.

86. Park, J.W.; Kim, D.K..Im, S.S. Crystallization behaviour of poly(butylene succinate) copolymers. *Polymer International* (2002), *51*, 239-244.

87. Flory, P.J. Theory of crystallization in copolymers. *Trans. Faraday Soc* (1955), *51*, 848-857.

88. Papageorgiou, G.Z..Bikiaris, D.N. Crystallization and melting behavior of three biodegradable poly(alkylene succinates). A comparative study. *Polymer* (2005), *46*, 12081-12092.

89. Baur, V.H. Einfluß der sequenzlängenverteilung auf das schmelz-ende von copolymeren. *Die Makromolekulare Chemie* (1966), *98*, 297-301.

90. Krevelen, D.W.v. *Properties of Polymers*, Elsevier Science: (1997).

6. Conclusions

This PhD work concludes that ultrasound (US) micromolding is a technique with high potential to produce micropieces from biodegradable and biocompatible polyesters and nylons loaded with external agents such as pharmacological drugs, inorganic compound and nanoparticles. Specifically, US micromolding demonstrated to be useful technique to obtain polymeric drug controlled drug release systems and to produce clay nanocomposites that render exfoliate distribution. For neat polymers and loaded samples it is critical to have a proper optimization of micromolding conditions (amplitude, force and time) to avoid polymer degradation. Conclusions related to the specific objectives are extracted from each block of this PhD work and are below listed:

Ultrasound Micromolding: Biomedical Applications

- Chlorhexidine (CHX) and triclosan (TCS) were successfully loaded into a polylactide matrix with a uniform distribution and negligible polymer degradation by means of US micromolding with a short processing time. In this sense, the decrease in the final mechanical properties of pieces loaded with CHX is minimal compared to those obtained by classical melt processing.
- Ultrasound heating did not have a negative effect in the bioactivity of both antibacterial drugs. PLA/CHX and PLA/TCS (3 wt-%) presented clear bactericide and bacteriostatic effect against both Gram-positive and Gram-negative. CHX had a high bactericide effect within the first 24h while TCS delayed the bacterial growth for 10-15h. Bacterial growth could be reduced to 20% in comparison with neat PLA specimens.
- Microporous PLA scaffolds were successfully prepared by a combination of US micromolding and salt leaching techniques. PLA/NaCl specimens were properly ultrasound micromolded without cavitation problems and polymer degradation. Nevertheless, pores interconnections were insufficient and subsequent salt leaching process was inefficient. A small amount of water soluble polyethylene glycol was required in order to improve it. Final specimens could be prepared with a relatively homogeneous porous distribution that was appropriate to favor cell proliferation respect the non-porous sample.
- Polylactide and hydroxyapatite hybrids (PLA/HAp) with relatively homogeneous distribution of HAp particles and a maximum load of 60 wt-% could be micromolded under similar molding condition that those used for neat polymer. HAp incorporation provided thermal stability, improved mechanical properties and allowed to increase the hydrophilicity, an interesting feature for biological applications
- Antibacterial scaffolds were prepared with hydrophobic drugs, triclosan, with an insignificant solubilization during the leaching step. The presence of a high density of pores considerably improves the TCS release. Moreover, cell proliferation of MDCK epithelial cells was higher for TCS loaded porous scaffolds (200%) than for initial scaffold (170%). Porous scaffolds of

PLA/HAp could also be prepared with a porosity degree close to 35% with relatively good mechanical properties and enhanced cell colonization and proliferation.

Ultrasound Micromolding: Preparation of Nanocomposites

- Nanocomposites using multi-walled carbon nanotubes (MWCNT) or clays were successfully prepared by ultrasound micromolding. The use of appropriate amplitude, force and processing time were crucial to fill mold cavities completely and avoid molecular degradation for both neat polymers and their nanocomposites.
- US micromolding technique resulted to be a promising method to get directly molded nanocomposite specimens with the final shape to the selected application and without performing a subsequent processing as in the case of nanocomposites prepared by solvent casting, melt mixing or in situ polymerization.
- PLC/MWCNT nanocomposites with a proper nanotubes distribution and good dispersion of them were attained when solvent casting nanocomposite films were processed by ultrasound equipment.
- Carbon nanotubes were effective nucleating agents and had an influence on crystallization rate and even on lamellar morphology. Specifically, amorphous layer thickness was greater for the nanocomposite, facilitating a reordering process that led to an increased melting point. The nanocomposite rendered thicker lamellas at the beginning of the crystallization process due to the nucleation effect and the higher crystallization temperature.
- Nylon 12/N757 nanocomposites with an exfoliated microstructure were achieved without necessity of using typical organ modifiers in order to improve compatibility between the clay and the polymer matrix. In that sense, US micromolding overwhelms conventional method in the clay nanocomposite preparation.
- The incorporation of the clay prepared by US micromolding had a remarkable influence on the final crystalline. Nylon 12/N757 processed by ultrasounds presented an α' Form structure at room temperature which was an unusual result since neat polymer and nanocomposite samples obtained by solvent casting and melt crystallization presented an stable α' at high temperature, these rendered α or γ Form structures at RT.

Even-Odd polyamides: Crystalline structures and Polymorphic transitions

New series of polyamides based on azelaic acid (nylon 4 9, 8 9 and 12 9) and copolyamides 4 5+9_X (polyamides based on 1,4 butanediamine with different ratios of glutaric and azelaic acid), were

synthesized, characterized and structurally studied by real time calorimetric, spectroscopic and synchrotron X-ray diffraction data. These even-odd nylons had three polymorphic forms related to structures where hydrogen bonds were established in two planar directions. Two of them, named as Form I and Form II, are structures stablished at low temperature and are characterized by two strong reflections,. Form II is an intermediate crystalline structure usually developed on heating of Form I and its diffraction reflections are closer than in Form I. Typical pseudohexagonal arrangement characterized by a single reflection is achieved at high temperature after the named Brill transition, this crystalline structure is named as Form III.

- Nylon 8 9 and 12 9 performed transition to intermediate Form II on heating before merging to Form III, while nylon 4 9 Form I remained practically constant until the formation of high temperature pseudohexagonal packing (Form III). Although these observation seem to point out that low amide density favor the development of intermediate Form II this does not fit with the previous results seen for nylon 4 7 and 6 9 and the nylon 4 5 behavior shown in this work. Nylon 4 7 and 4 5 experimented typical transition Form I to III with the developing the intermediate Form II, while nylon 6 9 did not. New hypothesis postulate that the presence of reminiscent crystals having the intermediate Form II structure in the as-synthesized sample could probably favor the occurrence of this transition. It is clear if as-synthesized structures of nylon 12 9 and 4 9 are compared. Four X-ray diffraction reflections could be clearly observed in the initial pattern of nylon 12 9 which indicated coexistence of Form I and II, while for nylon 4 9 just two spacings related to Form I were present. Nylon 8 9 showed similar behavior as nylon 12 9 with lower ratio of Form II. Moreover, assays done with nylon 12 9 on cooling reflected that different ratios of Form I/II could be attained depending on thermal treatment.
- Nylon 4 9 showed complex structural transitions during heating and cooling processes being the ratio between the different crystalline forms stablished at room temperature (Form I and II) clearly dependent on the preparation method. As-synthesized sample presented pure Form I while samples crystalized from the melt gave rise to some Form II impurities. X-Ray profiles of samples obtained by solvent casting indicated that formation of Form II was favored when HFIP was changed by formic acid and when the polymer concentration in the solution increased. It is important to highlight that polymorphic transitions during heating processes was again clearly dependent on the presence of Form II. Thus, profiles indicated a direct transition from Form I to Form III or from Form I to Form II when traces of the intermediate structure (Form II) were absent or present, respectively. Before melting, nylon 4 9 achieved a typical pseudohexagonal arrangement (Form III) that was consequence of the Brill transition.
- Additionally, spherulites of melt crystalized nylon 4 9 were evaluated. Significant changes in morphology were detected despite the narrow crystallization temperature range (229-238 ºC). Flat-on and edge-on lamellar dispositions were detected at the highest and the lowest crystallization temperatures, changing the morphology from axialites to ringed spherulites and

the formation of speckled spherulites at intermediate temperatures. These morphology differences were not related to a change on the crystalline structure, nylon 4 9 presented Form III within this range of temperatures. Crystallization kinetic analysis for nylon 4 9 indicated two crystallization regimes which involved temperatures were in agreement with the observed morphologic changes.

- Initial X-Ray diffraction patterns of the as synthesized copolyamides based on 1,4 butanediamine with different ratios of glutaric and azelaic acid showed typical Form I structure of even-odd nylons with significant differences in the relative intensity of the two observed reflections. Intensity of the lower spacing reflection decreased while the content of glutaric acid increased due to the increase of the amorphous halo intensity and the presence of a secondary crystalline structure (Form II). The development of Form II on heating was independent of the chemical constitution of the crystalline fraction and was clearly dependent on the presence or absence of a second structure, named Form II in the as-synthesized samples. Thus, copolymers rich in glutarate units as well as the homopolymer (nylon 4 5) followed the typical development of Form II and its transition to From III, whereas nylon 4 9 and nylon 4 5+9_85 and 4 5+9_60 retained its Form I until the formation of Form III.
- All melt crystallized samples were constituted by forms I and II, being the later the minority one. Although, the presence of foreign units clearly hindered the crystallization spherulites were developed even when the comonomers content was high (i.e. nylon 4 5+9_50). Moreover, equilibrium melting temperature evaluation supported that comonomers units were excluded from the crystalline domains (i.e. were incorporated into the amorphous folding surfaces or into the amorphous interlamellar spherulitic regions).

Scientific Publications

- Olmo, C.; Rota, R.; Carlos Martínez, J.; Puiggalí, J..Franco, L. Temperature-induced structural changes in even-odd nylons with long polymethylene segments. *Journal of Polymer Science Part B: Polymer Physics* **2016**, *54*, 2494-2506. https://doi.org/10.1002/polb.24245
- Olmo, C.; Amestoy, H.; Casas, M.T.; Martínez, J.C.; Franco, L.; Sarasua, J.-R..Puiggalí, J. Preparation of Nanocomposites of Poly(ε-caprolactone) and Multi-Walled Carbon Nanotubes by Ultrasound Micro-Molding. Influence of Nanotubes on Melting and Crystallization. *Polymers* **2017**, *9*, 322. https://doi.org/10.3390/polym9080322
- Olmo, C.; Casas, M.T.; Martínez, J.C.; Franco, L..Puiggalí, J. Thermally Induced Structural Transitions of Nylon 4 9 as a New Example of Even–Odd Polyamides. *Polymers* **2018**, *10*, 198. https://doi.org/10.3390/polym10020198
- Olmo, C.; Casas, M.T.; Martínez, J.C.; Franco, L..Puiggalí, J. Crystalline Structures and Structural Transitions of Copolyamides Derived from 1,4-Diaminobutane and Different Ratios of Glutaric and Azelaic Acids. *Polymers* **2019**, *11*, 572. https://doi.org/10.3390/polym11040572
- Olmo, C.; Franco, L.; del Valle, L.J..Puiggalí, J. Preparation of Medicated Polylactide Micropieces by Means of Ultrasonic Technology. *Applied Sciences* **2019**, *9*, 2360. https://doi.org/10.3390/app9112360
- Olmo, C.; Franco, L.; del Valle, L.J..Puiggalí, J. Biodegradable Polylactide Scaffolds with Pharmacological Activity by Means of Ultrasound Micromolding Technology. *Applied Sciences* **2020**, *10*, 3106. https://doi.org/10.3390/app10093106
- Olmo, C.; Franco, L.; Vidal, A.; del Valle, L.J..Puiggali, J. Ultrasound micromolding of porous polylactide/hydroxyapatite scaffolds. *Express Polym. Lett.* **2021**, *15*, 389-403. https://doi.org/10.3144/expresspolymlett.2021.34

Abbreviations

%-wt	Weight percentage
ATR	Attenuated Total Reflectance
CFU	Colony Forming Units
CHX	Chlorhexidine
CNT	Carbon nanotubes
DSC	Differential Scanning Calorimetry
DTGA	Differential Thermogravimetric
E. Coli	*Escherichia coli*
EDTA	Ethylenediaminetetraacetic acid
EtOH	Ethanol
FDA	Food and Drug Administration
FRP	Fibre Reinforced Polymer
FT-IR	Fourier Transform Infrared Spectroscopy
GPC	Gel Permeation Chromatography
HAp	Hydroxyapatite
HFIP	1,1,1,3,3,3-hexafluoroisopropanol
MDCK	Madin-Darby Canine Kidney
Mn	Number average molar mass
Mw	Mass average molar mass
MWCNT	Multi-Walled Carbon Nanotubes
N757	Nanofil 757
PBS	Phosphate-Buffered Saline
PCL	Poly-ε-caprolactone
PD	Polydispersity
PE	Polyethylene
PLA	Polylactide
PMMA	Polymethymethacrylate
PP	Polypropylene
RMN	Nuclear Magnetic Resonance
S. epidermidis	*Staphylococcus Epidemidis*
SAXS	Small Angle X-ray Scattering
SEM	Scanning Electron Microscopy
SWCNT	Single-Walled Carbon Nanotubes
T_B	Brill Temperature
TCS	Triclosan
TEM	Transmission Electron Microscopy
TGA	Thermogravimetric Analysis
US	Ultrasound
USM	Ultrasound micromolding
UV-Vis	Ultraviolet-Visible spectroscopy
WAXS	Wide Angle X-ray Diffraction
XRD	X-Ray Diffraction